University of Southampton

Faculty of Engineering and Physical Sciences

School of Engineering

Strength analysis and failure prediction of glass adhesive joints

By

Ioannis Katsivalis

ORCID ID: 0000-0001-9614-0515

Thesis for the degree of Doctor of Philosophy in Engineering and the Environment

September 2019

University of Southampton

Abstract

Faculty of Engineering and Physical Sciences
School of Engineering
Thesis for the degree of Doctor of Philosophy in Engineering and the Environment

Strength analysis and failure prediction of glass adhesive joints

by
Ioannis Katsivalis

This research study seeks to evaluate the load response and failure prediction of glass/steel adhesive joints. The need for sustainable construction materials along with recent architectural trends and technological developments have made glass more accessible than ever before in the construction industry. Limited attempts have been made to compare the performance of bolted and adhesive connections for glass/steel structures, while interface characterisation studies are also lacking. Damage initiation and propagation in the adhesive layer is rarely modelled numerically, and the development of cohesive zone models has been restricted to reference values as hybrid coupon tests are difficult to test successfully. Lastly, while the degradation of glass/steel adhesive joints has been examined experimentally, a numerical tool for the prediction of the performance of the joints after exposure is currently lacking.

Benchmark designs of glass/steel bolted and adhesive joints were introduced and tested experimentally in four different load cases. Adhesive joints were found to be stronger and stiffer for all load cases examined. It was also observed that lower strength ductile adhesive (in terms of bulk properties) produced joints with higher failure loads. Numerical analyses showed that ductile adhesives developed a large plastic zone and redistributed the stress concentrations more effectively from the corners of the joints. Therefore, a larger adhesive area was resisting the loading. This understanding of the synergistic property combinations of strength and ductility of the adhesives led to the development of a numerical tool for the optimum selection of adhesives based on the joint design. The identified adhesive led to a significant strength increase for every load case examined.

The long term performance of glass/steel adhesive joints was evaluated by exposing the joints to conditions of high temperatures and humidity, and the degradation of the bulk properties and the interfaces was recorded. It was shown that the bulk properties and the interface properties degrade at different rates. The glass/adhesive interface degradation was shown to be more significant and controlled the failure performance of the joints.

Numerically, a continuum mechanics and a cohesive zone modelling (CZM) approach were evaluated for their suitability in predicting the failure load of glass/steel adhesive joints before and after environmental exposure. Input parameters for continuum mechanics approaches are based on bulk properties only and are easier to evaluate than CZM interface parameters. An in-house heat strengthening methodology development was necessary to increase the strength of small coupon sized glass substrates for accurate interface characterisation. It was shown in this work that both numerical methods were accurate in predicting the performance of the unaged joints. After environmental exposure, the CZM approach, which allows to account for the more severe interface degradation, performed significantly better. This finding highlights the need for reliable enhanced experimental testing procedures for interface characterization for hybrid glass/steel joints.

Table of Contents

Table of Tables

Table of Figures

Research Thesis: Declaration of Authorship

Print name:	Ioannis Katsivalis
Title of thesis:	Strength Analysis and Failure Prediction of Glass Adhesive Joints

I declare that this thesis and the work presented in it are my own and has been generated by me as the result of my own original research.

I confirm that:

1. This work was done wholly or mainly while in candidature for a research degree at this University;
2. Where any part of this thesis has previously been submitted for a degree or any other qualification at this University or any other institution, this has been clearly stated;
3. Where I have consulted the published work of others, this is always clearly attributed;
4. Where I have quoted from the work of others, the source is always given. With the exception of such quotations, this thesis is entirely my own work;
5. I have acknowledged all main sources of help;
6. Where the thesis is based on work done by myself jointly with others, I have made clear exactly what was done by others and what I have contributed myself;
7. Parts of this work have been published as:

Journal papers

1. Katsivalis I., Thomsen O.T., Feih S., Achintha M., Development of Cohesive Zone Models for the Prediction of Damage and Failure of Glass/Steel Adhesive Joints, *Int J Adhes Adhes*, (2019) 102479.
2. Katsivalis I., Thomsen O.T., Feih S., Achintha M., Failure prediction and optimal selection of adhesives for glass/steel adhesive joints, *Eng Struct*, 201 (2019) 109646.
3. Katsivalis, I., Thomsen, O.T., Feih, S. and Achintha, M., (2018), Strength evaluation and failure prediction of bolted and adhesive glass/steel joints. *Glass Structures & Engineering*, 3 (2), 183-196.

Conferences

1. Katsivalis, I., Thomsen, O.T., Feih, S. and Achintha, M., (2019), Development of cohesive zone models for glass/steel hybrid joints featuring environmental exposure effects, Paper presented at *5th International Conference on Structural Adhesive Bonding*, Porto, 11-12 July 2019
2. Katsivalis, I., Thomsen, O.T., Feih, S., Achintha, M. (2019), Optimisation and failure prediction of glass/steel adhesive joints, Poster presented at *SIMTech Poster Symposium*, Singapore, 25 January 2019
3. Katsivalis, I., Thomsen, O.T., Feih, S., Achintha, M. (2018), Numerical failure prediction and optimisation of glass adhesive joints, Paper presented at *SIMULIA ASEAN Regional User Meeting 2018*, Singapore, 24 October 2018
4. Katsivalis, I., Thomsen, O.T., Feih, S., Achintha, M., (2018), Strength evaluation and failure prediction of bolted and adhesive glass/steel joints. *Challenging Glass Conference Proceedings*, [S.l.], v. 6, p. 402, Delft, 17-18 May 2018. ISSN 2589-8019.
5. Katsivalis, I., Thomsen, O.T., Feih, S., Achintha, M. (2017), Failure modelling of bolted and adhesive glass joints, Paper presented at *SIMULIA ASEAN Regional User Meeting 2017*, Singapore, 12-13 October 2017
6. Katsivalis, I., Thomsen, O.T., Feih, S., Achintha, M. (2017), Strength evaluation and failure prediction of glass in bolted and bonded joints using digital image correlation, Poster presented at the *19th Young Researcher's Conference*, London, 5 April 2017

Signature: Date:

Acknowledgements

Many people have contributed to this thesis and I would like to thank all of them for their assistance, advice and support. Without them this PhD thesis would not have been possible.

First of all, I would like to thank my supervisors Dr Mithila Achintha, Professor Ole Thybo Thomsen and Dr Stefanie Feih. Mithila, thank you for giving me the opportunity to work in this interesting project and for all the dedication and support throughout this 4 year period. Ole, I would like to thank you for being involved and interested in the project even though you only joined in the 2nd year. Your ideas, suggestions and corrections helped to take this project to a very interesting direction that I could not imagine before you joined.

Stefanie, I can’t express how grateful I am for having the opportunity to work with and learn from you. Your availability whenever needed, your enthusiasm and interest on the project, the endless hours you spent correcting my drafts and your smile whenever we were meeting were an invaluable help and support. I could never imagine having a better mentor and supervisor for my PhD study and I am sure this project would not be the same without you.

Besides my supervisors, I would like to thank all the technical staff in both the University of Southampton and A*STAR (Singapore) who assisted me in conducting my experimental and numerical analyses. In particular, I would like to thank Dr Andy Robinson for the invaluable technical support in the TSRL. Andy, thanks for everything, it was a pleasure working with and learning from you. In addition, Wu Zi An has been an incredible colleague and friend in SIMTech. Zi An thanks for making my time in the lab (and the travelling between different locations) much easier. I would also like to thank Dr Andy Chipperfield for all the invaluable support during the first two years of my studies.

During my PhD, I also met many PhD researchers who all helped to make this experience much easier and enjoyable. At first, I would like to thank my friends and colleagues from the University of Southampton, Orestis Vryonis, Vaggelis Senis, Tim Harrell, Amy Welch, Martina Patone, Eirini Tzouka, Despoina Manouseli, Edgar Ferro, Bogdan Balan and my flatmate Onur Uraz. In addition, I would also like to thank my friends and colleagues from A*STAR and Singapore, Daniela Pirri, Lefteris Statharas, Francesca Mandino, Will Ambler, Srdjan Masirevic, Judith Fuelle and Gioia Fusaro. Finally, I should thank my friends Thanasis Georgiadis and Alkistis Krimpeni for always being available and listening to all my thoughts and problems.

I must also express my very profound gratitude to my parents Anna and Apollon and my sister Alkistis for providing me with support and encouragement, not only during my thesis but during my entire life. This accomplishment would not have been possible without you!

This research was financially supported by the Faculty of Engineering and the Environment of the University of Southampton, UK and the Agency for Science, Technology and Research (A*STAR), Singapore and their support is much appreciated.

Nomenclature

α_{T}	Nominal value of average coefficient of linear expansion between 20°C and 300°C.
β	Dilation angle
γ	Angle of the laser beam
δ	Optical retardation
δ_n^c	Critical opening displacement in mode I
δ_s^c	Critical opening displacement in mode II
ε	Emissivity
ε_{c}	Critical strain
$\varepsilon_{\mathrm{eng}}$	Engineering strain
$\varepsilon_{\mathrm{fC}}$	Failure strain in uniaxial compression
$\varepsilon_{\mathrm{fT}}$	Failure strain in uniaxial tension
ε_{true}	True strain
η	Stress triaxiality
λ	Thermal conductivity
μ	Friction coefficient
ρ	Density
σ	Current stress tensor
$\bar{\sigma}$	Undamaged stress tensor
$\sigma_1, \sigma_2, \sigma_3$	Principal stresses
σ_{eng}	Engineering stress
σ_{fC}	Failure stress in uniaxial compression
σ_{fT}	Failure stress in uniaxial tension
σ_{n}	Peel stress
σ_{true}	True stress
σ_{yC}	Yield stress in uniaxial compression
σ_{yT}	Yield stress in uniaxial tension
τ	Shear stress
b	Width
c	Half of overlap length
C	Photoelastic constant
c_{p}	Specific heat capacity
D	Damage variable
d	Diameter of bolt
E	Young's modulus
e_{c}	Critical strain at damage initiation
F	Axial force of bolt
G	Shear modulus
G_n	Fracture energy in mode I
G_n^c	Critical fracture energy in mode I
G_s	Fracture energy in mode II
G_s^c	Critical fracture energy in mode II
K	Bending stiffness

k	Bending moment factor
k'	Transverse force factor
l	Overlap length
M	Bending moment
n	Main refractive index to visible radiation
P	Applied load
$\overline{P}$	Load per unit length
p	Hydrostatic pressure
t_{a}	Thickness of adhesive
t_{b}	Thickness of bottom adherend
t_{eff}	Effective stress
T_{g}	Glass transition temperature
t_{n}	Traction in mode I
t_n^c	Critical traction in mode I
t_{s}	Traction in mode II
t_s^c	Critical traction in mode II
t_{t}	Thickness of top adherend
v	Poisson's ratio
w	Width of DCB/SLB specimens
X	Normalised position along the adhesive layer
x	Origin of longitudinal co-ordinate

Chapter 1 Introduction

1.1 Background and motivation

Concrete and steel are the most common structural materials used in the construction industry [1]. The production of cement, the basic constituent of concrete, is responsible for 5-7% of the total CO_2 emissions in the world [2]. At the same time steel, compared to other construction materials, has the highest embodied energy [3] leading to global warming and climate change. The need for sustainable construction materials along with recent architectural trends and technological developments have made glass more accessible than ever before in the construction industry.

Glass is reusable and recyclable and can potentially reduce the energy needs of buildings [1]. Glass also produces perceived aesthetic advantages due to its transparency. From massive structures in which glass has been used like the Shard [4] to experimental designs like the glass truss bridge as shown in Figure 1.1 [5], glass has the potential to be used extensively in the construction industry if it can be designed and used safely while carrying structural loads. In order to achieve this aim, glass needs to be understood better in terms of material properties, design, performance, durability, post breakage scenarios and repairs. This understanding will help in assessing and correctly utilising the vast amount of products that are currently available.

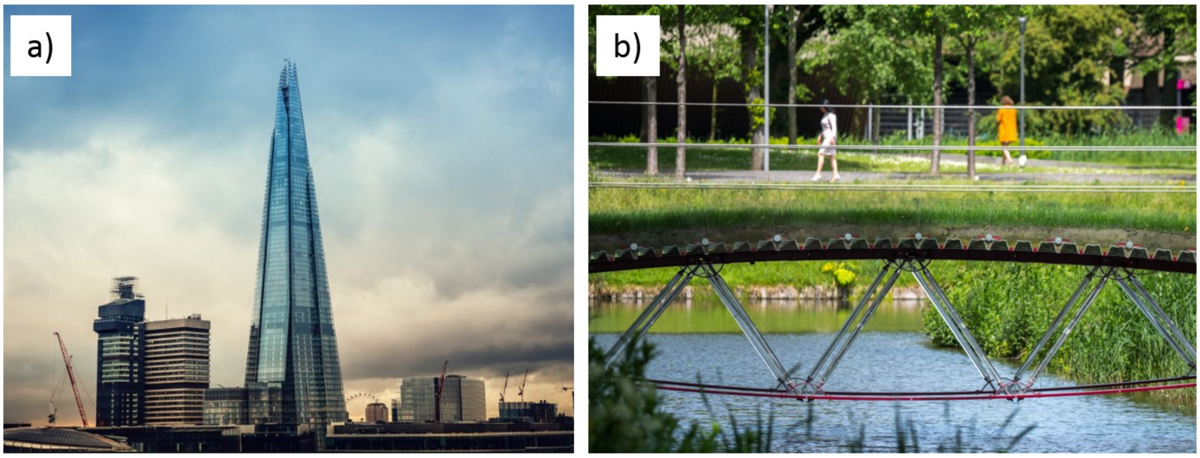

Figure 1.1: Examples of a) large scale (the Shard) and b) smaller scale glass structures (the glass truss bridge).

One of the main challenges when using glass as a structural material is its brittleness and the relatively low tensile strength. The main difference between glass and other structural materials, such as e.g. steel, is that it does not display plastic yielding, but instead fails in a stochastic way [6]. In other words, glass exhibits brittle behaviour with a perfectly linear elastic load response up to failure, but with no ability for redistribution of stress concentrations. The failure of glass can happen without any warning in a catastrophic manner once the critical strength is reached. The lack of a plastic region makes the concentration of stresses particularly dangerous for any glass structure. Accordingly, it is important to eliminate or avoid stress concentrations in structural glass members. Among the most susceptible areas for the stresses to concentrate are load introduction or connection points, typically realized by bolted connections. Therefore, even though bolted joints are being used extensively, they lack structural efficiency and reliability. The main reason for that is because of the drilling process, which introduces flaws and discontinuities on the glass surface. In practice, this leads to designers applying highly conservative safety factors, hence increasing the weight and cost of the structure.

This thesis aims to explore another type of connection: adhesively bonded joints. This type of connection has structural advantages as it limits the development of high stresses as well as avoids the formation of additional surface flaws. Unlike conventional mechanical joints, adhesive joints do not significantly increase the weight of the structure and have aesthetic advantages since they offer uninterrupted surfaces and possibly transparency. Adhesive joints, however, are very sensitive to environmental exposure, especially when bonded to glass surfaces. A reliable prediction method for their performance is currently lacking.

Soft elastic adhesives like silicone have been used effectively in glazing systems, but have not been used for load-carrying applications. On the other hand, stiff adhesives, such as acrylics and epoxies, have been used in other industries, such as structural adhesive joints in FRP composite materials [7], but are relatively unproven in applications relating to structural glass [8]. However, the research in this field is growing constantly, and some commercial projects utilising glass adhesive joints have already been constructed.

In summary, the motivation for this thesis arises from the following shortcomings of the current state-of-the-art knowledge, hindering wider applications of glass in structural and load-bearing applications:

1. Glass needs to be understood better in terms of material properties, design, performance, and durability;
2. Bolted joints are the most common joining method, but should be replaced by other joining methods as they lack structural efficiency and reliability for glass substrates; and
3. Structural adhesive joints are relatively unproven in applications relating to structural glass.

1.2 Aims and objectives

The aim of the project is to develop an understanding of the load response and failure behaviour of hybrid glass/steel adhesive joint configurations by using experimental and numerical methods. The objectives of the project are:

1) To develop a complete experimental programme for the testing of bolted and adhesive hybrid glass/steel joints under different load cases and to compare the respective performances.

2) To develop a validated finite element (FE) modelling approach of the quasi-static load response and failure behaviour of hybrid glass/steel adhesive joints. Two different modelling approaches based on (1) continuum mechanics and (2) cohesive zone modelling are compared.

3) To develop a methodology for the optimum selection of adhesives for increased joint strength based on their mechanical properties for given designs and joint geometries.

4) To develop a methodology to predict the effect of the environmental exposure on glass/steel adhesive joint strength by exposure to conditions of high humidity and temperature. The effects need to be separated into (1) degradation of the bulk properties of the adhesives and (2) the glass/steel interfaces.

1.3 Outline of the thesis

This section provides an overview of the structure of the thesis. More specifically, *Chapter 1* of the thesis serves as an introduction to the topic, presenting the research question along with the aims and objectives. Finally, a brief outline of the whole report is given in the first chapter.

Chapter 2 of the thesis provides an extended review of the literature on the topic. More specifically, the review provides some of the most important analytical solutions for adhesive joints, reviews the failure criteria that are commonly used and finally discusses some recent developments on the modelling of these joints. Moreover, the review focuses on research and industrial applications of glass adhesive joints highlighting the relevant experimental and numerical work that has taken place.

C*hapter 3* of this thesis introduces the material characterisation testing methodology. This includes tests of adhesive coupons in tension and compression and also includes details about the measurement of the residual stresses in the glass. Finally, a methodology for the in-house glass heat-strengthening of small glass coupons is also presented and validated. This work is required to addresses objectives 1 and 2.

In *Chapter 4,* standardised interface characterisation tests were modified and used for the extraction of the cohesive laws in modes I and II. The experimental set-up, the testing procedures and the subsequent numerical data fitting are presented, and cohesive zone models are established. This work is required to address objectives 1 and 2.

In *Chapter 5,* an initial experimental comparison between bolted and adhesive joints takes place. For the comparison, two different adhesives are used, a brittle and a ductile one. The comparison between the two different adhesive joints and the bolted joints is performed in four different load cases and the load response and failure loads and mechanisms are studied. The findings in this chapter complete objective 1.

In *Chapter 6,* FE models of the joints described in Chapter 5 are developed and validated against the experimental observations. Two different FE methods are employed and both are compared with the experimental data. In addition, failure analysis of the adhesive layers leads to a better understanding of the performance of the joints and indicates that optimum combinations of strength/ductility might exist for given designs. This work completes objective 2.

In *Chapter 7,* FE methods are employed to lead to an optimum selection of adhesives based on their mechanical characteristics. A parametric methodology is developed and leads to a better understanding of the effect of the strength/ductility on the bonded areas. An optimum adhesive is selected, characterised and evaluated numerically and experimentally, leading to very significant strength increases in all load cases examined. This work presents a novel approach to complete objective 3.

In *Chapter 8,* the effect of environmental exposure is studied. The exposure cycle is based on European guidelines for the use of sealants in buildings. The degradation of the bulk properties, the interfaces and the glass/steel joints is studied and cohesive laws capturing degradation effects are developed. The numerical model is validated against experimental data. This work addresses and completes objective 4.

Finally, in *Chapter 9,* the conclusions drawn from the previous chapters are summarised, critically assessed and presented. In addition, the limitations of the current work are reported and future work is suggested.

Chapter 2 Literature review

2.1 Introduction and structure of the review

The use of adhesive joints has expanded significantly to almost every industrial sector in recent years. In engineering, adhesive joints are common practice in the aerospace and the automotive industries, but their use is still limited in the construction industry. However, the presence of precise analytical solutions, the implementation of accurate failure criteria and the development of advanced numerical models has made the analysis and application of adhesive joints more approachable to designers and engineers.

The main properties of glass as outlined briefly in Chapter 1 indicate that the joints between glass members are of great importance. Using bolted joints is a well-established method, but introduces a number of problems when used in glass connections. Just to state a few:

1. Bolt holes need to be drilled leading to concentration of stresses in these areas.
2. Concentration of stresses can also be a result of dimension inaccuracies and eccentric loads.
3. Introduction of surface flaws due to drilling of glass.
4. Drilling has to be performed before the tempering process.
5. The aesthetic result is not ideal due to interrupted glass surfaces.
6. Self-loosening of the bolts can be the result of cyclic loading which eventually reduces the strength of the joint.

As an alternative to bolted joints, adhesive joining of glass for load-carrying applications is also the subject of extensive research. This method avoids drilling, can be applied before or after the tempering process and leads to uninterrupted surfaces. At the same time, glass adhesive joints also have disadvantages, mainly due to the lack of knowledge and practical applications. Just to state a few:

1. Enormous range of physical and mechanical properties of adhesives.
2. Difficulties in modelling and predicting the complex material behaviour of adhesives and quantifying the long-term performance and durability of these connections.
3. Experienced personnel needed for the manufacturing of these joints.
4. Lack of standards for the design and testing of adhesive joints.
5. Catastrophic failure events are more likely to cause irreversible damage to adhesive joints compared to bolted joints. In the latter case, bolts can act as crack stoppers and the damage may be progressive.

6. Repair or replacement of adhesive joints is difficult.

Practical applications and ongoing research cover most types of adhesives namely, acrylates (e.g. Araldite 2047-1), epoxy resins (e.g. Araldite 2020), polyurethanes (e.g. Sikaflex 265) and silicones (e.g. DC993). The latter one has been used extensively in the construction industry, especially for structural sealant glazing systems (SSG). However, adhesives from the other groups are gradually being used more often in civil engineering applications, and some of these will be presented later in this report. The main difference between silicone and polyurethane compared to the other adhesive groups is that the first ones are normally designed to carry short term loads, like wind loads but not to transfer longer term loads (e.g. dead loads) [9].

Elastomers such as silicone and polyurethane have a low cross-link density and are generally very flexible. Moreover, silicones have a very low modulus of elasticity (in the range of 10-50 MPa) which means that they are unable to provide effective connections for built up sections of glass [8]. On the other hand, thermosets like acrylics and epoxy resins have a very high cross-link density, set irreversibly and are very stiff and strong [8]. As a result, they can be designed for carrying long term loads as well. As a rule of thumb it can be said that adhesives with low modulus of elasticity are suitable for holding glass in place, while adhesives with higher elastic modulus are suitable for carrying shear forces.

In recent years, research has focused on the use of stiff adhesive joints in glass structures due to the structural and architectural advantages that this technology has to offer. This literature review presents the most common analytical solutions being used for the estimation of stresses within the adhesive, strength-based failure criteria and non-linear constitutive models and finally techniques that combine continuum and fracture mechanics for the modelling of adhesive joints. The last part of the review focuses on applications of glass adhesive joints. Finally, the limitations of the current research are discussed so that the novelty of the current project can be highlighted.

2.2 Structural use of glass

Glass has been used in the construction industry for a long time, mostly for non-load bearing applications. However, glass behaves differently compared to most other structural materials like concrete and steel, thus leading designers and engineers to limit its usage. At the same time, recent architectural trends along with the huge progress that has taken place recently in the computing power and the development of finite element analysis packages have made the use of glass for load bearing applications a realistic possibility.

The main difference between glass and other structural materials, such as e.g. steel, is that it does not show plastic yielding, but instead fails in a stochastic way [6]. In other words, glass exhibits brittle behaviour with a perfectly linear elastic load response up to failure, but with no ability for redistribution of stress concentrations. The behaviour of a structure however, should not depend on the failure of a single element, and also, failure of a single element should not threaten the safety of the structure and its users. Accordingly, it is important to eliminate or avoid stress concentrations in structural glass members. In practice, this leads to designers applying highly conservative safety factors, hence increasing the weight and cost of the structure.

In addition, glass is reusable and recyclable and can also help to significantly reduce the energy needs of a structure [1]. For instance, the needs for lighting in a glass structure are much lower compared to conventional concrete/steel buildings. As a result, glass has the potential to be used extensively in the construction industry if it can be designed and used safely while carrying structural loads. In order to achieve this aim, glass needs to be understood better in terms of design, performance, durability, post breakage scenarios and repairs.

2.2.1 Production-Composition

Float glass is currently the most widely used type of glass. Its manufacturing process as seen in Figure 2.1, was developed by the Pilkington company in the 1950's and revolutionised the glass industry offering high quality glass without the need for time consuming and expensive finishing. Float glass today accounts for 35% of all glass products [10] and its applications include glass for windows, facades and furniture and structural glass among others. The composition of float glass is summarised in Table 2.1. Occasionally, depending on the demands of the production and for altering some properties of glass, other substances might also be introduced to the composition. However, the amounts of these substances are relatively small.

Table 2.1: Composition of float glass [11].

Silicon dioxide (SiO_2)	69-74%
Calcium oxide (CaO)	5-14%
Sodium Oxide (Na_2O)	10-16%
Magnesium Oxide (MgO)	0-6%
Aluminium Oxide (Al_2O_3)	0-3%
Others	0-5%

The main principles of glass production are that the raw materials are melted at 1600-1800°C, formed at 800-1600°C and cooled at 100-800°C. This method is used for manufacturing windows and of relevance to this project structural glass. It offers significant advantages since it is cost effective, has better aesthetic results and can consistently produce large glass panes.

Figure 2.1 shows the float glass production process. The raw materials, which are silica sand, lime and soda along with recycled broken glass (cullet) are inserted in a furnace where they are allowed to melt. Afterwards, the materials that have become the molten glass are going through a tin bath at temperatures that range between 1000°C at one end of the bath to 600°C at the other. The reason why the bath is made of tin is because of its physical properties. Not only does tin remain in liquid state over the range of the temperatures that the glass is produced but it is also heavier hence allowing the glass to flow over it in the tin bath. Finally, the glass goes through the annealing lehr where it is gradually cooled down from about 500°C to 100°C. The speed of the process determines the thickness of the glass [12].

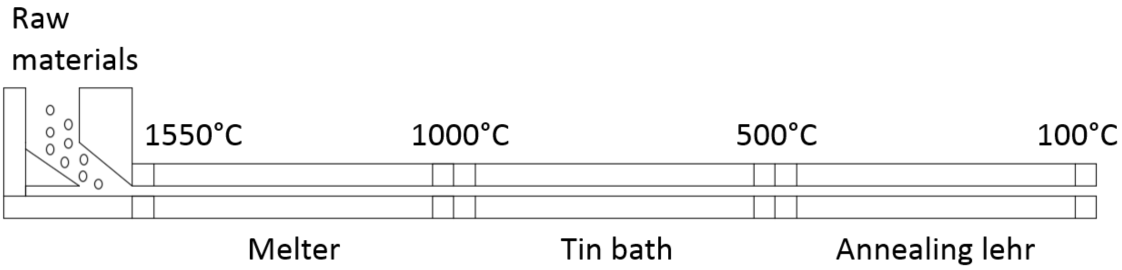

Figure 2.1: Float glass production process.

This process shows that the two sides of glass are treated differently. One side is in contact with the air the whole time, while the other is in contact with the tin. It is easy to distinguish which side was in contact with the tin by using ultraviolet radiation. According to Haldimann et al. [8], the tin side has limited strength compared to the air side and the adhesion might be influenced as well in glued joints. The product of this process is annealed glass which can later be processed in various ways. For instance, annealed glass can later be cut, drilled or thermally treated depending on the needs.

2.2.2 Physical and mechanical properties of glass

The physical and mechanical properties of soda lime silicate glass (SLSG) are summarised in Table 2.2.

Table 2.2: Physical and mechanical properties of float glass [6, 11].

Physical properties of float glass		
Characteristic	Symbol	Value and Unit
Density	ρ	2500 kg m^{-3}
Young's modulus	E	70 GPa
Poisson's ratio	v	0.23
Specific heat capacity	c_p	720 J kg^{-1} K^{-1}
Nominal value of average coefficient of linear expansion between 20°C and 300°C.	α_T	9×10^{-6} K^{-1}
Thermal conductivity	λ	1 W m^{-1} K^{-1}
Main refractive index to visible radiation	n	1.5
Emissivity	ε	0.837
Fracture toughness	G_{Ic}	0.7 MN m$^{-3/2}$
Glass transition temperature	T_g	570°C

It should also be noted that the behaviour of glass is governed by its tensile strength even though its compressive strength is significantly higher. Buckling and transverse contraction effects due to Poisson's ratio lead to tensile stresses which in turn exceed the tensile capacity of the material long before it is loaded compressively to failure [8]. The tensile strength of glass, however, is not a material property. On the contrary, the effective tensile strength of glass depends on the load amplitude and duration, the presence of initial surface flaws, the residual stresses and the environmental conditions [8]. Especially flaws, which range from sub-micro-cracks, not visible to the naked eye, to visual flaws on the surface, play a governing role. Unlike the tensile strength, the critical combination of stress and crack length for fast fracture is a material constant [6]. This property is defined as the fracture toughness of glass.

2.2.3 Tempered glass

Compressive strength of glass is much higher than its tensile strength. This led to the idea of processing the glass in such a way such that advantage of the high compressive strength can be taken. Float glass is heated up to about 650°C (about 100°C above its glass transition temperature) in a furnace and then cooled rapidly using a jet of cold air. The result of this procedure is that the surface of the glass solidifies first and is then followed by the internal regions of the glass. As a consequence of this gradual solidification, residual stresses are developed, with the surfaces under compression, a favourable stress state for the glass due to the potential surface flaws, and the interior in tension.

The cooling rate determines if glass undergoes a full tempering or a heat strengthening procedure. In theory, optimum tempering is achieved if the solidification of the surface occurs when the temperature difference is maximum. The effect of tempering can be seen in Figure 2.2. Here, tempering creates a layer in compression close to the surfaces of the glass. This layer prevents the opening and growing of surface flaws due to tensile stresses and therefore increases the strength of the glass significantly. Characteristic values for the residual compressive stresses for fully tempered glass are between 80-170 MPa, while for heat strengthened glass they are between 40-80 MPa [8].

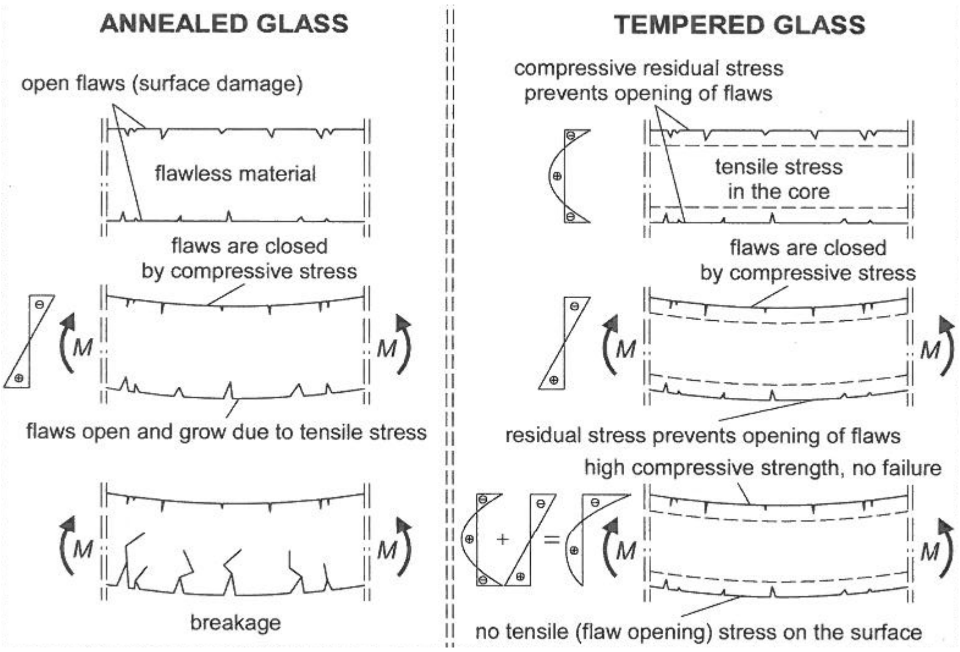

Figure 2.2: Different structural performance under loading of float and tempered glass [8].

A series of textbooks are available in the literature for further information on glass [6, 8-10, 12, 13] and provide extensive reviews.

2.3 Structural adhesives

The term adhesive is used for materials that are used to bond two surfaces together. The surfaces that are glued by the adhesive are called adherends, while the result of gluing two surfaces is called adhesion. Adhesives based on synthetic polymers are one of the most used materials in today’s world. Especially, in the last 100 years the application of adhesives has extended to almost every industrial sector. The range of applications of adhesives indicates that there is a wide range of types depending on the use. This project focuses on adhesives used for structural applications. Adhesives are polymer materials and can be divided into three categories based on their thermo-mechanical properties:

- Thermoplastics which are controlled by weak intermolecular forces (e.g. polyvinyl butyral (PVB)).
- Elastomers which are rubbery materials that can be stretched significantly and return to their original shape once the loading is removed (e.g. silicones).

- Thermosets which set irreversibly in the presence of heat and further heating cannot reshape the material (e.g. epoxies).

Typically, elastomers experience high elongation when loaded due to their low cross-linking density and have relatively low elastic modulus. Characteristic examples of elastomers are silicone and polyurethane. Thermoset adhesives, like acrylics and epoxies, are stiff, stronger and less ductile compared to elastomers. Elastomers and thermosets are the two main adhesive families that are being used in the construction industry, each of them for different purposes. Table 2.3 summarises the main commercial adhesive types and highlights their characteristic features.

Table 2.3: Adhesive types and their main mechanical features [14].

Adhesive type	General properties
Silicones	Low strength and stiffness
	High durability and resistance against UV-radiation
	Hyper-elastic material behaviour
MS-polymers	Medium strength and stiffness
	Medium resistance against moisture and UV-radiation
	Hyper-elastic material behaviour
Polyurethanes	Medium strength and stiffness
	Low resistance against UV-radiation
	Hyper-elastic material behaviour
Acrylates	Generally high shear strength and small optimal thickness
	Generally low resistance against moisture
	Visco-elastic material behaviour
Epoxies	High strength and stiffness, brittle
	Small optimal thickness
	Linear-elastic material behaviour

2.3.1 Adhesion theories

Adhesion only occurs under certain circumstances. According to Adams et al. [7] the following are the main theories that lead to adhesion:

- The weak boundary layer theory proposes that clean areas that are not contaminated are capable of producing strong bonds.

- The diffusion theory suggests that identical non-cross-linked polymers that come to contact have their molecules interdiffuse so that the boundary cannot be found anymore.
- Chemical bonding theory suggests that covalent or ionic bonds are formed across the interface leading to very strong bonding.
- The mechanical interlocking theory applies to surfaces of adherends that are significantly uneven. The adhesive enters the gaps and hardens afterwards.
- The physical adsorption theory assumes that the adhesive and adherends have intimate molecular contact and are connected with each other by van der Waals forces.

The latter one is considered to be the main mechanism that occurs in adhesive joints. This does not mean that the other theories are not applicable or do not contribute in the joint, but most of the strength is coming from physical adsorption [7].

2.3.2 Adhesive properties

The behaviour of adhesives depends highly on temperature and therefore will vary significantly in different environments. The main temperatures that characterise an adhesive are the glass transition temperature, the melting temperature and the decomposition temperature. The most important of these in relation to structural adhesive joints is the glass transition temperature (T_g). T_g does not lead to a sudden change in the properties of the adhesive, but leads to molecular motion instead. However, gradually properties like the strength and the modulus of the adhesive will degrade once service temperatures approach or exceed T_g. When the adhesive is below its glass transition temperature, it is considered to be in its glassy state where the molecules are considered to be frozen.

The effects of the glass transition temperature in an adhesive are easier to be understood by the free volume theory. According to that an adhesive consists of occupied and free volume. After a certain temperature the free volume decreases due to expansion of the polymer until a critical point at which the chain segments become mobile. This molecular motion leads to the degradation of the adhesive properties [7]. This value is different for each adhesive given that it depends on the cross-linking density of the polymer. For instance, epoxies tend to have higher glass transition temperatures compared to acrylates and thus are more suitable for high temperature applications [8].

Apart from the thermal properties, the mechanical properties need to be considered as well before modelling, testing or designing an adhesive joint. Key parameters could include the elastic and shear modulus, Poisson's ratio, yield and failures stresses and strains and the fracture toughness in different modes among others. Under loading an adhesive can be considered to undergo three phases before failure: i) the elastic region, where the behaviour of the material is governed by its elastic modulus,

ii) the non-linear region also known as yielding and iii) the plastic region where the behaviour of the adhesive is highly non-linear.

2.3.3 Adhesive joints

Figure 1.4 shows the most common adhesive joint configurations in construction engineering. Single or double lap joints are very important in order to understand the performance of an adhesive. As a matter of fact, single and double lap joints are used mostly for testing purposes rather than in actual construction applications. They tend to load the adhesive in shear, which is a favourable stress state for the adhesives especially compared to peel stresses, which act normal to the bonded surface. Even though single or double lap joints are not directly used as actual structures, most other types of joints used are loaded in a similar manner. Another important type of adhesive joint is the butt joint. This type should generally be avoided in actual structures because it mostly leads to peel stresses. However, it is very important as a testing method since it helps in determining the limit conditions of adhesive joints. The rest of the joints that are shown in Figure 2.3 can be considered a combination of lap and butt joints.

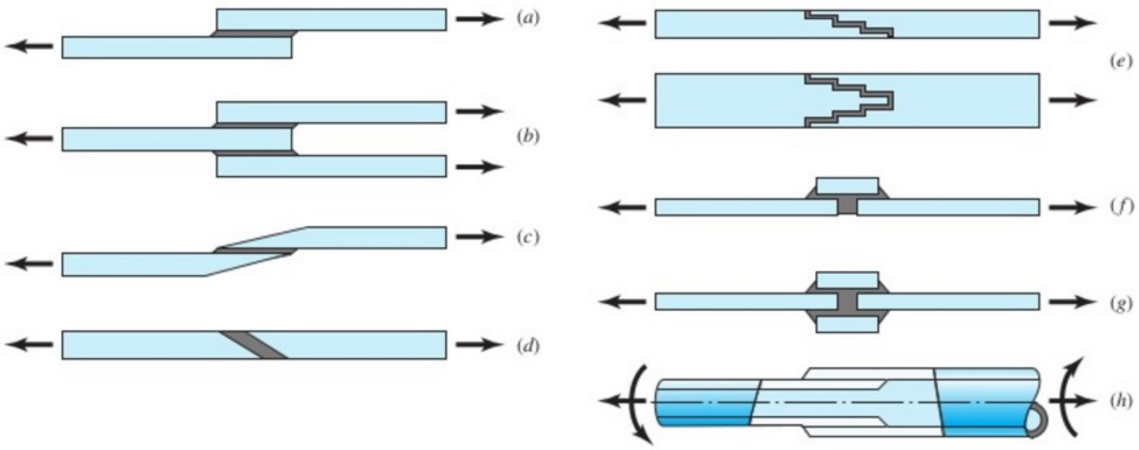

Figure 2.3: Various joint types: a) single lap, b) double lap, c) scarf, d) bevel, e) step, f) butt strap, g) double butt strap, h) tubular lap [15].

A series of textbooks are available in the literature for further information on adhesives and adhesion [7, 16-18] which provide comprehensive reviews.

2.4 Analytical methods

In recent years computing power has increased significantly, and the development of validated and robust commercial finite element packages with well-developed and convenient user interfaces has made stress analysis of bonded joints more approachable for designers and engineers. However, finite element modelling is still non-trivial (requires considerable skill and knowledge to be done correctly), takes time and there are a lot of parameters that need to be considered before meaningful or trustworthy results can be made available. Therefore, there is still a need for simplified analytical solutions that can be used as preliminary analysis tools prior to commencing FE modelling. Such analytical models can provide a faster and easier way to predict stresses within a joint, and also can be a useful tool for initial parametric studies. Obviously, the accuracy and the applications of analytical solutions are limited and for complex joints FE models are still preferable. However, for simple applications like single lap joints, as the one shown in Figure 2.3a, there are a number of analytical solutions that will be discussed in this section.

The most simple and straightforward analysis that can be performed for a single lap joint is to use a simple equation which would relate the average shear stress τ within the adhesive with the load applied P, the overlap length l and the width of the joint b as follows

$$\tau = \frac{P}{bl}. \tag{2.1}$$

In this simple equation the adherends are considered to be rigid and the adhesive is considered to deform only in shear [7] which is the optimum stress state for an adhesive joint. This is a very coarse approach since it complete neglects the stress peaks in the ends of the overlap.

2.4.1 Volkersen's analysis

A further development of this theory was proposed by Volkersen [19], which included the concept of differential shear. Here, the adherends are no longer considered rigid but can deform elastically in tension or compression. Therefore, the shear stresses within the adhesive vary over the bond line length, which is much closer to the realistic scenario. According to Volkersen the maximum shear stresses occur at the ends of the adhesive layer, while the minimum shear stresses are located in the middle of the overlap. The analysis of Volkersen did not take into account the eccentric load path that leads to bending within the adhesive joint. However, it is quite accurate when double lap joints are considered, since these joints do not have eccentric load paths. The adhesive shear stress (eq. 2.2) according to Volkersen can be calculated as

$$\tau = \frac{P}{bl}\frac{w}{2}\frac{\cosh(wX)}{\sinh(\frac{w}{2})} + \left(\frac{\psi - 1}{\psi + 1}\right)\frac{w}{2}\frac{\sinh(wX)}{\cosh(\frac{w}{2})}. \tag{2.2}$$

Once again P is the load, l the overlap length and b the width of the joint. In addition, w is a parameter that is related to the thickness of the top and bottom substrates, their respective elastic modulus and the overlap length while X is the ratio between the longitudinal coordinate (with the origin considered in the midpoint of the overlap) divided by the overlap length. Equations for these parameters can be found in Appendix A.

2.4.2 Goland and Reissner's analysis

The next development in the calculation of the stresses within an adhesive single lap joint was proposed by Goland and Reissner [20]. In their analysis the eccentric load path that leads to transverse forces and bending moments was also considered. This is achieved by using a bending moment factor k which relates the bending moment M acting on the adherend (of thickness t_t) to the acting load P as follows

$$M = kP\frac{t_t}{2}. \tag{2.3}$$

The shear (eq. 2.4) and peel (eq. 2.5) stresses can be calculated as

$$\tau = -\frac{1}{8}\frac{\bar{P}}{c}\left[\frac{\beta\, c}{t}(1+3k)\frac{\cosh\left(\left(\frac{\beta\, c}{t}\right)\left(\frac{x}{c}\right)\right)}{\sinh\left(\frac{\beta\, c}{t}\right)}+3(1+k)\right], \tag{2.4}$$

$$\begin{aligned}\sigma_n = \frac{\bar{P}t}{\Delta c^2}\Bigg[&\left(R_2\lambda^2\frac{k}{2}+\lambda k'\cosh(\lambda)\cos(\lambda)\right)\cosh\left(\frac{\lambda\, x}{c}\right)\cos\left(\frac{\lambda\, x}{c}\right)\\ &+\left(R_1\lambda^2\frac{k}{2}+\lambda k'\sinh(\lambda)\sin(\lambda)\right)\sinh\left(\frac{\lambda\, x}{c}\right)\sin\left(\frac{\lambda\, x}{c}\right)\Bigg].\end{aligned} \tag{2.5}$$

In equations 2.4 and 2.5, $\bar{P}$ is the load per unit width, c is half of the overlap length, β, γ, λ, R_1, R_2, Δ are parameters related to the stiffness and the thickness of the adherends and the adhesive and the geometry of the joint, t is the thickness of the adherend, k' is the transverse force factor and is related to the loading conditions and the geometry, and finally x is the longitudinal co-ordinate and its origin is considered to be in the middle of the overlap. Equations for these parameters can be found in Appendix A.

2.4.3 Hart-Smith's analysis

Hart-Smith [21] also developed an analytical solution that predicts the distribution of shear and peel stresses within the adhesive. Similarly to Goland and Reissner, Hart-Smith has also considered the eccentric load-path of the single lap joint. The main difference with the previous theory is that large deflections along with the individual deformations of the adherends were considered [22].

The distribution of shear stress (eq. 2.6) and peel stresses (2.7) can be calculated as

$$\tau = A_2 \cosh(2\lambda' x) + C_2 \, , \tag{2.6}$$

$$\sigma_n = A \cosh(\chi \, x) \cos(\chi \, x) + B \sinh(\chi \, x) \sin(\chi \, x) \, . \tag{2.7}$$

In these equations, the parameters $A_2, \lambda', C_2, A, \chi, B$ depend on the loading conditions, the geometry and the mechanical properties of the adherends and the adhesive. Finally, x is the origin of the longitudinal co-ordinate and is found in the midpoint of the adhesive overlap. Equations for these parameters can be found in Appendix A.

Similar analytical methods of varying complexity have been developed by various researchers [23-30]. In [22, 31] excellent reviews and critical evaluations of these solutions are provided.

2.4.4 Comparison of analytical methods

A comparison between the three analytical methods presented above is provided in this section. The geometry of the joint studied in these calculations is based on the joints that were tested experimentally and are described in Chapters 5-7. The joint geometry, however, was adjusted to the assumptions of the analytical solutions and therefore a single lap joint was studied with glass substrates and with no fillet endings. Therefore, glass substrates with 6 mm thickness and an adhesive overlap area of 50 mm x 50 mm with thickness 0.2 mm were considered. A sketch of the studied joint can be found in Figure 2.4. The stress results were normalised but given that non-linearities were not considered at this stage, the relationship between the stresses and the load applied is linear. The analytical solutions of Volkersen, Goland & Reissner and Hart-Smith are compared with a simple FE analysis on a single lap joint with the same geometry. Figure 2.5 shows the distribution of the shear and peel stresses along the length of the overlap. Finally, Table 2.4 summarises the main features and limitations of the analytical methods.

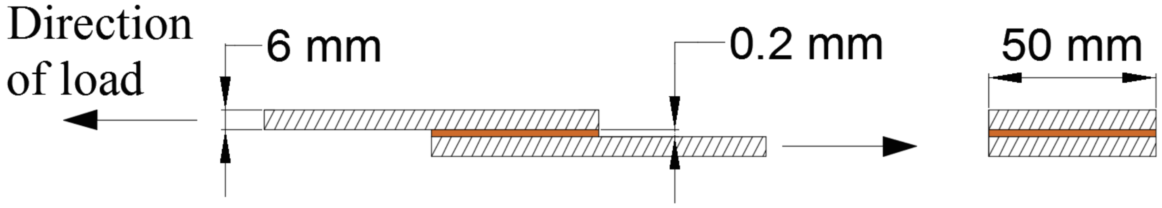

Figure 2.4: Sketch of the single lap joint studied with the analytical and FE methods.

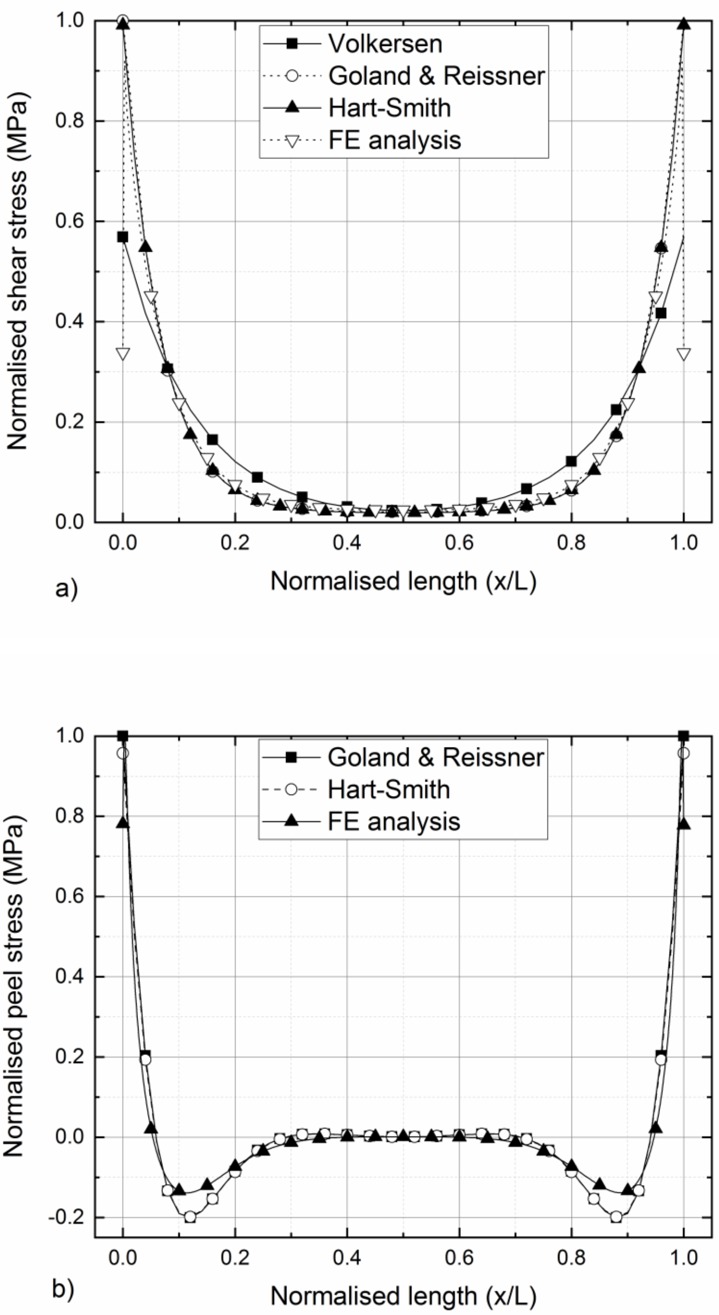

Figure 2.5: Distribution of a) shear and b) peel stresses in an adhesive overlap according to the analytical solutions of Volkersen, Goland & Reissner and Hart-Smith and comparison with simplified FE predictions.

Table 2.4: Comparison table for the four methods analytical methods that were described.

Method	Adherends	Adhesive	Bending	Dissimilar thickness	Dissimilar material	Shear stress	Peel stress
Average shear stress	rigid	elastic	No	No	No	Yes	No
Volkersen	elastic	elastic	No	Yes	No	Yes	No
Goland and Reissner	elastic	elastic	Yes	No	No	Yes	Yes
Hart-Smith	elastic	elastic	Yes	No	No	Yes	Yes

It can be seen that the three analytical methods provided similar results and are in very good agreement with the FE prediction. Especially, Goland & Reissner's and Hart-Smith's solutions provided almost identical results with the FE analysis. The only significant difference between the analytical and the numerical solutions can be found in the ends of the overlap for the shear stresses. The analytical solutions predict that the maximum shear stresses can be found at the end of the overlap. However, this violates the stress-free condition and therefore the analytical solutions overestimate the shear stresses in these regions and provide conservative failure load predictions [22, 31] . In addition, the analytical solutions described above consider only the elastic response of the substrates and the adhesive. Analytical solutions that consider plasticity for both the substrates and the adhesive have also been developed [7, 26-30]. However, the inclusion of plasticity in the models makes these solutions rather complex. Therefore, the primary target of achieving a faster, easier and reliable way of predicting stresses within the adhesive ceases to exist and the advantage over FE solutions becomes questionable [31].

2.5 Failure criteria for adhesive joints

Numerous failure criteria have been proposed for adhesive joints considering the complex stress state of the adhesive layer. Most of these criteria assess the response of the adhesive by evaluating a critical stress or strain and are based on a continuum mechanics approach [7, 18, 32, 33]. Characteristic examples of these criteria include the maximum principal stress [7], the maximum shear stress [34, 35], the von Mises stress [36], the maximum principal strain [37] and the maximum shear strain [21, 35] among others. The validity of these criteria however, strongly depends on the accurate prediction of stresses/strains in the adhesive layer [38]. Therefore, the material models that describe the deformations in the adhesive layers are very significant for the accurate prediction of damage/failure of adhesive joints.

In addition, adhesives are generally highly non-linear materials, and therefore both the elastic and the plastic responses need to be properly evaluated. A number of constitutive models have been used for the prediction of the elasto-plastic response of adhesives (Von Mises, Tresca, linear and exponent

Drucker-Prager and Mohr-Coulomb among others). Adhesives also display pressure sensitivity and their plastic performance is affected by changes in both the deviatoric and the hydrostatic stress tensor [38, 39]. Due to the pressure sensitivity of these materials, different levels of yield strength will be reached when the adhesive material is subjected to different stress states. For the complex multi-axial stress state usually encountered in adhesive connections, it is important to introduce models that take this sensitivity into account. According to Adams et al. [7] the yield stress in uniaxial compression is typically 1.2-1.4 times higher compared to uniaxial tension. Some of the aforementioned yield criteria are hydrostatic independent (von Mises, Tresca) while others consider have pressure sensitivity (Drucker-Prager, Mohr-Coulomb). Two characteristic examples of these criteria are presented below.

2.5.1 Von Mises criterion

The von Mises yield criterion (also known as distortion energy yield criterion) is a simple criterion which was originally proposed for ductile metals. The basic principle behind this criterion is that yielding occurs when the effective stress t reaches a critical value. The effective stress t_{eff} is calculated from the squared difference in principal stress components $\sigma_1, \sigma_2, \sigma_3$ (eq. 2.8) as

$$t_{\text{eff}} = \sqrt{\frac{1}{2}[(\sigma_1 - \sigma_2)^2 + (\sigma_2 - \sigma_3)^2 + (\sigma_3 - \sigma_1)^2]}\,. \tag{2.8}$$

This value is then related to the yield stress in simple tension σ_{YT} [40, 41]. This can be expressed mathematically (eq. 2.9) as

$$t_{\text{eff}} = \sigma_{YT}\,. \tag{2.9}$$

The von Mises criterion has been used extensively for ductile metals and is easy to formulate since data from only one stress state are required (normally uniaxial tension) [38-40]. However, the von Mises criterion completely ignores the pressure sensitivity that adhesives typically display. Simple modifications of these criteria can lead to pressure-sensitive criteria as described in section 2.3.2.

2.5.2 Linear Drucker Prager criterion

Figure 2.6 provides a graphical representation of the yield envelope associated with the Linear Drucker Prager plasticity model while Equation (2.10) defines the model as follows

$$t_{\text{eff}} - p\tan\beta = d\,. \tag{2.10}$$

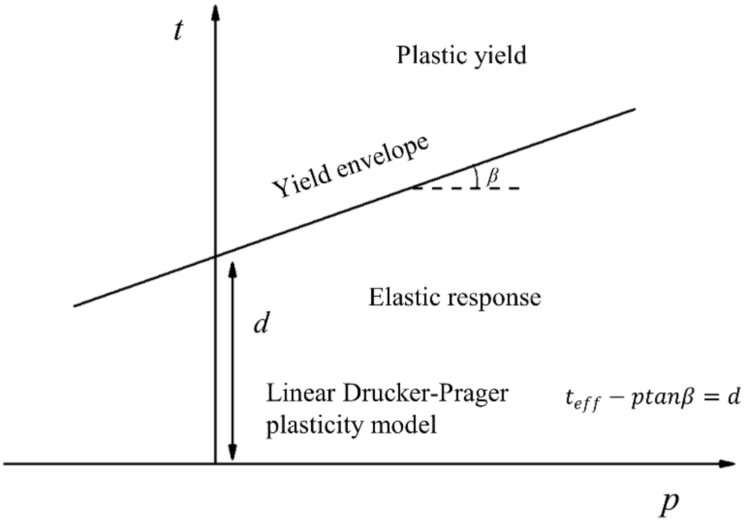

Figure 2.6: Graphical representation of the yield surfaces of the linear Drucker-Prager plasticity model on the meridian plane.

In equation (2.10), the effective stress is denoted by t_{eff} (eq. 2.8), the hydrostatic pressure stress by p (eq. 2.11), d is a material property related to the yield stress in pure shear (eq. 2.12), while the pressure sensitivity factor is introduced by $\tan\beta$ (eq. 2.13). The parameters d and $\tan\beta$ are material properties and can be defined after material characterisation testing in two stress states. For instance, for tests conducted in uniaxial compression and tension, the parameters are expressed in equations (2.12) and (2.13) using the respective yield stresses σ_{yC}, σ_{yT}. Equations 2.11-2.13 follow as

$$p = -\frac{1}{3}(\sigma_1 + \sigma_2 + \sigma_3)\,, \tag{2.11}$$

$$d = \frac{2\sigma_{yC}}{\left[\left(\sigma_{yC}/\sigma_{yT}\right) + 1\right]}, \tag{2.12}$$

$$\tan\beta = \frac{3\left[\left(\sigma_{YC}/\sigma_{YT}\right) - 1\right]}{\left(\sigma_{yC}/\sigma_{yT}\right) + 1}. \tag{2.13}$$

As shown in Figure 2.6, the pressure sensitivity in the model is introduced by the inclusion of the dilation angle β. When the dilation angle becomes zero, the yield envelope is parallel to axis p and the Linear Drucker Prager criterion simplifies to the von Mises criterion. The pressure sensitivity effect can also be seen in Figure 2.7, which shows the yield envelopes for the von Mises and the Linear Drucker Prager criteria in the principal stress space. The pressure sensitivity that the Linear Drucker-Prager model exhibits has led to its extensive use in the past for modelling yielding/failure of adhesive layers [38, 39, 42-46]. However, it should be noted that extracting the parameters for the

Linear Drucker Prager models requires material characterisation testing in two stress states (typically tension and compression or shear), while the von Mises criterion requires only in one (typically tension).

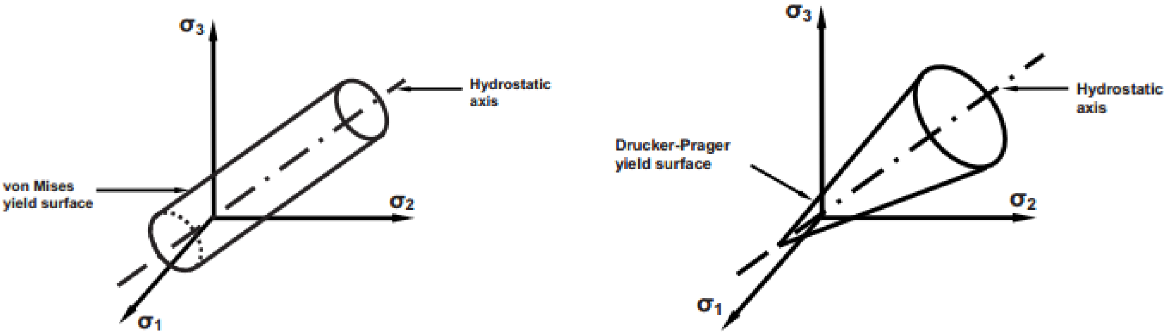

Figure 2.7: Von Mises and Drucker Prager yield surfaces in the principal stress space [47].

Criteria such as the von Mises and the Drucker Prager are used to describe yielding of materials and they are usually coupled to another failure criterion which models the damage initiation and propagation in the plastic regime. For instance, the ductile damage model has been used in the past to simulate damage initiation and propagation in an adhesive layer [48, 49]. According to this model, the strain at damage initiation, ε_c, depends on the stress triaxiality value. The stress triaxiality (eq. 2.14) is a dimensionless ratio between the hydrostatic (eq. 2.11) and the effective stress (eq. 2.8) and can be calculated as

$$\eta = \frac{p}{t_{\text{eff}}}. \tag{2.14}$$

To simulate damage progression in an explicit solver, elements of the model are removed when their stiffness has fully degraded, where at any given time step the stress tensor is described by equation 2.15 as

$$\sigma = (1 - D)\bar{\sigma}\,. \tag{2.15}$$

In equation 2.15, $\bar{\sigma}$ is the undamaged stress tensor, and D is the damage variable that can be attributed values between 0 and 1. The elements of the model are considered to have lost all load-carrying capacity when $D = 1$, and are consequently deleted. The damage propagation is specified as linear softening with respect to the fracture energy of the adhesive [50].

However, numerically, it is also common that a damage evolution law is not included in the analysis and failure is assumed once a critical stress/strain is reached. Figure 2.8 shows the difference between a damage only and a damage-failure model. Shape abcd' is a result of a model where generalised plasticization is assumed without damage evolution. Contrary to that, shape "abcd" predicts damage onset, followed by a degradation of stiffness until complete failure [33].

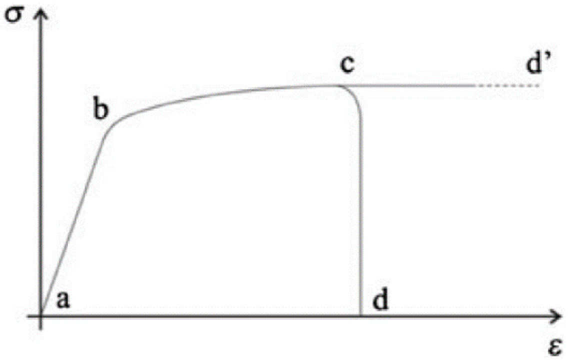

Figure 2.8: Difference between damage only and damage-failure models for a ductile material [33].

2.5.3 CZM approach

The element-based failure criteria described in the previous section have been used extensively in the past [7, 31, 35, 48, 51-53], but inhibit significant disadvantages as they are mesh size-dependent [54, 55], assume perfect bonding between the substrates and the adhesive, and they generally adopt the bulk properties of the constituent materials as model input.

An alternative to continuum mechanics approaches that has been widely adopted recently for the modelling of bonded connections is the use of cohesive zone models (CZM). Traction-separation laws are used to characterise the bonded substrate-adhesive interface, and this type of analysis is mostly mesh size independent since energetic criteria govern the crack growth [56]. However, the quantitative determination of cohesive laws under different failure modes can be challenging. Traction-separation laws are sensitive to the surface chemistry of the substrates used and also to the bondline thickness.

CZM is used for the simulation of the elastic region, damage initiation, damage evolution and final failure of an interface. Traction-separation laws relate stresses to relative displacements of the nodes of the cohesive elements. Traction-separation laws can have different shapes, but generally the elastic deformation of a material is followed by a peak value of stresses after which the damage initiates leading to complete failure after a given relative displacement [18, 33]. The area under each traction-separation law graph represents the fracture energy of the interface.

The main types of cohesive laws typically adopted are triangular, exponential and trapezoidal [18, 33] as shown in Figure 2.9. Generally, the triangular CZM shape is mostly used for brittle adhesives with small plastic deformations after yielding [56]. The trapezoidal shape allows for plastic deformations and therefore is more suitable for ductile materials [57]. It is worth noting that a direct method can also be used for the extraction of the exact shape of the cohesive laws as in [58-61], but in this work a simple triangular law is used since it provides good agreement with the experimental data in terms of maximum failure loads and progressive failure response.

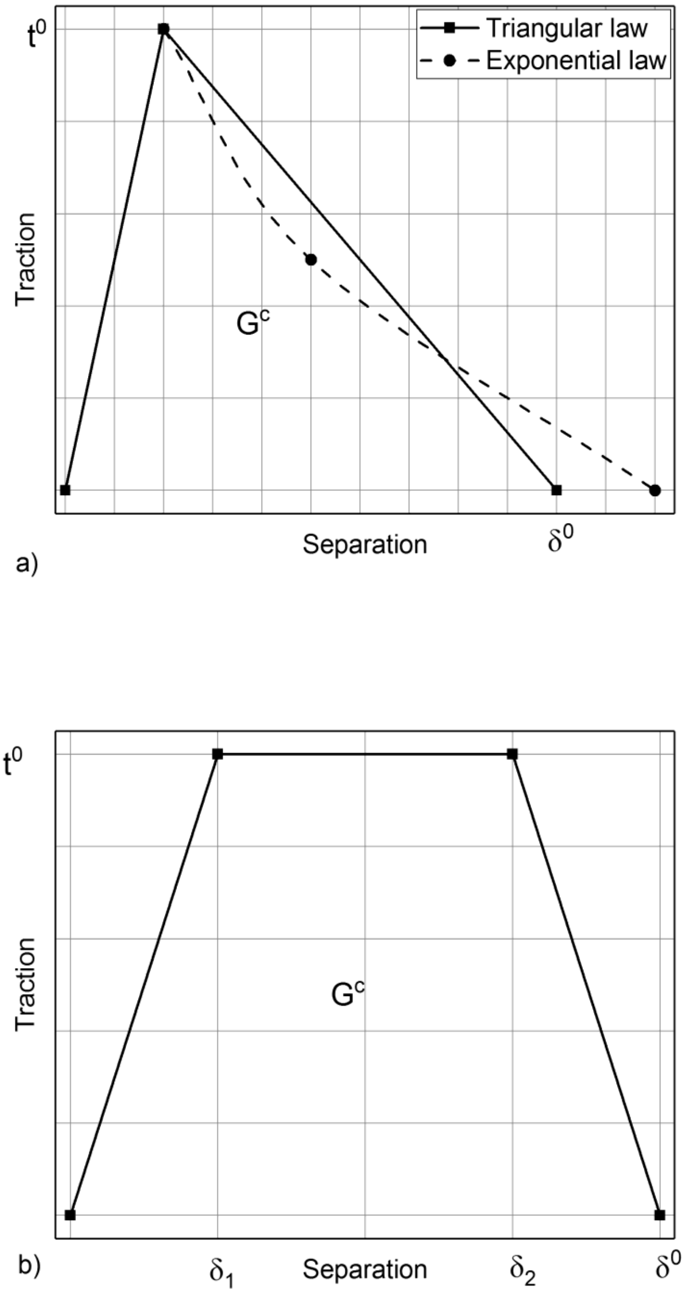

Figure 2.9: a) Triangular/Exponential and b) Trapezoidal traction-separation laws.

Different criteria can be used for the modelling of damage initiation (maximum/quadratic nominal/principal stress/strain) and damage evolution (displacement or energy controlled). A criterion that has been used extensively [56, 57, 62-64] for the damage initiation in adhesive joints is the quadratic nominal stress criterion as follows

$$\left(\frac{t_n}{t_n^c}\right)^2 + \left(\frac{t_s}{t_s^c}\right)^2 = 1\,. \tag{2.16}$$

In equation 2.16, t_n and t_s are the tensile normal and shear stresses, respectively, while t_n^c are t_s^c are the initiation stresses in tension and shear, respectively. It is further assumed that damage is not caused by normal compressive stresses [62]. When equation 2.16 is fulfilled, the softening process of the material's stiffness begins. A criterion that has been used extensively [56, 62, 63, 65, 66] for the damage propagation in adhesively bonded joints is the linear mode-mixity fracture energetic criterion [50] as follows

$$\frac{G_n}{G_n^c} + \frac{G_s}{G_s^c} = 1\,. \tag{2.17}$$

In equation 2.17, G_n and G_s are the fracture energies in tension and shear, while G_n^c and G_s^c are the critical fracture energies in modes I and II.

Normally, the determination of the cohesive properties (traction and fracture toughness) in mode I is achieved using the Double Cantilever Beam (DCB) [60, 67, 68]. ASTM D3433-9 [69] describes the DCB test for similar metal substrates, and the method has been used extensively. Similarly, for the determination of the cohesive properties for mode II loading, the End Notched Flexure (ENF) test is used [18, 70, 71]. ENF generally generates significant stresses in both substrates and when high stresses need to be avoided, mixed mode tests can be used as an alternative. The Single Leg Bending (SLB) test [72], for example, is a simple modification of the ENF test which introduces mode-mixity [64, 73], but also significantly reduces the stresses in the substrates. Figure 2.10 provides sketches of the three aforementioned tests.

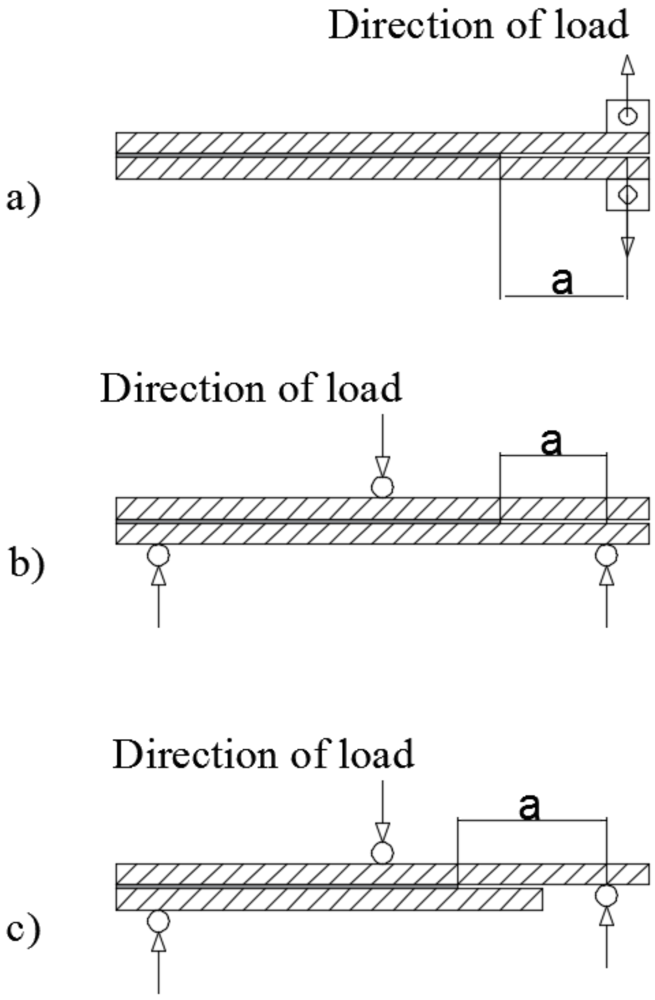

Figure 2.10: Sketches of the a) DCB, b) ENF and c) SLB tests. The pre-crack length (a) is indicated in the sketch.

2.6 Applications of glass adhesive joints

There exists a notable lack of standards and design recommendations regarding the use of glass adhesive joints in buildings for structural applications. The Institution of Structural Engineers with two publications [13, 74] has attempted to introduce some design principles in the use adhesive joints in glass structures. The main principles described in the two publications follow:

- The time and temperature dependency of the adhesives needs to be considered. Adhesives are viscoelastic materials and creep can have a significant effect on the performance of an adhesive joint.
- The capillary action of water can reduce the strength of a joint. The use of primers is advised in such cases.
- There is a wide range of adhesives and different applications require different materials.

- Certain adhesives can be stronger compared to glass and for these cases glass failure might take place first.
- Preparation before bonding is crucial for the joint performance. Generally, for the glass surfaces only degreasing is advised since etching the surface would improve adhesion but on the same time reduce the strength of the glass by introducing surface flaws.
- In shear lap joints the ends of the overlap carry most of the load.
- The behaviour of two-part adhesives depends strongly on the quality of the mixing of the two components.
- There is a wide range of uncertainties related to the use of adhesive joints and therefore conservative safety factors need to be applied. The EUROCOMP Design Code [75] suggests safety factors relating to the mechanical properties of adhesives used in the construction industry. However, it needs to be noted that the design code is over 20 years old and considering the improvements for both adhesion science and analysis of adhesive joints can be considered outdated.

Another attempt to introduce guidelines for the use of adhesive joints in the glass construction industry was made by ETAG 002 [76], a European directive for the use of sealants in buildings. However, it is important to note that ETAG 002 covers only the use of structural sealants, mainly silicones [77] and does not expand to the use of stiffer adhesives such as epoxy resins and acrylates. It can therefore be seen that the guidelines stated above are not specific and can be considered outdated.

2.6.1 Experimental and numerical investigations

Several research groups have studied the performance of glass adhesive joints experimentally and numerically. These studies have focused on joints connecting glass/glass and glass/metal and a few of them also examined glass/composites adhesive connections. This section presents characteristic examples of these studies highlighting their features and limitations. The focus is on both the experimental and numerical approaches.

2.6.1.1 Experimental investigations

Different joint configurations were tested in the past. Watson et al. [78] manufactured a glass/glass double lap shear joint that avoided direct contact of the glass and the grips. The set-up which involved five pieces of glass connected to two pieces of steel with UV-cured acrylic adhesives can be seen in Figure 2.11. The authors performed short term tests and intended to perform long term testing as well. However, the introduction of a constant load (about 50% of the short term failure load) in the joint led to failures within 1 to 11 hours, questioning the long-term performance of these adhesives.

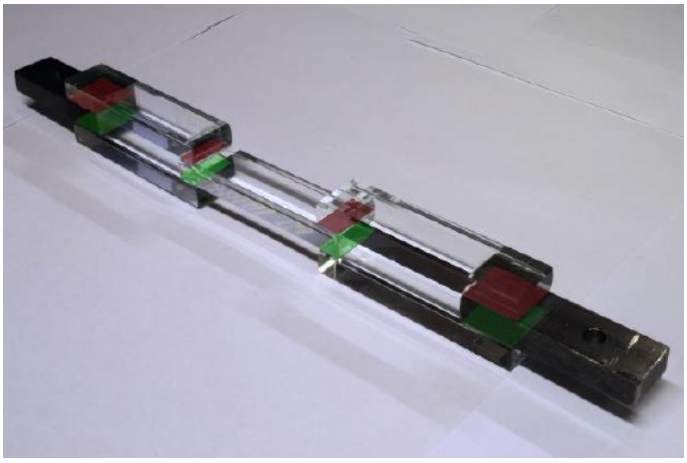

Figure 2.11: Glass-glass double lap joints tested by Watson et al. [78].

Watson et al. [78] also tested a modified single lap joint, similar to the one shown in Figure 2.12, connecting two pieces of mild steel to one piece of toughened glass with a UV-cured acrylic adhesive. Load-displacement curves were recorded from the test and compared with FE solutions. However, premature failure in glass in most cases did not allow the adhesive to show its full potential in the joint. Moreover, large deviations were recorded in the failure loads. The authors concluded that this was due to the random distribution of flaws in the glass surface. However, the damage initiated most of the times close to the adhesive area ends confirming that this area experiences the highest stresses.

Overend et al. [79] tried a similar approach by connecting mild steel with toughened glass. Apart from the modified single lap joint, the authors also tested a T-peel joint and for the connections a wide range of adhesives were tested (silicone, polyurethane, epoxy, 2P-acrylic, UV-acrylic) Comparisons of experimental and numerical load-displacement curves were performed along with analytical and numerical comparisons of the distribution of stresses in the adhesive. Stress whitening was observed in the UV-acrylic and the 2P-acrylic with increasing load. The primary aim of the study was to identify suitable adhesives for load-bearing glass/steel adhesive connections, and it was concluded that the epoxy and the 2P-acrylic provided the best results.

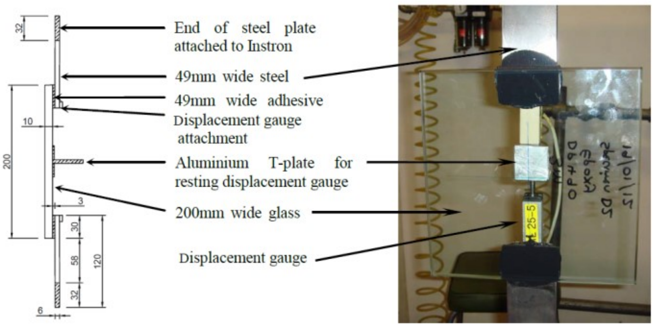

Figure 2.12: Experimental set-up used in [78-80].

Nhamoinesu and Overend [80] built on previous research by testing a similar modified single lap joint. Once again, a wide range of adhesives was tested for the selected joint configuration and also conditioning at elevated temperature was considered. Comparisons took place between linear-elastic and non-linear viscoelastic-plastic FE analyses and results from experiments and analytical solutions. The effects of heat soaking in 80°C led to strength loss for every adhesive. The best performing adhesive however was the ductile methacrylate, Araldite 2047-1, which only displayed an 18% joint strength reduction. Figure 2.13 shows load-displacement curves for the modified single lap joints. It can be seen that after heat soaking the strength of the joint decreased while the ductility increased. It has to be noted, however, that all the joints had a 3 mm bondline thickness. This is obviously not the optimum thickness for every adhesive. As a result, the conclusions cannot be generalised to a wide range of bondline thicknesses.

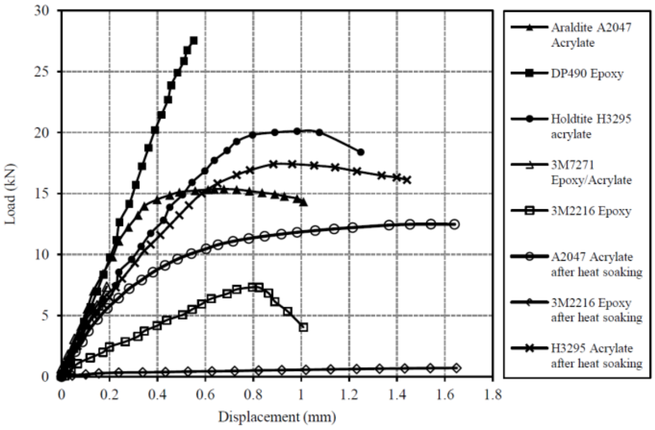

Figure 2.13: Effect of heat soaking in adhesive joints [80].

Machalicka et al. [81] and Machalicka and Eliasova [82] studied glass/steel butt and double lap shear joints. In addition, the same authors [82] also performed tests in double lap glass/glass joints. The authors addressed the issue of gripping the glass by applying a compressive load, in the middle glass substrate instead of a tensile one. Also, in order to avoid outspreading of the joint they constrained the remaining two glass elements as shown in Figure 2.14. Using these configurations the authors studied experimentally the effect of various substrates, the effect of different surface treatments and finally the effect of the bondline thickness. Once again, various types of adhesives were considered (1-Part polyurethane, 2-Part polyurethane, 2-Part acrylate and two UV-curing acrylates).

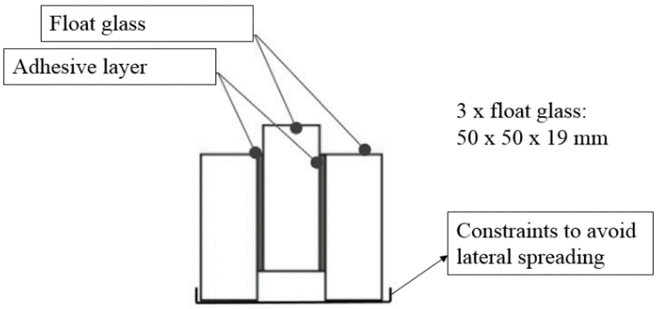

Figure 2.14: Glass/glass double lap shear adhesive joint tested by Machalicka and Eliasova [82].

Load-displacement curves were recorded and were later converted to stress-strain curves for the adhesive. Analysis of the experimental results revealed that sandblasting of the glass substrates improved adhesion on the weaker glass interface significantly, while the same trend was not observed for the metal substrates. In addition, the strength of a joint decreased with the increase of the bond-line thickness of the adhesive. The effect was more significant the more rigid the adhesive was.

Adhesive point-fixings that can be used in facades, and suspended canopies have been researched previously both numerically and experimentally [39, 83-90]. More specifically, Dispersyn et al. [85] studied the influence of the distance between the connection and the corner/edge of a 1 m x 2 m glass pane under out of plane bending loading. In their study, the authors showed that similarly to bolted joints, in adhesive joints small edge distances generate significant stresses. In [84] a combined experimental and numerical parametric study was developed on the response of adhesive point-fixing under uniaxial loadings. The authors showed that the stresses in the adhesive layer were increasing while the diameter of the joint, the thickness of the adhesive and the glass substrate was decreasing and while the adhesive stiffness was increasing.

Figure 2.15 shows the experimental set-up of adhesively bonded point fixings used by Belis et al. [90]. In the suspended canopy two laminated glass plates with a surface of 1 x 1 m and a thickness of 8 mm were used. Cases of fully tempered and heat strengthened glass plates were examined. The adhesive used was a 3M Scotch Weld 9323 epoxy. A series of tests were performed in these canopies. Most notably, the canopies were loaded for 24 hours with a distributed load of 1.5 kN/m^2, then were tested against impact loadings with 4 kg steel balls being dropped from 3 m height and finally reloaded for 24 hours with 0.5 kN/m^2. In the case of heat-strengthened glass the connections supporting the canopy did not fail, and no glass fragments fell down even though the lower glass sheets broke after the impact loading.

On the other hand, when fully tempered glass was used the results were similar up to the last stage of the experiment. When the canopies were reloaded after the ball dropping, they lasted for about 12 hours before the glass panels completely collapsed. According to the authors the better performance of the heat-strengthened glass canopies is explained by the fact that the fully tempered glass has a denser crack pattern after breakage. Therefore, the overall post-breakage residual stiffness is significantly lower leading to failure. It is worth noting that even in the case of fully tempered glass the adhesive connections were not damaged and certainly the failure did not initiate there.

Figure 2.15: Adhesively bonded point fixings for a suspended canopy test [90].

Silvestru et al. [91] examined adhesive connections of laminated glass and steel under tensile and shear loading while similar connections were examined under tension, compression and shear [92] and under cyclic loading [93].

Santarsiero et al. [94, 95] extensively studied the use of laminated connections for structural glass applications. More specifically, in [94] they performed a full-scale experimental study on connections between laminated glass beams aiming to investigate the structural response under monotonic quasi-static in-plane bending loading. The authors compared different configurations, studied the creep response under constant load and finally assessed the response to vandalism damage under constant loading. A numerical study based on the same configurations and designs was also presented in [96].

The authors assessed three different configuration as shown in Figure 2.16, and the experimental set-up can be seen in Figure 2.17. The study showed that the configuration with the inserts at the top-bottom location sustained significantly higher loads and displayed a ductile structural behaviour. In addition, the failure of this configuration did not initiate in the joint zone, but far from the connection.

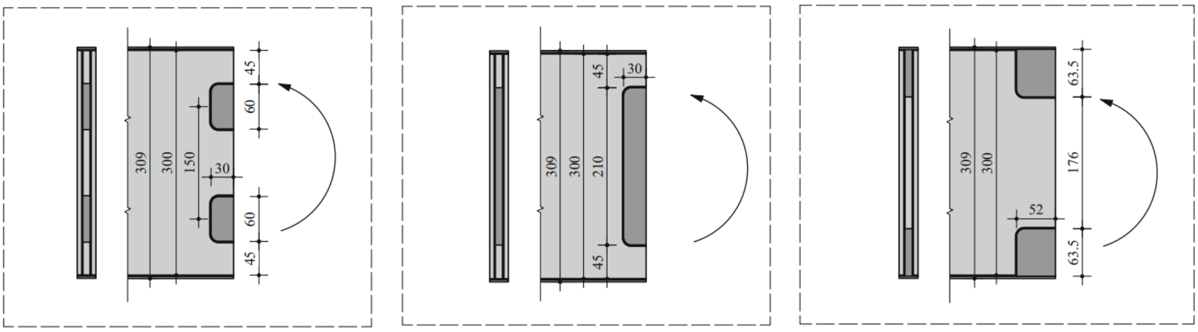

Figure 2.16: Three different types of laminated connections for glass beams [94].

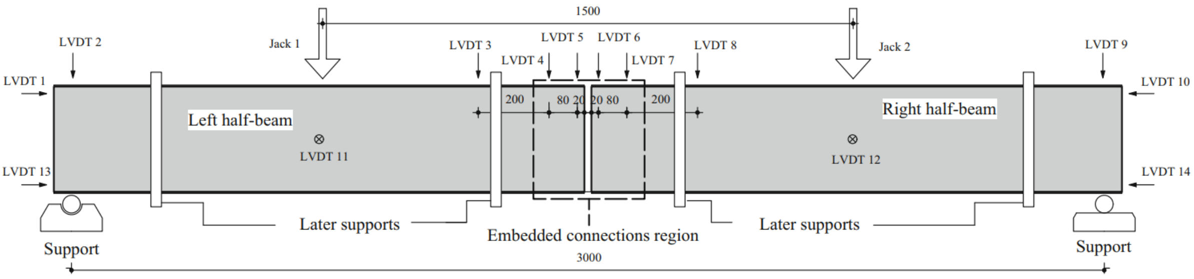

Figure 2.17: Experimental set-up studied by Santarsiero et al. [94].

Santarsiero et al. [95] examined similar thick embedded laminated glass connections. In this study, small-scale pull-out tests were performed as the ones shown in Figure 2.18 over a range of temperatures (20°C, 40°C, 50°C and 60°C). LVDT sensors were used for measuring the relative displacements between the metal insert and the glass panels. The temperature range significantly affected the performance of the joints in terms of stiffness response, failure loads and mechanisms. At lower temperatures, the response was stiffer with a relatively small plastic zone and failure was observed in the glass substrates. As the temperature was rising, the non-linear response and ductility of the joints was increasing. Failure was due to adhesive yielding and delamination and the strength capacity of the joints dropped about 83% as shown in Figure 2.16.

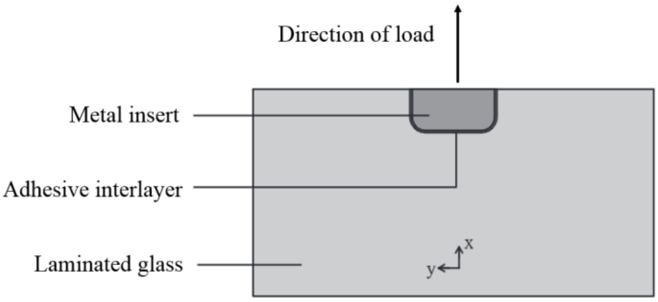

Figure 2.18: Experimental set-up for the pull-out tests performed in [95].

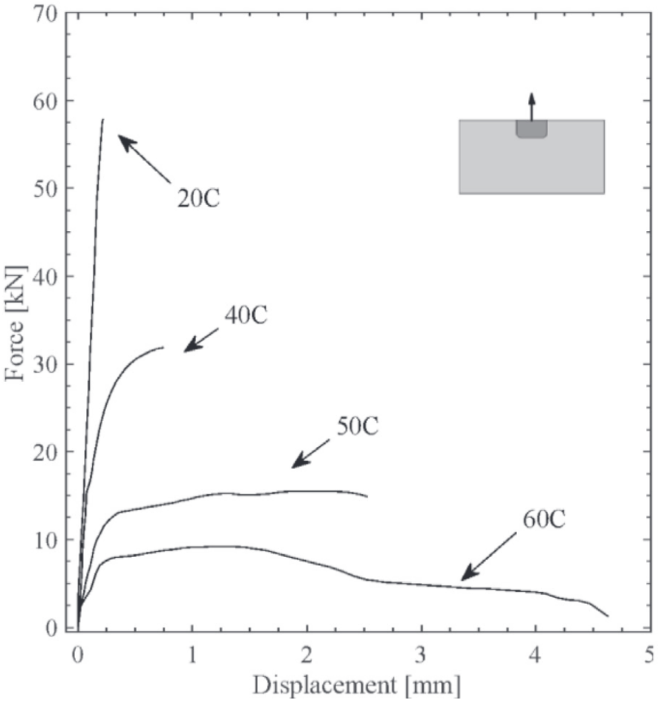

Figure 2.19: Load-displacement response of the pull-out specimens over a range of temperatures [95].

Experimental and numerical studies on the performance of glass/steel composite panels were presented in [97, 98]. Medium scale (700 mm x 300 mm) and large scale (3500 mm x 1500 mm) panels were considered, and a ductile methacrylate was used for the 3mm thick adhesive glass/steel connections. LVDT sensors and strain gauges were used to monitor the response of the panels.

Overend et al. [99] also compared experimentally bolted and adhesively bonded joints for glass structures. More specifically, the authors manufactured and tested nominally identical glass/steel double lap shear bolted connections and single and double lap adhesive joints. The designs they proposed were visually equivalent since the diameter of the bolt hole in the bolted joints was similar to the area bonded in the adhesive joints. For the adhesive joints three different adhesives were used, namely a 2P-epoxy (3M 2261B/A), a 2P-acrylic (Holdtite 3295) and a 1P-acrylic (Loctite 326). The authors concluded that the strength of the best performing adhesive joints was significantly higher compared to the best performing bolted joints. In the case of single lap joints the strength was 31% higher while in the case of the double lap joints the strength was 189% higher. One more interesting conclusion reached by the authors was that due to progressive damage development, strain softening and stress-whitening in the adhesives the failure of the adhesive joints was less catastrophic.

2.6.1.2 Numerical investigations

Numerically, different methods have been developed for the prediction of the response of glass adhesive joints. Several studies considered viscoelasticity and the strain rate dependency of the adhesives [39, 79, 80, 96, 97]. Other studies considered the pressure-sensitivity of the adhesives [39], others proposed failure criteria for the adhesives [39, 100] and others have proposed failure criteria for the glass substrates [95, 96, 100, 101] .

More specifically in [39] the authors have developed a novel Generalized Triaxial Model (the authors called it GTM) for adhesive connections which takes the pressure sensitivity of the adhesive along with the sensitivity to strain rate and temperature variation into consideration. The proposed model was validated against tensile-torsion tests for two adhesives under a range of temperatures with very high accuracy. Bedon et al. [100] also developed a failure model for glass adhesive joints by introducing a triangular traction-separation law to model the damage initiation and propagation in the glass/steel interface. The values of the traction-separation law, however, were calibrated against the strength of the joints, and therefore a methodology for the extraction of these parameters is still lacking. In addition, in the same paper, damage and failure of the glass substrates was introduced by utilising the brittle cracking model [50] in a similar approach as in [96, 101]. The same mechanism (failure by exceeding the maximum principal stress) was achieved in [95] by introducing the concrete damage plasticity model [50].

2.6.2 Environmental exposure

As discussed earlier, one of the biggest limitations of glass adhesive joints is related to their durability and performance during environmental exposure. Several groups have studied the performance of glass adhesive joints under environmental exposure by exposing the joints to conditions of high/low temperatures, humidity and UV-radiation.

Machalicka and Eliasova [82] developed a laboratory ageing cycle for glass/glass and glass/metal adhesive joints. The cycle included moisture, high/low temperature variation and UV exposure, simulating 5 years of outdoor exposure in the climate of Czech Republic. The cycle can be found in Figure 2.20.

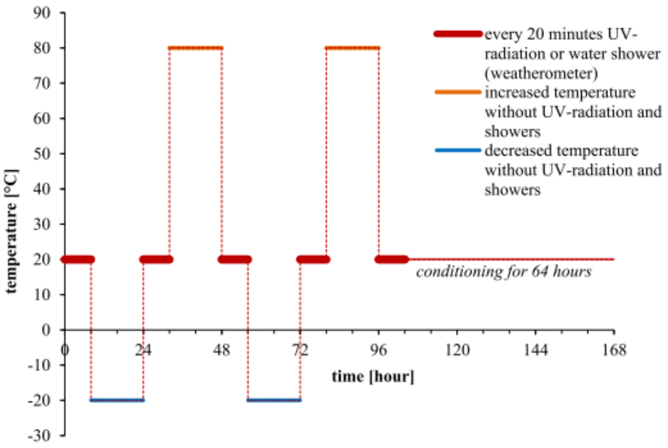

Figure 2.20: Artificial ageing cycle used in [82].

The study included different adhesives which displayed significantly different responses following environmental exposure. A 2-Part polyurethane adhesive increased its mechanical properties after exposure, probably due to unreacted components in the polymer prior to the exposure start. A 2-Part acrylate adhesive increased its shear strain significantly while the shear strength remained unaffected. The properties of the first UV-curing adhesive used in the study deteriorated significantly, making it unsuitable for structural use, while the properties of the second UV-curing adhesive also dropped significantly (about 40% drop of the shear strength). The authors also highlighted that the environmental degradation of an adhesive has a non-linear relationship with time, and therefore it is not possible to predict the behaviour of adhesive joints at different times.

Van Lancker et al. [87] developed a different exposure cycle to assess the performance of glass/steel adhesive connections. The cycle proposed considers moisture (in the form of 100% relative humidity or water immersion), high/low temperature variation and UV exposure and can be found in Figure 2.21. In addition, the cycle is designed in a way that attempts to uncouple the effect of moisture and heat, as the two are studied both together and separately.

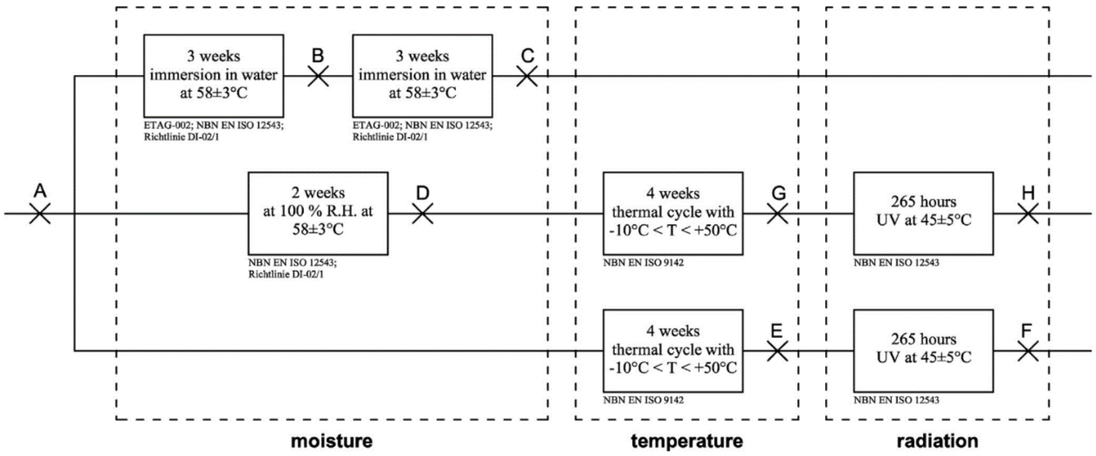

Figure 2.21: Artificial ageing cycle used in [87].

The authors studied the effect of the cycle on point-fixings by examining two adhesives, an epoxy resin and an MS-polymer. The epoxy resin considered was significantly damaged by moisture since both the strength and the stiffness of the point fixings decreased. In contrast, the effect of the thermal ageing was not as significant and only very small drops were recorded in the stiffness and strength of the joints. The UV-radiation did not have a significant effect when applied after thermal ageing but had a more significant effect after the moisture ageing. The MS-polymer was also significantly damaged by humidity with both stiffness and strength decreasing significantly. Thermal ageing however led to the improvement of the mechanical properties of the adhesive, while UV-exposure had a very limited effect on the performance of the joints. In both cases, the exposure cycles led to changes in the stiffness and strength of the joints compared to the unaged specimens. Therefore, according to the authors, it is important to consider the changes in the properties in the design stage.

Different ageing procedures have also been followed for the study of exposure of adhesive joints in façade applications [102-104]. The authors of these three publications have performed a comprehensive study on the durability of two adhesives intended for use in facades. However, the authors of these three publications have not used glass substrates for their studies.

ETAG 002 [76] suggests an ageing cycle based on exposure to high temperature/humidity conditions which was followed in [102, 103]. According to ETAG 002, the specimens were immersed in water for a total duration of 21 days at a constant temperature of 45°C. After exposure the specimens were conditioned for a 24 hours prior to testing. In addition, in [102] a second ageing methodology was followed, which was based on ISO 9142, procedure E4 [105]. In the second exposure cycle, the specimens were exposed to neutral salt spray at 35°C for 21 days, and followed by exposure to 95% relative humidity and 40°C for 7 more days. After exposure the specimens were conditioned for 10 days prior to testing. Finally, in [104] the authors studied the effect of humidity on bonded joints by performing the extended cataplasm test, described in ISO 9142, procedure E2, which can be schematically seen in Figure 2.22.

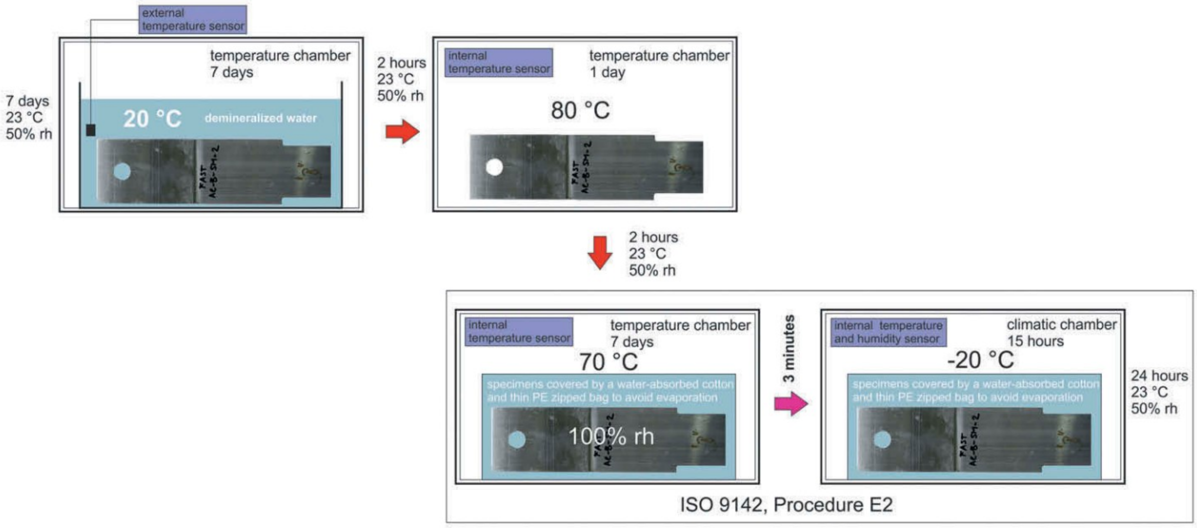

Figure 2.22: Modified cataplasm exposure used in [104].

It is worth noting that in all the studies presented the focus was on the experimental analysis of adhesive joints following exposure to certain conditions. A tool for the prediction of the performance of glass adhesive joints after environmental exposure using FE methods is currently lacking. Finally, it should be noted that various studies in the past with non-glass substrates have tried to predict the effect of the degradation in adhesive connections either by taking into consideration the degraded bulk properties of the adhesive (when the damage was cohesive) [106-108] or by considering the interface degradation (when the damage was adhesive) [109-111]. Combined experimental and numerical research studies on the environmental degradation of hybrid glass/steel adhesive joints are therefore lacking.

2.6.3 Large scale applications

Blandini in 2004 constructed the glass dome [112]. The glass dome is a shell structure consisting of only glass and adhesives as shown in Figure 2.23. The span of the shell is 8.5 m and consists of several glass panes connected at the ends with 10 mm thick butt joints.

Blandini [113] performed a series of tests prior to deciding on the adhesives to be used in the glass dome. The tests focused on butt joints, so the author performed a series of tensile butt joints tests with varying adhesive thickness over a wide range of temperatures, shear tests and four-point bending tests. Moreover, the author tested the performance of the joints under constant loading (1000 hours). Finally, epoxy DP 490 was selected. One interesting conclusion of the testing campaign was that the 10 mm thick joints maintained about 50% of the strength of the 1 mm thick joints.

It has to be noted that the glass dome has been in place since June 2004, being exposed in an environment of high humidity with significant temperature variation. In addition, one more thing that stands out in Blandini's work is that he tried to optimise the use of the joints by taking into account the mechanical characteristics of both the glass and the adhesives. As a result, he chose an adhesive which has similar tensile strength with glass. This indicates that the tensile strength of the structure is not compromised by the use of adhesive joints. On the other hand, the glass used in the glass dome has optimum structural performance since it is mostly loaded under compression.

Figure 2.23: The glass dome designed and constructed by Blandini [112].

Weller et al. [114] carried out an interesting study on a bonded frame corner. Using a technique well known in the carpentry industry and building on previous research of the Leibniz Institute for Solid State and Material Research (IFW) in Dresden, they attempted to manufacture a fully transparent glass column-beam joint. This joint was later used as a part of the refurbishment work at the palace in Grimma, Saxony.

The joint configuration, test set-up and indicative results can be seen in figures 2.24 and 2.25. The bonded area was 300 × 300 mm, while the thickness of the joints was 1.5 mm. Finally, for the laminated glass elements, four fully-tempered glass plies were used. Weller et al. [114] conducted a preliminary study before performing the tests in order to select the appropriate adhesive and concluded that the one-part acrylate Delo-Photobond GB VE would be used. This particular adhesive exhibited transparency, had low-shrinkage, limited voids, was resistant to moisture and had a good load-bearing performance within a wide range of temperature, from −25°C to 75°C.

Moreover, the authors also conducted tests on single lap joints using compressive forces and studied the effect of ageing of the joints in climate chambers. Finally, they tested 10 samples of the bonded frame corner. In seven cases the glass failed, while three times the limit of the testing machine was reached. However, a mean maximum load of 90 kN was achieved while the mean maximum stress within the glass was calculated at 156 MPa (after strain gauge measurements).

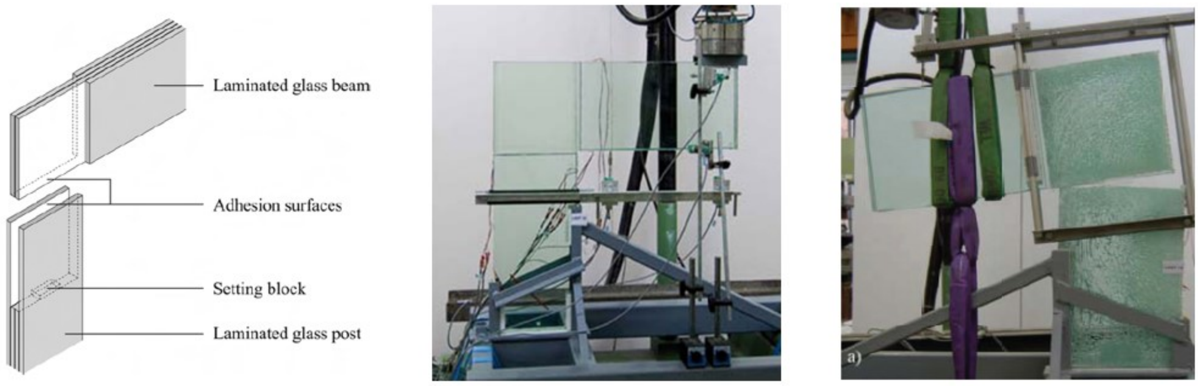

a) b) c)

Figure 2.24: Bonded frame corner a) design, b) experimental set-up and c) specimen failure [114].

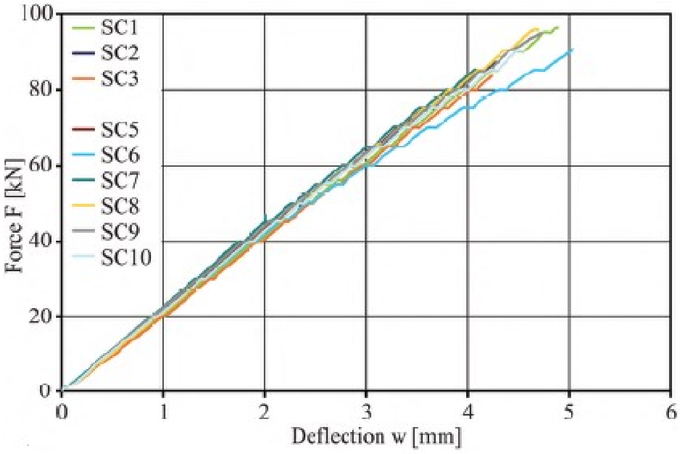

Figure 2.25: Results for the 10 samples of bonded frame corners tested by Weller et al. [114].

Recently, the Crystal Houses Façade was completed in Amsterdam designed by MVRDV and Gietermans & Van Dijk architectural offices. The self-supporting, novel glass façade aimed to reproduce the architectural design of the brick facades used in the Netherlands in the 19th century. Therefore, glass bricks were used which were connected with a transparent UV-curing acrylate. The challenges in the construction of the façade and the preliminary testing can be found in [115, 116], respectively. Soda-lime glass was used for the fabrication of the approximately 6000 glass bricks needed in the project, while the annealing process of the glass ensured that the bricks are free of internal residual stresses. The front view of the Crystal Houses can be seen in Figure 2.26.

Figure 2.26: View of the Crystal Houses

The size of the structure introduced a number of challenges, the most important of which proved to be the tight tolerances during the construction. Given that the structure is located in a central street of Amsterdam, the visual result is of great importance. Therefore, no entrapped air and no capillary action in the adhesive was allowed. Eventually, after a series of mock-ups, a ± 0.25 mm precision in size, rectangularity and flatness was decided, a level of accuracy that had never been realised before in a similar project [115].

After the tolerances were determined the preliminary tests for the development of the construction method started. Initially, compression tests in three different column configurations were performed, which revealed that the strength of the columns was lower than expected bust still could sufficiently meet the requirements of the design. According to the authors, the reduced strength of the glass is due to the manufacturing process of thick glass elements which unavoidably introduces internal defects.

Moreover, four point in-plane and out-of-plane bending tests were performed in prototype specimens to assess the flexural strength of the glass masonry system. Finally, impact and vandalism tests were also performed along with thermal shock tests.

2.7 Summary, limitations and novelty

The review presented in this chapter demonstrates that there is a wide range of analytical solutions for the stress analysis of single lap joints. These solutions vary from simple one formula solutions to complicated elasto-plastic analyses. The analytical solutions can provide a quick first estimation of the stress distribution in a joint.

However, modern adhesive joints have complicated geometries, and non-linearities strongly affect their performance. Therefore, for a thorough stress and failure analysis of an adhesive joint, FE analysis is the preferred method. For FE analyses, the selection of the correct constitutive models that describe the complicated elasto-plastic response of the adhesive and the selection of an appropriate failure criterion is still challenging. This review presents characteristic examples of constitutive models with and without pressure sensitivity and also presents the most common failure criteria that have been adopted. In addition, damage mechanics approaches, like cohesive zone modelling, can be combined with classic FE models to improve their accuracy and add extra features like interface failure and damage propagation in the analysis. Constitutive and failure models however, require extensive material and interface characterisation testing before they can be implemented.

The second part of the literature review presented focuses on applications of glass/steel adhesive joints and showed that a considerable amount of research has taken place. Adhesive point-fixings that can be used in facades and suspended canopies have been researched previously both numerically and experimentally [39, 83-89]. In addition, single lap joints of tempered glass connected to mild steel using different adhesives were also tested and different modelling approaches were assessed [80, 99]. Silvestru et al. [91] examined adhesive connections of laminated glass and steel under tensile and shear loading, while Machalicka and Eliasova [82] tested double lap joints connecting glass-to-glass and glass-to-metal. In addition, thick embedded laminated glass connections have been studied both numerically and experimentally [95, 96]. UV-curing acrylics were used for glass to glass connections and showed potential to be used in commercial projects [114, 117].

Overend et al. [99] has compared the performance of adhesive and bolted joints for a given design under two different load cases. However, a thorough experimental and numerical assessment of bolted versus bonded joints including the joint's failure prediction is currently lacking.

In terms of numerical modelling, several methods have been developed for the prediction of the response of the joints, including damage and failure propagation in the glass substrates and the adhesive layers. However, detailed investigations of the failure mechanisms of glass/steel adhesive joints (considering failure criteria for both the adhesives and the glass substrates) under different stress states for different adhesive types are currently lacking.

In addition, cohesive zone models have been used for the simulation of damage initiation and propagation in a glass/steel bonded connection [100]. However, the extraction of traction-separation laws for glass/steel connections is complicated due to the small size of the coupon specimens and the relatively low-strength of glass. The authors in [100] used reference values and calibrated the traction-separation laws based on the failure loads of the double lap shear joints they were investigating. Therefore, a robust and validated methodology for the characterisation of glass/steel adhesive interfaces in bonded joints loaded in modes I and II using a modified and improved testing methodology based on current standards is currently lacking.

Over the past few years, the durability and long term performance of glass adhesive joints has started to be researched systematically as well. Exposure cycles, including high/low temperatures, increased humidity, UV-radiation and salt spray have been introduced and the deterioration of the joints was recorded in terms of reduction in the properties of the adhesive and the strength/stiffness of the joints [82, 87, 102-104].

All the studies cited above focused on the experimental analysis of joints under exposure without developing models that could predict and incorporate the degradation effects. In studies with non-glass substrates such modelling attempts have been made either by predicting failure based on the reduction of the bulk properties or based on the weakening of the interface. A similar predictive tool for joints with glass substrates, however, is currently lacking.

Table 2.5 summarises the findings of the literature review, identifies the gaps in the existing research and relates them with the objectives of this PhD project presented in section 1.4.

Table 2.5: Summarising table correlating the findings of the literature review with the objectives of the project.

Activity related to research on adhesive joints	Adherends		Covered by PhD project objective:
	Non-Glass	Glass	
Material characterisation for adhesives	🟩 [79, 80, 83, 86]		1
Interface characterisation	🟩 [66-68, 70, 71]	🟧	1
Experimental analysis in different load cases	🟩 [39, 89, 91, 92]		1
Comparison with bolted joints	⬜	🟨 [99]	1
Combined experimental and numerical analysis of adhesive joints	🟩 [39, 56, 65, 88, 95]		1, 2
Large scale testing	🟩	🟩 [113, 114, 117]	-
Durability studies	🟨 [102-104]	🟨 [82, 87]	4
Use of pressure-sensitive yield criteria	🟩 [38, 42-46]	🟨 [39]	2
Use of models for damage initiation and propagation in the joints	🟩 [48, 49]	🟧	2
Cohesive zone modelling	🟩 [56, 62, 63, 65, 66]	🟨 [100]	2
Numerical tool for the prediction of environmental degradation in joints	🟩 [106-111]	🟧	4
Numerical tool for the selection of adhesives with optimum mechanical properties	🟧	🟧	3
* Examples of relevant studies			
⬜ Colour indicates that similar studies are not relevant to the current project			
🟩 Colour indicates that similar studies have been performed in the past.			
🟨 Colour indicates that similar studies have rarely been performed in the past.			
🟧 Colour indicates that similar studies have not been performed in the past.			

2.7.1 Novelty

Based on the critical analysis of the literature review and concluding Table 2.2, the novelty of the thesis and its findings is summarised below:

1) Development of a combined numerical and experimental methodology that provides the ability to predict failure for hybrid glass/steel adhesive joints by considering yield and failure criteria for both glass and adhesive. The numerical approach is based on continuum mechanics principles and is used to explain the experimental observations. Bolted and adhesive joints are tested and modelled under different loading conditions.

2) Development of a numerical screening methodology to assist in selecting the best commercial adhesive for a given joint design. Numerical failure analysis highlights synergistic property combinations of strength and ductility depending on joint geometry. The identified commercial adhesive achieves significant strength improvement for a range of typical load cases as verified via experimental benchmark studies.

3) Development of a test methodology to determine interface properties of brittle glass / steel joints under mode I and mixed mode loading. Brittle glass substrates are heat-strengthened in-house to withstand higher stresses. The Double Cantilever Beam (DCB) and the End-Notched Flexure (ENF) tests are modified to a) allow the use of dissimilar glass / steel substrates and b) reduce stresses in the glass substrate. This allows for extraction of surface-sensitive traction-separation laws. Validation of the cohesive properties is completed successfully against experimental data of glass/steel adhesive double lap shear joints under a wide range of different loading conditions.

4) Study on the effect of high temperature/humidity on hybrid glass/steel adhesive joints. The degradation due to the environmental conditions can be monitored by analysing the degradation of the bulk adhesive properties, the interfaces and finally the large double lap shear joints. Different numerical methodologies are evaluated for the prediction of damage after exposure. Models with ability to predict interface degradation are found to result in a much improved agreement with the experimental joint degradation.

Chapter 3 **Material characterisation testing**

3.1 Introduction and structure

The material characterisation testing performed for the adhesives and the glass substrates used in this project is presented in this chapter. This chapter initially provides an overview of the methodologies behind every measurement, describes the relevant standards followed and finally presents the results of each measurement.

The tests described in this section are critical for the development of the numerical work described in Chapters 6 and 7. The tests for the determination of the bulk properties of the adhesives were used for the development and the calibration of elastic-plastic and failure models for the adhesive. The work highlights the importance to thermally strengthen small coupon sized float glass in-house, leading to higher strength in the glass substrate as required for the tests described in Chapter 4.

Part of the results presented in this chapter were published as full paper in [118].

3.2 Adhesive characterisation

Three adhesives with different characteristics were used throughout this thesis. Araldite 2020 [119], a high strength, brittle epoxy resin, Delo-Duopox 03 rapid thix [120] an intermediate strength but ductile epoxy resin and Araldite 2047-1 [121] a low-strength, ductile methacrylate (Araldite 2047-1). Tests in tension and compression were performed for the three adhesives in order to identify the elastic modulus and the yield and failure stresses and strains. Furthermore, the pressure sensitivity of the adhesives was identified based on stress-strain data in two stress states.

3.2.1 Tensile tests

The tensile tests performed in this study followed ISO 527-1:2012 and ISO 527-2:2012 [122, 123]. According to the standards, a wide range of sample sizes can be tested. However, all the samples have a similar dumbbell shape. Longer specimen are typically used for more stiff adhesives, while shorter ones are usually used for more flexible adhesives according to da Silva et al. [18]. The standard size of dumbbell that was used in this thesis can be seen in Figure 3.1.

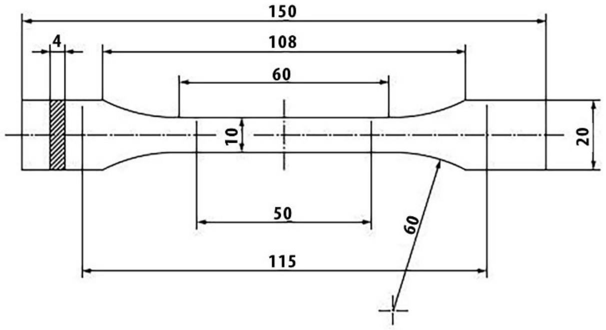

Figure 3.1: Sample type 1B that was used for the tensile testing (dimensions in mm) [122, 123].

According to the standards the preferred thickness for these samples is 4 mm, but it is advised that the thickness of the bulk specimen should be as close as possible to the thickness of the adhesive layer that will be used in a given application. In this project, the specimens studied had a thickness of 4 mm. However, thinner specimens were also tested which yielded similar results. Manufacturing of the samples was achieved by pouring the adhesive in a mould. Finally, curing of the samples followed the recommendations of the manufacturers, and the samples were cured for one week in ambient conditions.

The tests were performed on Instron electro-mechanical universal testing machines, and the rate of loading was 1 mm/min. Strain measurements can be achieved by strain gauges, extensometers and video extensometers. All methods have advantages and limitations, but in general contactless options are preferred since contact and interference with the samples is avoided. In this study, both strain gauges and video extensometers were used.

According to the standard the elastic modulus of the adhesive should be calculated at very low strains $(0.05\% - 0.25\%)$ to ensure that the adhesive is still in the elastic region. The 0.2% offset method was used in this study for the determination of the yield stress and strain.

3.2.2 Compression tests

The compression tests performed in this study followed ASTM D695-15 [124]. According to the standard, the standard geometry is a right cylinder or prism whose length is twice its principal width or diameter. The standard also suggests different preferred specimen sizes depending on the type of measurement. When the strength of the material is required then the suggested specimen have dimensions 12.7 by 12.7 by 25.4 mm for prisms or 12.7 mm diameter by 25.4 mm length for cylinders. When the modulus of the material is required, longer specimen should be used, with slenderness ratio between 11 and 16:1 (approximately two times longer). The suggested rates of loading depend based on the application, however for low strains a testing speed of 1.3 ± 0.3 mm is suggested.

In this study, given that the elastic modulus was already determined during the tensile tests, only the short specimens were used. In addition, the compressive failure strength and strain of the intermediate and ductile adhesives were not possible to measure due to the excessive ductility of the materials. Therefore, the tests were stopped after the yield strength was reached (approximately 2-3% strain). Finally, the strains were recorded with video extensometers.

3.2.3 Results for tensile and compressive tests

The results of the tests described above are presented in this section. Figure 3.2 shows typical tensile and compressive specimens during testing. The two dots on each specimen are used to track extension/compression with the video extensometer. Figure 3.3 shows representative stress-strain curves of the three adhesives in tension and compression. Finally, Table 3.1 summarises the results of the tests. A minimum of five specimens per adhesive were tested.

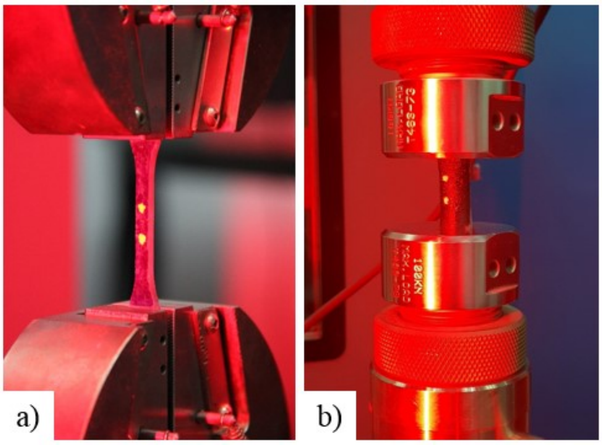

Figure 3.2: a) Tensile and b) compressive tests.

The results initially obtained are in the form of engineering stress/strain, however, these are later converted to true stress/strain. Engineering stress is the force applied in the specimens divided by the original cross-section, while true stress is the force applied in the specimens divided by the actual cross-section as it changes with the load applied. The conversion from engineering stress/strain to true stress/strain was based on the assumption that the volume remained constant during loading. Therefore, the true strain was derived from equation 3.1, while the true stress was derived from equation 3.2 as follows

$$\varepsilon_{\text{true}} = \ln(1 + \varepsilon_{\text{eng}}), \tag{3.1}$$

$$\sigma_{\text{true}} = \sigma_{\text{eng}}\left(1 + \varepsilon_{\text{eng}}\right). \tag{3.2}$$

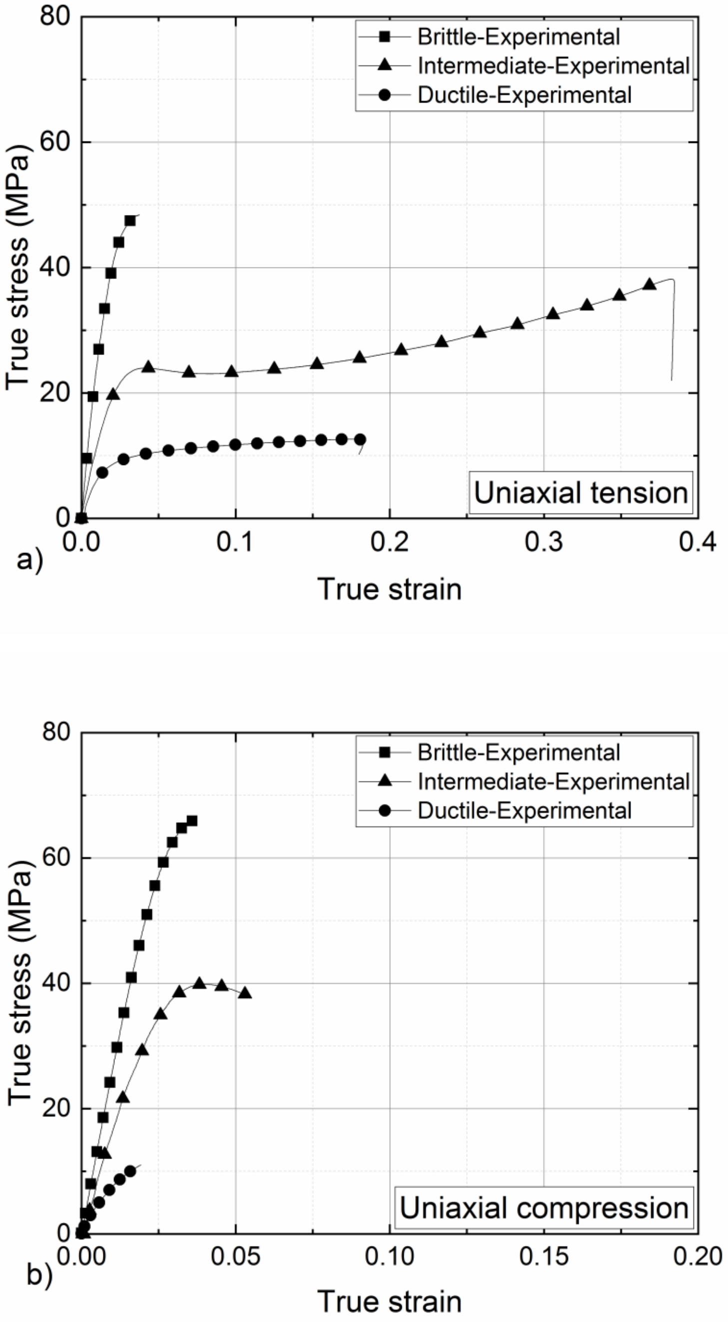

Figure 3.3: Representative true stress-strain curves obtained from a) tensile and b) compressive testing for the brittle, the intermediate strength and the ductile adhesive used in this study.

Table 3.1: Results of material characterization testing for Araldite 2020, Araldite 2047-1 and Delo-Duopox 03 rapid thix.

	Araldite 2020 (Brittle)	Delo-Duopox 03 rapid thix (Intermediate)	Araldite 2047-1 (Ductile)
Resin system	Epoxy	Epoxy	Methacrylate
Young's modulus (E)	2.57 ± 0.08 GPa	1.54 ± 0.23 GPa	0.89 ± 0.084 GPa
Poisson's ratio (v)	0.38 ± 0.004	0.4 ± 0.002	0.42 ± 0.001
Tensile yield strength (σ_{yT})	31.33 ± 2.73 MPa	13.52 ± 2.22 MPa	5.56 ± 0.11 MPa
Compressive yield strength (σ_{yC})	56.76 ± 5.01 MPa	22.46 ± 2.53 MPa	6.75 ± 0.45 MPa
Tensile failure stress (σ_{fT})	45.39 ± 2.61 MPa	37.2 ± 3.4 MPa	13.1 ± 1.13 MPa
Compressive failure stress (σ_{fC})	65.66 ± 0.4 MPa	-	-
Tensile failure strain (ε_{fT})	3.1 ± 0.6 (%)	35.6 ± 4.5 (%)	17 ± 4.1 (%)
Compressive failure strain (ε_{fC})	3.5 ± 0.3 (%)	-	-

The properties measured experimentally are in agreement with the manufacturer datasheet [121] for the ductile adhesive (Araldite 2047-1) where the strength is estimated at 13-15 MPa, the strain to failure at 13-15% and the elastic modulus at 750-900 MPa. The values provided by the manufacturer for the intermediate strength adhesive (Delo-Duopox 03 rapid thix) [120] are higher for the elastic modulus (2000 MPa compared to 1540 MPa measured) and lower for the strength and strain to failure (33 MPa compared to 37 MPa and 20% compared to 35% respectively). Finally, the datasheet of the brittle adhesive (Araldite 2020) [119] only provides value for the flexural modulus which is comparable to the tensile modulus measured (2468 MPa compared to 2570 MPa).

3.3 Substrate characterisation

3.3.1 Measurement of tempered glass residual stress profile

Figure 3.4 shows the residual stress profile of the professionally tempered glass pieces that were used. The measurement was achieved by using a scattered light polariscope (SCALP). The intensity of the scattered light depends on the birefringence caused by the stresses. The main principles of the method can be found in [125, 126], and a short overview is provided here. The scalp device has been used successfully used in estimating the residual stress profile for both annealed and tempered glass [95, 127-130].

The device consists of a laser and a camera as shown in the Figure 3.5. A polarised laser beam passes through the glass, and the glass becomes birefringent due to the photoelastic effect. The magnitude of the birefringence depends on the stress distribution and the photoelastic constant of the material. The stresses can then be computed as

$$\sigma = \frac{1}{C}\frac{\delta}{\sin^2\gamma}. \tag{3.3}$$

In equation 3.3, σ is calculated stress, C is the photoelastic constant of the material, γ is the angle of the laser beam and δ is the optical retardation measured by the device. Since C and β are known and δ is measured by the device, the normal stresses can be calculated.

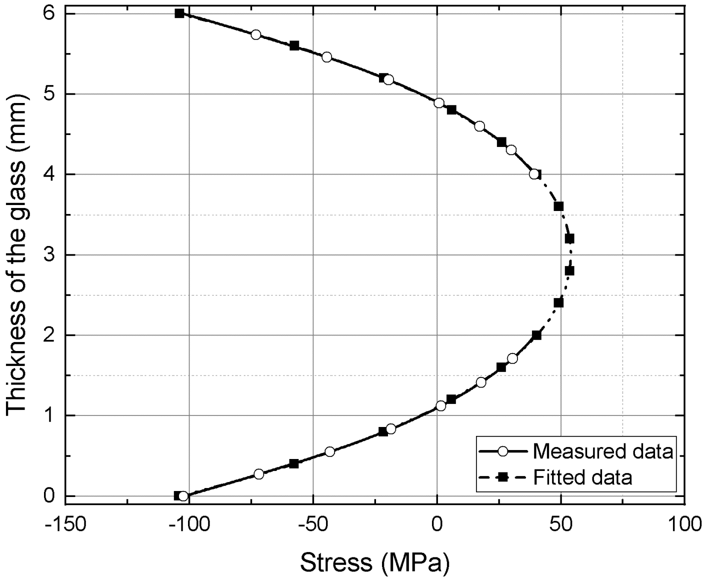

Figure 3.4: Measured and fitted data of the residual stress profile of the 6 mm thick tempered glass.

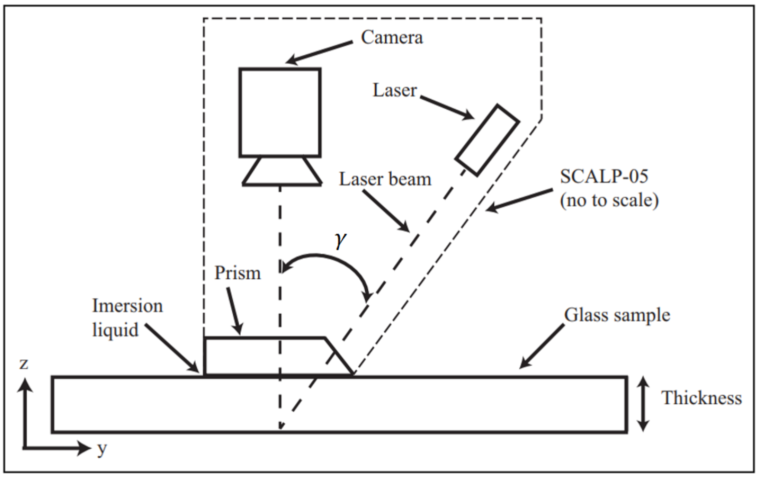

Figure 3.5: Sketch of the measurement of the residual stresses n glass using SCALP-05 [129].

One of the limitations of the device is that it can only measure residual stresses up to a depth of 2.2 mm, while the glass used in our tests is 6 mm thick. Therefore, a 5th degree fitting polynomial was employed in order to complete the typical characteristic shape of the residual stress profile [130]. Figure 3.4 shows the measured and the fitted data of the residual stress of the glass. It can be seen that the compressive surface stresses exceed 100 MPa, which makes the tempered glass less susceptible to surface flaws. In the absence of any internal flaws, this compressive stress needs to be overcome first for failure to occur from the surface.

3.3.2 In-house thermal strengthening of annealed glass

Tempered glass is the glass type mostly used in the construction industry, and it was therefore chosen as the main substrate for this study. It has to be noted however, that there is a minimum plate size that glass manufacturers can thermally strengthen. In most cases, the minimum size, readily available in the market, is 100 mm x 250 mm, and therefore this size was chosen for the glass substrates used in the double lap shear joints tested in this work. However, for the interface characterisation tests described in Chapter 4, smaller glass substrates were needed. Here, annealed glass had to be purchased due to size constraints. However, the strength capacity of annealed glass is significantly lower than that of tempered glass. Preliminary numerical and experimental studies showed that the stresses generated in the glass substrate during interface testing (see in Chapter 4) significantly exceeded the strength of annealed glass. Therefore, a methodology was developed in-house to thermally strengthen the smaller annealed glass coupons.

A furnace was used for the in-house heat strengthening process, and it was attempted to copy the technical procedures that glass manufacturers are using for glass tempering [8, 13]. The annealed glass specimens were heated up to 650°C and then quickly removed from the furnace and sprayed with jets of cold air. It is worth noting that different methodologies were also attempted for the cooling down of the glass specimens. The glass specimens were immersed into water and oil to ensure quick temperature drop, but it was also attempted to let the glass cool down in room temperature for a more gradual temperature drop. In the first case, the glass specimens instantly cracked while in the second case the temperature difference was not as significant for the generation of high residual stresses.

Figure 3.6 shows that the adopted method led to a strength increase of approximately 75% compared to the as-purchased, annealed glass substrates when tested under 3-point bending. Strain gauges were used to measure the strain in the tensile side of the glass and this was afterwards converted to the stress reported in Figure 3.6. The result of the in-house heat strengthening compared to the typical 200% strength increase [8] that can be achieved in automated tempering processes is relatively low, but the strength increase was adequate for the completion of the DCB and SLB tests since glass failure was eliminated.

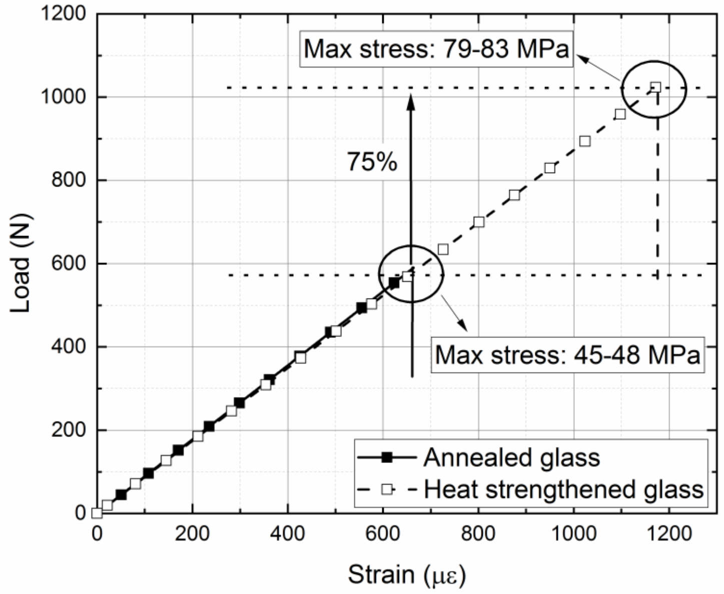

Figure 3.6: Effect of in-house strengthening on glass failure load under 3-point bending loading.

The 3-point bending test was selected for the evaluation of the residual stresses of the in-house strengthening of the glass samples given that the SCALP device described in 3.3.1 has certain size limitations and is not accurate on small coupons

3.3.3 Mechanical properties of glass and steel

Mild steel was used for the manufacturing of the hybrid joints tested. For the stiffness and strength of the mild steel (Young's modulus and yield stress), standard textbook values were assumed [131]. In the analyses that follow, the stresses generated in the mild steel were significantly lower than the yield/failure stresses, and therefore plasticity/failure of steel was not considered. Table 3.2 shows the main material properties that were used in the experimental and numerical work of this project.

Table 3.2: Properties of the materials used in the numerical and experimental work.

Material properties			
Material	E [GPa]	v	Failure/yield Stress [MPa]
Tempered Glass[1]	70	0.23	120-140
Mild Steel[2]	210	0.3	400

[1] Haldimann et al. [8], [2] Oberg and McCauley [131]

3.4 Summary

This chapter summarises the material characterisation testing performed for the adhesive and the glass substrates. Tensile and compressive tests were performed on three adhesives and the basic mechanical properties of the adhesives were extracted. More specifically, the tests gave information for the elastic modulus, the tensile and compressive yield, failure stress and strain and the pressure sensitivity of each adhesive. In addition, a scattered light polariscope was used for the measurement of the residual stress profile in the glass substrates while the in-situ heat strengthening process that was developed for annealed glass coupons of small size is also described and evaluated.

Chapter 4 **Glass-steel interface characterisation**

4.1 Introduction and structure

The characterisation of the glass/steel interfaces for the brittle and ductile adhesives that were used is presented in Chapter 4. The experimental set-up, the testing procedures, the results and finally the numerical fitting procedure to extract necessary numerical input data are described. The purpose of this chapter is to determine the glass/steel interface properties in order to establish numerical cohesive zone models that can later predict the fracture and failure of glass/steel adhesive joints.

The Double Cantilever Beam (DCB) and the End Notched Flexure (ENF) tests are typically used for the extraction of the cohesive laws in modes I and II. However, traction-separation laws are sensitive to the surface chemistry of the substrates and failure generally occurs on the glass surface for hybrid glass/steel joints. In the case of glass/steel adhesive joints, the same dissimilar materials should be bonded, and the stresses in the substrates then need to be reduced due to the relatively low strength of glass. As a result, the typical framework adopted for the characterisation of the interface properties in fracture/separation modes I and II as per standard test methodologies is not feasible unless it is modified.

A robust and validated methodology for the characterisation of glass/steel adhesive interfaces of bonded joints loaded in modes I and II using a modified and improved testing methodology based on these standards is currently lacking. Therefore, Cohesive Zone Modelling (CZM) approaches adopted for glass/steel connections have been limited to using reference and literature values [100].

Part of the results presented in this chapter were published as full paper in [132].

4.2 Numerical methodology

For the numerical simulations, both the implicit and explicit solvers of the commercial finite element (FE) code ABAQUS 6.14 [50] were used. The results presented in the subsequent sections were taken from the explicit solver. However, later analysis revealed that the implicit solver produced similar results.

The substrates were modelled using 3D stress (continuum), 8-node linear solid elements with reduced integration and hourglass control (C3D8R in ABAQUS). In addition, the cohesive layers were modelled with 8-node 3D cohesive elements (COH3D8 in ABQUS). The traction-separation laws were established by developing models for the modified DCB and SLB tests. In these tests, the adhesive layer was modelled as a single row of cohesive elements representing the bondline thickness.

In this work, a quadratic nominal stress criterion was used for the damage initiation, while a linear mode-mixity fracture energetic criterion [50] was used for the damage propagation of the cohesive elements. Both criteria were described in Chapter 2.

The cohesive properties were determined using the inverse method [33] performing numerical iterations until good agreement between the experimental calibration tests and numerical load-displacement curves was achieved. For numerical calibration purposes, it is important that consistent numerical data are obtained. The experimental variation based on maximum and minimum values obtained for each test set-up is therefore reported in the following sections. It is ensured that data calibration provides representative average values.

During the calibration process the stiffness of the cohesive elements remained constant (values for Young's modulus were taken from Table 3.1), while the traction and fracture energy were varied. The combined numerical and experimental approach for the determination of the cohesive properties (traction and fracture energy) in modes I and II is summarised in Figure 4.1.

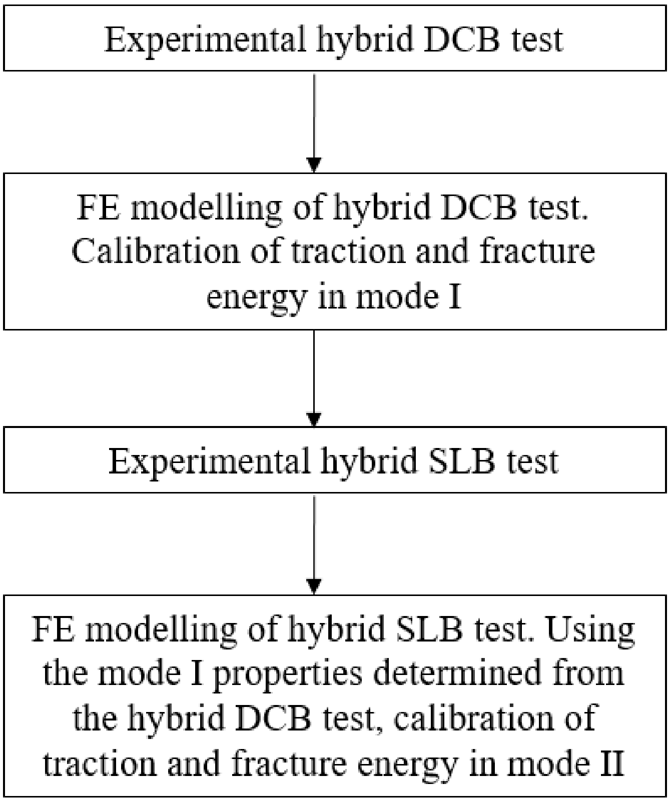

Figure 4.1: Flowchart describing the experimental and numerical procedure for the determination of the cohesive properties in modes I and II.

4.3 Modified DCB test

The DCB test is covered by ASTM D3433-9 [69] when similar metal substrates are used. Here, dissimilar substrates were used for the interface characterisation tests, and therefore it was important to match the bending stiffness of the two substrates to ensure that loading was symmetrical and the adhesive layer was deforming in pure mode I. In order to achieve this, the thickness of the two substrates was adjusted such that the thickness of the glass substrate was 12 mm and the thickness of the steel substrate was 8 mm as per the following

$$t_1 = \left(\sqrt[3]{E_2/E_1}\right)\, t_2 \,. \tag{4.1}$$

In equation (4.1), t_1 and t_2 are the thicknesses of the glass and the steel substrates, while E_1 and E_2 are the respective values for the Young's modulus. This modification resulted in the two arms of the DCB specimen having equal bending stiffness and thus leads to symmetrical loading in the adhesive layer [133].

The geometry of the modified DCB specimens and the experimental set-up is shown in Figure 4.2, and the dimensions are displayed in Table 4.1. A steel fixture was used for the alignment of the substrates, and 0.2 mm steel wires were used for controlling the bondline thickness. The steel substrates were sandblasted before bonding to improve adhesion, and both glass and steel substrates were degreased using acetone. The glass substrates used for these tests were the ones that were strengthened in-house as described in Chapter 3. Finally, before joint manufacturing both substrates underwent atmospheric plasma treatment with a mixture of argon and oxygen gas to clean the surface and to improve adhesion by surface activation.

Table 4.1: Summary of the geometry of the DCB test.

L_1	160 mm
L_2	100 mm
t_1	8 mm
t_2	12 mm
w	20 mm
Bondline thickness	0.2 mm

The tests were displacement controlled, a loading rate of 0.5 mm/min was used and a minimum of five specimens per adhesive were tested.

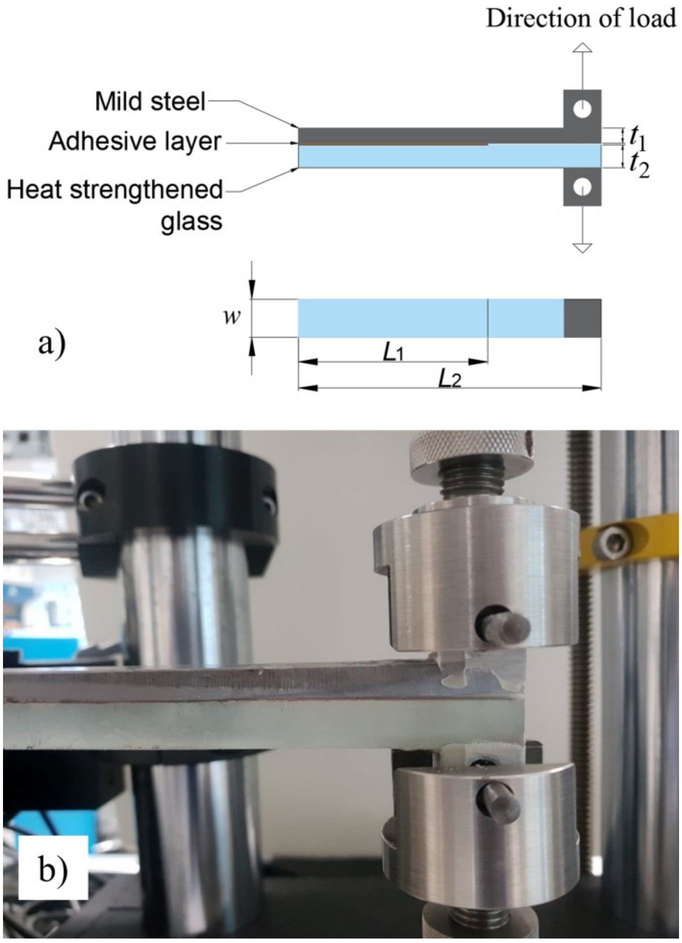

Figure 4.2: Modified DCB a) design and b) test set-up.

Finite element analysis of the test set-up was conducted. The set-up presented in Figure 4.2 produced a symmetrical loading condition and loading in pure mode I. The stress distribution in the substrates during crack initiation is shown in Figure 4.3. The stresses developed in the glass exceed the nominal strength of annealed glass (~ 40 MPa), but are within the limits of the in-house heat strengthened glass. Figure 4.4 shows the typical failure pattern of these specimens with the initially used annealed glass substrate.

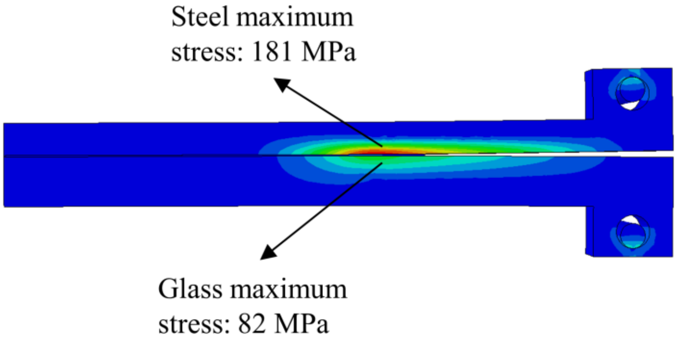

Figure 4.3: Maximum principal stress distribution at damage initiation for the modified DCB specimen.

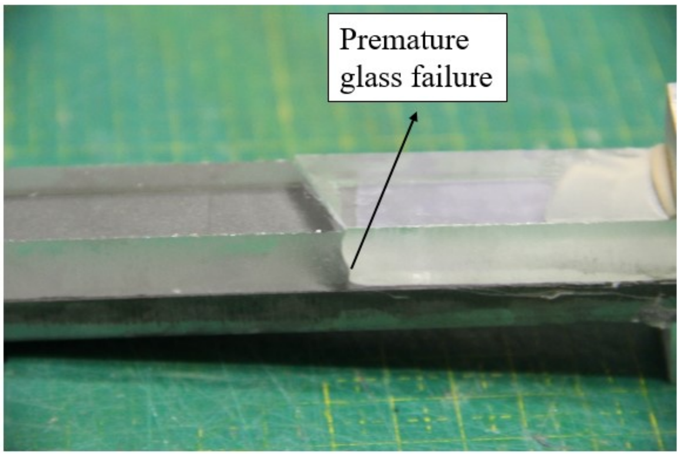

Figure 4.4: Premature glass failure in the crack tip area for annealed glass coupons.

Figure 4.5 shows load-displacement curves obtained experimentally for the joints with brittle and ductile adhesives, and also the corresponding FE simulation after numerical curve fitting. The shaded areas define the variation based on minimum and maximum values measured experimentally. The fitted curves represent the typical average experimental results. Figure 4.6 shows typical glass/steel interfaces after failure using the in-house heat strengthened glass substrates. It was observed that both adhesives failed at the interface, but whilst fully adhesive failure (failure in the interface between the adhesive and the substrates) was seen for the brittle adhesive, the ductile adhesive experienced a mixed mode of adhesive and cohesive failure (failure in the bulk part of the adhesive layer). Analysis of the failed interfaces revealed that the contribution of the cohesive mode of failure was in the range 20-50%, while the contribution of the adhesive mode of failure was in the range 50%-80%.

The different failure mechanisms highlight the importance of the CZM simulation and the calibration of the traction-separation laws on glass/steel interfaces. Table 4.2 presents a summary of the DCB tests performed, and Table 4.3 presents the properties that were calibrated numerically for mode I for the two adhesives. The calibration was based on characteristic specimens representing average results for each case. It is highlighted that the calibrated interface properties (Table 4.3) are different compared to the adhesive properties extracted from tensile tests (Table 3.1). The differences become more important when the failure mechanism is mostly adhesive.

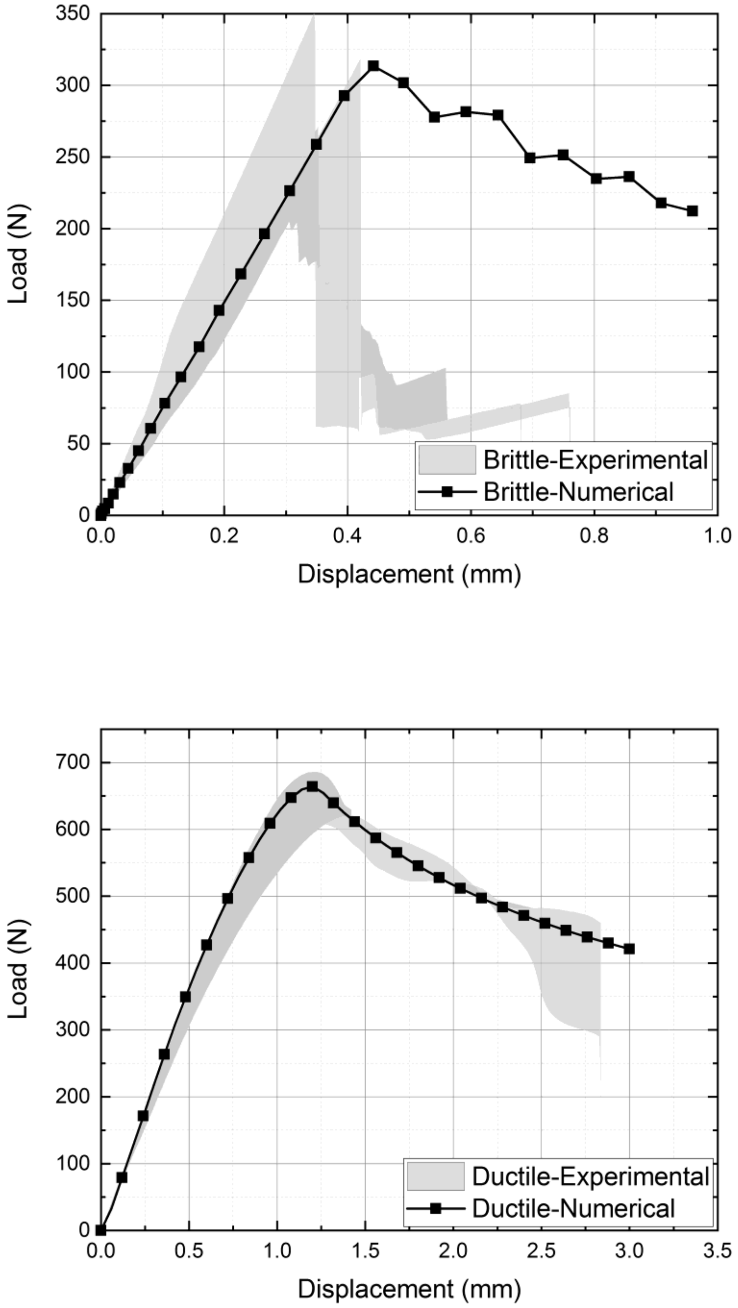

Figure 4.5: Load-displacement curves for the DCB tests and corresponding FE curve fitting for the a) brittle and b) ductile adhesives. The shaded areas define the variation based on minimum and maximum values measured experimentally.

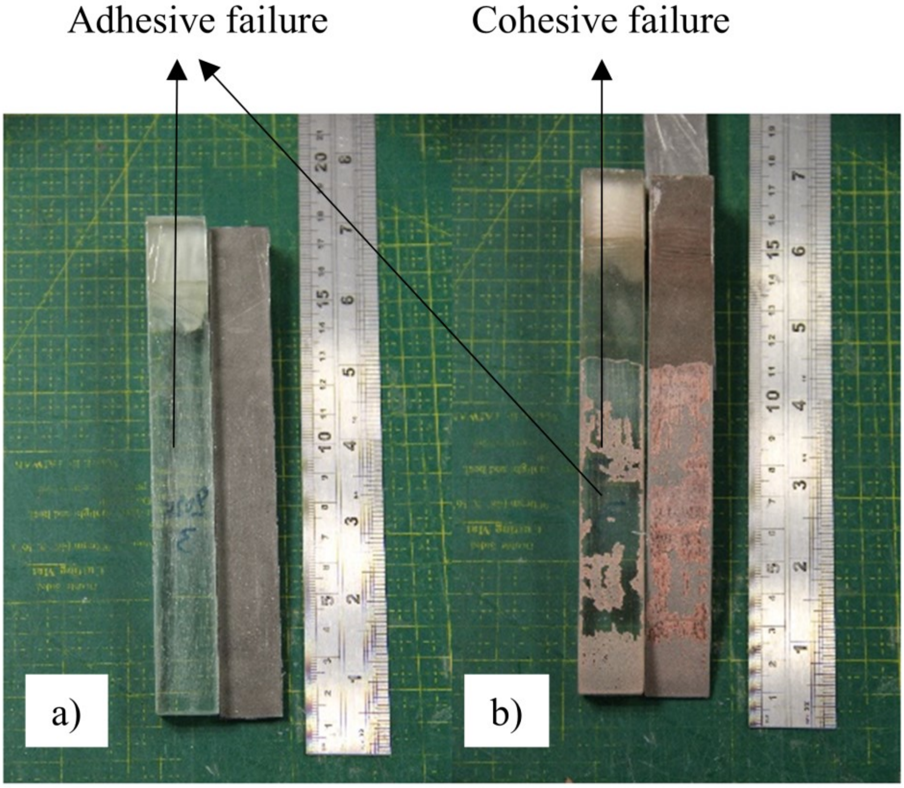

Figure 4.6: Glass/steel DCB typical interfaces after failure for the brittle (left) and ductile (right) adhesive.

Table 4.2: Summary table of DCB tests.

Specimen	Average Max Load (N)
Araldite 2020 (Brittle)	286 ± 55
Araldite 2047-1 (Ductile)	649 ± 29

Table 4.3: Cohesive properties in loading mode I for the two adhesives for dissimilar glass/steel joints (fitted with triangular cohesive law).

Property	Araldite 2020 (Brittle)	Araldite 2047-1 (Ductile)
E (GPa)	2.57	0.89
t_n^c (MPa)	25	10
δ_n^c (mm)	0.004	0.104
G_n^c(J/m^2)	50	520

Figure 4.5 shows that for the brittle adhesive a sudden load drop occurred after damage initiation (maximum load). This indicates that the crack did not propagate progressively, but that a significant length of the interface debonded instantly. Therefore, the calibration of the cohesive properties was only based on the maximum load. In contrast, for the ductile adhesive the damage propagated progressively, and the numerical calibration was based on both the maximum load and the load drop region. It is noted that both traction and fracture energy influence the maximum load, while the slope of the load drop region is affected only by the fracture energy.

It is important to highlight that steel or aluminium substrates could be used to perform the same tests to avoid the premature glass failures as per ASTM standards. However, assuming that the interface response between glass/steel and steel/steel behaves in a similar manner was a simplification that could not be physically justified, and was assumed to lead to overestimations of the cohesive law parameters and thus the strength of the joints. To demonstrate this, the response of the glass/steel DCB specimen was compared with a steel/steel DCB specimen for both the brittle and the ductile adhesive. The differences are shown in Figure 4.7.

It is observed from Figure 4.7 that the glass/steel DCB specimens failed at lower loads compared to the steel/steel joints. The steel/steel DCB specimen with the brittle adhesive failed at 83% higher loads compared to the glass/steel specimen. Similarly, for the ductile adhesive, the strength increase was 12% for steel/steel joints relative to steel/glass joints. This is due to the fact that, the steel/steel specimens failed mostly cohesively, while for the steel/glass specimens mixed adhesive/cohesive failure was observed. Accordingly, considering the correct substrate configuration for CZM evaluation is important in order to capture the effects of surface chemistry and substrate/adhesive bonding.

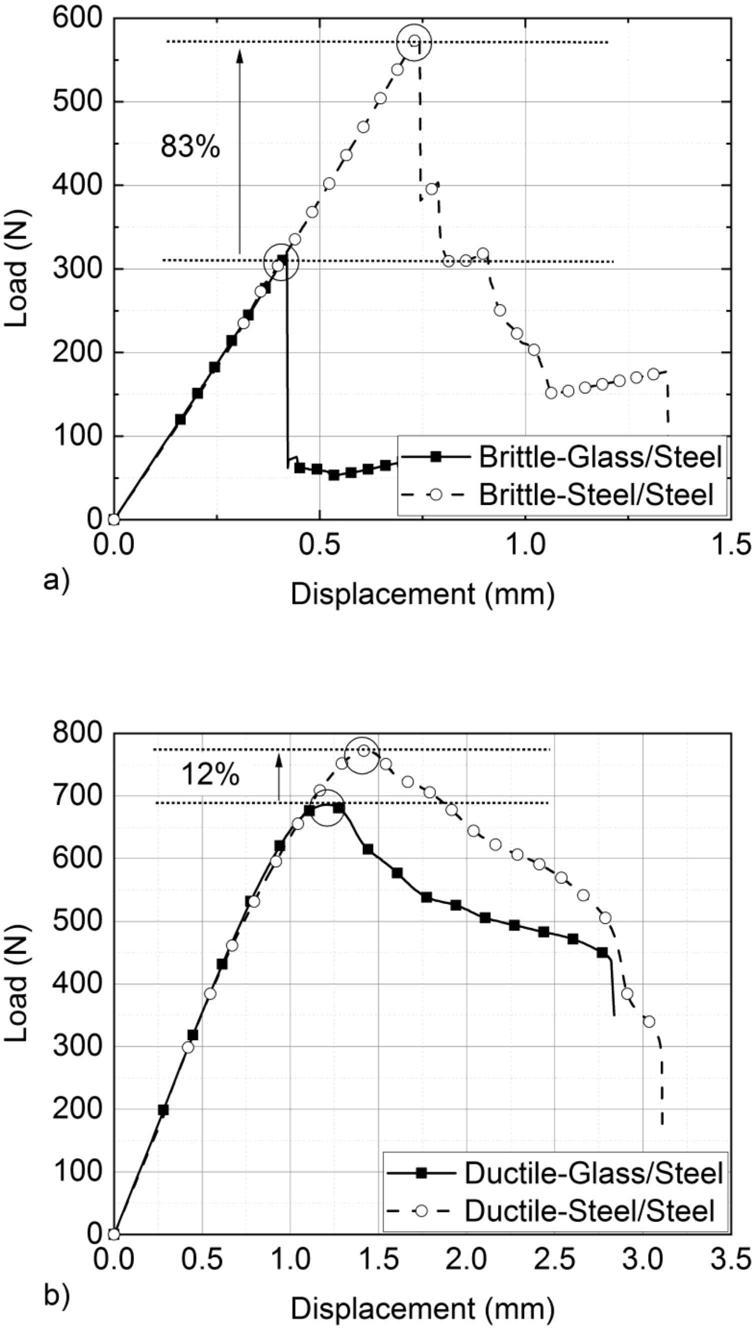

Figure 4.7: Load-displacement response of glass/steel and steel/steel DCB specimens for the a) brittle and b) ductile adhesives.

4.4 Modified SLB test

The Single Leg Bending (SLB) is a simple modification of the ENF test that introduces mode-mixity in the adhesive layer and also drastically reduces the stresses in the substrates, especially in the lower substrate. The thickness of the two substrates determines the relative combination of modes I and II during the test. Finite element analysis was again conducted to determine the optimum thickness of the two substrates, aiming to keep the tensile stresses generated in the glass substrate below 40 MPa to avoid the need for heat strengthening. Figure 4.8 shows the typical stress results of the chosen geometry highlighting the maximum principal stresses in the glass and steel substrates. As the stresses in the glass substrate are below 40 MPa, heat strengthening of the glass coupons was not necessary after geometry modification.

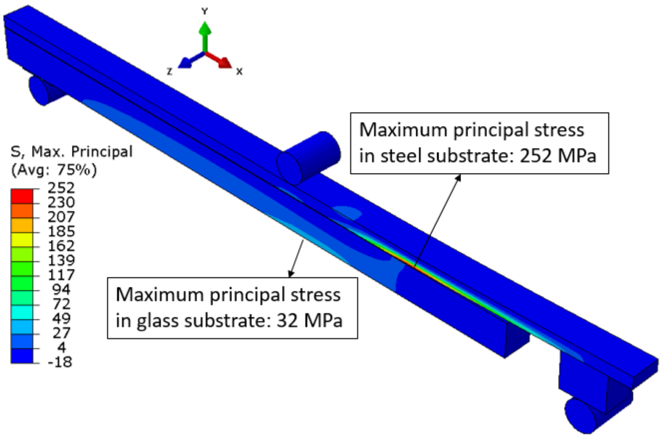

Maximum principal stress in steel substrate: 252 MPa

Maximum principal stress in glass substrate: 32 MPa

Figure 4.8: Preliminary FE analysis for the SLB test aiming to minimise the stress distribution in the glass substrate. Symmetry in the -z axis is used.

The final geometry of the SLB specimen and the experimental set-up is shown in Figure 4.9. The dimensions are given in Table 4.4. Similarly to the DCB test, a steel fixture was used for the alignment of the substrates, and 0.2 mm wires were used for controlling the bondline thickness. Load-displacement curves were recorded during the tests and subsequently compared with the FE simulation results. The CZM properties for mode I also needed to be included in the simulation due to the mode-mixity of the configuration. The comparison between the experimental observations and the numerical simulations led to the calibration of the traction-separation law for mode II loading.

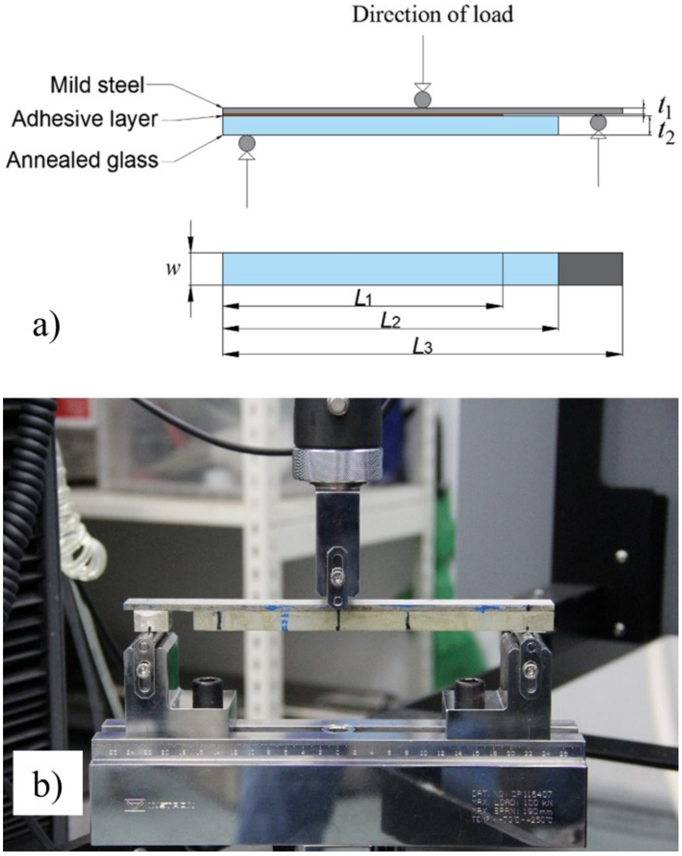

Figure 4.9: SLB a) design and b) test set-up.

The tests were displacement controlled, a loading rate of 0.2 mm/min was used and a minimum of five specimens per adhesive were tested.

Table 4.4: Summary of the geometry of the SLB test.

L_1	180 mm
L_2	210 mm
L_3	250 mm
t_1	4 mm
t_2	12 mm
w	20 mm
Bondline thickness	0.2 mm

Figure 4.10 shows load-displacement curves obtained experimentally for the SLB specimens with brittle and ductile adhesives, and also the corresponding FE simulation after numerical curve fitting. The shaded areas define the variation based on minimum and maximum values measured experimentally. The fitted curves represent the typical average experimental results. The sudden load drops indicate adhesive damage, while the gradual load drops indicate progressive damage in the adhesive layer, thus providing evidence of a process that involves a combination of adhesive and

cohesive damage. Table 4.5 summarises the SLB tests performed, and Table 4.6 presents the properties that were calibrated numerically for mode II loading for both adhesive types. Figure 4.11 shows typical specimens of each adhesive type after failure. It is observed that in all cases the damage is adhesive/cohesive. Furthermore, it is hard to distinguish between the two as the specimens were still bonded together after the tests were conducted.

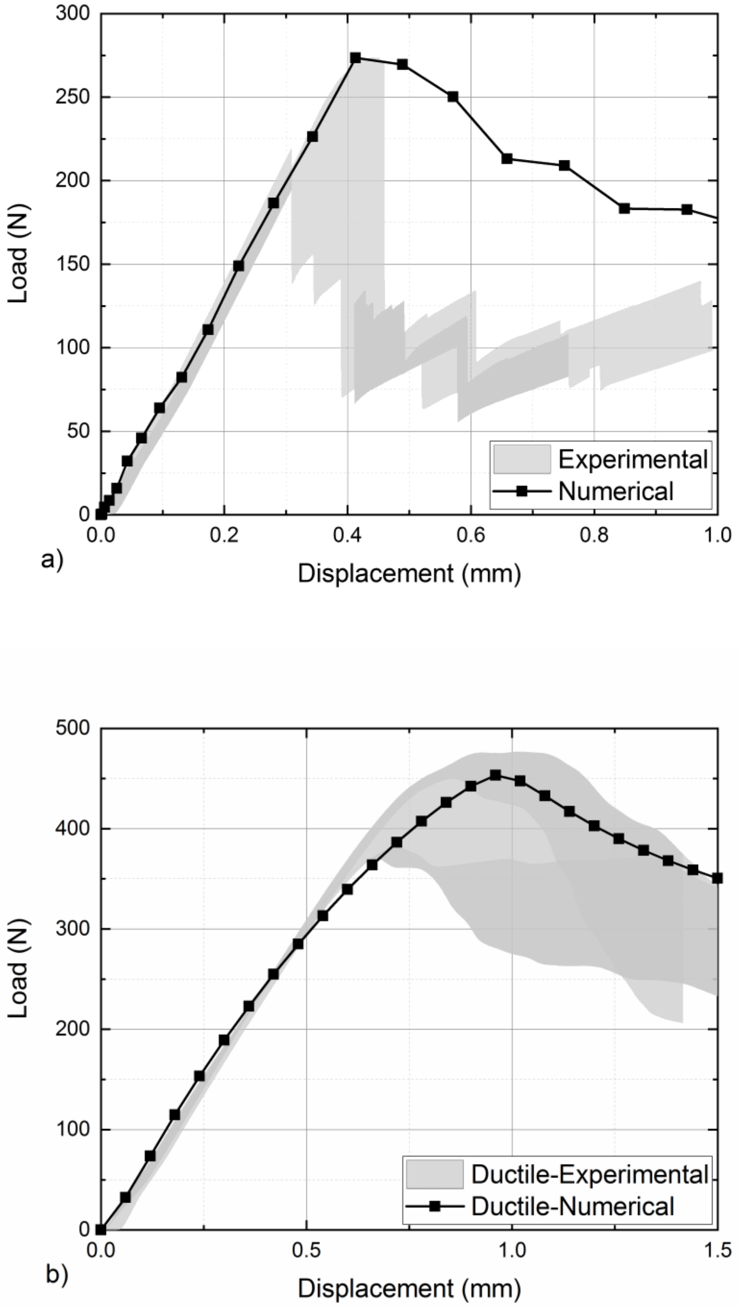

Figure 4.10: Load-displacement curves for the SLB tests and corresponding FE curve fitting for the (a) brittle and (b) ductile adhesives. The shaded areas define the variation based on minimum and maximum values measured experimentally.

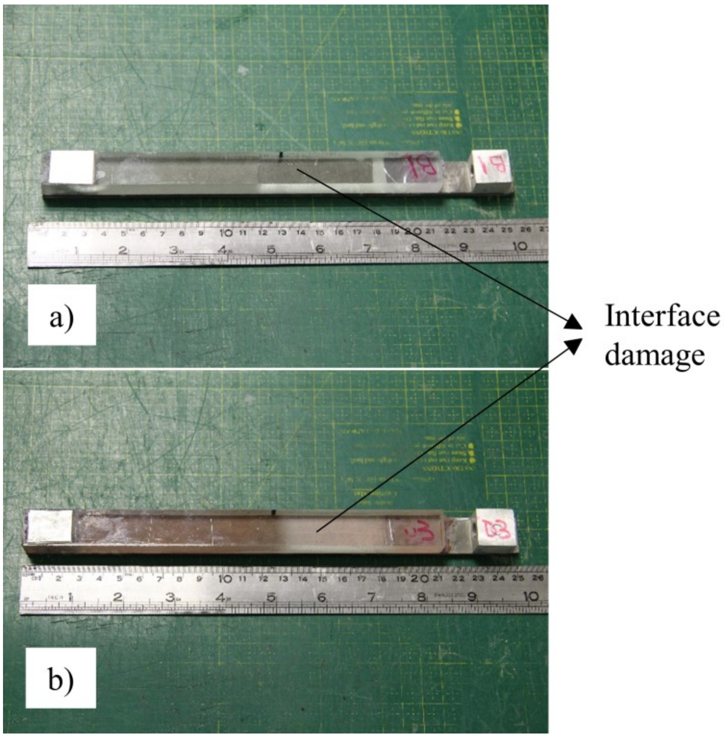

Figure 4.11: Glass/steel SLB typical interfaces after failure for the (a) brittle and (b) ductile adhesive.

Table 4.5: Summary table of SLB tests.

Specimen	Average Maximum Load (N)
Araldite 2020 (Brittle)	254 ± 21
Araldite 2047-1 (Ductile)	419 ± 45

Table 4.6: Cohesive properties in mode II for the brittle and ductile adhesives (fitted with triangular cohesive laws).

Property	Araldite 2020 (Brittle)	Araldite 2047-1 (Ductile)
G (GPa)	0.93	0.31
t_s^c (MPa)	15	2
δ_s^c (mm)	0.013	1.04
G_s^c (J/m^2)	100	1040

During the SLB tests a sudden load drop was recorded once the brittle adhesive reached its maximum load, similar to the DCB tests. Therefore, the properties for mode II were again calibrated against the maximum load reached during the SLB test. For the ductile adhesive however, damage propagated gradually and a smooth load drop was observed leading to the calibration of the cohesive properties in mode II. Once again, the sudden load drops indicate rapid interface (adhesive) failure, while a smooth load drop indicates mostly cohesive damage.

4.5 Summary

This chapter presents the interface characterisation for the glass/steel connections studied. Modified DCB and SLB tests were developed in such a way that premature glass failures could be avoided and the extraction of the cohesive properties of the interface was achieved. The tests led to the extraction of the traction-separation and the fracture energy in modes I and II. An inverse FE curve fitting iterative process was utilised until good agreement between the numerical and the experimental methods was achieved. The cohesive laws obtained from this chapter will later be evaluated on full scale testing of glass/steel double lap shear joints under different loading conditions.

Chapter 5 **Experimental analysis of benchmark designs of glass/steel joints**

5.1 Introduction and structure

The design, manufacturing and full-scale experimental testing of the bolted and adhesive glass/steel hybrid joints is presented in Chapter 5. The design of the double lap shear joints was based on a simplification of similar designs that can be found in almost any façade. The minimum size of tempered glass readily available in the market was also a restriction to be considered for the design. The tests of the joints were conducted in four load cases, representative of realistic loading conditions, namely tension, compression, in-plane and out-of-plane bending.

While the project focused on the use of adhesive joints, it was decided to also test functionally identical designs of bolted joints for reference so that comparisons between the two methods could be made. For the functionally identical designs the bonded area of the adhesive joints was kept equal to the contact area of the bolted joints. Therefore, both types of joints have the same visual impact in a structure. In addition, two adhesives with significantly different mechanical properties, as described in Chapters 3 and 4, were used.

The tests presented in this chapter act as benchmarks for the numerical validation study presented in Chapter 6, the optimisation study in Chapter 7 and the environmental exposure study in Chapter 8.

Part of the results presented in this chapter were published as full papers in [118] and [134].

5.2 Joint design and test set-up

The design of the double lap shear bolted and adhesive joints manufactured and tested is shown in Figures 5.1 and 5.2. The design is a simplification of similar designs found in glass structures [135]. In the design studied, one steel splice was used, which was either connected to the tempered glass substrates with one M10 pre-tensioned bolt or a 50 mm × 50 mm adhesive layer.

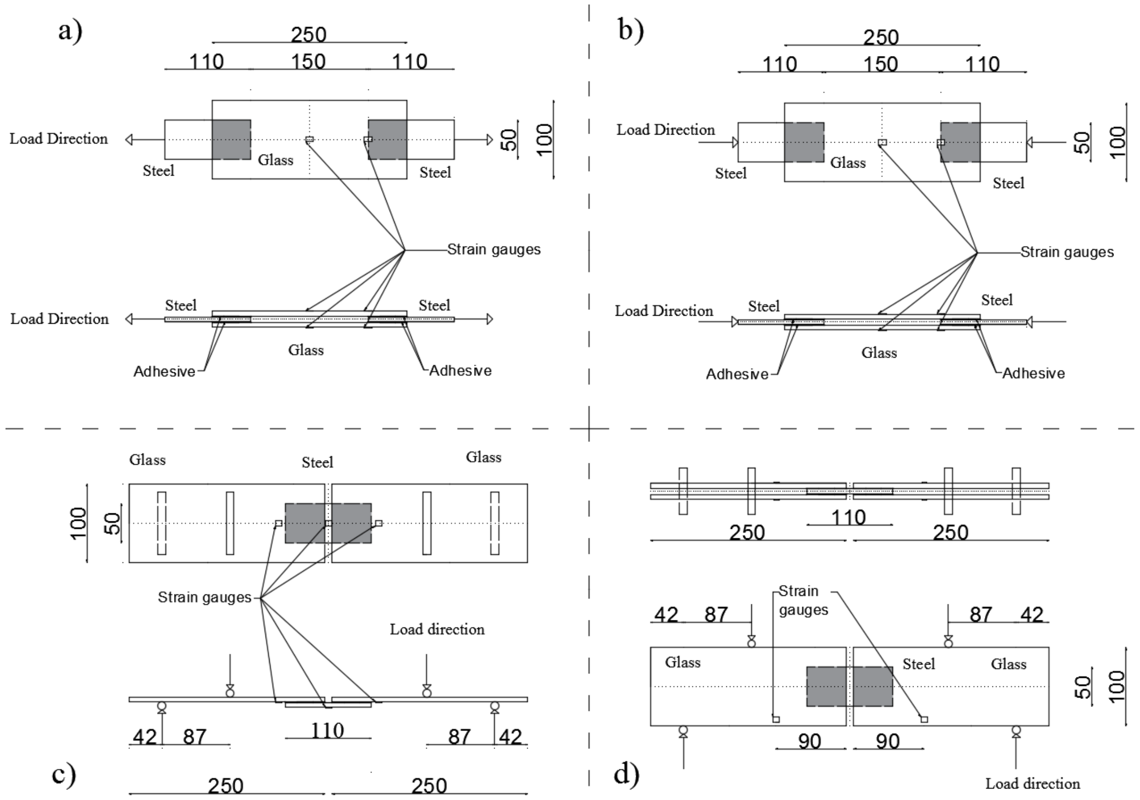

Figure 5.1: Design details of a) tension, b) compression, c) out-of-plane, d) in-plane bending tests for adhesive joints and locations of strain gauges.

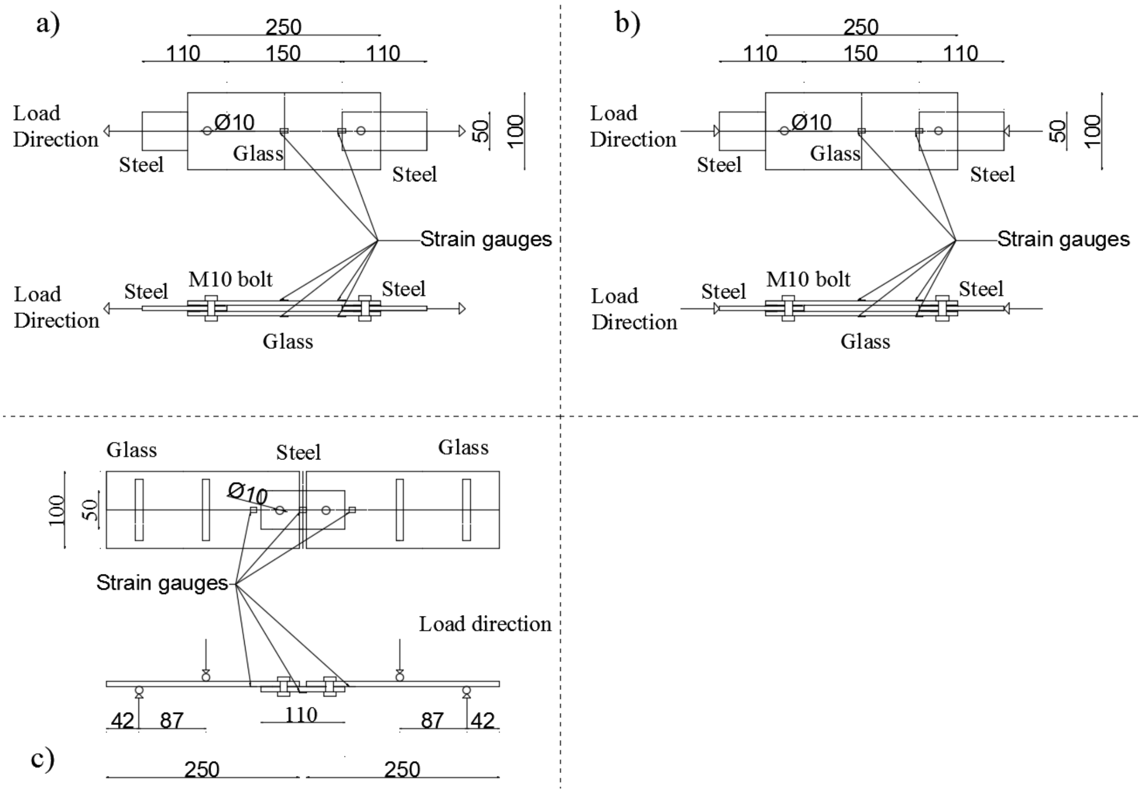

Figure 5.2: Design details of a) tension, b) compression, c) out-of-plane tests for bolted joints and locations of strain gauges.

Adhesive joints were tested in four load cases, namely tension, compression, in-plane and out-of-plane bending. For bolted joints the in-plane bending test led to free rotation of the joint, and therefore this test was not performed. The load cases were chosen to represent actual loading conditions in a glass structure. For instance, the in-plane bending test is representative of the dead loads of a structure in a glass beam while the out-of-plane bending test is representative of wind loads.

The joints consisted of fully tempered glass with dimensions 250 mm × 100 mm and thickness of 6 mm and steel splices with dimensions 110 mm × 50 mm and thickness of 6 mm. The substrates were connected either with one bolt or an adhesive layer with dimensions 50 mm × 50 mm and thickness of 0.2 mm. Manufacturer recommendations [119, 121] for the Araldite adhesives suggest that thin adhesive layers of 0.05 to 0.1 mm lead to the greatest lap shear strength. Here, thin adhesive layers were manufactured with bondline thickness of 0.2 mm to allow repeatable manufacturing and bondline control for the given size of the joint area. For consistency, the thickness was maintained uniform for both adhesives. It is noted that any additional thickness effect on the joint strength was not considered in this study. The thickness was controlled using 0.2 mm thick spacer wires. The contact area of the bolted joints was identical to the area of the adhesive layer, hence 50 mm × 50 mm.

The configuration of the M10 bolt (grade 8.8) can be found in Figure 5.3. Aluminium inserts were used to avoid direct contact of the glass and the steel, and a PTFE busing was used to avoid direct contact of the glass and the bolt. Finally, the clearance of fit was 3%, the pre-tensioning was achieved using a torque wrench and following relevant industry examples was set at 25 Nm [6].

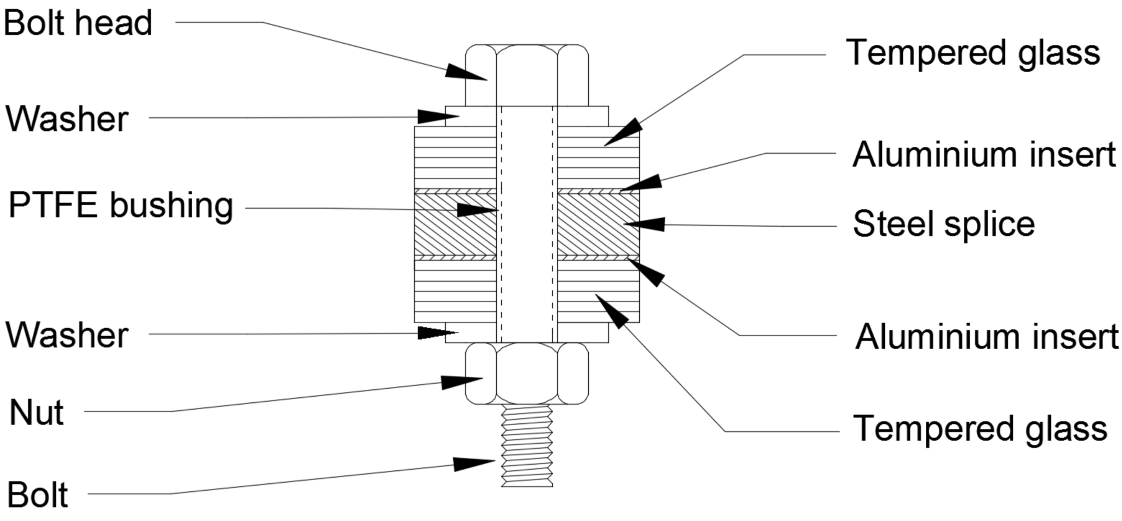

Figure 5.3: Detail of the M10 bolt in bolted joints for the case of tensile and compressive tests. The same principle is used for the out-of-plane bending test with one less tempered glass substrate.

Linear 120Ω strain gauges were used for the monitoring of the strains in critical locations of the joints. These locations can be identified in in Figures 5.1 and 5.2 and will be explained in more detail when each test is described. For the measurement of the strains Vishay's Strainsmart and TML's TDS-530 systems were used. In addition, for bolted joints high-speed cameras were also used to record damage initiation and propagation. High-speed cameras were not used for the adhesive joints given that adhesives display temperature sensitivity and the lights needed for the high-speed cameras were intense and were producing significant heat. Preliminary tests highlighted this effect, resulting in lower than expected load capacity of the joints as well as significant strength variation.

The tests were conducted on an Instron 5982 testing machine with 100 kN load cell capacity, the application of load was displacement controlled and the loading rate was consistently kept below 1 μstrain/sec ensuring quasi-static conditions throughout all tests. At least three specimens of each configuration were tested for every load case. For the in-plane bending tests an aluminium interlayer was used between the glass and the steel rollers to distribute the loads more uniformly on the glass substrates and to avoid local stress concentrations resulting in premature glass fracture.

The steel substrates were sandblasted before bonding to improve adhesion, and both glass and steel substrates were degreased using acetone. Finally, before joint manufacturing both substrates underwent atmospheric plasma treatment with a mixture of argon and oxygen gas to clean the surface and to improve adhesion by surface activation.

Figure 5.4 shows the steel fixture that was used for the alignment of the joints. The manufacturing of the joints took place over two days, since both sides of the steel splices were bonded to the glass substrates one after the other, and one day was allowed to achieve functional strength. Afterwards, the joints were left to cure for at least one week in ambient conditions as per manufacturer recommendations.

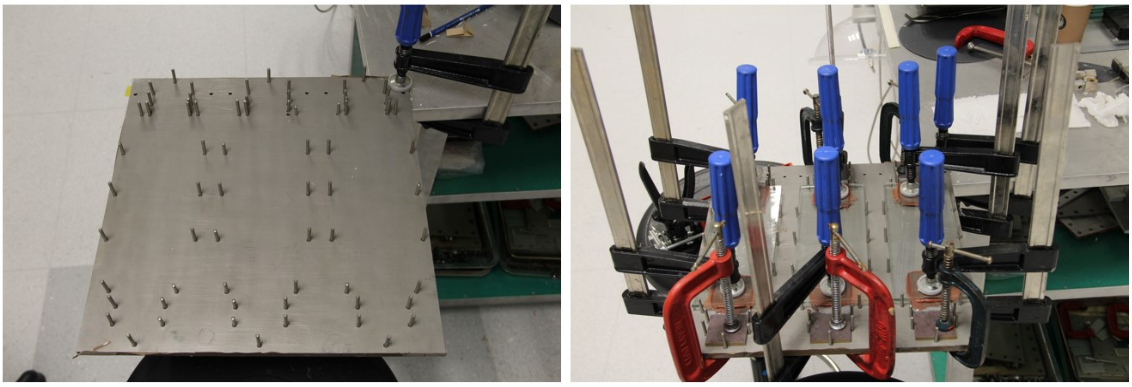

Figure 5.4: Alignment fixture before (left) and during (right) joint manufacturing.

5.3 Results of uniaxial tests in tension and compression

The normal and shear stress states developed in the adhesive layer during tensile and compressive loading are very similar; however, the effect of the loading condition in the glass is different since glass can sustain significantly higher loads in compression than in tension. In addition, eccentricities and imperfections in the samples are exacerbated in the compressive tests and can lead to out-of-plane buckling and hence premature failures. However, tension and compression are stress states that are easily comparable and will, therefore, be presented together in this section.

As shown in Figures 5.1 and 5.2, strain gauges were mounted on both sides of the joints. Two were located in symmetric locations in the midpoint of either side of the joints to capture the far field strain and possible asymmetric loading effects, while two more strain gauges were located in the areas of stress concentrations on the vicinity of the bolt hole for bolted joints or in the edges of the overlaps for adhesive joints. Figure 5.5 shows the bolted and adhesive joints during the tests.

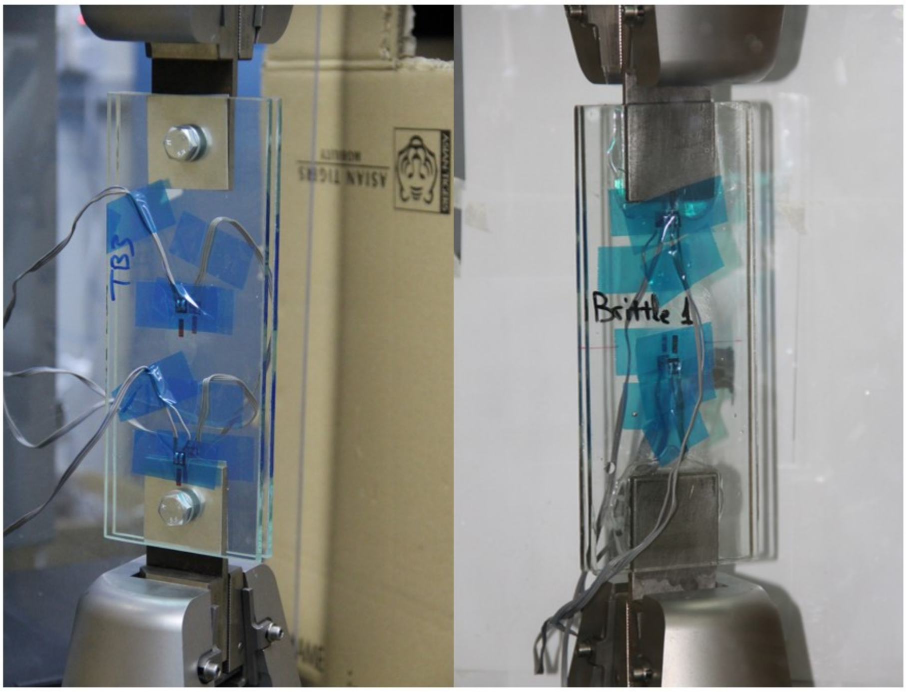

Figure 5.5: Set-up for the tensile/compressive tests for bolted (left) and adhesive (right) joints.

Bolted joints failed catastrophically in the glass, at relatively low loads. The joints displayed a non-linear, stick-slip stiffness response which can be explained by the relative sliding of the substrates due to the clearance of fit. The damage initiation of bolted joints took place in the vicinity of the bolt hole for each test, in a direction perpendicular to the direction of the load due to the development of high bearing stresses. Due to the nature of tempered glass, the damage propagated very fast and led to the complete shattering of the glass. Figure 5.6 shows the experimental observations of the high speed camera, while Figure 5.7 shows typical bolted joints after failure.

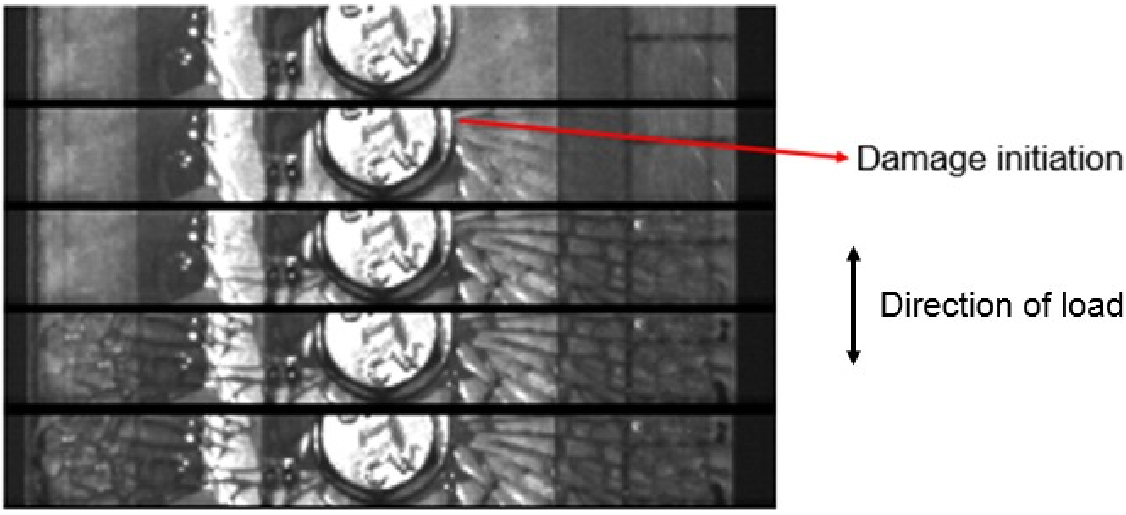

Figure 5.6: Damage initiation and propagation in bolted joint 3. The resolution for each picture is 512x32 and the time interval between each picture is 16.7 μs.

Figure 5.7: Bolted joint after failure.

The strain response of bolted joints was also plotted based on the strain gauges recordings. The strain response is recorded at the midpoint of the glass and also at the area of stress concentrations close to the bolt hole (see Figure 5.2). Figures 5.8 and 5.9 show the far field strain response for the front and the back substrates and the strain response in the area of stress concentration, near the bolt hole, in tension and compression, respectively. It needs to be noted that there is a significant nonlinearity in the load-strain curve at a load of about 3-5 kN. This is the point when the substrates overcome the bolt pre-tension and start to slide against each other. The bolt then comes into contact with the bolt hole. After the new contact area is established, the load-strain response is again mostly linear until failure.

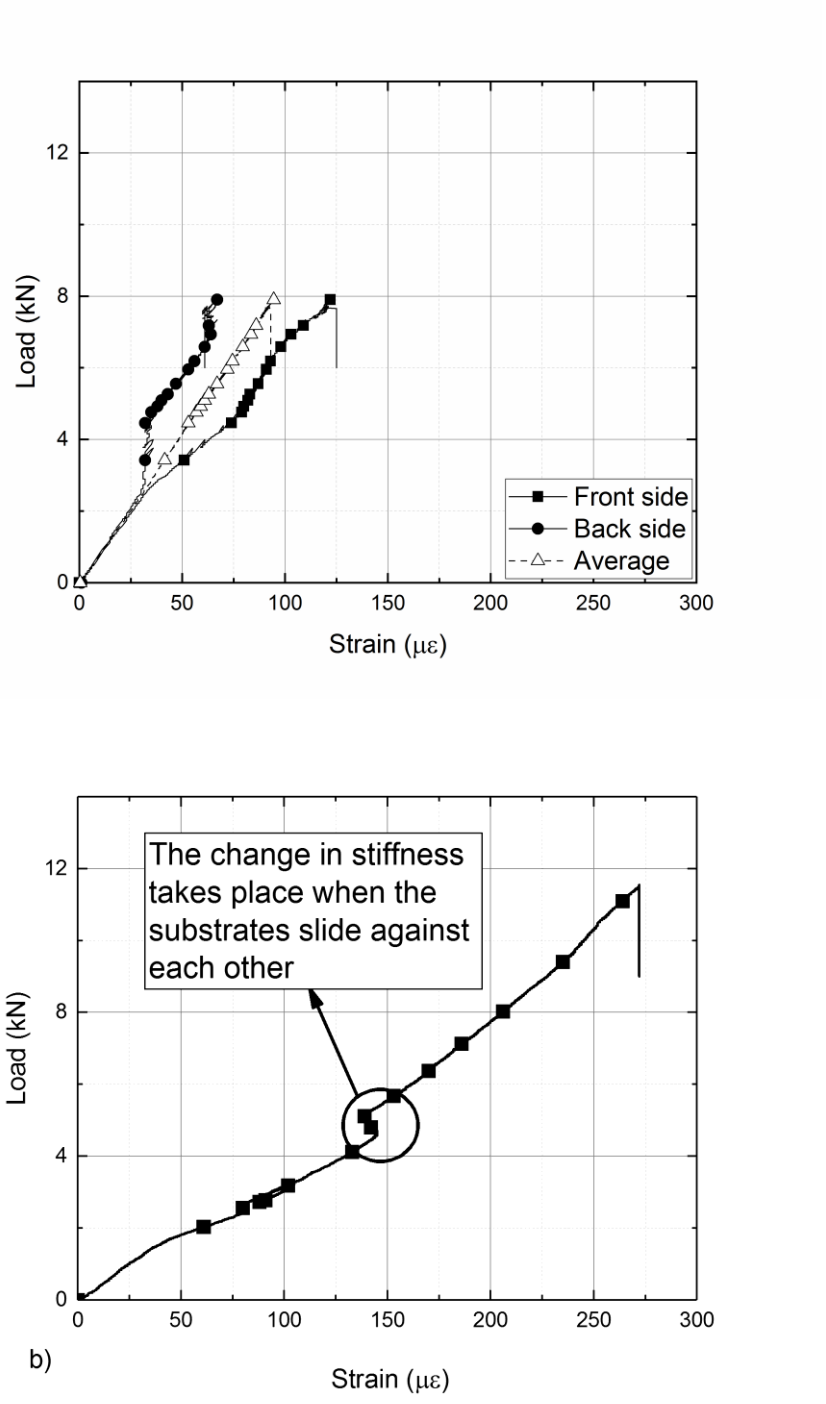

Figure 5.8: Load-strain response for bolted joints under tension at the a) glass midpoint and b) the stress concentration area.

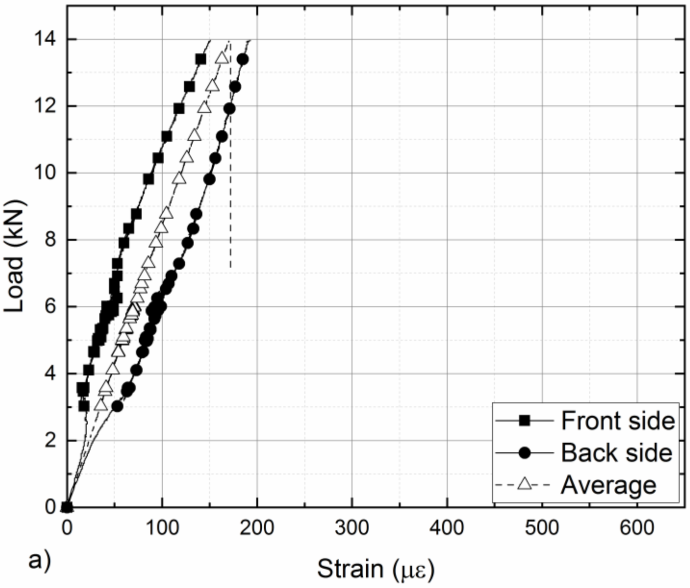

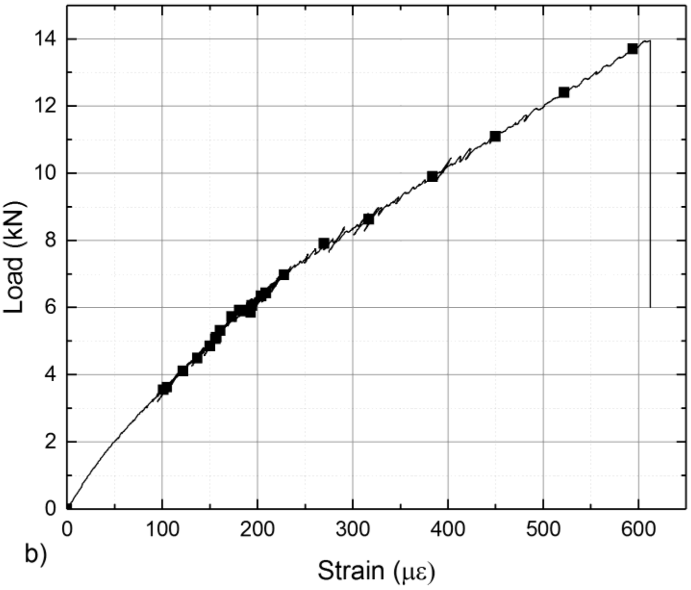

Figure 5.9: Load-strain response for bolted joints under compression at the a) glass midpoint and b) the stress concentration area.

In comparison, adhesive joints failed at significantly higher loads, displayed a linear stiffness response until failure and failed adhesively/cohesively at the joint interface. Both adhesives displayed stress whitening before failure, but this was observed more clearly for the ductile adhesive. Figure 5.10 shows the glass/steel interfaces after the failure of the joints. It can be seen that for the brittle adhesive the failure is mostly adhesive (with small parts also failing cohesively), switching sides between the glass and the steel substrates. For the case of the ductile adhesive, the damage was mostly cohesive and the stress whitening was preceded by void growth and coalescence.

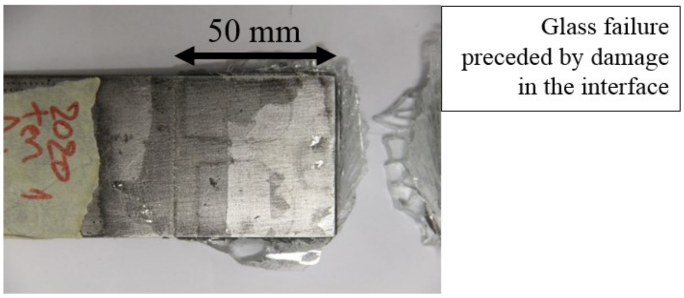

a) Brittle adhesive

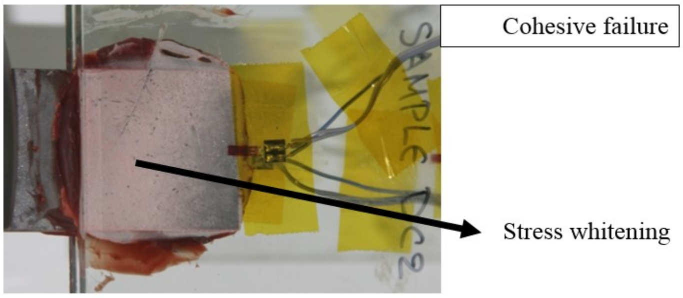

b) Ductile adhesive

Figure 5.10: Typical glass/steel interfaces after failure for a) brittle and b) ductile joints under uniaxial loading. All bonded overlap regions are 50 mm x 50 mm.

Figures 5.11 and 5.12 show the recordings of the strain gauges on both sides of the joints for the areas of stress concentrations and the far field responses under tensile and compressive loading. Characteristic responses of both types of adhesive joints are plotted. The recordings take place on both sides in order to identify possible asymmetrical loadings, eccentricities and/or buckling during the compressive test.

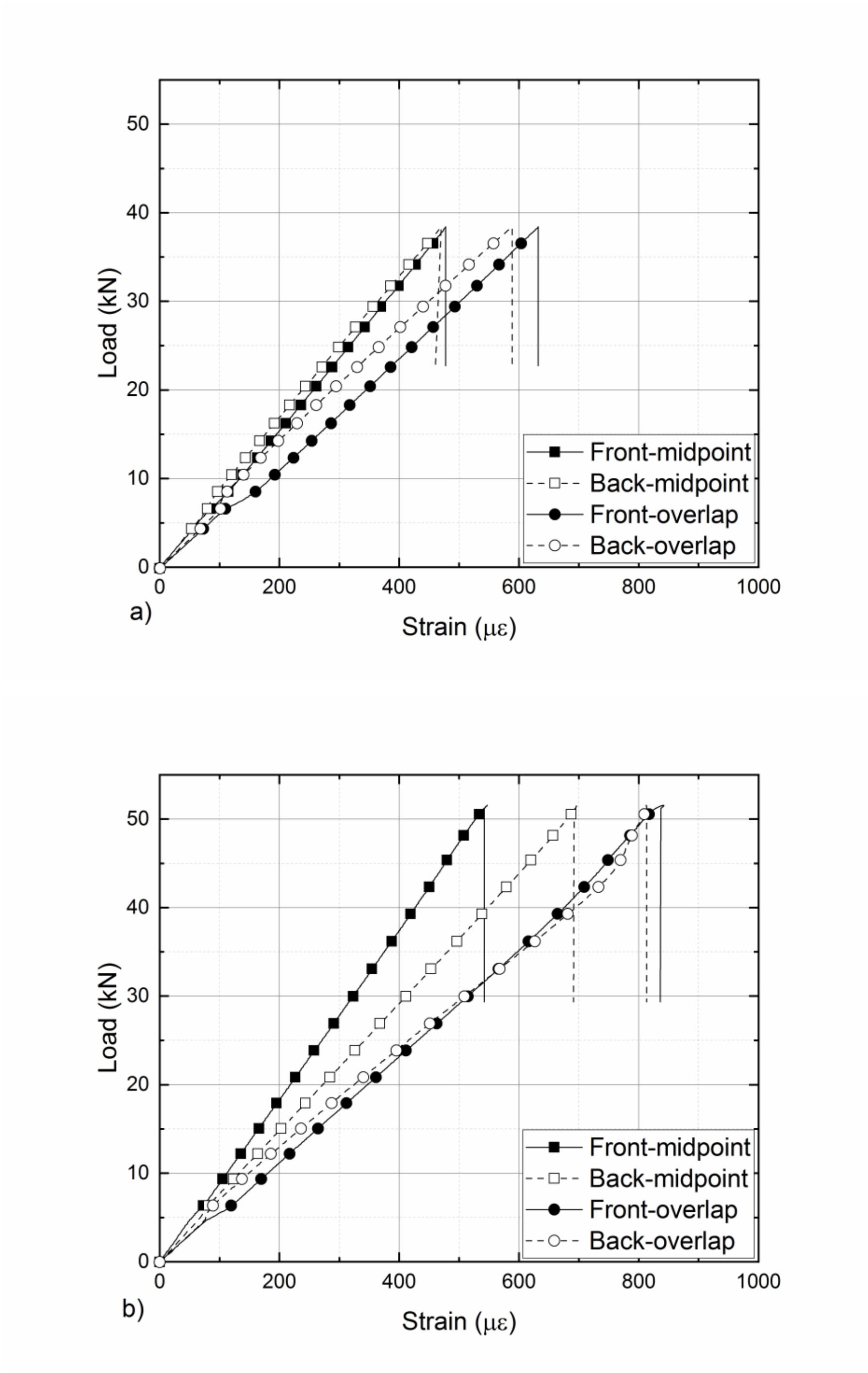

Figure 5.11: Load-strain response recorded on both sides of the joints under tensile loading for the a) brittle and b) ductile adhesive joints.

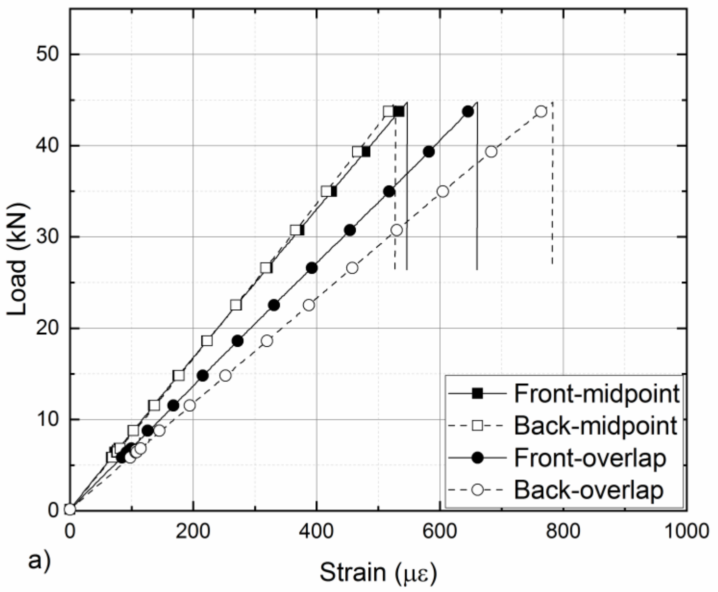

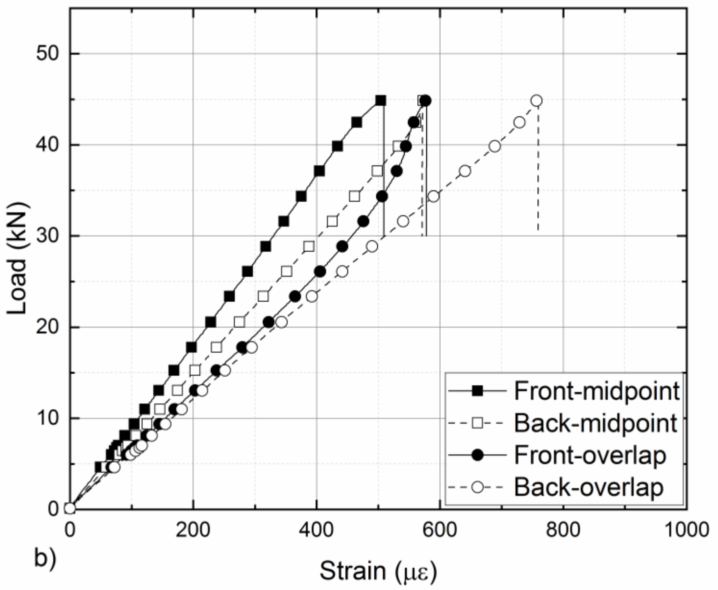

Figure 5.12: Load-strain response recorded on both sides of the joints under compressive loading for the a) brittle and b) ductile adhesive joints.

It can be observed that the responses of the glass substrates for both types of joints are similar and that eccentricities did not influence the joints significantly since the deviation between the two sides did not exceed 15%. The recordings during the compressive test of the ductile joints revealed some buckling close to the end of the test, which might have contributed to the joint failure. The strain responses on both sides were averaged and plotted so that comparisons between the brittle and ductile adhesive joints can be performed more easily.

Figure 5.13 shows the load-strain response both in the area of stress concentration (joint zone) and for the far field response during the tensile test, while Figure 5.14 shows the same for the compression test. It can be observed that even though small deviations between the two sides of the joints were revealed in Figures 5.11 and 5.12, the averaged response of both types of joints is almost identical. Finally, a summary for the uniaxial testing of bolted/adhesive joints can be found in Table 5.1.

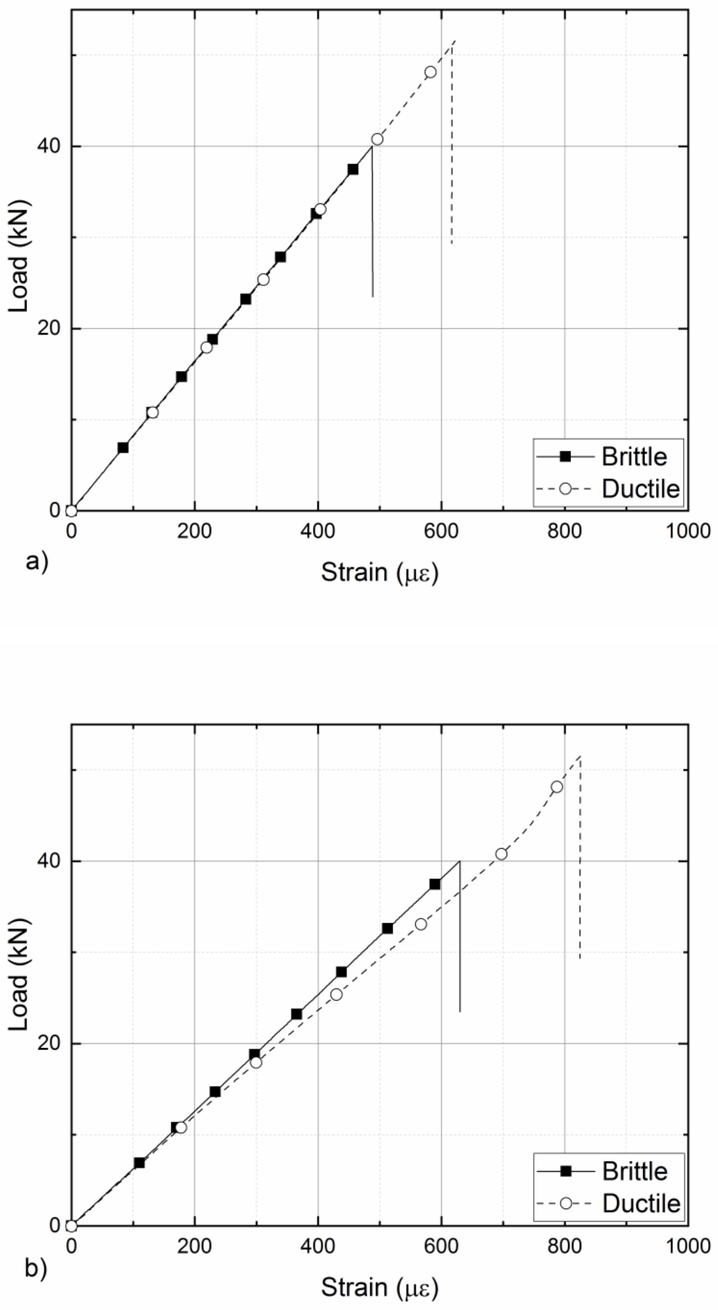

Figure 5.13: Load-strain response for the brittle and ductile adhesive joints under tension at the a) glass midpoint and b) the stress concentration area.

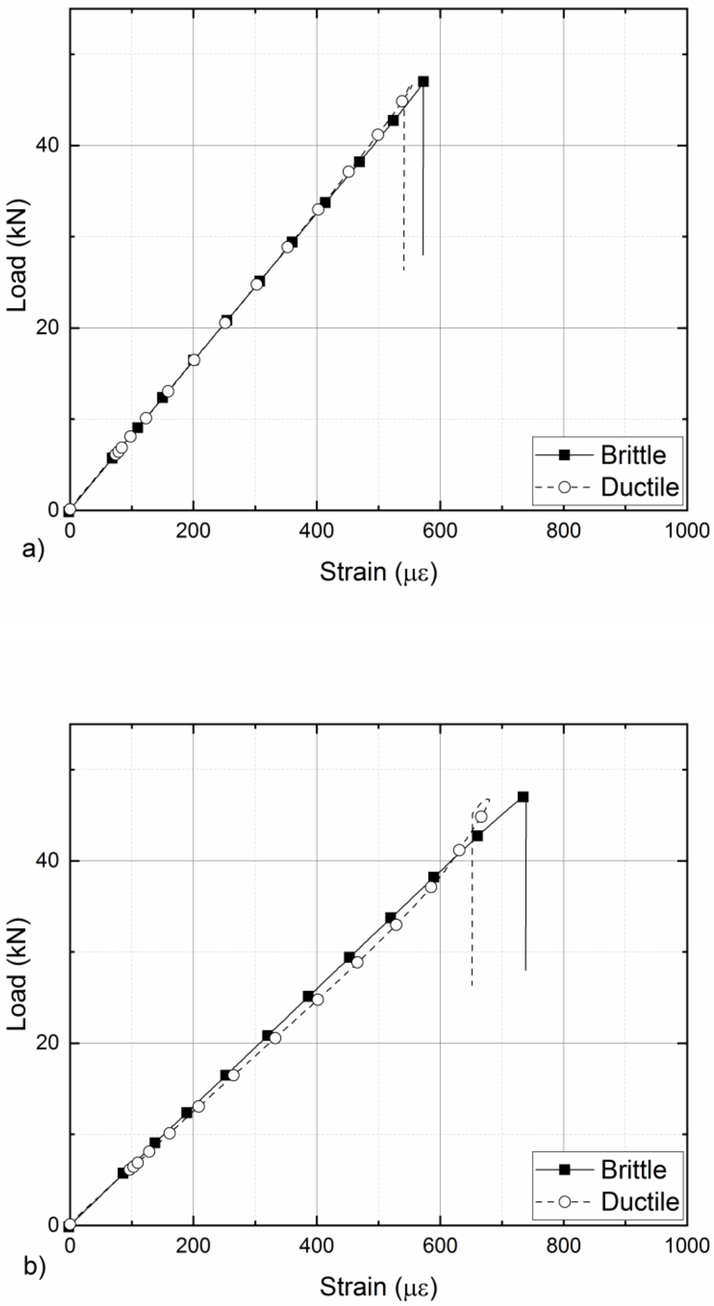

Figure 5.14: Load-strain response for the brittle and ductile adhesive joints under compression at the a) glass midpoint and b) the stress concentration area.

Table 5.1: Summary of the failure loads/mechanisms for the bolted and adhesive joints tested subjected to uniaxial tension and compression loads.

Type of joint	Tension		Compression	
	Measured failure load [kN]	Failure mechanism	Measured failure load [kN]	Failure mechanism
Brittle adhesive (Araldite 2020)	38.0 ± 1.8	Significant damage in the adhesive layer/interface leading to glass failure	42.4 ± 5.1	Significant damage in the adhesive layer/interface leading to glass failure
Ductile adhesive (Araldite 2047-1)	47.0 ± 4.6	Cohesive failure	45.5 ± 0.7	Cohesive failure
Bolted	8.0 ± 0.7	Glass failure	9.7 ± 3	Glass failure

When subjected to tensile loading the ductile adhesive joints outperform (in terms of failure load) the brittle adhesive and the bolted joints by 24% and 488%, respectively. For compressive loading the overall trend is the same. Both types of adhesive joints outperformed bolted joints, but in this case the ductile and brittle adhesives failed at comparable loads. The experimental scatter observed in the results can be explained by load and geometric eccentricities, surface flaws in the glass, and different void distributions in the adhesive layer as also reflected by the range of failure strains measured in Chapter 3.

5.4 Results of out-of-plane bending tests

The design of the out-of-plane bending tests and the location of the three strain gauges can be seen in Figures 5.1 and 5.2. The two strain gauges in the glass were located on the tensile side in symmetrical locations in the areas of stress concentration to detect any asymmetrical loading, while the third strain gauge was located on the steel substrate. Figure 5.15 shows the bolted and adhesive joints during the test.

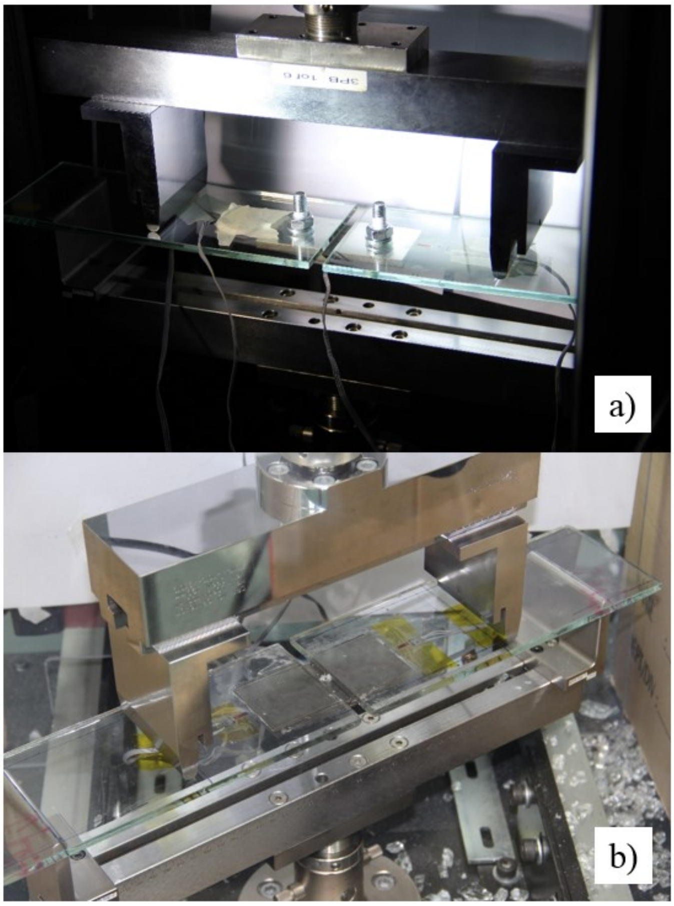

Figure 5.15: Set-up for the out-of-plane bending test for a) bolted and b) adhesive joints.

Bolted joints failed catastrophically in the glass displaying linear response throughout the test. The failure of bolted joints once again took place in the vicinity of the bolt hole for every test, due to the development of high bearing stresses. Figure 5.16 shows the crack initiation and quick propagation in the glass substrate as recorded by the high speed camera at a frame rate of 60000 frames per second. The fracture process takes place within around 50 μs. The load-strain response in the steel and both glass substrates is shown in Figure 5.17

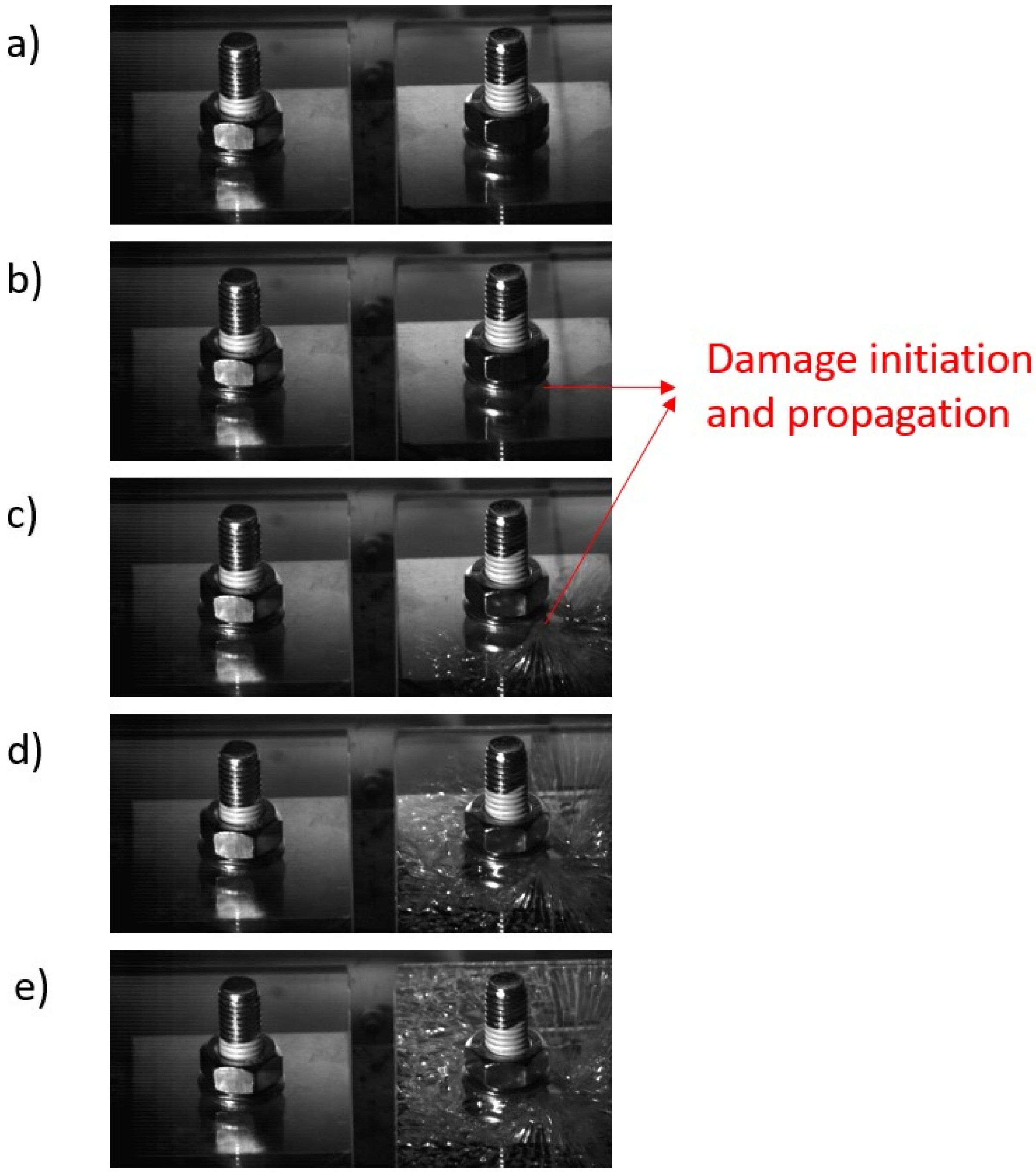

Figure 5.16: Damage initiation and propagation in bolted joints. The resolution for each picture is 512x32 and the time interval between each picture is 16.7 µs.

It can be seen that the response in both the steel and the glass was perfectly linear until failure. In addition, the responses on both glass substrates were plotted to detect unbalanced loading. Small differences were observed for very low loads (less than 200 N) which were attributed to initial uneven load distribution. The responses became identical once both sides established contact with the steel rollers.

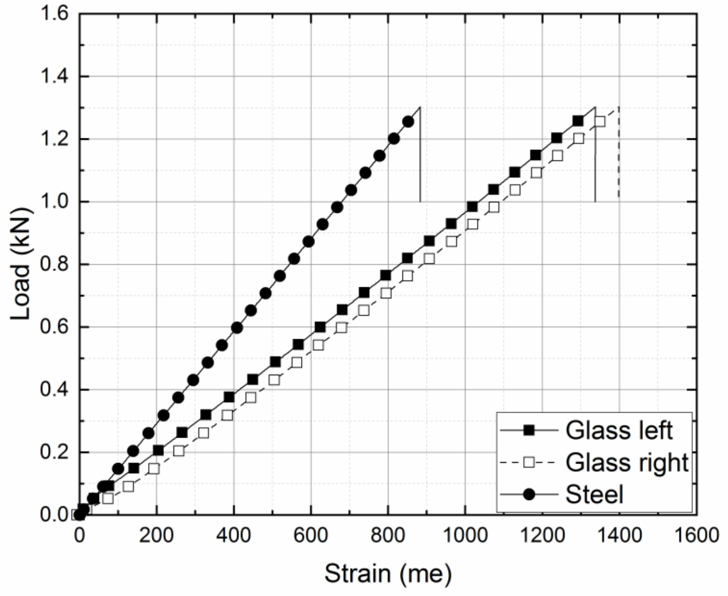

Figure 5.17: Load-strain response for bolted joints subjected to out-of-plane bending loading in the steel and the two glass substrates.

The two types of adhesive joints tested also displayed a linear strain response until failure. In terms of failure mechanism, however, the brittle adhesive joints failed adhesively/cohesively while the ductile adhesive joints failed in the glass at significantly higher loads following stress-whitening in the adhesive. The load-strain response in the steel and glass substrates is shown in Figure 5.18 for the brittle and ductile adhesives. Similarly to bolted joints, small deviations between the responses of the glass substrates can be observed for low loads. Once proper contact of the steel rollers is established with the glass substrates, the responses of both sides are similar.

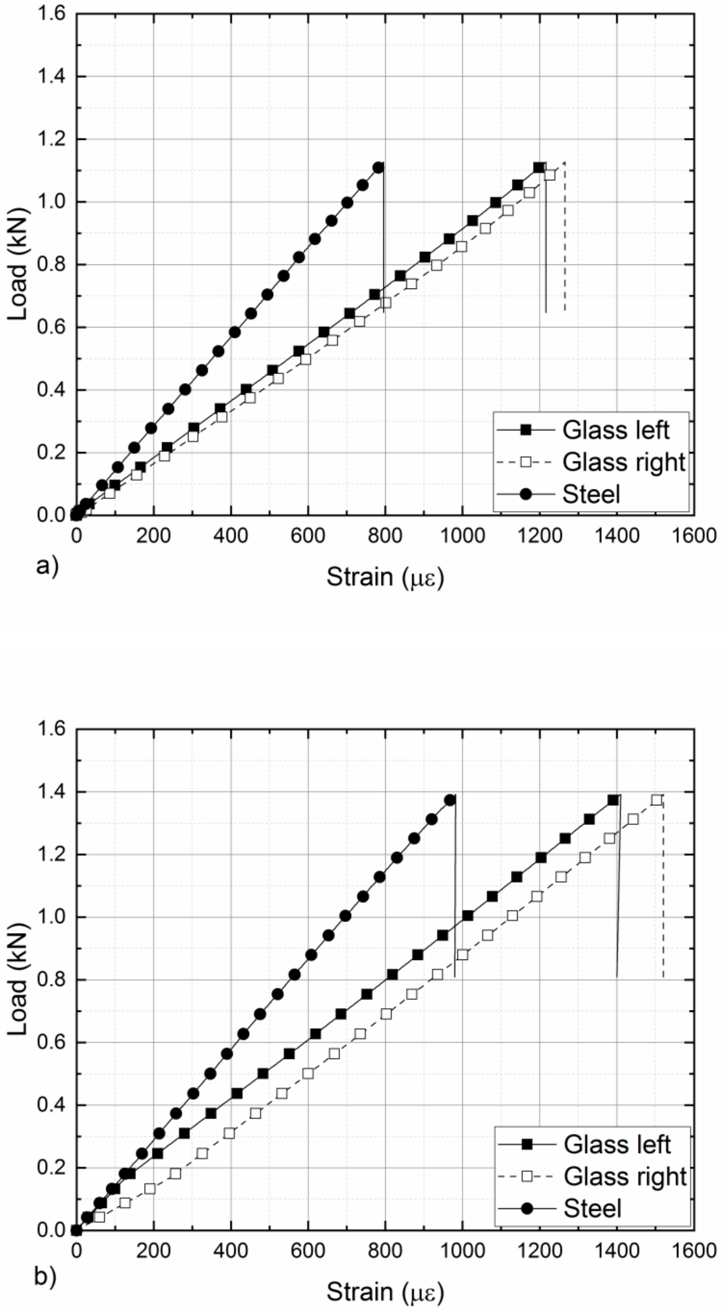

Figure 5.18: Load-strain response for a) brittle and b) ductile adhesive joints subjected to out-of-plane bending loading in the steel and the two glass substrates.

In addition, the responses for the two sides for both types are averaged and plotted in the same graph in Figure 5.19, showing complete agreement for both the steel and the glass substrates in terms of joint stiffness.

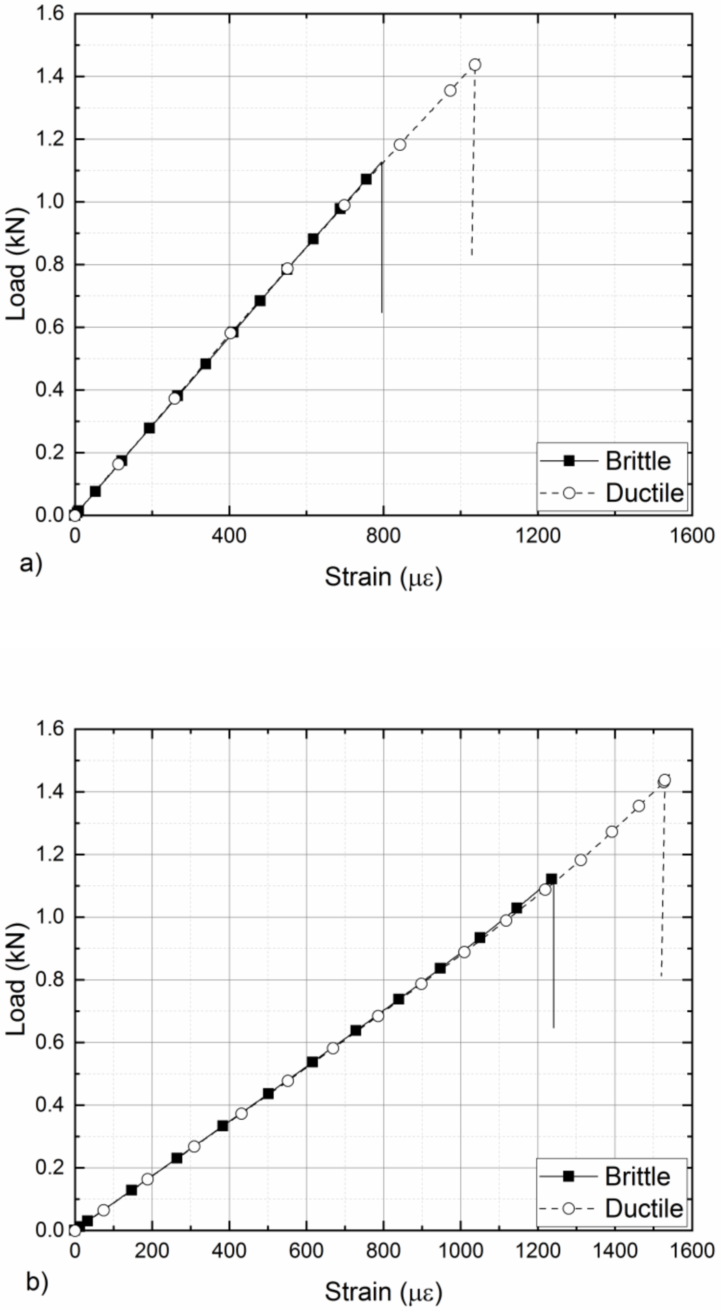

Figure 5.19: Load-strain response for brittle and ductile adhesive joints subjected to out-of-plane bending loading a) in the steel substrate and b) in the glass substrate.

Figure 5.20 shows the glass/steel interfaces after failure. Table 5.2 summarises the failure loads and observed failure mechanisms for the three different joint configurations. It can be seen that the ductile adhesive joints outperform (in terms of failure load) the brittle adhesive and bolted joints by 75% and 21%, respectively. It is noted that this is the only load case in which bolted joints display comparable behaviour to adhesive joints and fail at higher loads compared to the brittle adhesive joints and slightly lower compared to the ductile adhesive joints.

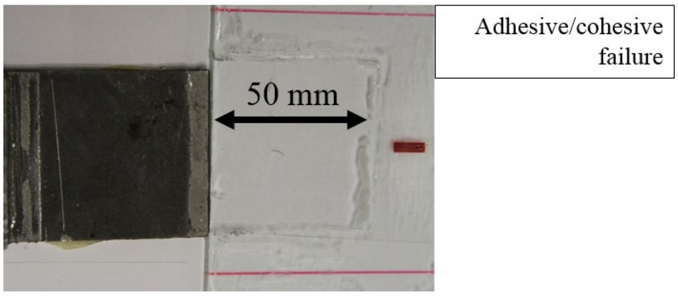

a) Brittle adhesive

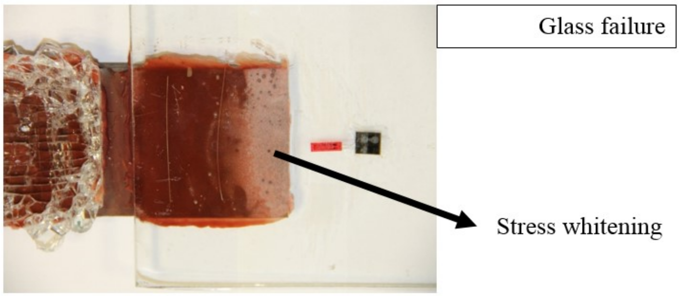

b) Ductile adhesive

Figure 5.20: Typical glass/steel interfaces after failure for a) brittle and b) ductile adhesive joints under out-of-plane bending loading. All bonded overlap regions are 50 mm x 50 mm.

Table 5.2: Summary of the failure loads and observed failure mechanisms for the bolted and adhesive joints tested subjected to out-of-plane bending.

Type of joint	Measured failure load [kN]	Failure mechanism
Brittle adhesive (Araldite 2020)	0.83 ± 0.21	Adhesive/cohesive failure
Ductile adhesive (Araldite 2047-1)	1.45 ± 0.04	Glass failure
Bolted	1.20 ± 0.08	Glass failure

5.5 Results of in-plane bending tests

The design of the in-plane bending tests and the location of the strain gauges can be seen in Figures 5.1 and 5.2. For this loading condition no significant stress concentrations are expected in the vicinity of the bonded area in the glass surface, and therefore the four strain gauges were mounted in symmetrical locations on the tensile side of the four substrates. However, in this test small inaccuracies or imperfections in the glass as well as asymmetric and non-uniform load distributions can lead to high stress concentrations in the vicinity of the load introduction points. To mitigate any arising stress concentrations, an aluminium interlayer of 20 mm x 20 mm was used for load spreading between the glass substrates and the steel rollers. Figure 5.21 shows the test set-up.

The in-plane bending test was not performed for bolted joints given that the initial single bolt design was leading to free-rotation of the glass substrates. The free rotation problem could be resolved if one more bolt was used on each side of the joint. Adding an extra bolt, however, changes the size of the contact area and makes the comparisons between the two methods less straightforward.

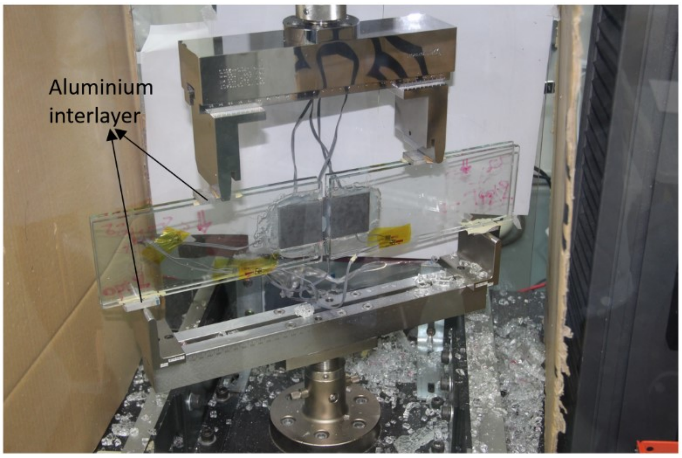

Figure 5.21: Set-up for the in-plane bending test.

Linear load-strain behaviour was observed for all the tested joints with brittle and ductile adhesives, and all samples were shown to display adhesive/cohesive failure modes. For two samples of the brittle and for one sample of the ductile joints, adhesive failure was followed by catastrophic glass failure. Figure 5.22 shows the glass/steel surfaces after failure, while Table 5.3 summarises the failure load and mechanisms.

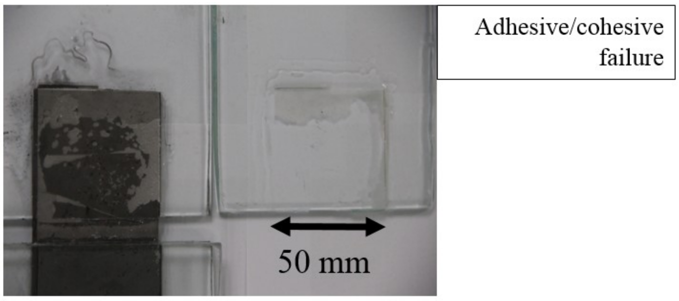

a) Brittle adhesive

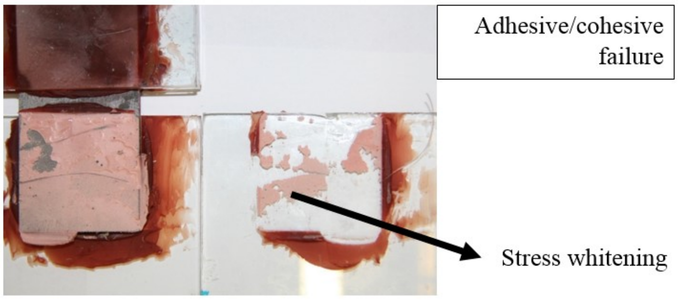

b) Ductile adhesive

Figure 5.22: Typical glass/steel interfaces after failure for joints with a) brittle and b) ductile adhesives subjected to in-plane bending loading. All bonded overlap regions are 50 mm x 50 mm.

Table 5.3: Summary of the failure load and mechanisms for the adhesive joints tested under in-plane bending.

Type of joint	Measured failure load [kN]	Failure mechanism
Brittle adhesive (Araldite 2020)	14.3 ± 0.7	1) Adhesive/cohesive failure 2) Glass failure preceded by significant damage in the adhesive layer
Ductile adhesive (Araldite 2047-1)	20.0 ± 0.4	1) Adhesive/cohesive failure 2) Glass failure preceded by significant damage in the adhesive layer
Bolted	N/A	This configuration is not applicable to bolted joints since it leads to free rotation

Compared to the previous three load cases, the glass experiences relatively low stresses in the vicinity of the bonded area, and thus the joint failure mode characteristics depend entirely on the adhesive layer. Therefore, in this particular load case the variability of joint strength caused by the glass strength variability is removed and the standard deviation between the measurements is significantly lower.

Figure 5.23 shows the strain response on the tensile side of all four glass substrates for the brittle and ductile adhesive joints. It can be seen that initially the loading is not distributed evenly with some substrates taking a significantly higher part of the load. However, at around 5 kN proper contact is established between all substrates and after that the responses are similar.

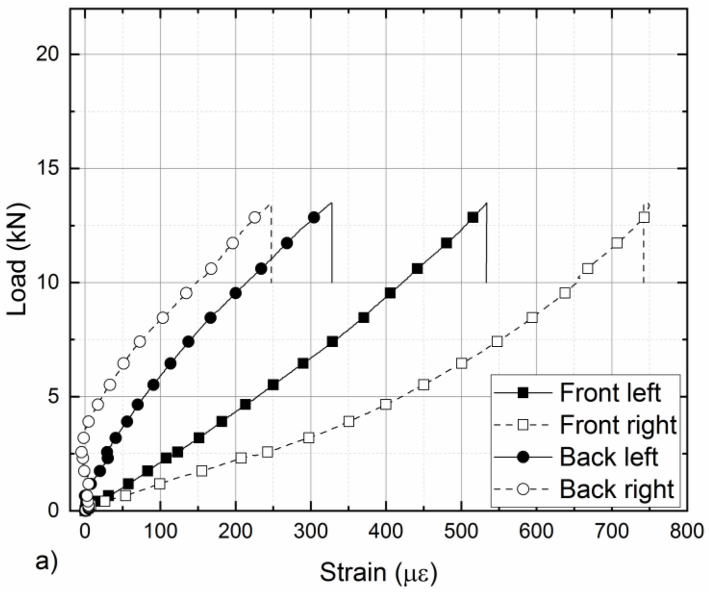

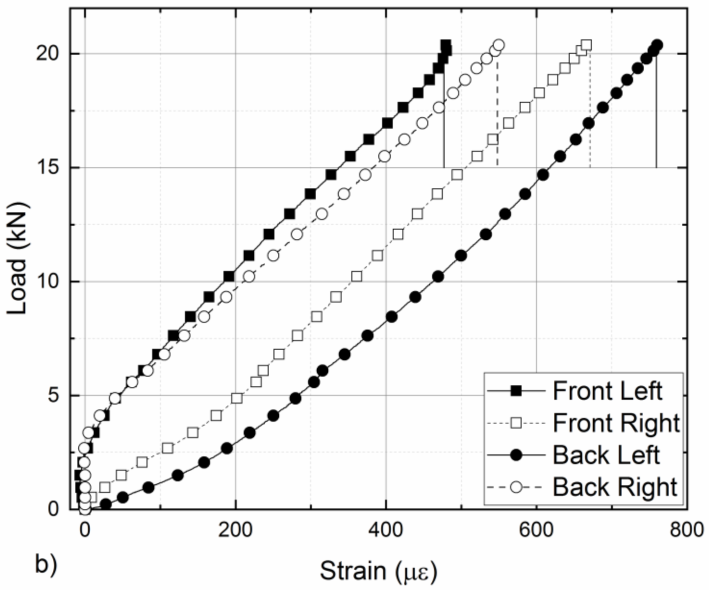

Figure 5.23: Load-strain response of the tensile side of the four glass substrates for the a) brittle and b) ductile adhesive joints under in-plane bending loading.

Figure 5.24 shows the average strain response for the tensile side of the glass for the two types of adhesive joints. The two types of joints are in almost complete agreement after initial contact is established.

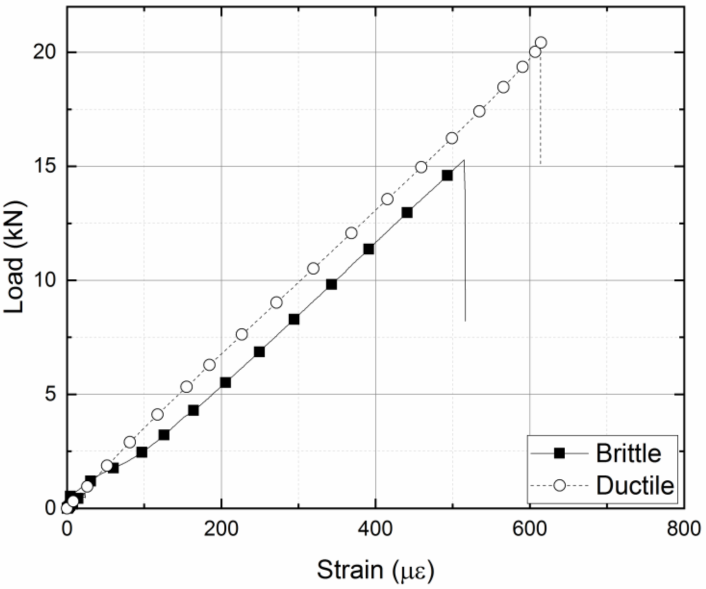

Figure 5.24: Load-strain response averaged over the four glass substrates for brittle and ductile adhesive joints subjected to in-plane bending loading.

5.6 Summary

Chapter 5 described the benchmark tests conducted on bolted and adhesive joints. These tests act as case studies for the numerical validation, the optimisation and the exposure studies that are presented in Chapters 6, 7 and 8 respectively.

In general, adhesive joints displayed significantly higher load capacity compared to bolted joints. It is worth noting that the more ductile adhesive outperformed both the stronger, brittle adhesive and the bolted configuration. This trend was observed for all load cases and is related to the joint size and the plastic zone development as will be highlighted in the following chapters. Chapters 6 and 7 will numerically analyse the performance of the adhesive layers and explain how plasticity affects the performance of the joint. This leads to correlation of the mechanical properties of the adhesive to the load capacity of the joint and justifies the experimentally observed trends.

Chapter 6 Numerical analysis of benchmark designs and calibration/validation of FE models

6.1 Introduction and structure

In this chapter a summary of the numerical work relating to the bolted and adhesive joints presented in Chapter 5 is provided. FE models were developed using the implicit and explicit solvers of ABAQUS 6.14 [50], considering geometric and material non-linearities, contact interactions as well as different damage and failure models for the glass and the adhesives. In addition, mesh sensitivity studies were conducted to determine the sensitivity of the chosen failure prediction methods to mesh refinement. Comparisons were performed between the experimental and numerical data, and the comparison of the two methods led to the calibration of certain simulation parameters and the validation of different numerical approaches. The comparisons were based on global and local strain responses of the joints, failure mechanisms and prediction of joint load capacity.

The numerical analyses of the performances of the brittle and ductile adhesive layers explain experimental observations highlighted in Chapter 5, emphasise the role of plasticity on the performance of the joints and correlate the effects of certain mechanical properties on the joint strength. These findings lead to the optimisation study presented in Chapter 7.

Part of the results presented in this chapter were published as full papers as per [118, 132, 134].

6.2 Constitutive models

Several constitutive models were utilised for the simulation of the performance of the different materials used in this study. Steel substrates were modelled as elastic materials given that the stresses developed never exceeded the yield/failure stresses found in literature. Glass was also modelled as an elastic material; however, the failure of glass needed to be considered as well. For this purpose, the brittle cracking model was employed which is an expression of the maximum principal stress criterion. Finally, for the adhesive two different approaches were used. The first one was based on continuum mechanics and coupled a pressure-sensitive Drucker-Prager model with a ductile damage model. The second was based on fracture mechanics and utilised traction separation laws to model the gradual degradation of the adhesive layers due to damage. The aforementioned constitutive models are briefly presented in the following sections.

6.2.1 Brittle cracking model

For glass, failure is assumed to occur according to a maximum principal stress criterion; hence failure takes place once the tensile stresses exceed a certain value. This criterion is introduced in the analysis by using a brittle cracking model, an in-built ABAQUS tool [50]. According to this model, the damage initiates once a maximum stress value has been reached (varies between 120-140 MPa in this study-see Table 3.2) and then propagates based on energy-based criteria (the fracture energy was 3 N/m^2 in this study [96]). The fracture energy of tempered glass is very low, hence rapid crack propagation occurs following first crack initiation leading to complete damage. The brittle cracking model has been used successfully in the past to introduce failure in annealed and tempered glass [96, 100, 101].

6.2.2 Linear Drucker-Prager model

The analytical mathematical description of the Linear Drucker-Prager theory was introduced in Chapter 2. This section describes the calibration of the model and the FE model inputs, as extracted and derived from experimental testing.

The linear Drucker-Prager model was calibrated numerically, and good agreement between predictions and bulk test data was achieved for the tensile and compressive stress-strain curves shown in Figure 3.3. Figure 6.1 shows the curve fitting achieved by FE analysis for the bulk data shown in Figure 3.3. Here, the hardening curve was obtained from experimental tensile testing and used as material input. The compressive test was then modelled, and values of β were varied until the best match was achieved for capturing pressure-sensitivity. For the brittle (Araldite 2020) and ductile (Araldite 2047-1) adhesives, σ_{yC}/σ_{yT} was calibrated at a value of 1.45, which is slightly higher than the 1.2-1.4 value suggested in [7].

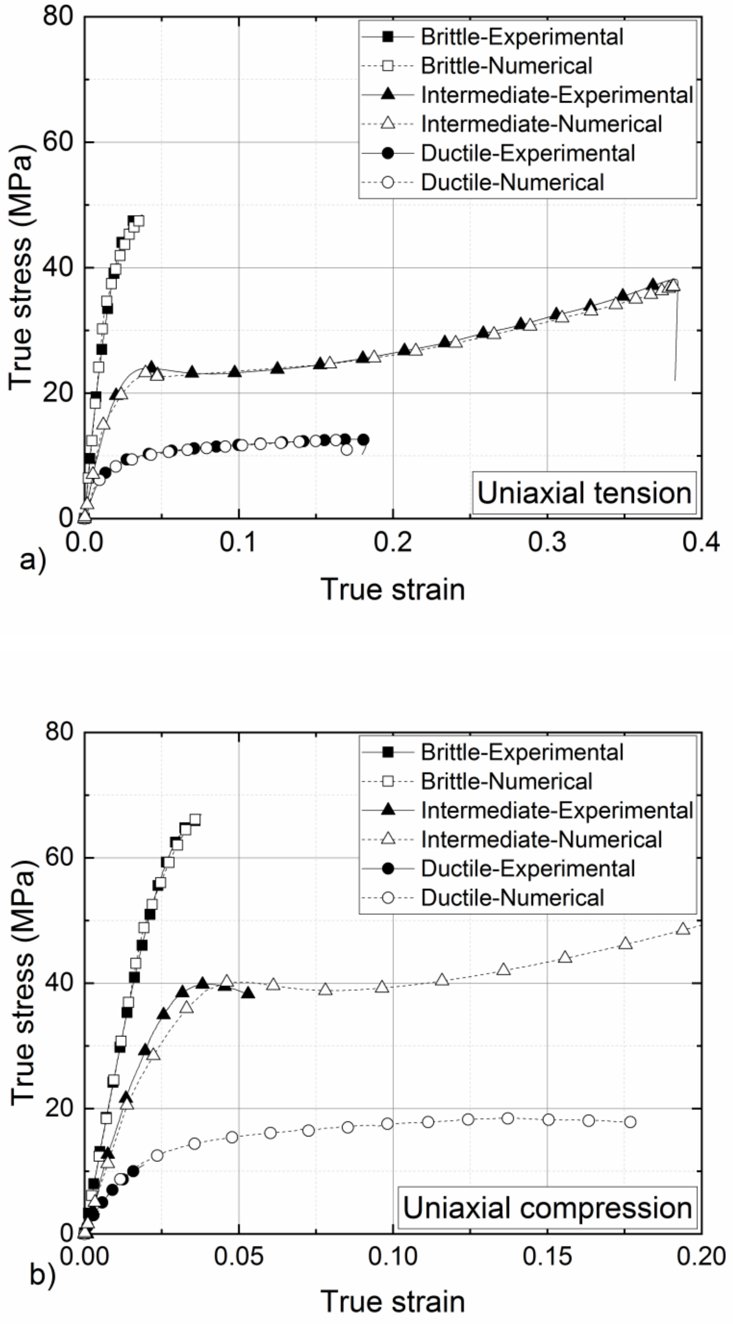

Figure 6.1: FE curve fitting for the stress-strain curves from a) tensile and b) compressive testing for the brittle, the intermediate strength and the ductile adhesive used in this study.

6.2.3 Ductile damage model

The ductile damage model theory is described in Chapter 2 and this section describes the calibration of the model and the FE model inputs as extracted from experimental testing.

The strain at damage initiation, ε_c, was derived from the experimental bulk data under tension (η=1/3). The shape of the stress triaxiality-fracture strain curve was then adapted from [48]. The derived values of equivalent fracture strain can be found in Table 6.1.

Table 6.1: Damage model material parameters.

	Brittle Adhesive (Araldite 2020)	Ductile Adhesive (Araldite 2047-1)
Fracture energy (J/m^2)	100	700
Stress triaxiality (η)	Fracture strain (ε_c)	
-0.33	0.186	1.31
0	0.01	0.077
0.33	0.019	0.131
0.5	0.027	0.162
0.75	0.015	0.104

6.2.4 Cohesive Zone Model (CZM)

The cohesive zone modelling approach adopted for the simulation of damage and failure of glass/steel adhesive joints was described in Chapters 2 and 4. More specifically, Chapter 2 describes the principles behind the method, while Chapter 4 describes the numerical methodology adopted for the extraction of the traction-separation laws. A simple triangular shape was adopted for both the brittle and the ductile adhesive. For the damage initiation the quadratic nominal stress criterion was employed while for the damage evolution the linear fracture energy criterion was used. The cohesive properties in modes I and II were extracted in Chapter 4 and can be found in Tables 4.3 and 4.6.

6.3 Main features of the models

For the meshing of the models a manual seeding procedure was followed. This procedure involved biasing towards the locations where stresses tend to accumulate. The required minimum element size depended on the location and the type of joint and was determined by mesh sensitivity analyses, presented in subsequent sections. The joints were modelled with 3D stress, 8-node linear solid elements with reduced integration and hourglass control (C3D8R in ABAQUS). In addition, for the cohesive zone modelling approach, 8-node three-dimensional cohesive elements were used (COH3D8 in ABAQUS).

Implicit and explicit solvers were employed for the analysis of the joints. ABAQUS/Explicit solver was utilized to allow for the introduction of damage and failure models with element deletion [50].

However, dynamic analyses may require significantly higher computational power and time depending on the stable time increment. For the models presented, semi-automatic mass scaling was introduced to reduce computational time with a stable time increment identified between 1 × 10^{-8} s to 1 × 10^{-9} s for an analysis time period of 1 s. The target time step/increment was set such that the kinetic energy remained a very small fraction of the total internal energy (below 1%).

The numerical results of bolted joints are very sensitive to the contact properties between the substrates and the pre-tensioned bolts. Small sliding, surface to surface contact was considered between all interacting surfaces. Tangential frictionless behaviour was assumed for the interaction of the bolt with the bolt holes while tangential behaviour with a penalty friction coefficient was considered for the sliding surfaces of the substrates. Initial values for the friction coefficients were found in the literature [136], but those were additionally calibrated numerically given their sensitivity to the surface roughness. In addition, normal behaviour contact properties were used for the transfer of normal forces between the substrates. The pre-tensioning of the bolt was achieved for the implicit solver using an in-built ABAQUS function at the first step of the analysis while, for the explicit solver (where the in-built bolt pre-tensioning option is not available) a predefined temperature field [137] was calibrated and was used to create the same effect by thermal contraction of the bolt.

The experimental bolt pre-tensioning was applied as a torque, but was given as input to ABAQUS as an axial force. The magnitude of the axial force was calibrated at 7 kN for the assumed penalty friction coefficient of $\mu = 0.2$ as shown in the following sections. Figure 6.2 shows the distribution of axial stresses through the thickness of the bolt using the in-built ABAQUS function and the predefined temperature field. It can be seen that the two methods agree well.

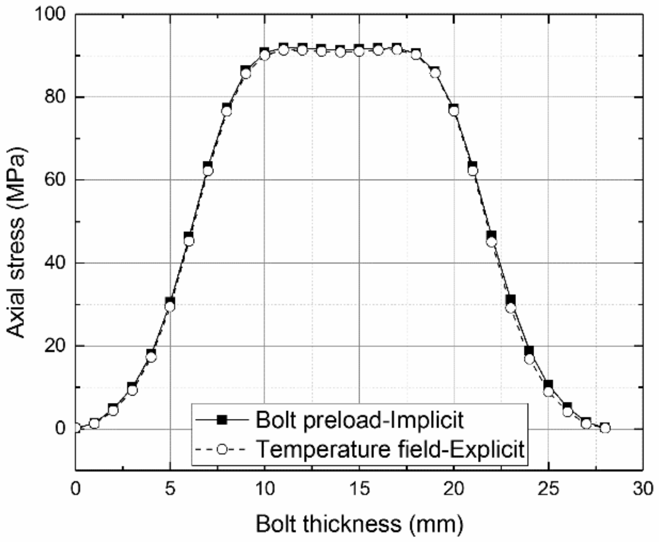

Figure 6.2: Distribution of axial stresses through the bolt thickness. Bolt pre-tensioning was achieved using the ABAQUS in-built tool and a predefined temperature field.

For adhesive joints, when the continuum mechanics approach was employed, perfect bonding between the substrates and the adhesive was assumed. Hence, the adhesive layer was connected via tie constraints to the substrates which allowed for a much finer mesh size to be used in the adhesive layer as required for the detailed stress and failure analysis and saved computational time. A 45° adhesive fillet was assumed at the ends of the overlap. When the cohesive zone modelling approach was employed, a single row of cohesive elements replaced the adhesive layer. The cohesive elements were also connected with tie constraints to the substrates.

6.4 Mesh sensitivity studies

Mesh sensitivity studies were carried out in order to determine the minimum element size in the critical areas of the models, such as the sharp edges and material discontinuities. For the case of bolted joints, the most critical location is around the bolt holes, while for the case of adhesive joints the critical locations are close to the ends of the adhesive joint overlap. Here, the extent of the stress concentrations is dependent on the fillet shape. The mesh sensitivity study was performed for the joints under tension, and the results were followed for the other load cases as well. In general, mesh size affected adhesive joints significantly while for the case of bolted joints the mesh size had less of an effect.

The effect of mesh refinement around bolt holes is studied through the influence on the failure load prediction. The size of the mesh was varied for the elements in the surrounding area of the bolt hole, the elements around the hole and finally the elements through the thickness of the bolt hole. Figure 6.3 shows the locations of mesh refinement and the effect on the failure load prediction, respectively. It is shown that good convergence of the models is achieved following mesh refinement for the three different locations examined. The required number of elements can be found in Table 6.2.

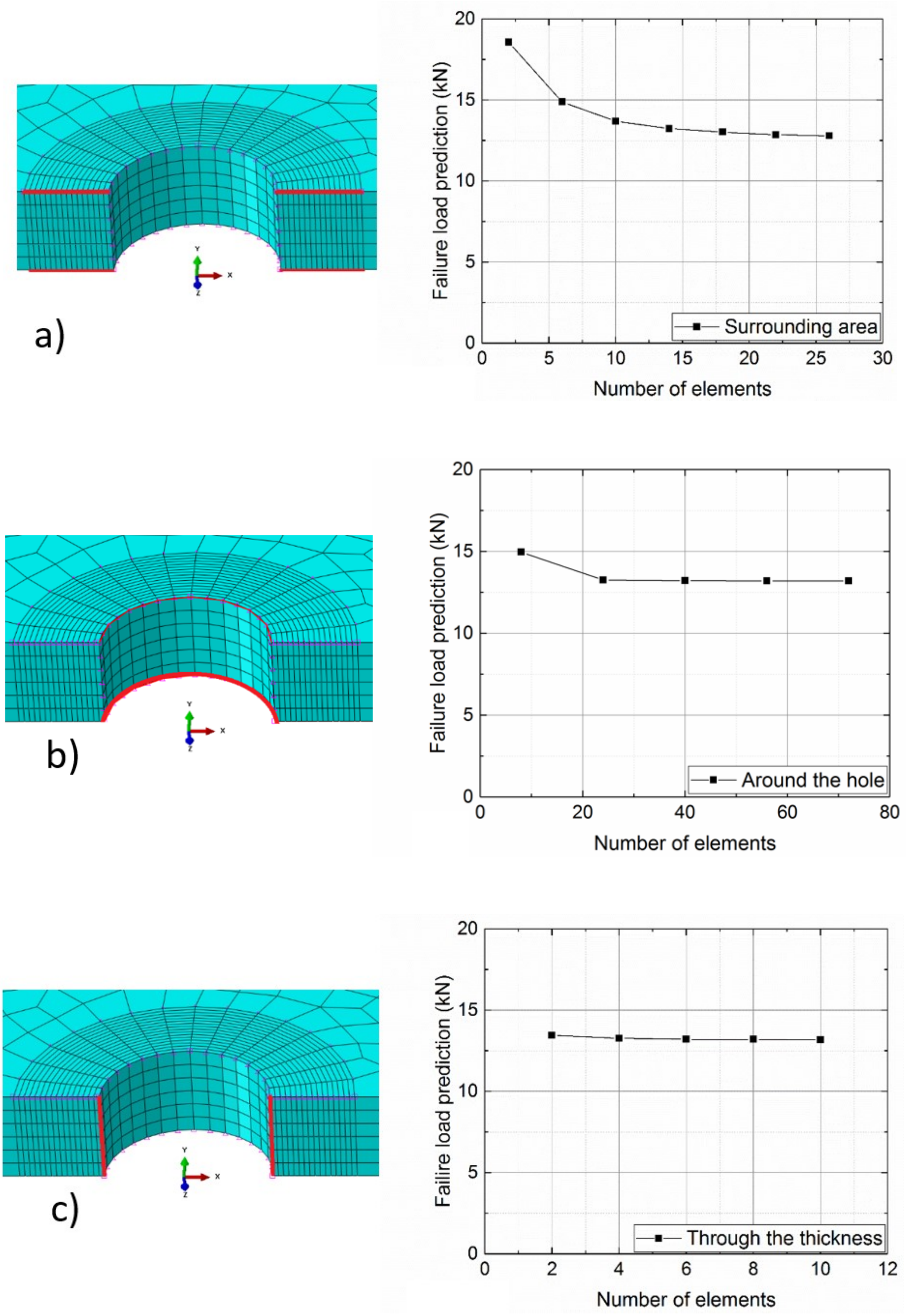

Figure 6.3: Effect of mesh size on the failure load prediction of bolted joints for the elements in a) the surrounding area, b) around the hole and c) through the thickness.

The mesh sensitivity study to assess stress distributions for the adhesive joints was performed within the elastic response region to ensure that plasticity did not affect the results. Additionally, the influence of mesh refinement on the failure predictions (nonlinear response) was also studied.

Figure 6.4 shows the sensitivity of the adhesive layer in the area of the singularity, and the correlation between the minimum element size and the failure load prediction for the two adhesive cases. The FE models with the brittle (Araldite 2020) adhesive displayed an increased stress sensitivity with mesh refinement. In this case, the presence of singularities not only affected the values of stress, but also reduced the prediction of the failure load for coarse meshes. The failure load reduced with mesh refinement due to the increase of maximum principal stresses at the singularity.

The ductile adhesive joints were also sensitive to mesh size in terms of stress distributions, but not in terms of failure load prediction. The extended plastic region of the ductile Araldite 2047-1 adhesive allowed the elements around the singularity to develop significant deformation, which explains the minimum effect in the failure load prediction. Considering these effects, a minimum mesh size of 0.05 mm was chosen for the presented results. This resulted in a total of approximately 80,000 solid elements for the bolted joints and 100,000 solid elements for the adhesive joints.

It is worth noting that the mesh sensitivity studies presented above are only relevant to the models employing a continuum mechanics approach for failure predictions. Even though, cohesive zone models are not sensitive to mesh size, a similar approach was also used to validate this assumption. Therefore, Figure 6.5 presents the effect of the mesh size on the failure load prediction for the two adhesives employing a CZM approach.

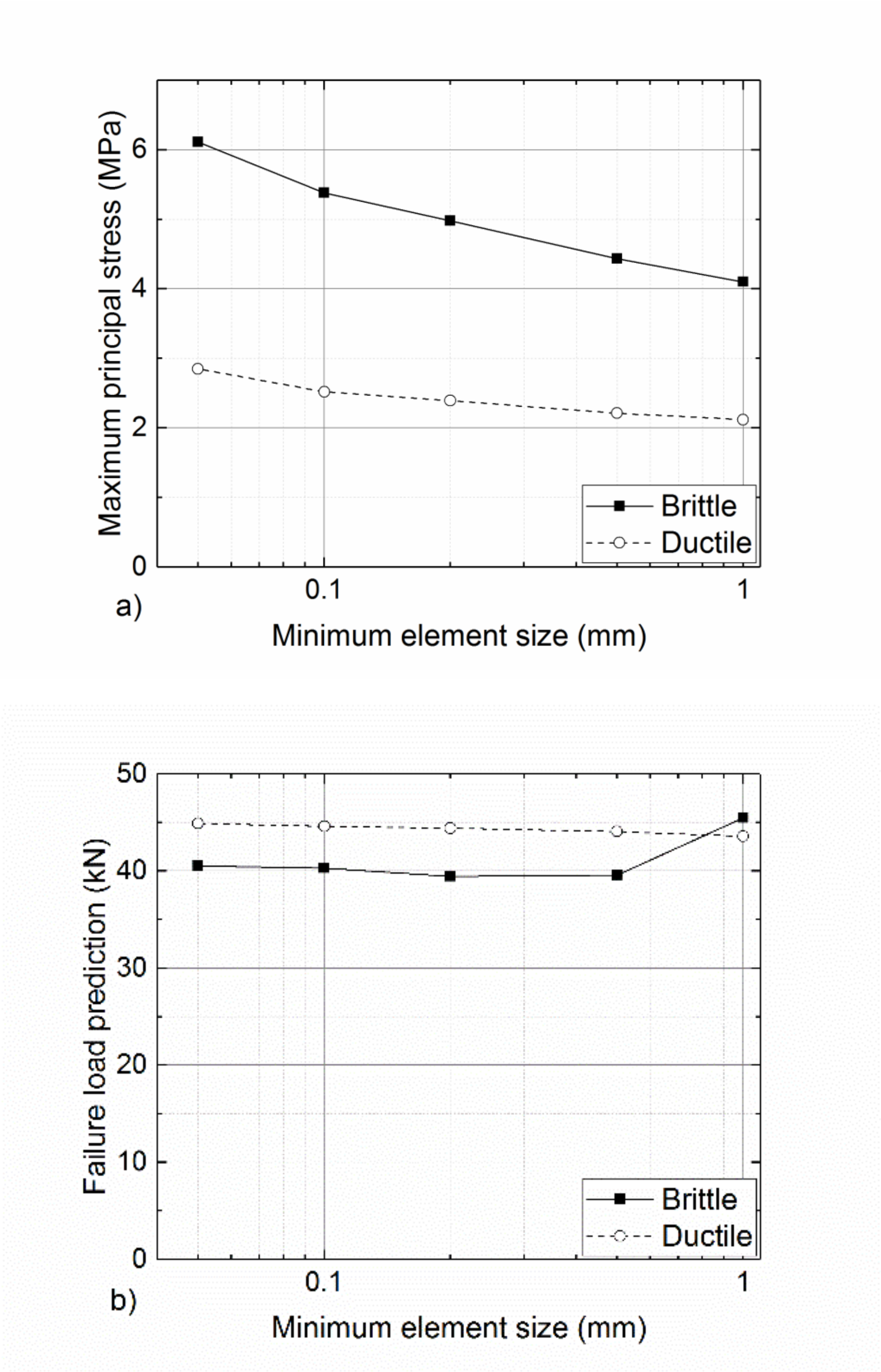

Figure 6.4: Mesh sensitivity study along the sides of the adhesive and effect of the mesh size to the failure load prediction for the continuum mechanics approach.

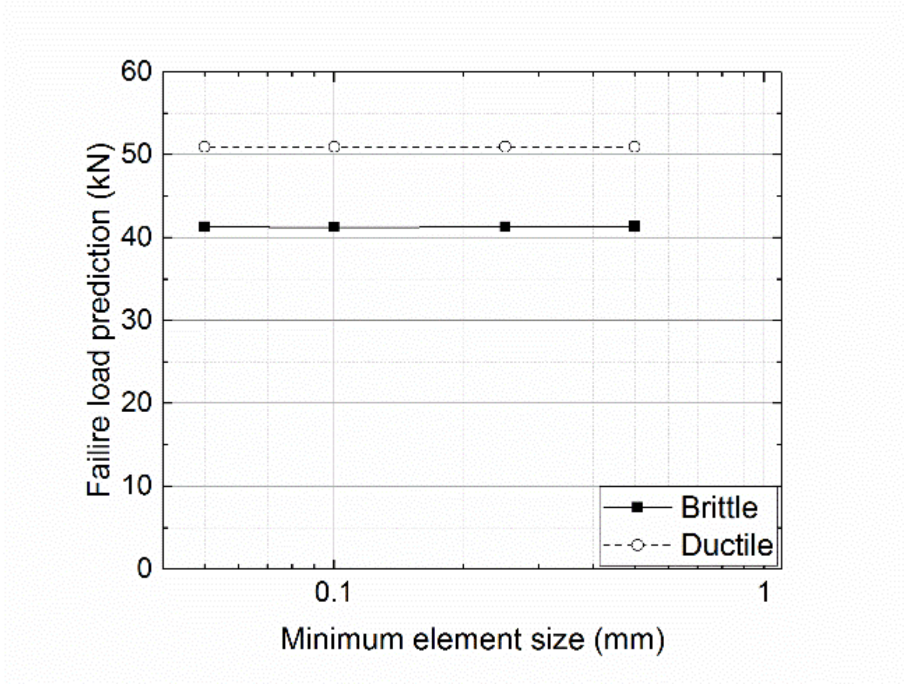

Figure 6.5: Mesh size sensitivity of the failure load prediction for the two adhesives using the CZM approach.

It can be seen that the mesh size has no notable effect on the failure load prediction for both the brittle and the ductile adhesive. Therefore, coarser meshes can also be used in CZM analysis, which reduces the computational time significantly, but does not affect the accuracy of the predictions. Table 6.2 summarises the findings of the mesh sensitivity analysis and presents the size or number of elements used throughout the rest of this chapter.

Table 6.2: Summary of the number of elements/minimum mesh size used for the simulations of the bolted joints and the two approaches used for adhesive joints.

Bolted Joints		Adhesive Joints			
		Continuum approach		CZM approach	
Location	Number of elements	Location	Minimum element size (mm)	Location	Minimum element size (mm)
Surrounding area	14	Adhesive corners	0.05	Throughout the adhesive layer	0.1
Around the bolt hole	40	Through the thickness	0.01		
Through the thickness	8				

6.5 Uniaxial loading

6.5.1 Geometry and boundary conditions

The geometry of the models created in ABAQUS was as close to the experimental test geometry as possible. Therefore, the dimensions of the glass substrates were 250 mm x 100 mm x 6 mm, the dimensions of the steel splice were 110 mm x 50 mm x 6 mm and the dimensions of the adhesive layers were 50 mm x 50 mm x 0.2 mm. Finally, the M10 bolt, the washers and the nuts were modelled as one part and the clearance of fit was 3% as in the experiments. Symmetries were used for both bolted and adhesive configurations. For the bolted configuration, symmetries in two axes (x- and z-axis) were used, due to the use of the bolt, and therefore one quarter of the joint was modelled. For the adhesive configuration symmetries in all three axes were employed and therefore one eighth of the joint was modelled. The loading condition was displacement controlled and was applied through a reference point that was tied to the steel splice. Figure 6.6 shows the models of the bolted and the adhesive joints and details in the areas of mesh refinement.

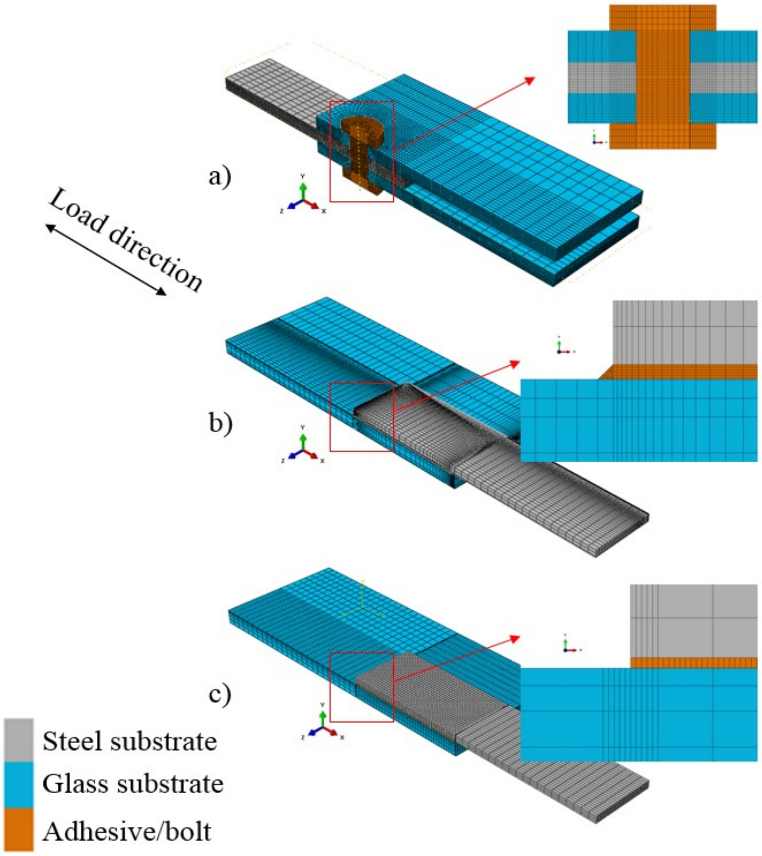

Figure 6.6: Geometry of the numerical models for the a) bolted, b) adhesive (continuum mechanics) and c) adhesive (CZM) configuration under tensile loading. Symmetries were used in x- and z- axis for the bolted and x-, y- and z- axis for the adhesive configurations.

6.5.2 Bolted joints calibration

The models developed for the bolted joints are very sensitive to the bolt pre-tensioning and the contact properties between the sliding surfaces. Therefore, the pre-tensioning load and the friction coefficient between the glass and the steel substrates had to be calibrated. The calibration was based on the relative sliding on the substrates which occurs at a load of about 5 kN. At this point, the contact between the glass and steel substrates is overcome, and the substrates start to slide against each other until the moment when the bolt comes into contact with the bolt hole in the glass substrate. A new contact area is then established and the loading continues. In the interval between losing the initial contact and establishing the new contact area, the load-strain relationship becomes non-linear. Therefore, the calibration of the bolt pre-tensioning and the friction coefficient was achieved by matching the experimental and numerical stress-strain curves at this point of non-linearity.

6.5.3 Joint response

The strain gauge measurements reported in Chapter 5 can be compared with the FE predictions for the validation of the stiffness response of the joint in the areas of the stress concentration and far field strain. Figures 6.7 and 6.8 show the load-strain response as measured experimentally and predicted numerically for bolted joints in the glass midpoints and the areas of stress concentrations under tension and compression. The corresponding plots for adhesive joints can be found in Figures 6.9 and 6.10.

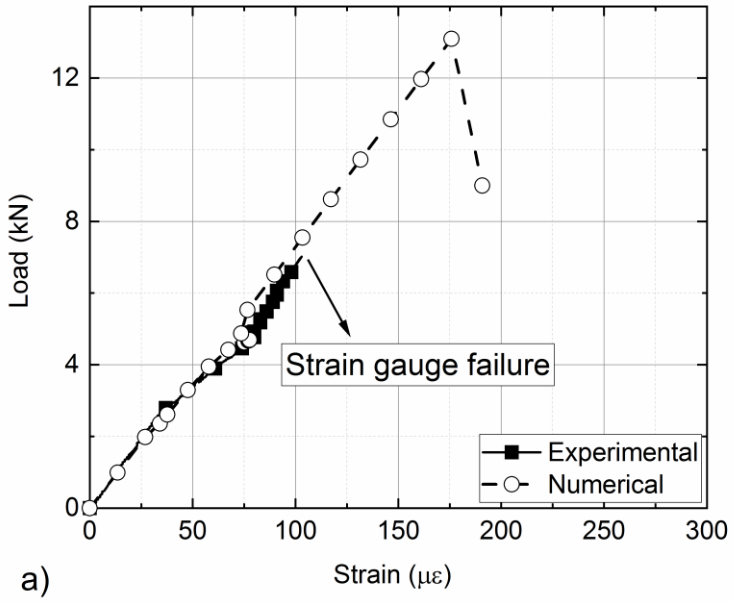

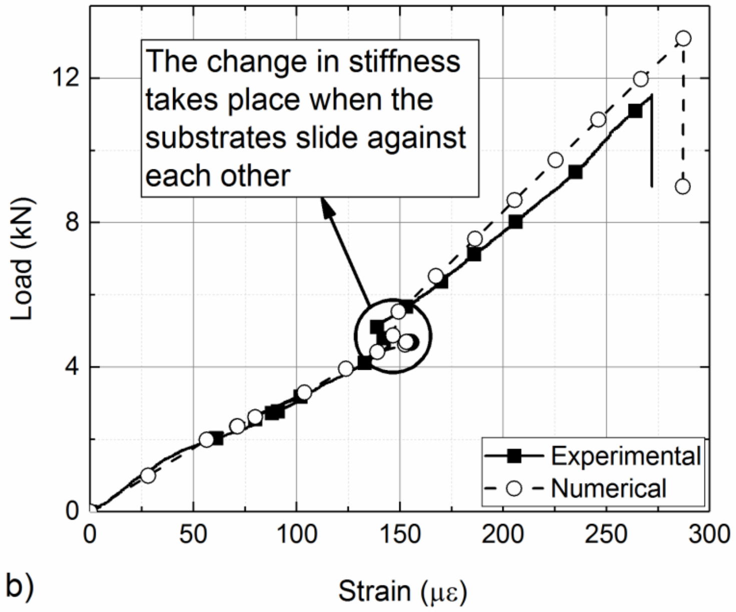

Figure 6.7: Comparison of load vs. strain gauge measurements and corresponding FE predictions for the bolted joint configurations subjected to tensile loading a) at the glass midpoint and b) at the areas of stress concentrations.

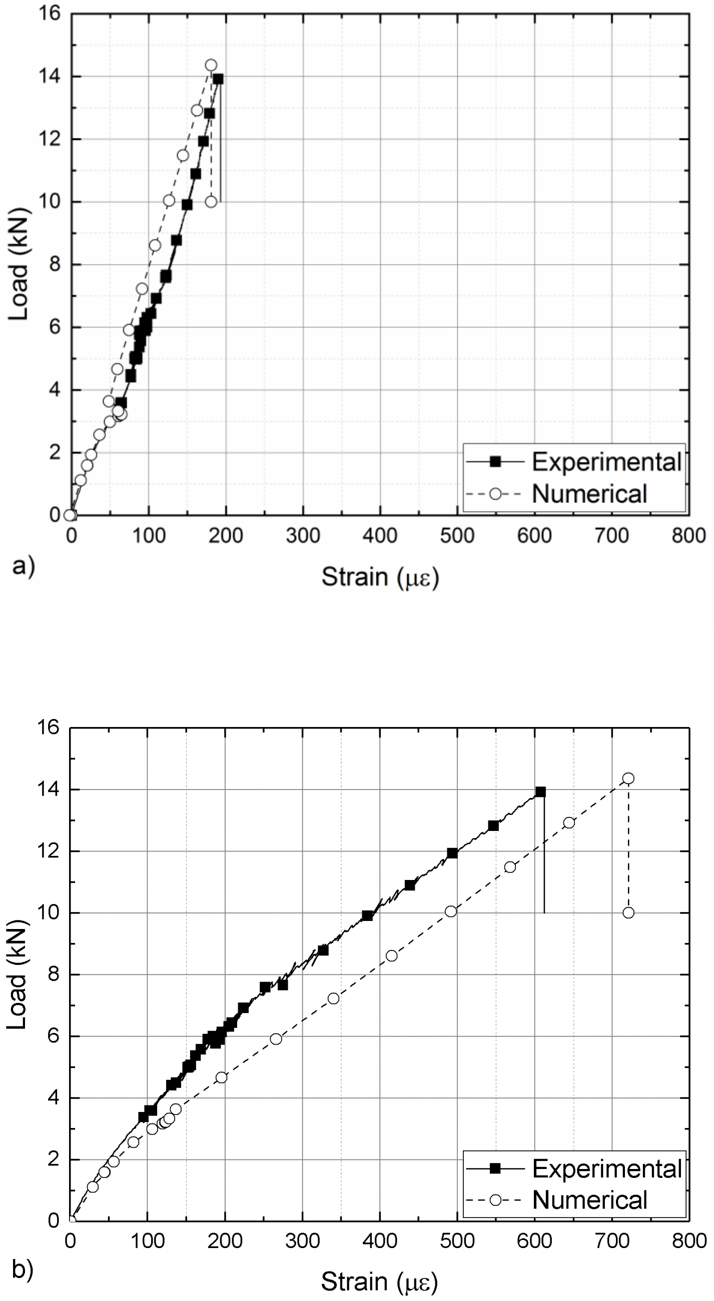

Figure 6.8: Comparison of load vs. strain gauge measurements and corresponding FE predictions for the bolted joint configurations subjected to compressive loading a) at the glass midpoint and b) at the areas of stress concentrations.

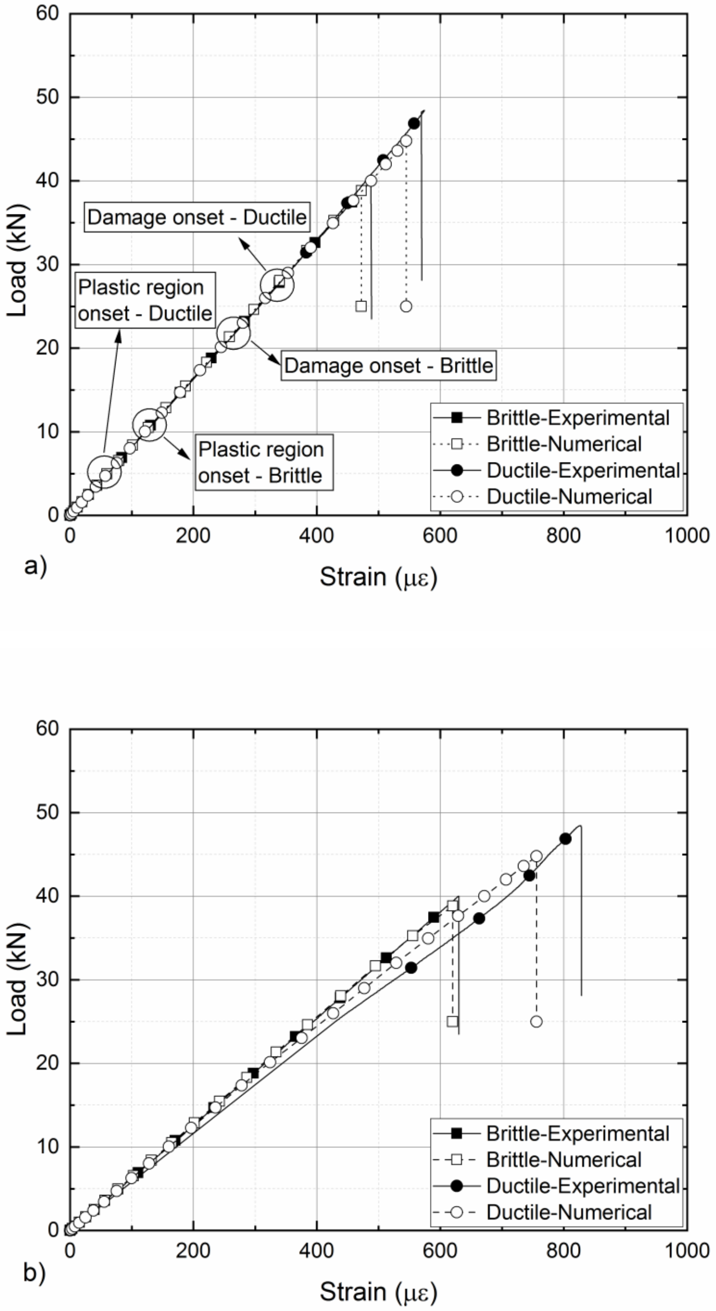

Figure 6.9: Comparison of load vs. strain gauge measurements and corresponding FE predictions for the adhesive joint configurations when subjected to tensile loading a) at the glass midpoint and b) at the areas of stress concentrations. Results based on a continuum mechanics approach.

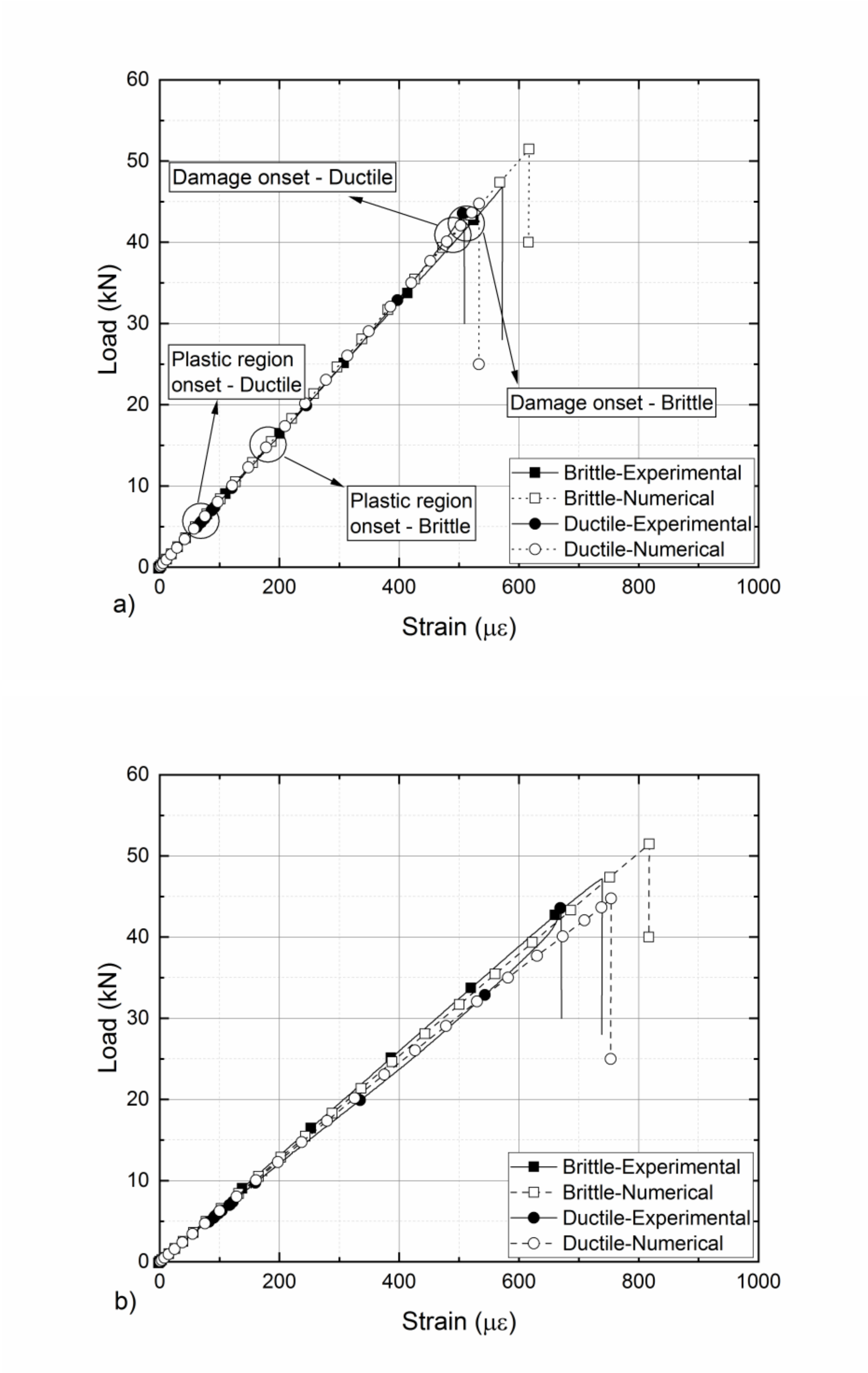

Figure 6.10: Comparison of load vs. strain gauge measurements and corresponding FE predictions for the adhesive joint configurations when subjected to compressive loading a) at the glass midpoint and b) at the areas of stress concentrations. Results based on a continuum mechanics approach.

It can be seen that good agreement is achieved between the numerical simulations and the experimental measurements. The models of bolted joints accurately capture their stick-slip response given that the sliding of the substrates takes place and a new contact area is established once the bolt comes into contact with the bolt hole. The calibration of the pre-tensioning parameters was performed for the tensile test, and it can be seen that is slightly inaccurate for the compression test since the sliding is predicted to start at a slightly lower load. However, once the relative sliding of the substrates is completed and the new contact area is established, the stiffness response becomes linear again and is predicted accurately by the models. The stiffness response of the adhesive joints is affected by the stiffness of the glass substrates, which explains the linear course of the graphs even though the adhesives display material non-linearities when tested in bulk format.

6.5.4 Joint failure prediction

The failure prediction for bolted joints depends entirely on glass fracture and was based on a maximum principal stress criterion on the glass surface while for adhesive joints failure was based on the two methods described in section 6.2. The properties for the first approach are based on the characterization of the mechanical properties of the adhesives found in Chapter 3. The second approach was based on modelling the interface with cohesive elements and the properties for the determination of the cohesive laws can be found in Chapter 4.

Tables 6.3 and 6.4 compare the experimental and numerical failure loads under uniaxial tension and compression. To provide an interpretation of the experimental scatter, a lower and an upper strength threshold was predicted through FE simulations. For the continuum mechanics approach the fracture strain of the brittle and ductile adhesives was varied based on the values of standard deviation given in of Table 3.1. For the case of the bolted joints, failure occurs in the glass substrate and hence glass strength variation (120-140 MPa for tempered glass) determines the maximum and minimal failure load thresholds.

Table 6.3: Summary of the experimental and numerical predictions of the failure load/mechanism for bolted and adhesive joints under tensile loading.

	Tension				
	Experimental		Numerical		
Configuration	Failure load (kN)	Failure mechanism	Failure load– Continuum mechanics (kN)	Failure load – CZM (kN)	Failure mechanism
Brittle Adhesive (Araldite 2020)	38.0 ± 1.8	Significant damage in the adhesive layer/glass side interface leading to glass failure	34.1-38.8	40.4	Interface failure
Ductile Adhesive (Araldite 2047-1)	47.0 ± 4.6	Cohesive failure	42.3-44.8	50.8	Interface failure
Bolted	8.0 ± 0.7	Glass failure	12.2-13.5	N/A	Glass failure

Table 6.4: Summary of the experimental and numerical predictions of the failure load/mechanism for bolted and adhesive joints under compressive loading.

	Compression				
	Experimental		Numerical		
Configuration	Failure load (kN)	Failure mechanism	Failure load – Continuum mechanics (kN)	Failure load – CZM (kN)	Failure mechanism
Brittle Adhesive (Araldite 2020)	42.4 ± 5.1	Significant damage in the adhesive layer/ glass side interface leading to glass failure	47.3-51.5	40.8	Interface failure-glass side
Ductile Adhesive (Araldite 2047-1)	45.5 ± 0.7	Cohesive failure	42-44.8	50.9	Interface failure-glass side
Bolted	9.7 ± 3	Glass failure	14.2-15.8	N/A	Glass failure

It can be seen that the numerical predictions for the adhesive joints are in good agreement with the experimental data for both the continuum mechanics and the CZM approach. For both adhesives, in both tension and compression, the failure load prediction is within 10% of the average experimental load and in most cases within the experimental standard deviation. In the case of tensile loading the CZM model predicted slightly higher strength compared to the continuum mechanics approach, while in the case of the compressive loading this trend was reversed and the continuum mechanics approach slightly overestimated the failure load. However, the differences between the predictions of the methods are within 10% and thus in good agreement. This was to some extend unexpected and warrants further discussion.

The ability of each numerical methodology to predict the joint strength, and hence the accuracy of the prediction, depends on the mode of failure of the joint. Generally, the continuum mechanics approach is better suited for cohesive failure events which are related to the bulk properties of the adhesive. In contrast, the CZM methodology is better suited for adhesive failure governed by the strength of the interface. The agreement of the two methods in the case of this study indicates that even when adhesive failure was observed, the interface bond strength was close to the bulk properties strength. Regarding failure prediction, each method has its respective advantages. The bulk adhesive properties are easier to evaluate experimentally compared to the interface properties.

Regarding damage progression, the continuum mechanics methodology takes the triaxial stress state of the adhesive layer into account, while the CZM methodology applies an interpolation between mode I and mode II. Despite these differences, damage progresses very similarly as shown in Figure 6.11 for the brittle adhesive. Here it can be seen that damage initiates from the corners and then progresses into the centre of the adhesive layer (continuum mechanics damage) or the adhesive interface (CZM damage). Similar results are obtained for both methods. Weaker interfaces failing adhesively are generally not captured by the bulk property analysis, and in this case the CZM methodology (which can capture both adhesive and cohesive failure) is preferred. This is further highlighted in Chapter 8 when discussing the influence of environmental exposure.

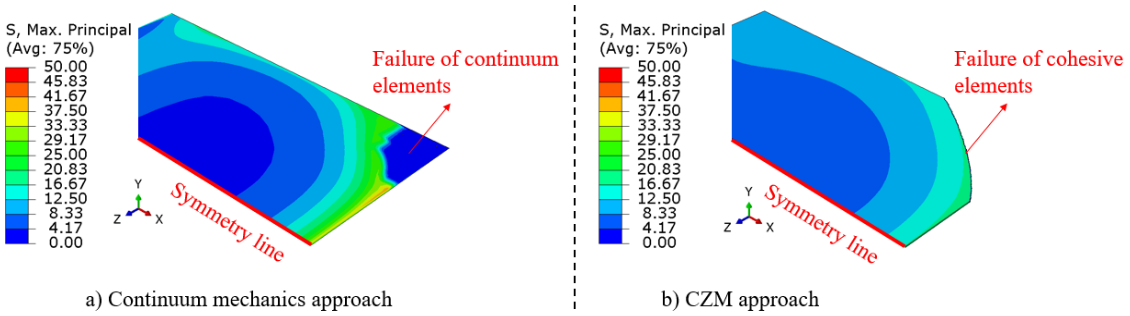

a) Continuum mechanics approach b) CZM approach

Figure 6.11: Damage progression of the brittle adhesive layer based on a) continuum mechanics methodology and b) CZM methodology. Due to symmetry half of the adhesive layer is displayed.

It is worth noting that hybrid models combining two single rows of cohesive elements (one at each interface) with continuum elements for the bulk part of the adhesive layer were also developed for comparison. Details of the model and the mesh design can be seen in Figure 6.12. The failure of these hybrid models, however, was shown to be governed on the interface properties (cohesive properties) and thus yielded identical results compared to the simple CZM approach. It was therefore decided to use the easier to implement simple CZM approach rather than the complicated hybrid model.

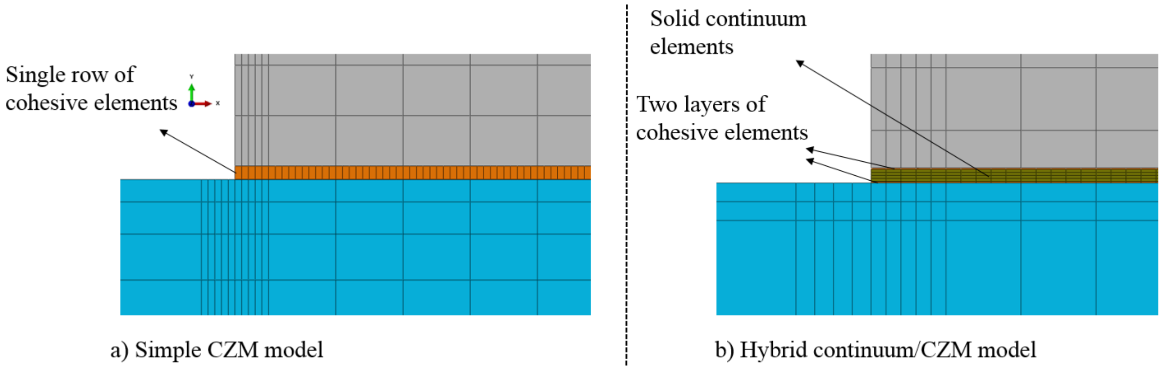

a) Simple CZM model

b) Hybrid continuum/CZM model

Figure 6.12: Modelling details of the a) simple CZM and the b) hybrid continuum/CZM modelling approaches.

For bolted joints, the experimental scatter was higher, which led to reduced agreement between the experimental and numerical methods. It is postulated that micrometer-sized surface flaws introduced during drilling might further reduce glass strength around the vicinity of the bolt hole, which cannot be captured with the current approach based on manufacturer's data. The numerical models, however, were accurate in predicting the maximum failure load measured experimentally.

In addition, the simulations were accurate in predicting the locations of damage initiation and failure mechanisms. For the case of bolted joints, the glass substrates failed in the vicinity of the bolt hole, in a direction perpendicular to the direction of load agreeing very well with the experimental observations. Figure 6.13 shows the location of failure and the stress distribution before and after the failure. Regarding both types of adhesive joints, failure was predicted by both methods to take place in the interface, agreeing with the experimental observations. Figure 6.14 shows the damage onset and propagation for the brittle and ductile adhesives under tension highlighting the different damage onset and propagation mechanisms. The failure mechanisms under uniaxial compression are very similar to the ones under uniaxial tension.

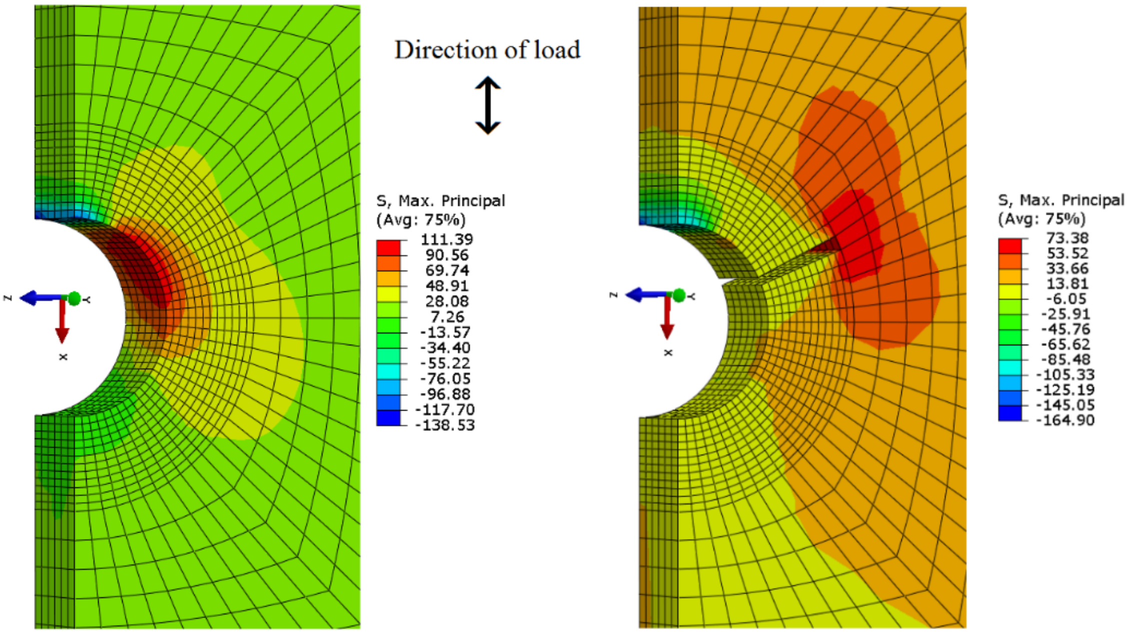

Figure 6.13: Numerical prediction of the damage initiation in the vicinity of the bolt hole under uniaxial tension. The figure shows the distribution of maximum principal stress on the glass surface (stresses in MPa).

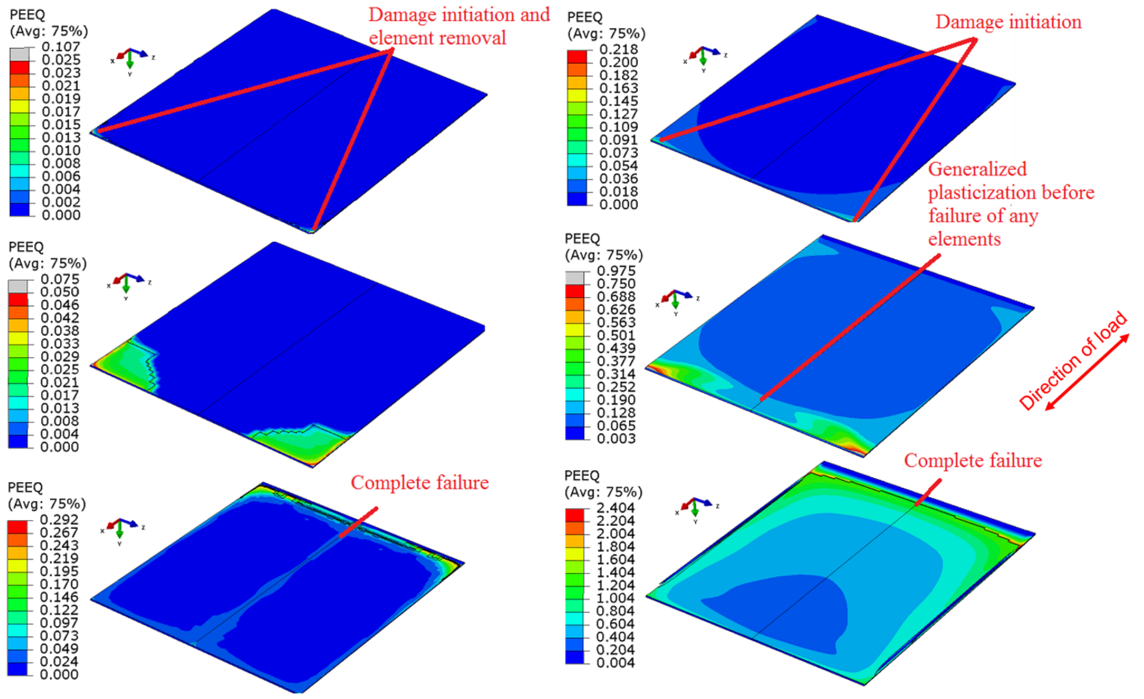

a) Brittle adhesive b) Ductile adhesive

Figure 6.14: Damage onset and propagation in the brittle (left) and ductile (right) adhesive layer under uniaxial tension. The size of the bonded area is 50 x 50 mm. The distribution of the equivalent plastic strain at damage initiation, propagation and complete failure is shown.

The lower strength, ductile adhesive (in terms of bulk properties) produces stronger joints (in terms of failure load in the joints). This can be explained by studying the damage initiation and propagation of the adhesive layers. Firstly, the elements around the corners of the overlap start to yield for both adhesives. The brittle adhesive, however, has a very small plastic region and damage initiates very quickly, leading to progressive failure of elements and element removal, while most of the adhesive layer has not even started to deform plastically. Contrary to that, the plastic zone in the ductile adhesive extends largely across the whole adhesive layer before any elements start to fail. This large area plasticization behaviour of the ductile adhesive layer allows the ductile joints to sustain higher loads. This effect is further studied in Chapter 7 and leads to a strategy for optimum selection of adhesives based on their mechanical properties.

6.6 Out-of-plane bending

6.6.1 Geometry and boundary conditions

The geometry of the models created in ABAQUS was as close to the experimental tests performed as possible. Therefore, the dimensions of the glass substrates were 250 mm x 100 mm x 6 mm, the dimensions of the steel splice were 110 mm x 50 mm x 6 mm and the dimensions of the adhesive layers were 50 mm x 50 mm x 0.2 mm. Finally, the M10 bolt, the washers and the nuts were modelled as one part and the clearance of fit was 3% as in the experiments. In addition, steel rollers were included in the models for the load application and contacts were defined between the steel rollers and the glass substrate.

Symmetries in two axes were used for both bolted and adhesive configurations, and therefore only one quarter of each joint was modelled. The loading was displacement controlled and was applied through reference points, which were tied to the steel rollers. Figure 6.15 shows the models of the bolted and the adhesive joints.

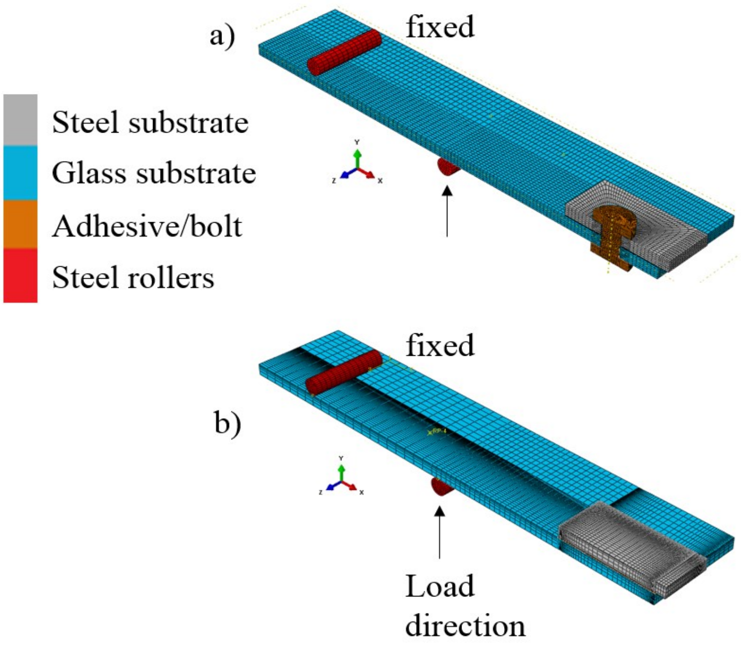

Figure 6.15: Geometry of the numerical models for the a) bolted and b) adhesive configuration (both continuum and CZM approaches) under out-of-plane bending loading. Symmetries were used in x- and z- axis for both configurations.

6.6.2 Joint response

The strain gauge measurements reported in Chapter 5 can be compared with the FE predictions for the stiffness response of the joints in the glass and steel substrates. Figures 6.16 and 6.17 show the load-strain response of the glass and the steel substrates under out-of-plane bending loading for adhesive and bolted joints respectively. It can be seen that there is very good agreement between the stiffness response measured experimentally and the FE predictions. The stiffness is affected by the steel and glass substrates, which explains the linear characteristics of the graphs. In addition, it is worth noting that the experimental strain of the glass substrates is averaged between the two sides of the joints, but as shown in Chapter 5 this has a very small effect just at the initial stages of loading.

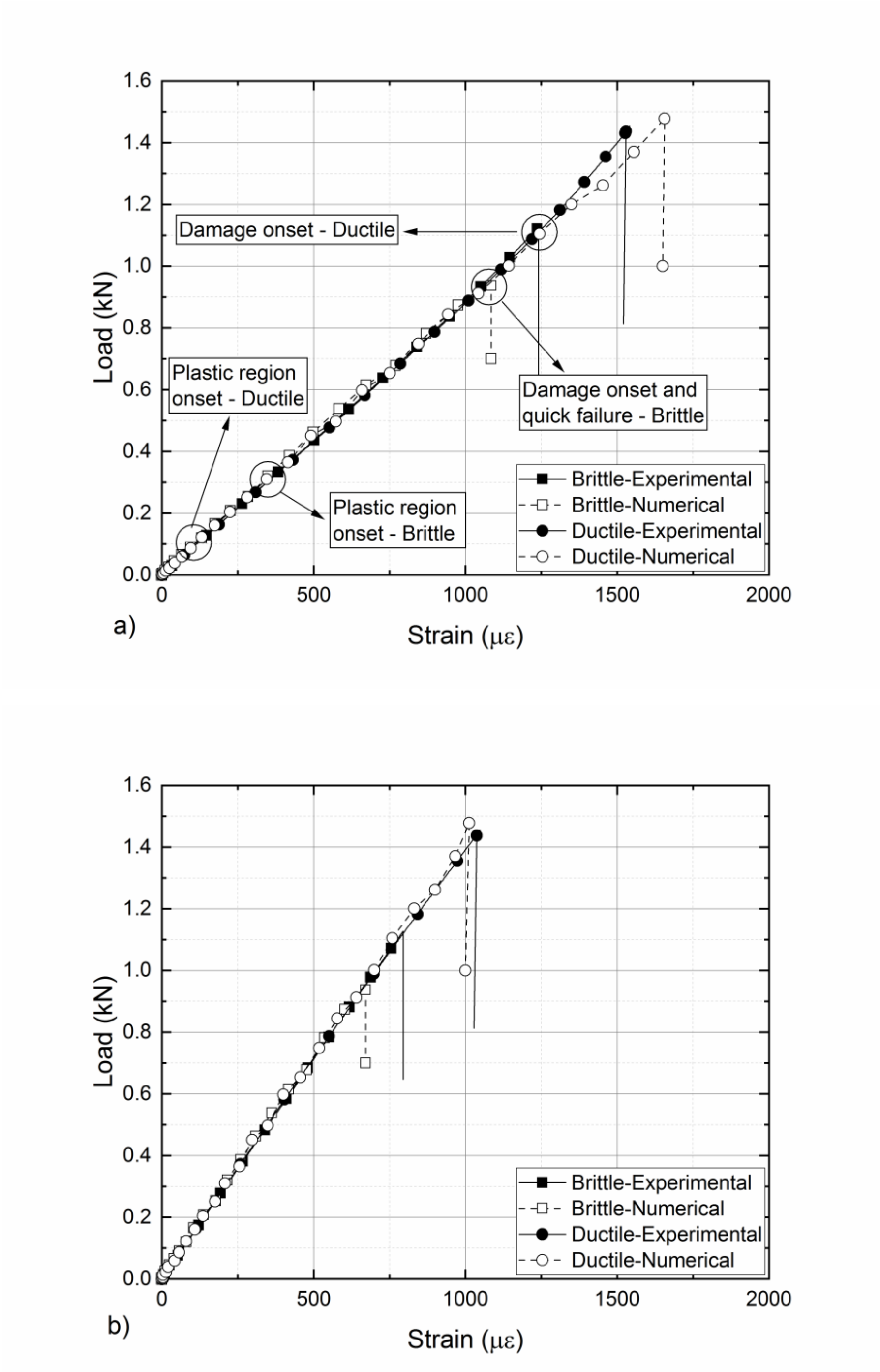

Figure 6.16: Comparison of load vs. strain gauge measurements and corresponding FE predictions for the adhesive joint configurations when subjected to out-of-plane bending loading a) in the glass substrate and b) in the steel substrate. Results based on a continuum mechanics approach.

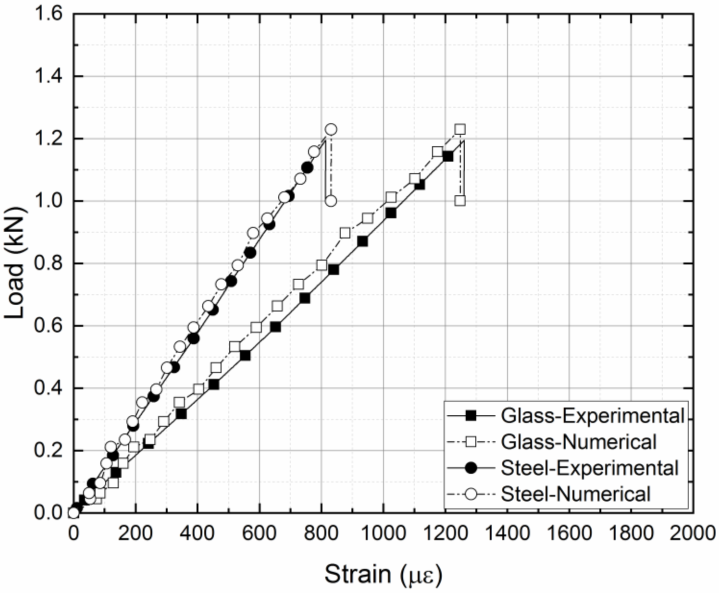

Figure 6.17: Comparison of load vs. strain gauge measurements and corresponding FE predictions for the bolted joint configurations when subjected to out-of-plane bending loading in the steel substrate and in the glass substrate.

6.6.3 Joint failure prediction

Table 6.5 summarizes the failure loads for the out-of-plane bending loading as measured experimentally and as predicted numerically. To provide an interpretation of the experimental scatter, a lower and an upper strength threshold was predicted through FE simulations, for the continuum mechanics approach. The fracture strain of the brittle adhesive was varied based on the values of standard deviation given in Table 3.1. For the case of ductile adhesive and bolted joints, failure occurs in the glass substrate as successfully predicted and hence glass strength variation (120-140 MPa for tempered glass) determines the maximum and minimal failure load thresholds. Figure 6.18 shows the distribution of stresses in the glass substrate (for bolted joints), and Figure 6.19 shows the distribution of the equivalent plastic strain in the adhesive layer (for adhesive joints) in the last increment before failure.

Table 6.5: Summary of the experimental and numerical predictions of the failure load/mechanism for bolted and adhesive joints under out-of-plane bending loading.

	Out-of-plane bending				
	Experimental		Numerical		
Configuration	Failure load (kN)	Failure mechanism	Failure load – Continuum mechanics (kN)	Failure load – CZM (kN)	Failure mechanism
Brittle Adhesive (Araldite 2020)	0.83 ± 0.21	Adhesive/cohesive failure	0.86-0.94	0.98	Interface failure
Ductile Adhesive (Araldite 2047-1)	1.45 ± 0.04	Glass failure	1.27-1.48	1.27-1.48	Glass failure
Bolted	1.20 ± 0.08	Glass failure	1.07-1.23	N/A	Glass failure

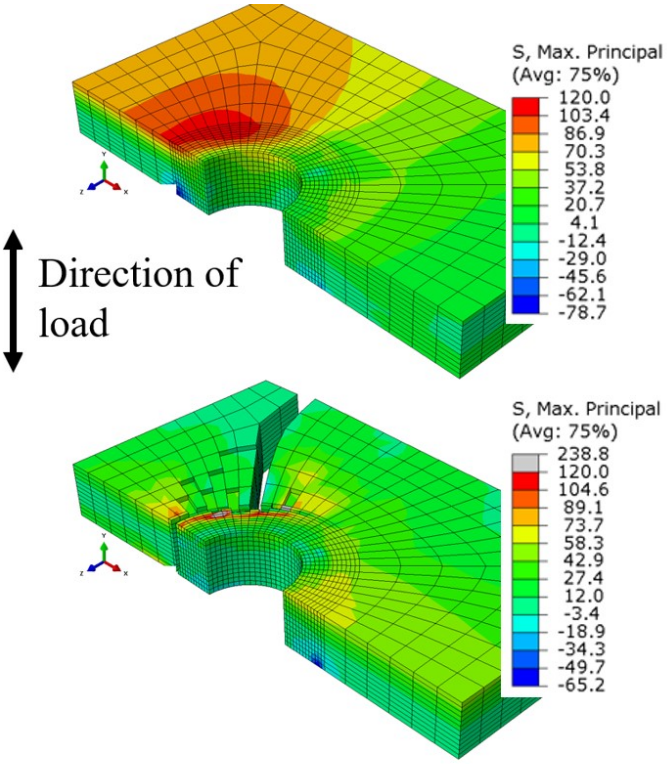

Figure 6.18: Numerical prediction of the damage initiation in the vicinity of the bolt hole under out-of-plane bending loading. The figure shows the distribution of maximum principal stress in the glass surface (stresses in MPa).

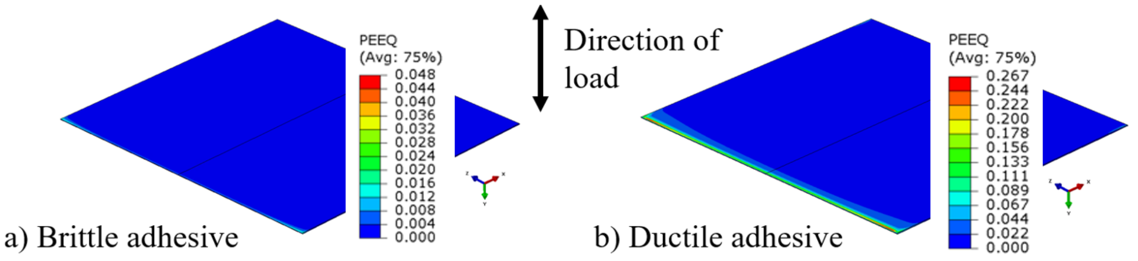

Figure 6.19: Equivalent plastic strain distribution for a) the brittle and b) the ductile adhesive layers in the last increment before failure under out-of-plane bending loading. The size of the bonded area is 50 mm x 50 mm.

It can be seen that there is very good agreement for the failure load prediction for both bolted and adhesive joints. For the case of adhesive joints both the continuum mechanics approach and the CZM approach yield comparable results. For the case of ductile adhesive joints, failure in the glass precedes interface failure and therefore the failure prediction depends only on the strength of the glass, hence the two methods yield identical results. For the case of the brittle adhesive joints, the CZM method slightly overestimates the performance of the joints predicting failure about 13% higher than the average experimental failure load and 4% higher compared to the continuum mechanics approach. Both predictions however, fall into the experimental standard deviation. Finally, for bolted joints the numerical simulations are very accurate in predicting the failure loads and the associated experimental scatter.

In terms of failure mechanisms the numerical predictions are in agreement with the experimental observations. Figure 6.18 shows that for bolted joints the damage initiates in the vicinity of the bolt hole in a location very closely related to the experimental observations shown in Figure 5.16. Figure 6.19 shows the distribution of the equivalent plastic strain on the brittle and the ductile adhesive layers in the last increment before failure. It can be seen that the damage initiated at the corners of the brittle adhesive layer, but was very limited before complete failure took place. Contrary to that, the ductile adhesive started to develop a large plastic zone which extended from the corners, and eventually failed in the glass substrates once the substrate strength was exceeded. The experimental observations also show that stress whitening is found in a limited part of the adhesive layer (Figure 5.20) before the glass substrates fail, validating the numerical models.

6.7 In-plane bending

6.7.1 Geometry and boundary conditions

The geometry of the models created in ABAQUS was as close to the experimental tests performed as possible. Therefore, the dimensions of the glass substrates were 250 mm x 100 mm x 6 mm, the dimensions of the steel splice were 110 mm x 50 mm x 6 mm and the dimensions of the adhesive layers were 50 mm x 50 x mm x 0.2 mm. In addition, steel rollers were included in the models for the load application. It was seen experimentally that glass failure was taking place during the contact of the steel rollers to the glass substrates. This failure was explained by local stress concentrations, and slightly unbalanced load distribution and was not captured numerically since the simulations assume idealistic contact stresses and perfectly flat surfaces in contact regions. Experimentally, this was addressed by adding aluminium interlayers between the steel rollers and the glass substrates to create a more uniform load distribution in the load introduction points. These interlayers were also modelled numerically as 20x20 mm aluminium blocks with 6 mm thickness. Contacts were introduced between the steel rollers/glass substrates and the aluminium interlayers.

Finally, symmetries in two axes were used for the adhesive configurations, and therefore only one quarter of each joint was modelled. The loading was displacement controlled and was applied through reference points, which were again tied to the steel rollers. Figure 6.20 shows the models of the adhesive joints and the detail focuses on the aluminium interlayer.

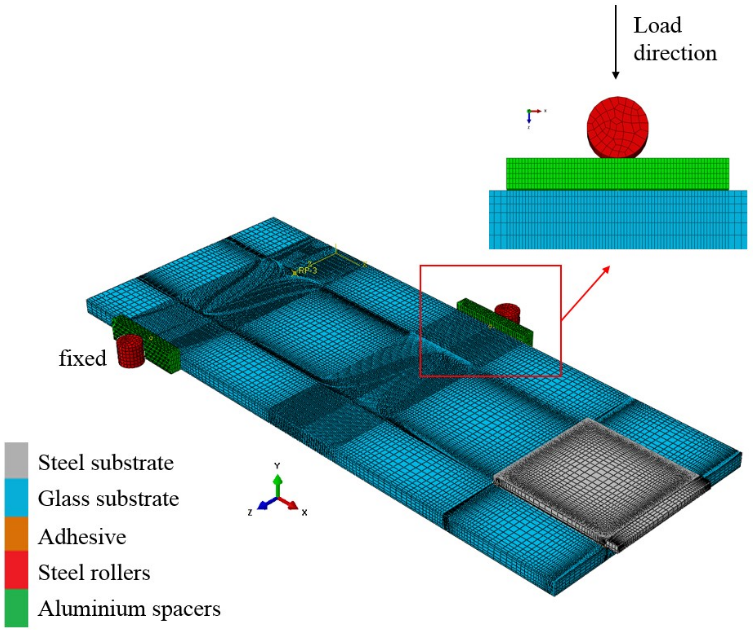

Figure 6.20: Geometry of the numerical models for the adhesive (both continuum and CZM approaches) configuration under in-plane bending loading. Symmetries were used in x- and y- axis.

6.7.2 Joint response

The strain gauge measurements reported in Chapter 5 can be compared with the FE predictions for the stiffness response of the joint in the glass substrates. Chapter 5 showed that the glass substrates experienced slightly uneven load distribution and therefore for this comparison the strain response is averaged between the four glass substrates. Figure 6.21 shows the load-strain response as measured experimentally and predicted numerically for the brittle and ductile adhesive joints in the glass substrate. It can be seen that there is very good agreement. There are some small differences between the experimental and FE methods for the first 2-3 kN of loading, but once all four glass substrates are evenly loaded the stiffness response is similar.

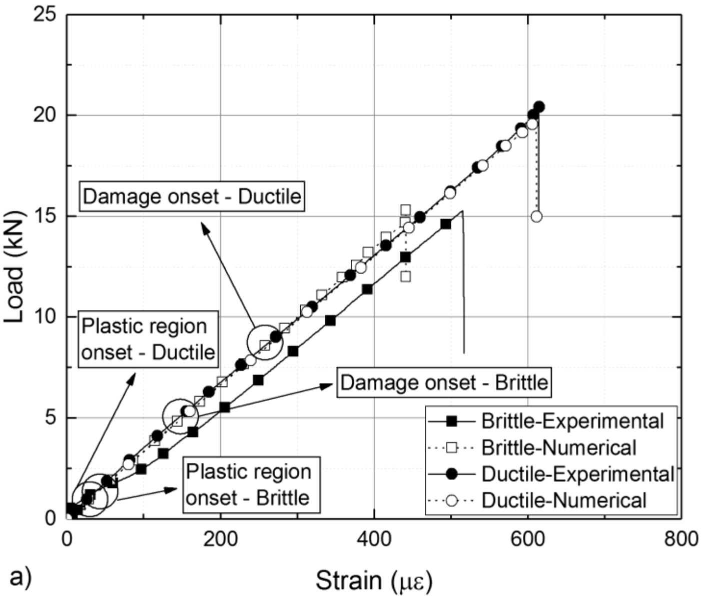

Figure 6.21: Comparison of load vs. strain gauge measurements in the glass substrate and corresponding FE predictions for the adhesive joint configurations when subjected to in-plane bending. Results based on a continuum mechanics approach.

6.7.3 Joint failure prediction

Table 6.6 summarizes the failure loads for the in-plane bending loading as measured experimentally and as predicted numerically. To provide an interpretation of the experimental scatter, a lower and an upper strength threshold was predicted through FE simulations for the continuum mechanics approach. The fracture strain of both adhesives was varied based on the values of standard deviation given in Table 3.1. Figure 6.22 shows the distribution of the equivalent plastic strain in the brittle and ductile adhesive layers as the damage initiates and propagates.

Table 6.6: Summary of the experimental and numerical predictions of the failure load/mechanism for adhesive joints under in-plane bending loading.

	In-plane bending				
	Experimental		Numerical		
Configuration	Failure load (kN)	Failure mechanism	Failure load – Continuum mechanics (kN)	Failure load – CZM (kN)	Failure mechanism
Brittle Adhesive (Araldite 2020)	14.3 ± 0.7	1) Adhesive/cohesive failure 2) Glass failure preceded by significant damage in the adhesive layer	11-15.3	12.1	Interface failure
Ductile Adhesive (Araldite 2047-1)	20.0 ± 0.4	1) Adhesive/cohesive failure 2) Glass failure preceded by significant damage in the adhesive layer	17.9-19.6	18.8	Interface failure
Bolted	N/A				

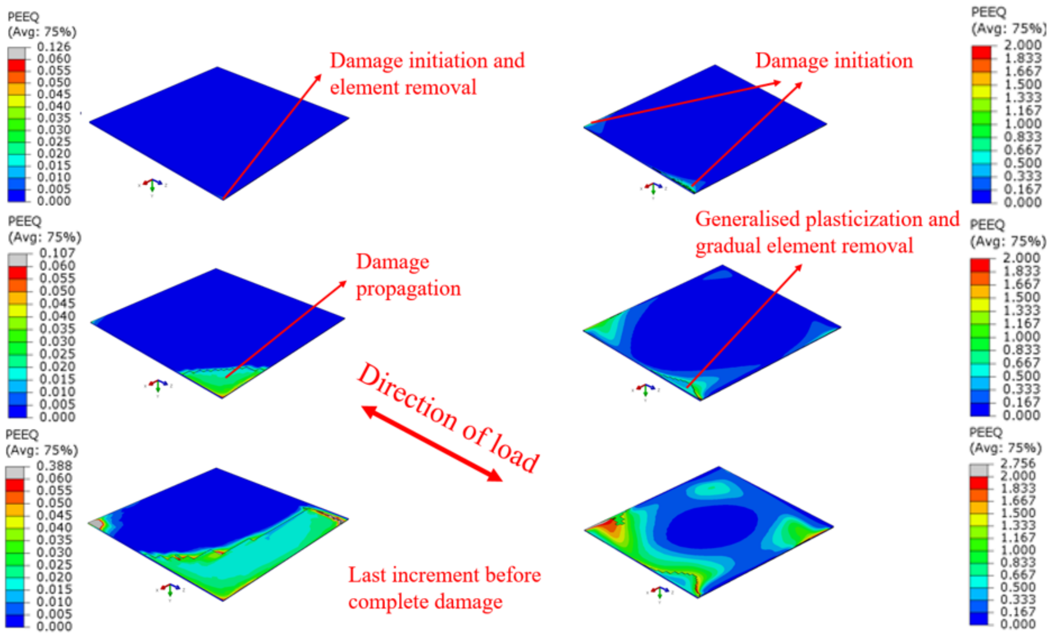

a) Brittle adhesive b) Ductile adhesive

Figure 6.22: Damage onset and propagation in the brittle (left) and ductile (right) adhesive layer under in-plane bending loading. The size of the bonded area is 50 mm x 50 mm and the figure plots the distribution of the equivalent plastic strain as the damage initiates and propagates.

It can be seen that there is very good agreement between the experimental measurements and the failure load prediction under in-plane bending loading. The numerical prediction of the CZM approach is within the range predicted from the continuum mechanics approach. For both the brittle and the ductile adhesive joints, the CZM method slightly underestimates the failure load compared to the experimental measurements. However, the predictions are still within 15% and 6 % compared to the experimental values. The continuum mechanics approach in this load case is more accurate than the CZM method, since the predictions fall within the experimental scatter for both the brittle and the ductile adhesives.

In terms of failure mechanisms the numerical models predict that failure will take place at the interface being in line with the experimental observations. Figure 6.20 shows the equivalent plastic strain distribution in the brittle and ductile adhesive layers during damage initiation and propagation. It can be seen that for both adhesives the damage initiates in the bottom left corners but for the brittle adhesive elements start to fail before the rest of the adhesive layer starts to resist the loading leading to complete failure. Contrary to that, the ductile adhesive starts to develop a large plastic zone throughout the adhesive layer and elements start to fail in all corners of the adhesive layer before final failure. The development of plastic zone that covers the entire adhesive layer is in line with the experimental observations of stress whitening which could be seen throughout the bonded area (Figure 5.22).

6.8 Summary

Chapter 6 described the numerical validation of the experimental tests on bolted and adhesive joints presented in Chapter 5. Chapter 6 initially introduces the numerical methodology, presenting the constitutive models that were used to simulate the damage and failure in the glass substrate and the adhesive/interface. These constitutive models considered pressure-sensitive plasticity, in the form of the Linear Drucker-Prager model which was combined with progressive damage evolution for the adhesive and the glass in the form of the ductile damage model and the brittle cracking model respectively. In addition, cohesive zone models were also developed to model the interface damage by employing the traction-separation laws described in Chapter 4.

The models developed covered all four load cases that were tested experimentally. The numerical validation was based on the comparison of the strains in critical locations of the joints as measured by strain gauges and as predicted numerically. In addition, the validation was also based on comparing the failure loads and mechanisms between the experimental and numerical methods.

Once the models were validated, they were also used for explaining the performance of the joints. The most interesting finding of the experimental study was that the ductile adhesive produced stronger joints in all four load cases, compared to the stronger (in terms of bulk properties), but brittle adhesive. The failure mechanisms of both adhesive layers were studied for all different load cases and it was shown that the ductile adhesive was able to redistribute local stress concentrations by plastic zone development unlike the brittle adhesive. Therefore, for this particular design and geometry, the ductility of the adhesive was shown to play a more critical role in the performance of the joint. The role of ductility/plasticity, however, also depends on the geometry of the joint and especially the size of the bonded area. These considerations led to the optimisation study presented in Chapter 7.

Chapter 7 Optimum selection of mechanical properties of adhesives

7.1 Introduction and structure

The experimental and numerical studies on glass adhesive joints presented in Chapters 5 and 6 revealed that in general the ductile adhesive (in terms of bulk properties) produced stronger joints (in terms of failure load in the joint) for every load case investigated. While studying the performance of the adhesive layers during damage initiation and propagation, it was shown that the ability of the ductile adhesive to develop a large plastic zone was crucial in the performance of the joints. However, the important arising question is how to select optimal adhesive properties for a given joint geometry and loading cases by assessing the strength and ductility characteristics of an adhesive.

In this chapter, the market was surveyed thoroughly and adhesives with different mechanical characteristics were identified. A parametric study evaluating the failure load prediction of joints under uniaxial tension was developed. This study was based on the mechanical properties of the identified adhesives in order to further understand the effect of strength/ductility on the failure behaviour of the joints.

Part of the results presented in this chapter were published as full paper in [134]

7.2 Optimum selection

To assess the effect of different mechanical properties on the joint geometries and load cases included in this study, the market for structural adhesives was surveyed thoroughly. A range of adhesives with different property characteristics resulting in an upper bound curve were chosen for a parametric study to determine the maximum failure load as a function of strength and fracture strain. The adhesives surveyed range from stiff and strong adhesives to flexible and ductile, and their mechanical properties are summarized in Table 7.1 as established from manufacturers' data sheets [120, 138-143].

Table 7.1: Mechanical properties of adhesives selected for the optimal screening selection. Data collected from various manufacturers' datasheet and other literature sources [120, 138-143].

Adhesive	*E* (MPa)	σ_y (MPa)	ε (%)	Fracture energy (J/m^2)	Predicted failure load (kN)
Hysol EA 9394	4420	60	4.6	50	41.8
Hysol EA 9628	2377	52	7.5	100	49
Loctite 5452	114	10	58	1200	25.2
Delo-Duopox 03 rapid thix	2000	33	20	400	88.8
Araldite 2024	760	20	42.5	700	70.6
Araldite 2026	200	18	50	800	61.5
Araldite 2021-1	1800	42	12.5	200	69.4

The graphs in Figure 7.1 demonstrate the general trends for commercially available adhesives based on this upper bound selection: (1) with increasing strength the strain-to-failure reduces (Figure 7.1a), (2) strength increases and strain-to-failure decreases with an increase in stiffness (Figure 7.1b) and (3) fracture toughness increases with strain-to-failure and decreases with strength (Figure 7.1c). Nonlinear trend-lines of the upper limit adhesive selection as per best data fit were plotted for all three graphs to visualize these relationships.

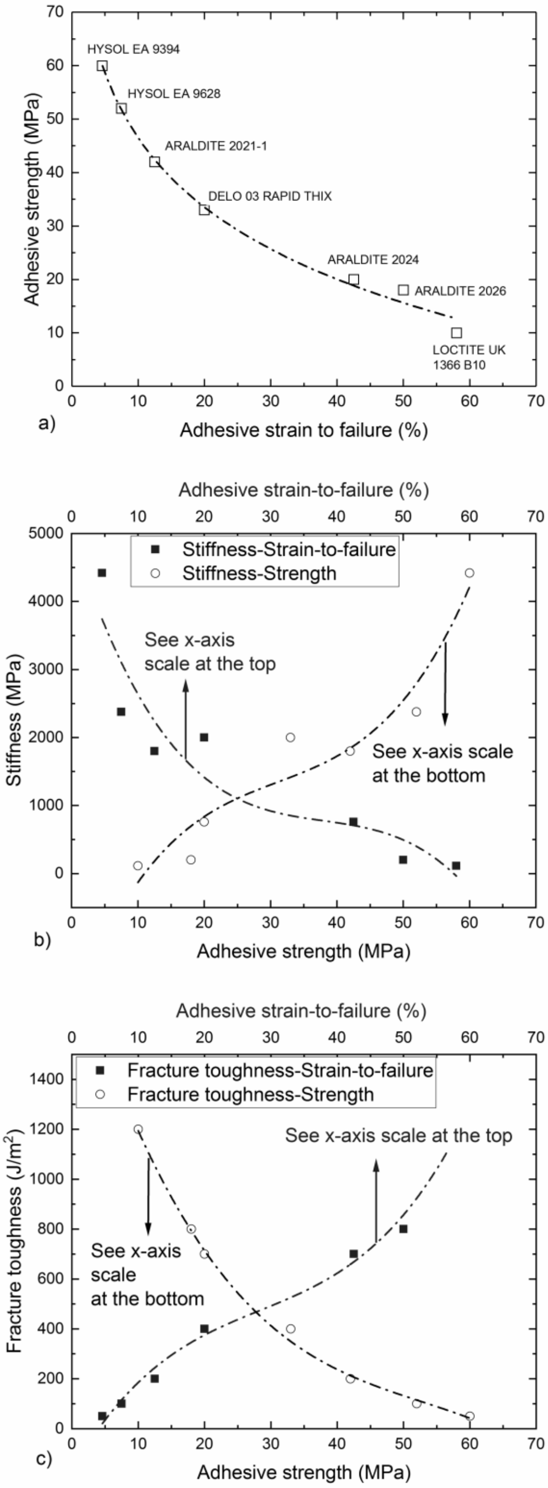

Figure 7.1: Correlation of a) adhesive strength vs strain-to-failure, b) adhesive strength and strain-to-failure vs stiffness, and c) adhesive strength and strain-to-failure vs fracture toughness for common structural adhesives. For figures (b) and (c) the adhesive strength is plotted on the primary (lower) *x* scale, while the adhesive strain-to-failure is plotted on the secondary (upper) *x* scale. The adhesive strength and strain-to-failure are correlated as per Figure 7.1a. Data collected from various manufacturers' datasheet [120, 138-143].

Joint strength simulations were conducted for all data points shown in Figure 7.1. Figure 7.2 shows the distribution of the predicted joint failure loads, assuming simplified perfect elastic-plastic behaviour and standard values for pressure-sensitivity. The numerical methodology followed for these simulations is described in Chapter 6 and utilises the continuum mechanics approach. It is observed that a peak of the predicted failure load occurs around an adhesive strength value of 30 MPa and an adhesive strain to failure of ca. 23%. The presence of such distinctive joint strength peaks suggests that an optimal choice of adhesive exists for the considered joint configuration and tensile load case.

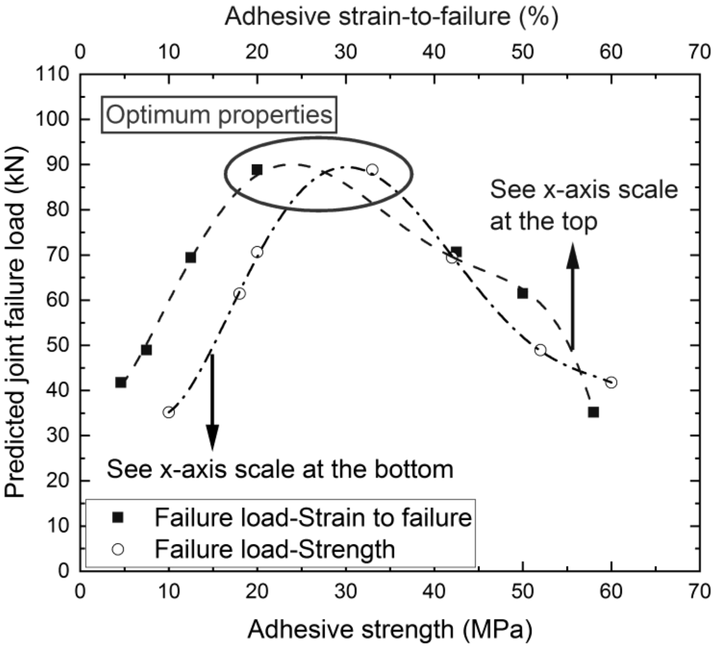

Figure 7.2: Predicted tensile failure load of bonded joints with respect to the adhesive strength and adhesive strain-to-failure. The strength is plotted on the primary (lower) *x* scale, while the adhesive strain-to-failure is plotted on the secondary (upper) *x* scale. The adhesive strength and strain-to-failure are correlated as per Figure 7.1a.

Finally, it is noted that these 'optimal' adhesive properties are most closely associated with the adhesive system 'Delo-Duopox 03 rapid thix'. Therefore, this adhesive was characterised experimentally in terms of bulk properties as shown in Chapter 3 and was also evaluated in joints numerically and experimentally as shown in this chapter. It is worth noting that the values provided by the manufacturer for Delo-Duopox 03 rapid thix [120] compared to the experimental values obtained are higher for the elastic modulus (2000 MPa compared to 1540 MPa measured) and lower for the strength and strain to failure (37 MPa compared to 33 MPa and 35% compared to 20% respectively). Based on the mechanical properties of Delo-Duopox 03 rapid thix, the adhesive will be classified in this work as an intermediate strength adhesive.

7.3 The role of plasticity

The presence of such distinctive peaks in Figure 7.2 is an interesting and unexpected finding which warrants further investigation. Figure 7.3 shows the predicted equivalent plastic strain distributions induced in the joints with the two adhesives studied in Chapters 5 and 6 and the selected intermediate strength adhesive presented above. It should be noted that Figure 7.3 shows the deformations in the adhesive layer of a joint subjected to tensile loading, but the similar observations were made for all four load cases despite the different stress states induced in the adhesive layers for each load case.

It can be seen that the limited plastic region of the brittle adhesive leads to failure in the corners of the joints before the rest of the adhesive layer starts to deform plastically. Unlike the brittle adhesive, both the ductile and intermediate strength adhesives are able to develop a large plastic zone (due to their higher ductility) that extends from the corners and completely covers the 50 mm x 50 mm area of the adhesive layer. Therefore, a larger volume of adhesive material is deforming and utilised to resist the loading. This delays the failure and results in higher joint strength despite the lower strength of the adhesives.

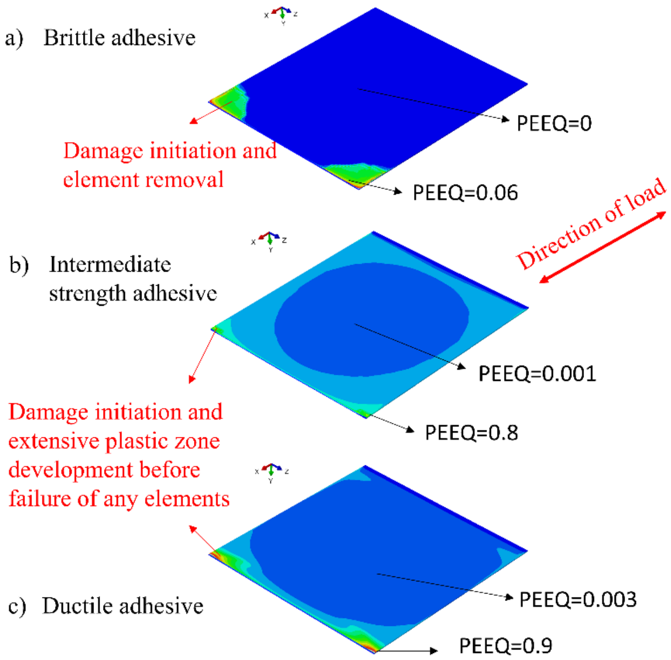

Figure 7.3: Equivalent plastic strain (PEEQ) distribution, plastic zone development and damage onset for tensile loading of the joint configurations with a) brittle, b) intermediate, and c) ductile adhesives. The adhesive layer size shown is 50 mm x 50 mm as per experimental test set-up.

The development of a much larger plastic zone explains why the ductile adhesive is less sensitive to the fracture strain variation compared to the brittle adhesive (as shown in Chapter 6). A relatively small change in the adhesive failure strain changes the failure load prediction significantly for the case of the brittle adhesive, but a bigger change has a smaller effect in the case of ductile adhesive joints.

It has to be noted, however, that the plastic zone development does not only depend on the properties of the adhesive but also on the size of the bonded area. To further investigate the effect of the bonded area, a numerical parametric study with the bonded area as a varying parameter was developed. The analysis is based on the tensile test but similar results are expected for the other load cases.

Figure 7.4a shows the percentage of the elements that yield in the last increment before failure for the three adhesives. Figure 7.4b shows the effect on the failure load of the three adhesives as the bonded area changes by presenting the failure load ratios between the three adhesives examined. The failure load ratios are useful since they indicate which adhesive joint configuration is stronger (for ratios over 100%) or weaker (for ratios below 100%) for a given size of the bonded area. It can be seen that for the intermediate and ductile adhesives, the variation of the bonded area does not have an effect on the percentage of elements that yield since the whole adhesive layer deforms plastically. However, the effect for the brittle adhesive is very important, since the percentage of elements that yield drops from about 50 % (for a bonded area of 100 mm^2) to less than 3% (for a bonded area of 2500 mm^2).

The size of the plastic zone is therefore very important when the failure load of a joint is considered. It can be seen that for smaller bonded areas, where a significant amount of the brittle adhesive layer yields, the brittle adhesive outperforms the ductile adhesive (ratio over 100%) and has comparable performance to the intermediate strength adhesive (ratio close to 100%). As the joints' bonded area sizes increase, the plastic zone develops in a smaller part of the joint, and therefore the performance of the brittle adhesive starts to deteriorate (ratio dropping below 100%) compared to the other two adhesives.

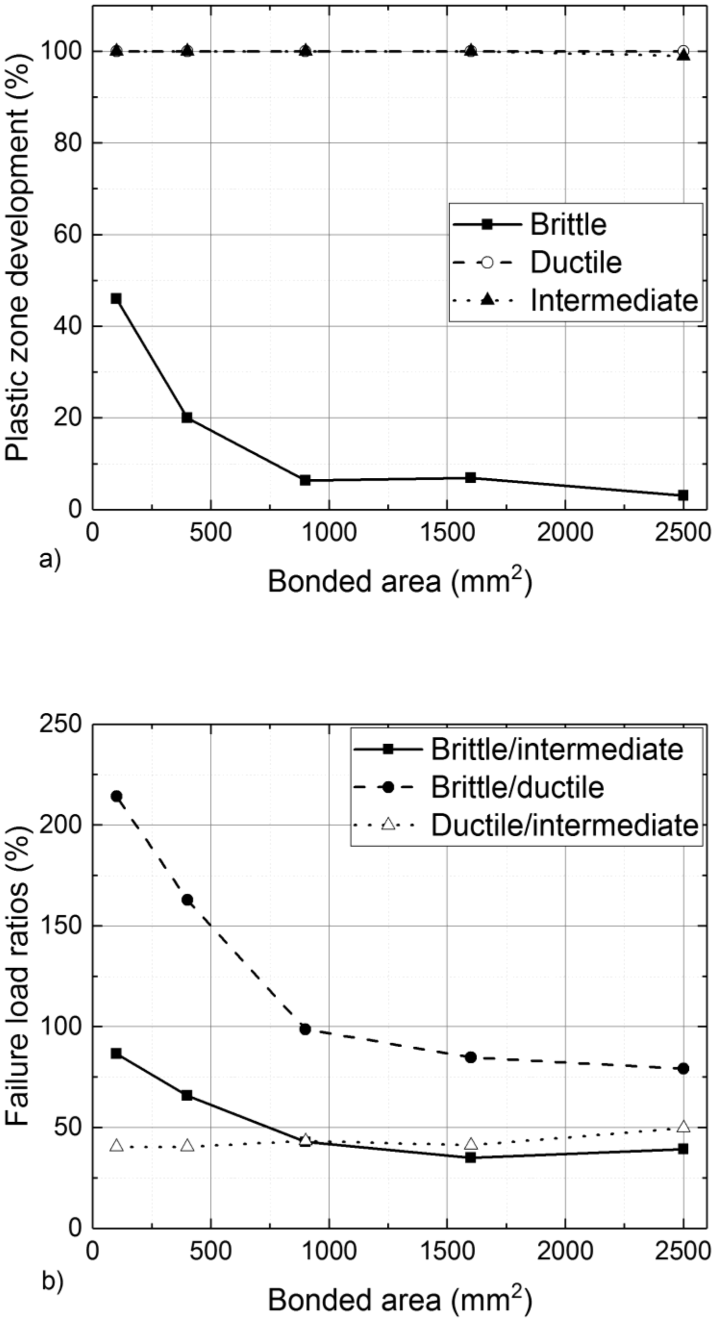

Figure 7.4: Effect of the size of the bonded area on a) the size of the plastic zone, and b) on the joint strength for the three different adhesives.

7.4 Experimental assessment and numerical validation of optimum adhesive joints

To validate the findings of the parametric study, joints were manufactured with the intermediate strength adhesive. The designs and load cases examined are the same as the ones presented in

Chapters 5 and 6 and therefore direct comparisons between the brittle/ductile and intermediate strength adhesives can be undertaken.

In addition, Delo-Duopox 03 rapid thix (intermediate strength adhesive) was characterised experimentally under tension and compression as shown in Chapter 3 (Figure 3.3 and Table 3.1). For the numerical simulation of the intermediate strength adhesive joints, the continuum mechanics approach was utilised as described in Chapter 6. Therefore, the Drucker Prager model was coupled with the ductile damage model. For the intermediate strength adhesive, the pressure sensitivity ratio, σ_{yC}/σ_{yT} was calibrated at a value of 1.60 slightly higher than the 1.2-1.4 value suggested in [7], while the parameters of the ductile damage model can be found in Table 7.2.

Table 7.2: Damage model material parameters for the Intermediate strength adhesive.

Fracture energy, (J/m^2)	400
Stress triaxiality (η)	Fracture strain (ε_c)
-0.33	3.67
0	0.21
0.33	0.367
0.5	0.551
0.75	0.294

It is worth noting, that in the case of the intermediate strength adhesive, the joints for every load case failed in the glass substrate and therefore the adhesive damage parameters were not activated at any point of the analysis. As in Chapter 6, comparison between the experimental recordings and numerical predictions are presented in terms of stiffness response of the joint and failure load prediction for the four different load cases. Figure 7.5 shows the strain response under tensile loading at the midpoint of the glass/steel adhesive joint and the area of stress concentration as measured experimentally and predicted numerically. Similarly, Figure 7.6 shows the strain response in the same locations when the joints were subjected to compressive loading.

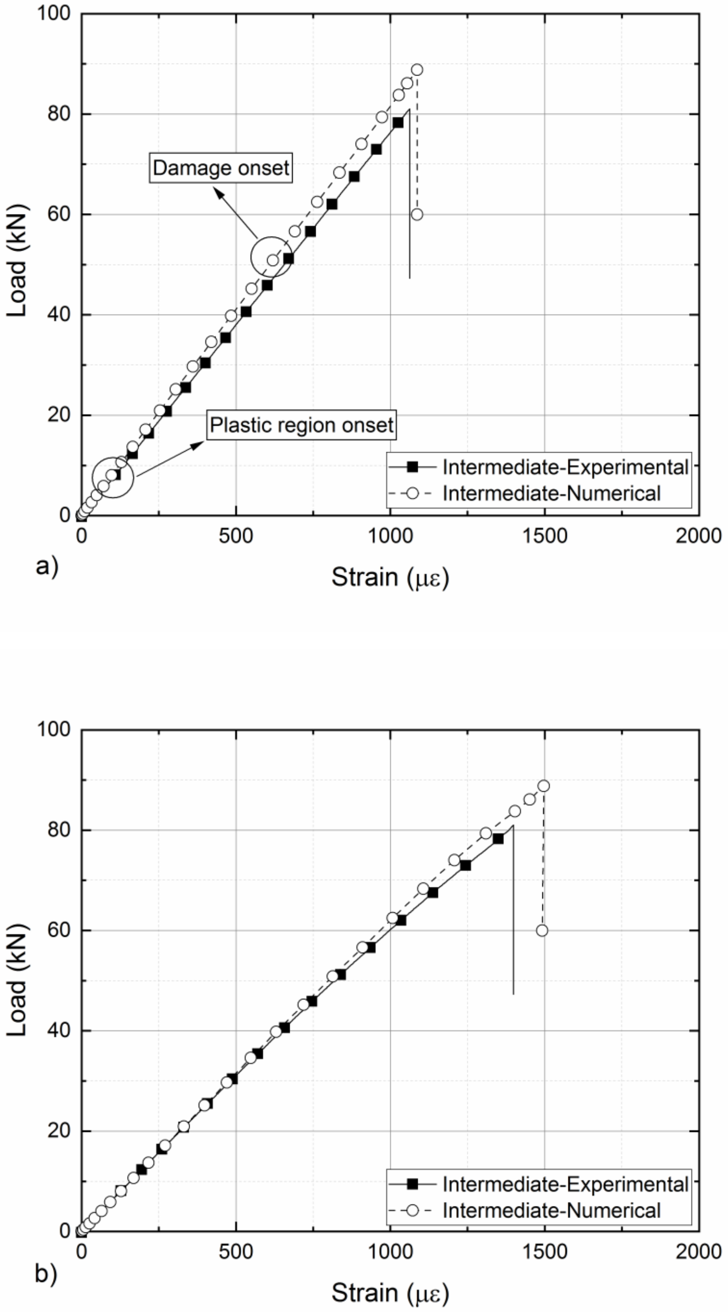

Figure 7.5: Comparison of load vs. strain gauge measurements and corresponding FE predictions for the intermediate strength adhesive joint configurations subjected to tensile loading a) at the glass midpoint and b) at the areas of stress concentrations.

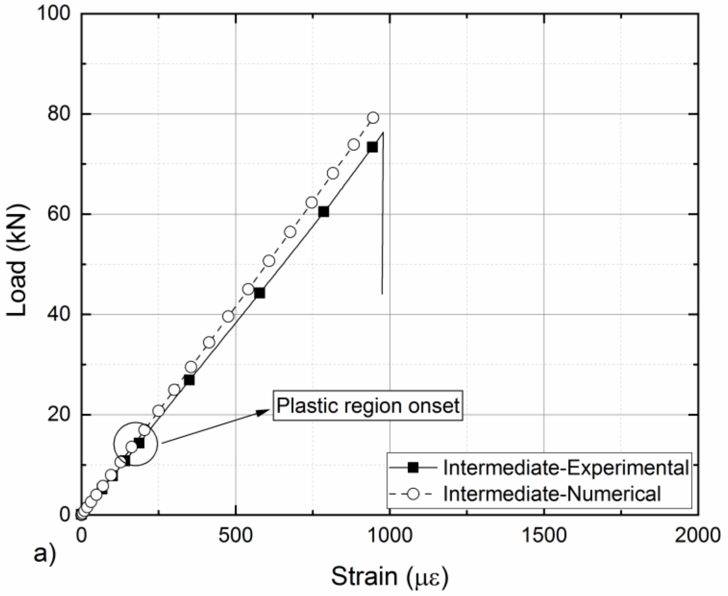

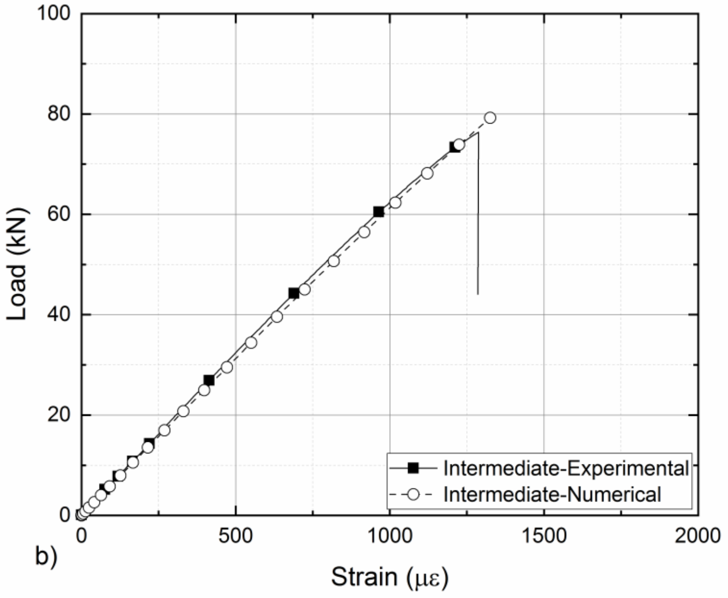

Figure 7.6: Comparison of load vs. strain gauge measurements and corresponding FE predictions for the intermediate strength adhesive joint configurations subjected to compressive loading a) at the glass midpoint and b) at the areas of stress concentrations.

It is worth noting that for the case of compression of the intermediate adhesive strength joints, the failure load is predicted to be significantly higher than observed experimentally, assuming a perfectly straight geometry in the numerical model. The reason for this is that the FE simulations assume perfect loading distribution between the two substrates and exclude the possible occurrence of buckling. However, in the actual tests buckling was observed via strain reading bifurcations on opposite sides of the specimen, and this effect became more significant as the load was increasing. Therefore, numerical models were developed taking buckling into consideration. An initial imperfection was added in the models, following the process outlined by Feih et al [144] in the form of a small offset from the symmetry line to initiate out-of-plane buckling behaviour in the numerical simulations. The offset value was calibrated at a maximum deflection of δ=0.4 mm at the centre of the joint over a length of 370mm for the intermediate strength adhesive case. Figure 8 shows the load vs. strain response of the front and the back substrates, as measured experimentally using strain gauges and predicted numerically. It can be seen that this adjustment leads to a significantly improved prediction for the both the load-response and the failure load. The buckling effect was insignificant for the other two adhesive joint configurations due to the lower failure load.

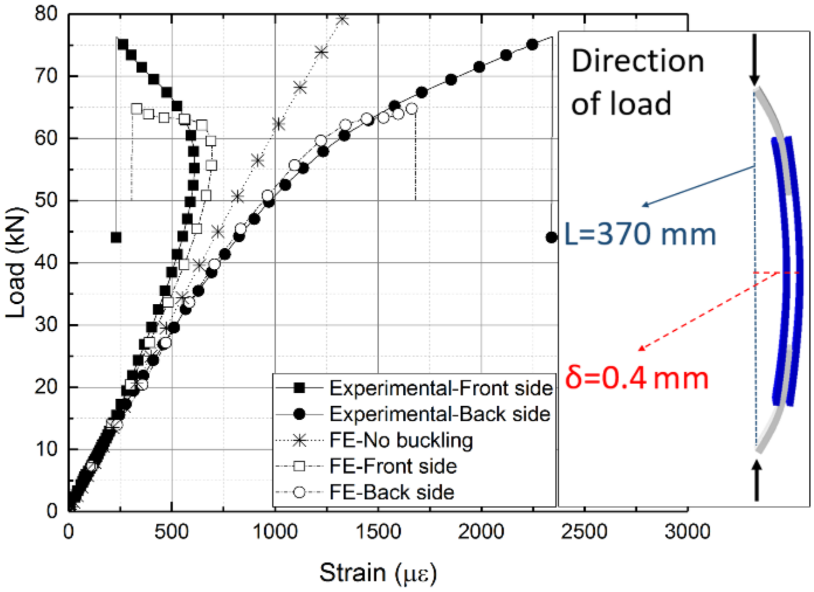

Figure 7.7: Load-strain response displaying buckling behaviour for the high loads achieved with the intermediate strength adhesive. The deformations indicated in the sketch to the right are exaggerated.

The failure mechanism of the intermediate strength adhesive under uniaxial loading switched from adhesive/cohesive to glass substrate failure as shown in figure 7.8. However, it needs to be highlighted that the strength increase in tension is 87% and 51% compared to the brittle and ductile adhesive, respectively, while the corresponding strength increase in compression is 55% and 44%.

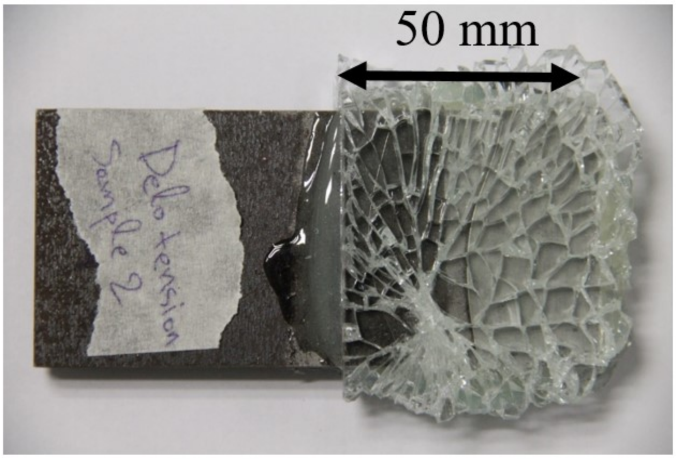

Figure 7.8: Uniaxial mode of failure for the intermediate strength adhesive.

Figure 7.9 shows the experimental measurements and the numerical predictions for the brittle, ductile and intermediate strength adhesives subjected to uniaxial loading and highlights the strength increase achieved. Therefore, the optimisation strategy followed in section 7.2 is validated for uniaxial loading.

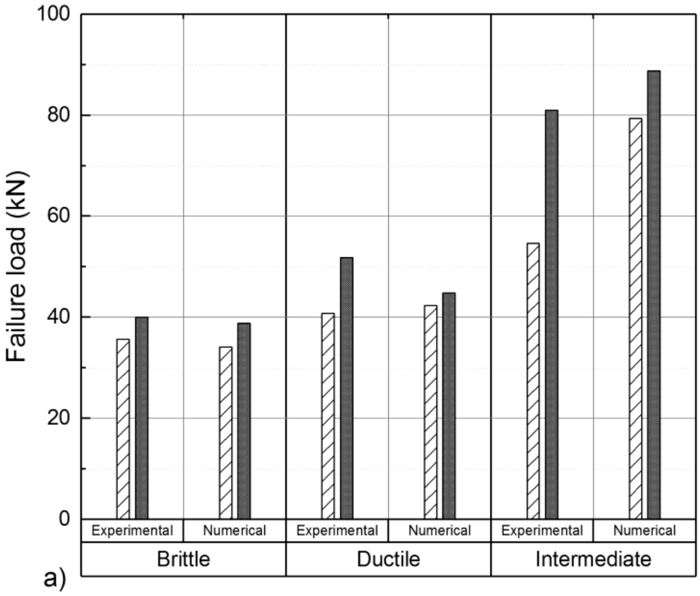

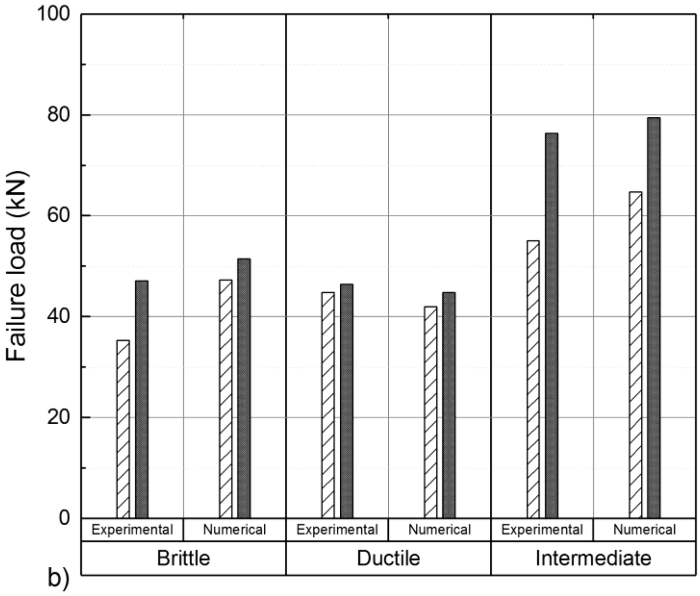

Figure 7.9: Summary of the failure loads for the three adhesives as measured experimentally and predicted numerically for a) tension and b) compression loaded joints.

Similarly, tests with the intermediate strength adhesive were repeated for the out-of-plane and the in-plane bending load cases. Figure 7.10 shows the strain response in the glass and the steel substrate as measured experimentally and predicted numerically for the out-of-plane bending load case. It can be observed that while good agreement is achieved for the strain response, the numerical prediction slightly underestimates the failure load. For these joints the glass appears to fail at a slightly higher stress than the maximum stress specified numerically (~140 MPa). This is not captured by the models which accurately predicted the glass substrate failure, but at about 10% lower load. The failure mechanism can be seen in Figure 7.11.

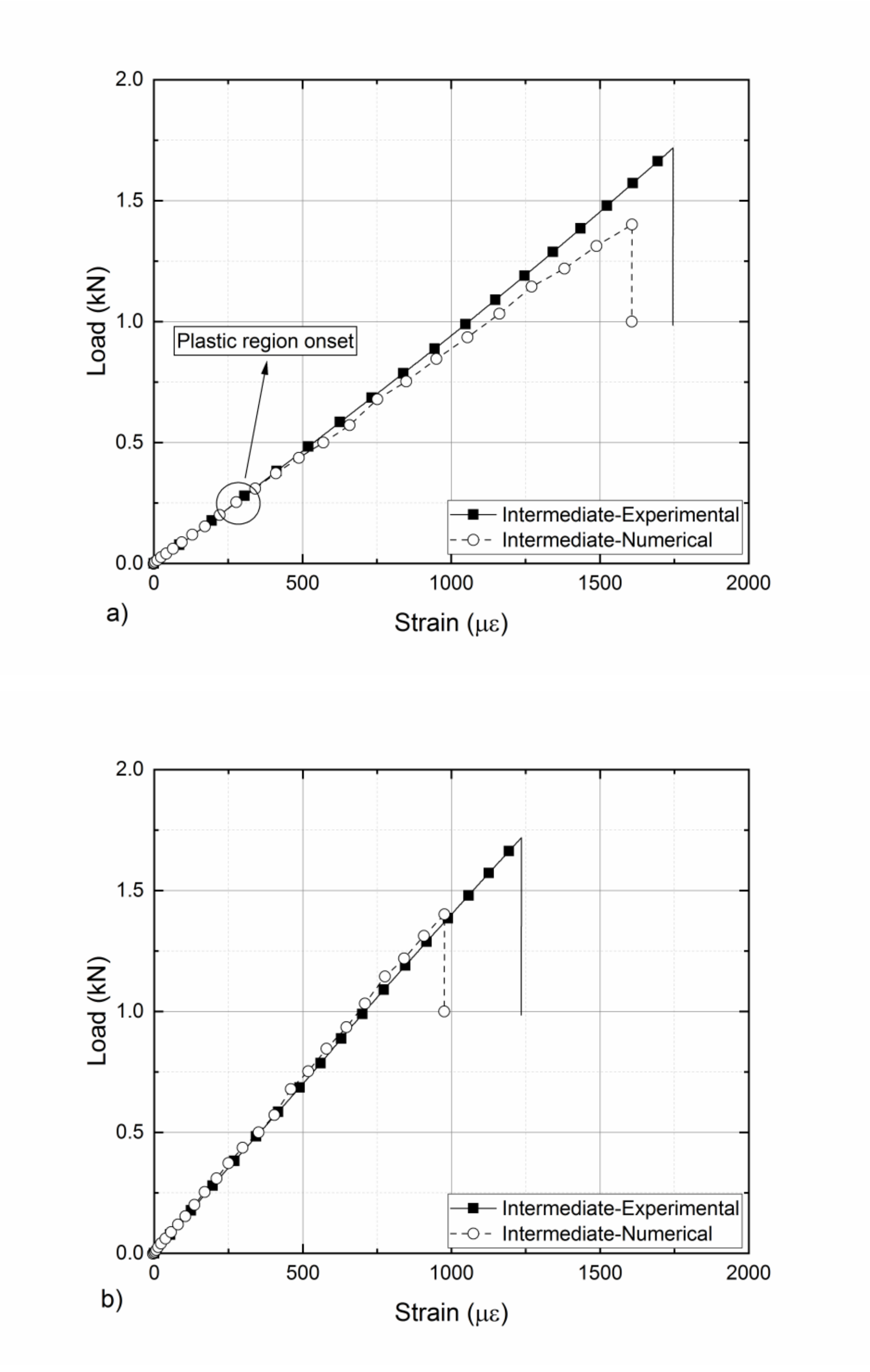

Figure 7.10: Comparison of strain gauge measurements and FE predictions for the intermediate strength adhesive joints subjected to out-of-plane bending loading a) at the glass substrate, and b) the steel substrate.

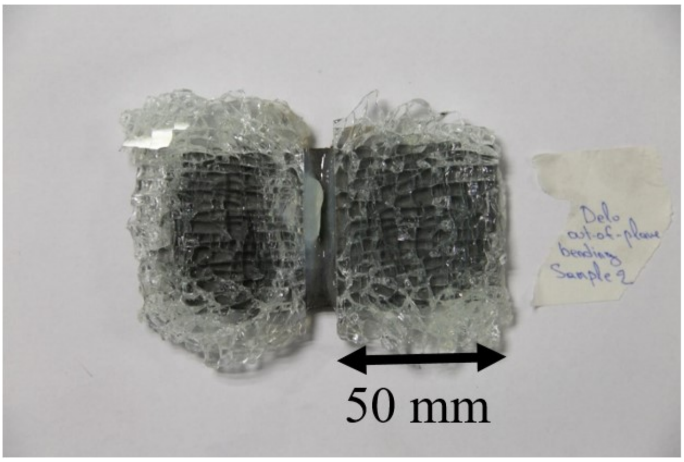

Figure 7.11: Out-of-plane bending mode of failure for the intermediate strength adhesive.

Once again, strength increase is achieved with the intermediate strength adhesive as shown in Figure 7.12. The strength increase is 99% and 14%, respectively, compared to the brittle and ductile adhesives.

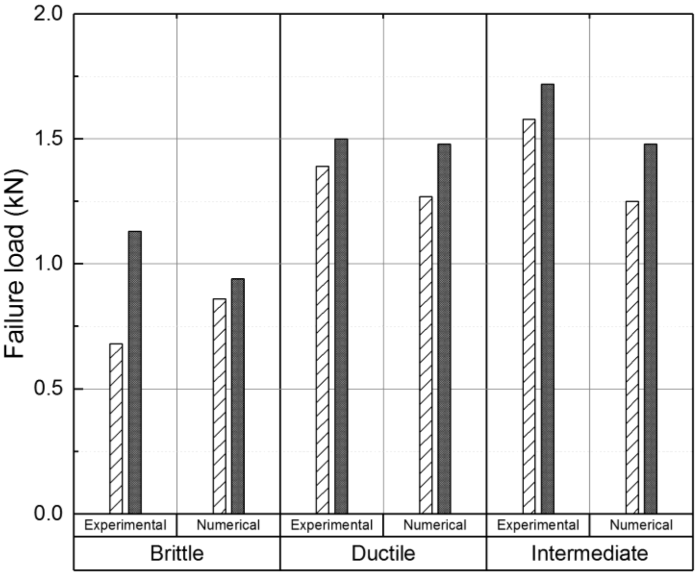

Figure 7.12: Summary of the failure loads for the three adhesives as measured experimentally and predicted numerically for the out-of-plane bending tests.

Figure 7.13 shows the strain response in the glass substrate for the joints subjected to in-plane bending loading. All the joints with the intermediate strength adhesive failed in the glass before any damage was introduced in the adhesive. The failure in the glass occurred at the contact point between the glass and the aluminium interlayer in the area of the load introduction points as shown in Figure 7.14. In addition, Figure 7.15 shows the failure in the area of the interface.

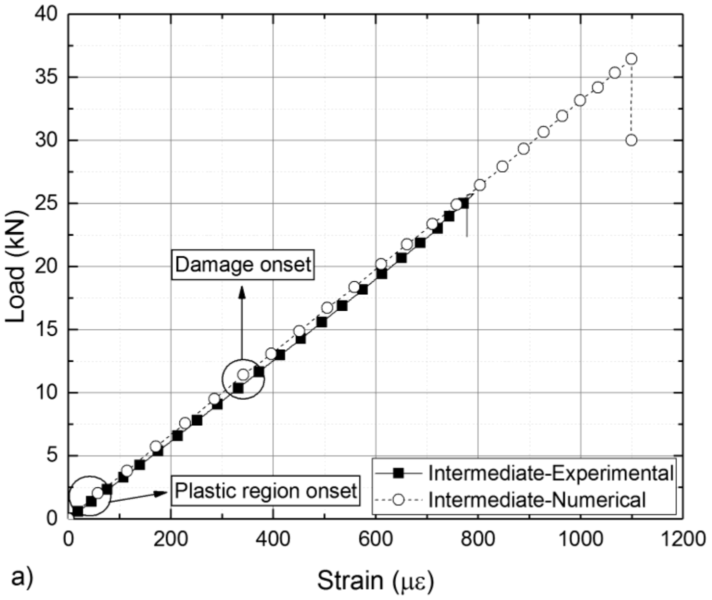

Figure 7.13: Comparison of strain gauge measurements and FE predictions for the intermediate strength adhesive joints subjected to in-plane bending loading.

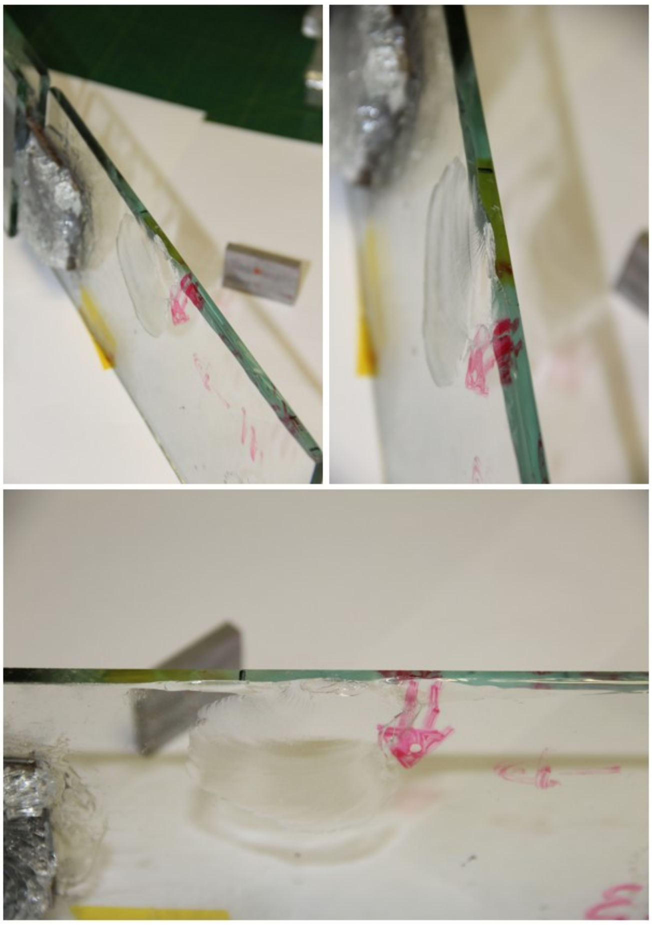

Figure 7.14: Damage introduced in the glass substrate due to the contact with the aluminium interlayer.

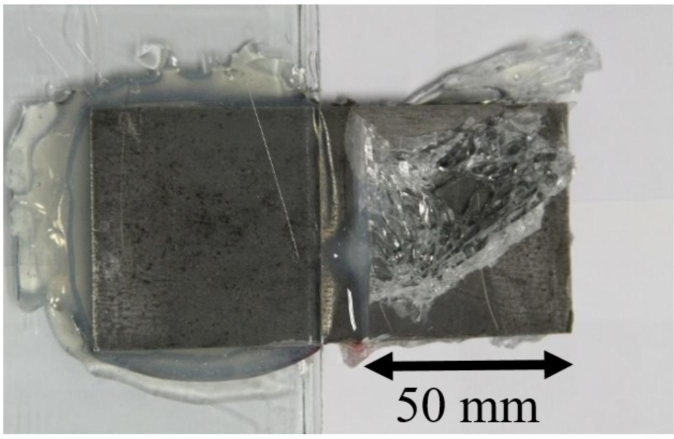

Figure 7.15: In-plane bending mode of failure for the intermediate strength adhesive.

Different interlayers at the load application points could be used to further control the stress concentrations in the contact region, but optimisation of this test set-up is considered outside the scope of this study, especially considering that even with the premature failure there is a significant strength increase compared to the brittle and ductile adhesive joints (82% and 30% higher failure loads, respectively). Figure 7.16 summarises the experimental measurements and the numerical predictions for the brittle, ductile and intermediate strength adhesive under in-plane bending loading. It is noted that finite element analysis did not predict the glass failure at the load introduction points, most likely due to the assumptions of (a) uniformly distributed contact stresses and (b) perfectly flat surfaces in contact regions.

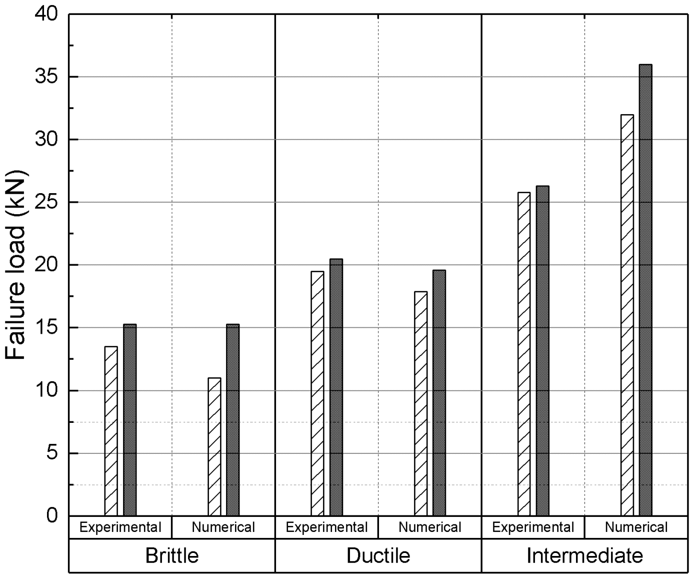

Figure 7.16: Summary of the failure loads for the three adhesives as measured experimentally and predicted numerically for the out-of-plane bending tests.

7.5 Summary

Based on observations from Chapters 5 and 6, in this chapter, a numerical parametric study was conducted to screen commercial adhesive systems systematically. The study showed that for the joint designs and geometrical configurations examined, adhesives that combine intermediate values of strength and ductility produce significantly stronger bonded joints. The study identified a commercial adhesive, with intermediate strength/ductility, as an optimum adhesive for the given geometry.

In addition, the failure mechanisms associated with different adhesives were studied, and it was shown that adhesive ductility plays a critical role. Unlike the brittle adhesive, the intermediate strength and the ductile adhesives develop an extended plastic zone, which redistributes the loads and suppresses or reduces the effect of local stress concentrations. However, the plastic zone development, and hence the strength of the joint, does not only depend on the properties of the adhesive but also on the geometry of the joint. It was shown that adhesive strength is more important for smaller size joints, while ductility becomes more critical as the bonded area increases in size.

Adhesive joints using the identified optimum adhesive were manufactured and tested experimentally, while they were also analysed numerically. The experimental study showed that the joints with an intermediate strength adhesive system outperformed all other joints for every load case. The strength increase comparted to the brittle and ductile adhesives ranged from a minimum of 14% to a maximum of 99%. The failure mechanism switched from a predominantly adhesive/cohesive mode to failure in the glass, limiting the measured and validated strength increase.

The developed adhesive selection strategy reveals that this particular resin system can indeed be considered an optimal choice for the considered load cases. It should be noted that a similar approach can be utilized as an initial screening test for any type of joint geometry and loading condition. The experimental test campaign conducted as part of the research presented in this chapter confirms this conclusion and further validates the capability of the nonlinear FE analyses for joint design and optimisation.

Chapter 8 **Environmental Exposure**

8.1 Introduction and structure

All results presented in Chapters 5-7 described tests in ideal laboratory conditions (23°C and 50% R.H.) under quasi-static loading. However, adhesive joints are known to be very sensitive to environmental exposure as described in Chapter 2. Therefore, in this chapter, the effect of environmental exposure on adhesive joints was studied. More specifically, humidity and elevated temperatures were introduced according to ETAG 002 [76], a European guideline for the use of structural sealants in buildings.

In order to study the effects of humidity and temperature, the degradation of both the bulk and interface properties was measured by repeating the tensile tests described in Chapter 3 and the modified DCB and SLB tests described in Chapter 4. Glass/steel double lap shear adhesive joints as described in Chapters 5-7 were also exposed to the same conditions and tested experimentally. The numerical modelling methodologies previously developed were evaluated with the new input data to quantify the environmental degradation and the subsequent strength drop of the joints. The exposure study considered the brittle and ductile adhesives only. The intermediate strength adhesive had a very low T_g and extensive damage was taking place for the conditions examined. Therefore, it was excluded from this study.

8.2 Exposure conditions

ETAG 002 [76] is a European directive for the use of sealants in buildings and one of the few attempts to standardise the use of adhesives in buildings. The cycle proposed for the environmental exposure of adhesive joints was adopted although ETAG 002 is not designed for stiff adhesives like the ones used in this study. The test specimens were fully immersed (at least 20 mm below the water level) in demineralised water for 21 days at a temperature of 45°C. Afterwards, they were removed from the chamber and conditioned at (23 ± 3) °C and (50 ± 5) % R.H. for (24 ± 4) hours. After that, they were tested following the methodology described in Chapters 3 (for the bulk specimens), 4 (for the DCB/SLB specimens) and 5 (for the double lap shear joints specimens). A Memmert universal oven was used for controlling the temperature and Figure 8.1 shows the typical set-up during the exposure of all samples. According to the guideline, joints consisting of glass substrates should also be exposed to UV-exposure. However, it was decided to focus study on the effect of elevated temperature and humidity, and therefore UV radiation was not considered.

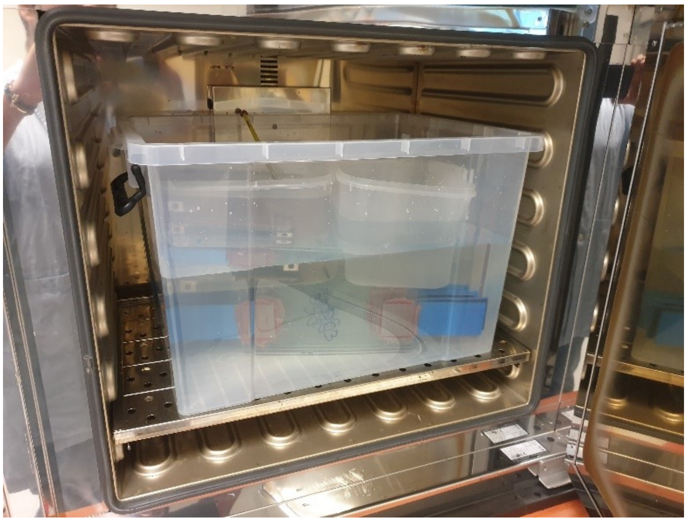

Figure 8.1: Exposure of glass/steel double lap shear adhesive joints.

The DCB specimens were initially used to evaluate the effect of humidity and elevated temperatures on the interfaces for shorter exposure periods. Exposure periods of 7, 14 and 21 days were considered. The DCB specimens were also exposed to heat only (45°C without water immersion) in order to specify which parameters contribute more to the degradation of the joints.

8.3 Effect of exposure on the bulk properties

For the effect of the environmental exposure on the bulk properties of the adhesives, tensile specimens were manufactured following ISO standards [122, 123] as described in Chapter 3. Figure 8.2 shows typical tensile specimens for the brittle and ductile adhesive before and after exposure. It can be observed that there was a slight decolourisation for both adhesives after exposure.

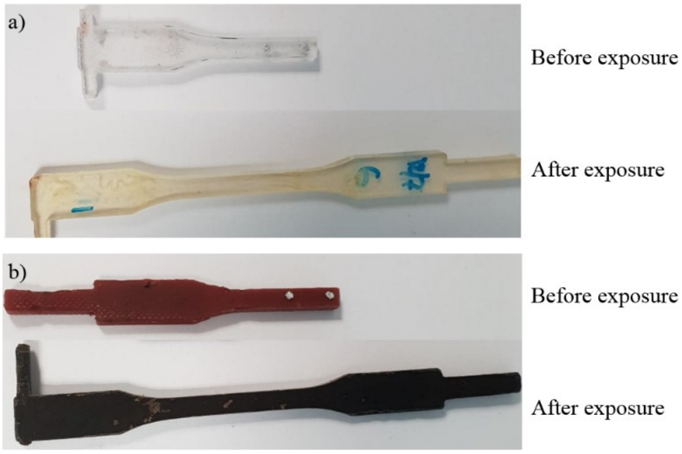

Figure 8.2: Decolourisation of a) brittle (Araldite 2020) and b) ductile adhesive (Araldite 2047-1) after exposure.

Table 8.1 summarises the key mechanical properties before and after exposure for the brittle and the ductile adhesives while Figure 8.3 shows characteristic stress-strain responses. It can be seen that the elastic modulus, yield and failure stresses dropped for both adhesives. However, for both adhesives an increase in the ductility was also observed. A minimum of 5 specimens per adhesive were tested.

Table 8.1: Summary of the mechanical properties of the brittle and ductile adhesives before and after exposure (21 days in water at 45°C).

	Araldite 2020 - Before exposure	Araldite 2020 - After exposure	Percentage change (%)	Araldite 2047-1 - Before exposure	Araldite 2047-1 - After exposure	Percentage change (%)
Young's modulus (E), GPa	2.57 ± 0.08	1.87 ± 0.21	-27	0.89 ± 0.08	0.54 ± 0.05	-39
Tensile yield strength (σ_{yT}), MPa	31.33 ± 2.73	27.88 ± 4.04	-11	5.56 ± 0.11	2.03 ± 0.30	-63
Tensile failure stress (σ_{fT}), MPa	45.39 ± 2.61	41.66 ± 1.00	-8	13.10 ± 1.13	9.17 ± 0.50	-30
Tensile failure strain (ε_{fT}), %	3.1 ± 0.6	4.37 ± 0.73	41	17 ± 4.1	24.89 ± 3.65	46

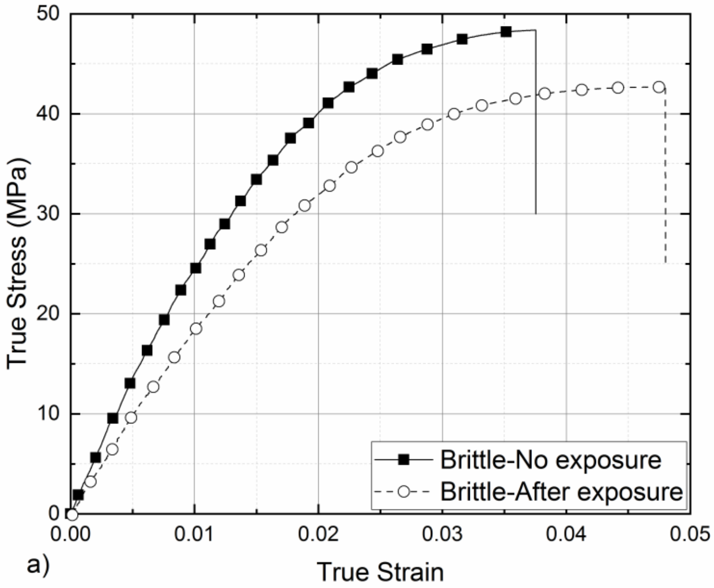

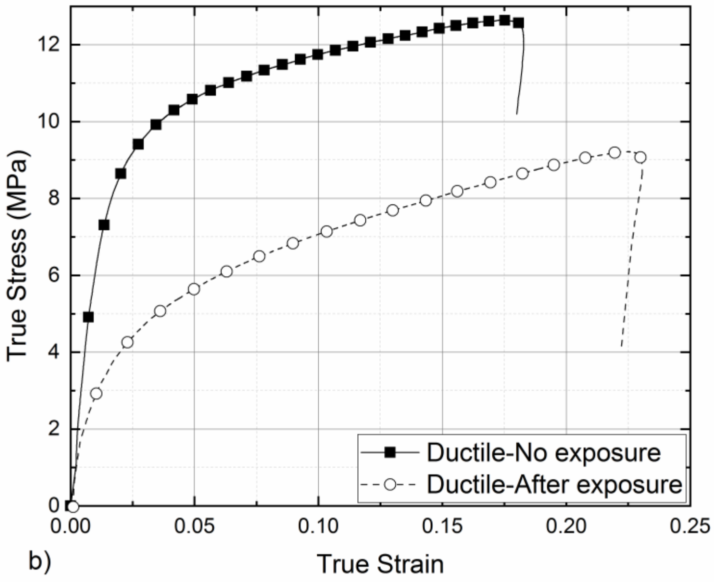

Figure 8.3: Characteristic stress-strain responses of the a) brittle and b) ductile adhesives before and after exposure (21 days in water at 45°C).

It can be seen that the ductile adhesive was affected more since the elastic modulus dropped 39%, compared to a 27% drop observed for the brittle adhesive. Similar trends were observed for the yield and failure stresses with the ductile adhesive dropping 63% and 30%, respectively, while the respective drops recorded on the brittle adhesive were 11% and 8%. Finally, it is worth noting that both adhesives increased their elongation by 41% and 46%, respectively. Table 8.1 shows that the ductile adhesive was affected more by the exposure since the percentage changes for the Young's modulus, the tensile yield strength and the tensile failure stress and strain are higher.

8.4 Effect of exposure on the glass/steel interfaces

8.4.1 Experimental analysis

To determine the effect of the environmental exposure on the glass/steel interfaces, the modified DCB/SLB samples were used. The DCB/SLB samples are smaller and easier to manufacture compared to the double lap shear joints, so they were used as an initial evaluation to determine the effect of exposure. In addition, shorter exposure periods were also evaluated. Another advantage of the DCB/SLB samples is that they lead to the evaluation of traction-separation laws for the exposed specimens and therefore provide a numerical methodology to predict the degradation of the double lap shear joints. The testing followed the methodology described in Chapter 4, and a minimum of 5 specimens per adhesive was tested.

Figure 8.4 shows characteristic load/displacement curves for the DCB samples after 7, 14 and 21 days of humidity/heat exposure and 7 days of heat only exposure for both adhesives. In addition, unaged specimens (the ones described in Chapter 4) are also included in order to make the comparisons and trends easier to follow.

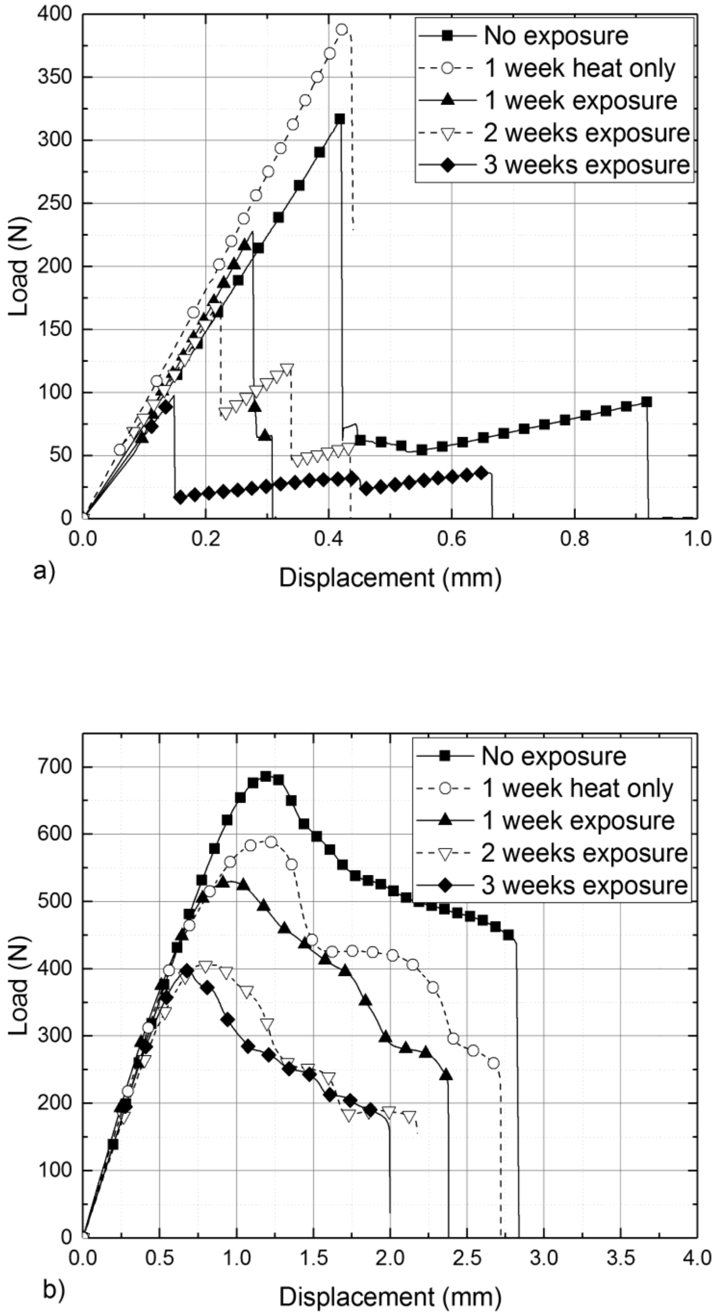

Figure 8.4: Characteristic load-displacement curves for the a) brittle and b) ductile DCB specimens for no exposure and 7, 14, 21 days of exposure.

Figure 8.5 summarises the drop of the average load for the brittle and ductile adhesives as a function of exposure time.

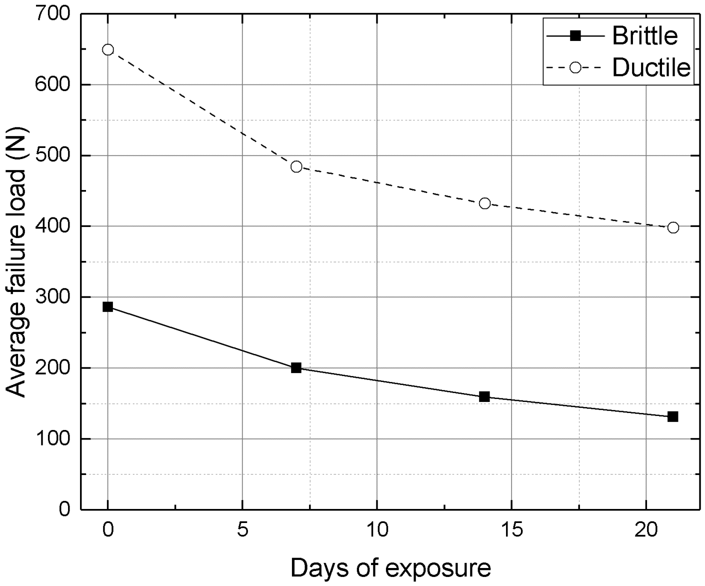

Figure 8.5: Load drop recorded in the DCB specimens for the brittle and ductile adhesives after 7, 14 and 21 days of exposure.

Table 8.2 summarises the experimental testing results for the modified DCB specimens. It can be seen that for both the brittle and the ductile adhesives the degradation gradually increased (as shown also in Figures 8.4 and 8.5). Most of the damage took place during the first week of exposure. Thereafter the degradation slowed down, which is in line with typical moisture uptake curves and with the experimental observations of similar studies [145-147]. Finally, after 3 weeks, the brittle DCB specimens retained 45% of their initial strength while the ductile adhesive retained 61%. Interestingly, the load drop of the brittle DCB specimens is bigger compared to the ductile ones, even though the degradation of the bulk properties is more significant for the ductile adhesive.

In addition, it can be seen that the heat only exposure did not have a very significant degradation effect on the ductile adhesive and in the case of the brittle adhesive it even led to strength increase, which was attributed to additional post-curing of the resin. It is also worth noting that as the exposure time increased, the coefficient of variation from the five test results also increased significantly, especially for the brittle adhesive.

Table 8.2: Summary of the experimental testing for the DCB samples under exposure.

Exposure	Specimen	Average Failure load (N)	Coefficient of variation (%)
No exposure	Brittle adhesive (Araldite 2020)	286 ± 55	19.2
7 days - at 45 °C		337 ± 54	16.0
7 days - water immersion at 45 °C		200 ± 51	25.5
14 days - water immersion at 45 °C		159 ± 51	32.1
21 days - water immersion at 45 °C		131 ± 64	48.9
No exposure	Ductile adhesive (Araldite 2047-1)	649 ± 29	4.5
7 days - at 45 °C		559 ± 45	8.1
7 days - water immersion at 45 °C		484 ± 49	10.1
14 days - water immersion at 45 °C		432 ± 43	10.0
21 days - water immersion at 45 °C		398 ± 37	9.3

Figure 8.6 shows the interfaces of the samples after failure for 7, 14 and 21 days of exposure. It can be seen that for the ductile adhesive a moisture ingress ring formed and moved from the sides to the centre of the specimen. The failure was mostly/completely adhesive on the glass side. The part of the adhesive layer that was not affected by the moisture developed the stress whitening that was previously observed in Chapters 4 and 5. Analysis of the failed interfaces revealed that the affected area of the ductile specimens increased from 25% to 37% after 1 and 3 weeks, respectively, which is in good agreement with the percentage drop of the average failure load of the DCB specimens for the respective periods. For the brittle adhesive, the moisture ingress was not as obvious. The specimens displayed an adhesive mode of failure, and the effect of the exposure could only be observed in the drop of the failure load.

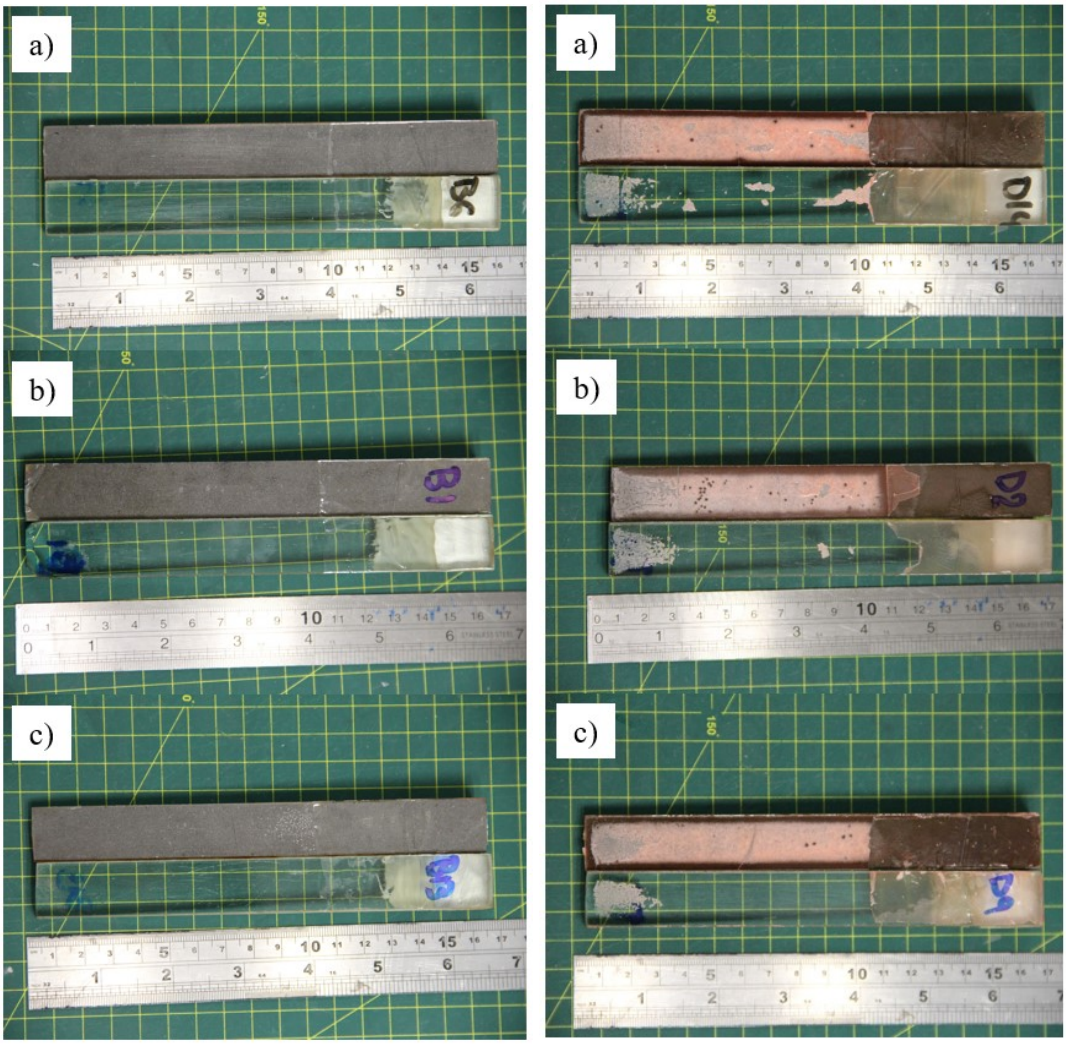

Figure 8.6: Failed glass interfaces of the DCB specimens for the brittle (left) and ductile (right) adhesives after a) 7 days, b) 14 days, c) 21 days of exposure.

The SLB samples were only tested after 21 days of exposure. Figure 8.7 shows characteristic load/displacement curves of the SLB specimens while the reference unaged specimens were also included in the figure for comparison purposes. Table 8.3 summarises the experimental testing for the SLB specimens after 21 days of exposure, while Figure 8.8 shows the glass/steel interfaces after failure. The moisture ingress effect observed for the ductile DCB specimens was also seen for the SLB specimens. In addition, some moisture ingress could also be observed in the brittle SLB specimens. It is worth noting that the brittle and ductile SLB samples retained 74% and 85% of their initial strength, which was significantly higher compared to the respective 45% and 61% measured for the DCB tests. However, once again the environmental exposure led to a significant increase in the coefficient of variation for the five test specimens.

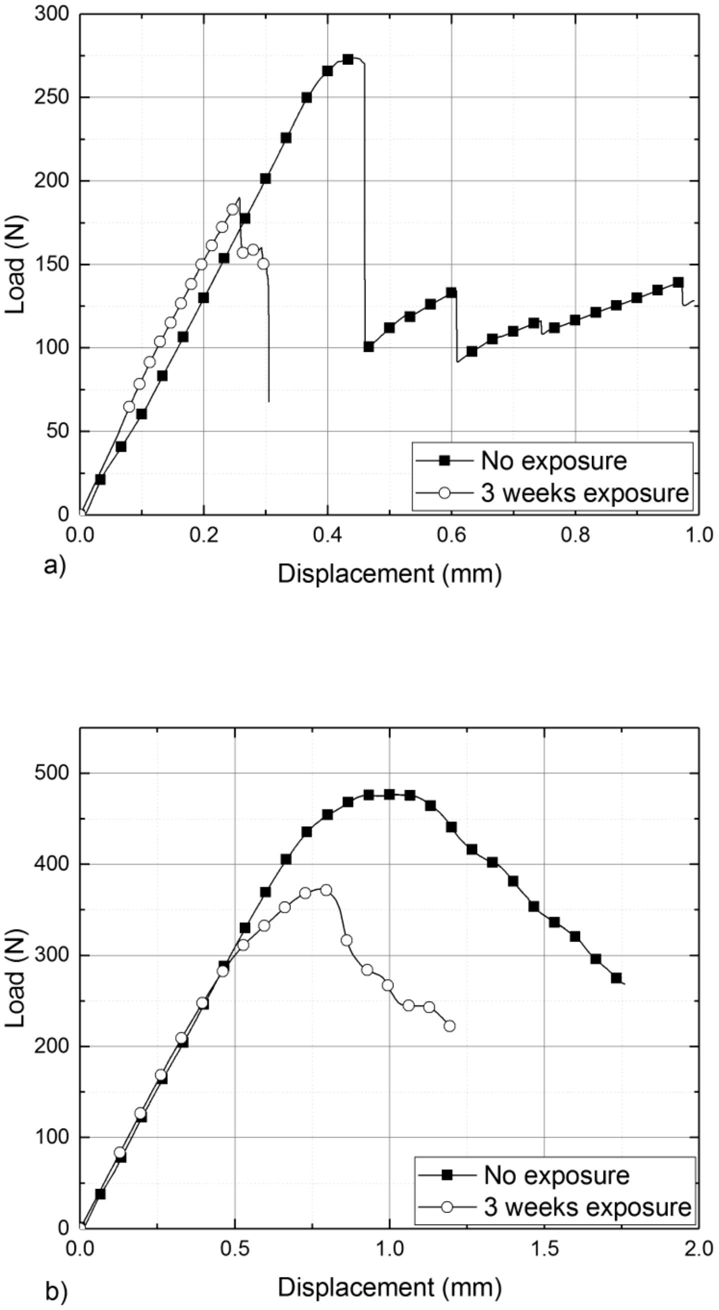

Figure 8.7: Characteristic load-displacement curves for the a) brittle and b) ductile SLB specimens for no exposure and 21 days of exposure (immersed in water at 45°C).

Table 8.3: Summary of the experimental testing for the SLB samples after exposure (immersed in water at 45°C).

Exposure	Specimen	Average Failure load (N)	Coefficient of variation (%)
No exposure	Brittle adhesive (Araldite 2020)	254 ± 21	8.3
21 days - water immersion at 45 °C		188 ± 51 (26% drop)	27.1
No exposure	Ductile adhesive (Araldite 2047-1)	419 ± 45	10.7
21 days - water immersion at 45 °C		355 ± 62 (15% drop)	17.5

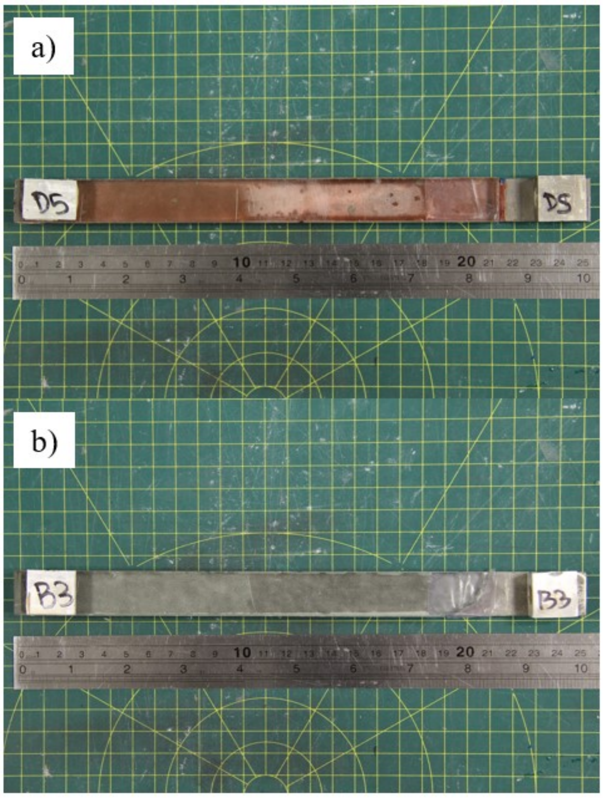

Figure 8.8: Failed interfaces of the SLB specimens for the a) brittle and b) ductile adhesives after 21 days of exposure.

8.4.2 Numerical Analysis

The inverse FE method [33] was again employed to extract the traction-separation laws after 3 weeks of exposure for the two adhesives. Initially, the traction and fracture energy were calibrated in mode I (DCB test), and then the mixed mode properties (SLB test) were also evaluated leading to the calibration of mode II.

Figure 8.9 shows characteristic experimental load-displacement response of the DCB specimens for the two adhesives and the subsequent numerical curve fitting that was achieved after 3 weeks of exposure. The shaded areas define the variation based on minimum and maximum values measured experimentally. The fitted curves represent the typical experimental results. Tables 8.4 and 8.5 summarise the calibrated properties for the two adhesives and compare them with the respective values before exposure.

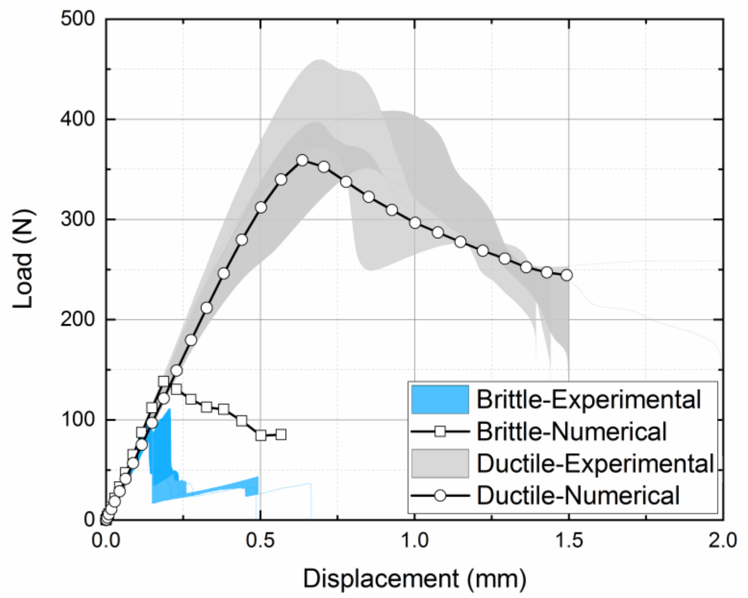

Figure 8.9: Characteristic load/displacement curves for the brittle and ductile DCB samples and numerical curve fitting after 3 weeks of exposure.

Table 8.4: Comparison of calibrated cohesive properties in mode I before and after exposure for the brittle adhesive (Araldite 2020).

Brittle adhesive (Araldite 2020)		
Property	Before exposure	After exposure
E (GPa)	2.57	1.87
t_n^c (MPa)	25	12
δ_n^c (mm)	0.004	0.004
G_n^c(J/m^2)	50	25

Table 8.5: Comparison of calibrated cohesive properties in mode I before and after exposure for the ductile adhesive (Araldite 2047-1).

Ductile adhesive (Araldite 2047-1)		
Property	Before exposure	After exposure
E (GPa)	0.89	0.54
t_n^c (MPa)	10	8
δ_n^c (mm)	0.104	0.075
G_n^c(J/m^2)	520	300

It can be seen that there is a significant drop in both the traction and the fracture energy for both adhesives. The brittle adhesive is more affected, since both the traction and the fracture energy record a 50% reduction, while the ductile adhesive has a small drop of 20% on the traction and about 40% for the fracture energy. It has to be noted, however, that the larger experimental coefficient of variation for the exposed DCB specimens made the agreement between the experimental data and the FE calibration less precise.

Figure 8.10 shows characteristic experimental load-displacement response of the SLB specimens for the two adhesives, and the subsequent numerical curve fitting that was achieved after 3 weeks of exposure. The shaded areas define the variation based on minimum and maximum values measured experimentally. The fitted curves represent the typical experimental results. Tables 8.6 and 8.7 summarise the calibrated properties and compare them with the respective values before exposure.

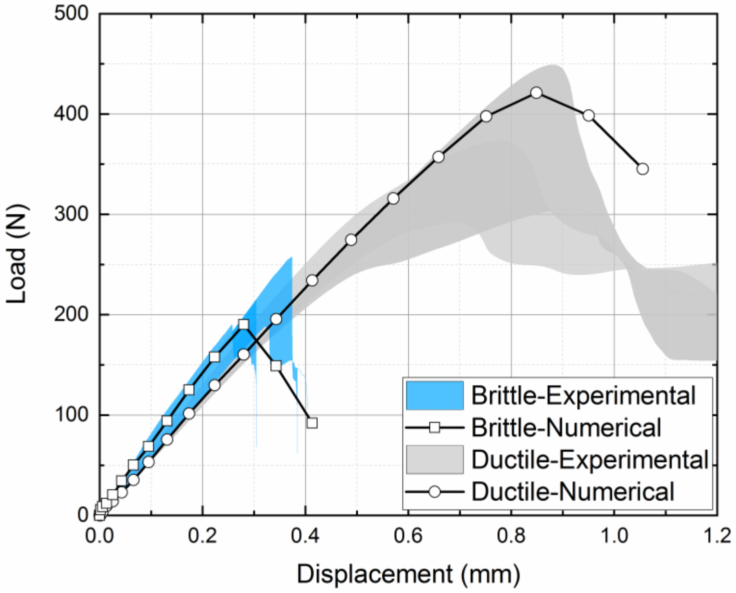

Figure 8.10: Characteristic load/displacement curves for the brittle and ductile SLB samples and numerical curve fitting after 3 weeks of exposure.

Table 8.6: Comparison of calibrated cohesive properties in mode II before and after environmental exposure for three weeks for the brittle adhesive (Araldite 2020).

Brittle adhesive (Araldite 2020)		
Property	Before exposure	After exposure
G (GPa)	0.93	0.67
t_s^c (MPa)	15	6
δ_s^c (mm)	0.013	0.05
G_s^c (J/m^2)	100	150

Table 8.7: Comparison of calibrated cohesive properties in mode II before and after exposure for the ductile adhesive (Araldite 2047-1).

Ductile adhesive (Araldite 2047-1)		
Property	Before exposure	After exposure
G (GPa)	0.31	0.19
t_s^c (MPa)	2	2
δ_s^c (mm)	1.04	0.5
G_s^c (J/m^2)	1040	500

It can be seen that mode II properties also degraded after exposure. The only exception to this trend is the fracture energy of the brittle adhesive, which was slightly higher. This was attributed to the increase of the ductility of the brittle adhesive. Similarly to the DCB samples, the experimental scatter was large, and therefore the calibration was not as accurate as for the unaged specimens.

Based on bulk material testing after environmental exposure, a decrease in strength and fracture toughness for the triangular law parameters was expected. It was also envisaged that the critical displacement value might increase in line with the enhanced ductility of the bulk specimens. This occurred for the data of the brittle adhesive in mode II as seen in Table 8.6, but was not detected for the other tests. In this context it is worth noting that the simple triangular law applied in this study might not be ideal for capturing the interface responses after the environmental degradation, especially considering the increase in the ductility of both adhesives. In addition, other possible combinations of traction/separation parameters capturing the DCB/SLB performance could exist which might better capture the interface response in line with the bulk material degradation. A direct method of measuring the cohesive law response from DCB/SLB tests would improve the confidence in the models and possibly the accuracy of the predictions. However, due to time constraints, this was unfortunately considered outside the scope of this thesis.

8.5 Numerical and experimental analysis of adhesive joints under exposure

This section presents the response and failure behaviour of the double lap shear joints after environmental exposure for 21 days. The load cases and the measurements for each test were identical to the ones described in Chapters 5-7. At least 3 specimens were tested for each load case. In addition, the numerical predictions of the continuum mechanics and CZM modelling approaches are also presented, compared to the experimental data and discussed.

Table 8.8 summarises the failure loads and mechanisms for the joints under uniaxial loading before and after exposure, while Table 8.9 summarises the failure loads and mechanisms for the joints under in-plane and out-of-plane bending loading. It can be seen that in all cases there was a significant strength drop ranging from 29% up to 48%. In addition, it is worth noting that in most cases the failure mechanisms did not change and, failures were mostly initiating at the interfaces. However, in most cases shock effects led to subsequent glass substrate fracture.

Table 8.8: Summary of the uniaxial tests for brittle and ductile adhesive joints before and after exposure.

		Before exposure		After exposure		Percentage change (%)
Load case	Joint type	Failure load (kN)	Failure mechanism	Failure load (kN)	Failure mechanism	
Tension	Brittle	38.0 ± 1.8	Significant damage in the adhesive layer/glass side interface leading to glass failure	21.4 ± 1.5	Significant damage in the adhesive layer/ glass side interface leading to glass failure	-44
	Ductile	46.7 ± 4.5	Cohesive failure	34.2 ± 5.7	Adhesive/cohesive failure	-27
Compression	Brittle	42.4 ± 5.1	Significant damage in the adhesive layer/glass side interface leading to glass failure	29.7 ± 4	Significant damage in the adhesive layer/glass side interface leading to glass failure	-30
	Ductile	46.2 ± 0.6	Cohesive failure	34.6 ± 5.5	Adhesive/cohesive failure	-25

Table 8.9: Summary of the bending tests for brittle and ductile adhesive joints before and after exposure.

		Before exposure		After exposure		Percentage change (%)
Load case	Joint type	Failure load (kN)	Failure mechanism	Failure load (kN)	Failure mechanism	
Out-of-plane bending	Brittle	0.83 ± 0.21	Adhesive / cohesive failure	0.42 ± 0.03	Damage initiation in the adhesive layer leading to glass failure	-49
	Ductile	1.45 ± 0.04	Glass failure	1.05 ± 0.16		-28
In-plane bending	Brittle	14.3 ± 0.7	1) Adhesive / cohesive failure 2) Glass failure preceded by significant damage in the adhesive layer	7.85 ± 1.25	Glass failure	-45
	Ductile	20.0 ± 0.4		13.8 ± 3.5	1) Adhesive/cohesive failure 2) Glass failure preceded by significant damage in the adhesive layer	-31

Figures 8.11, 8.12 and 8.13 show the interfaces of the glass/steel adhesive joints after failure. The stress whitening observed in the ductile adhesive joints before exposure was also evident after exposure. In addition, the moisture ingress ring that was observed in the DCB/SLB samples could also be seen in the double lap shear joints.

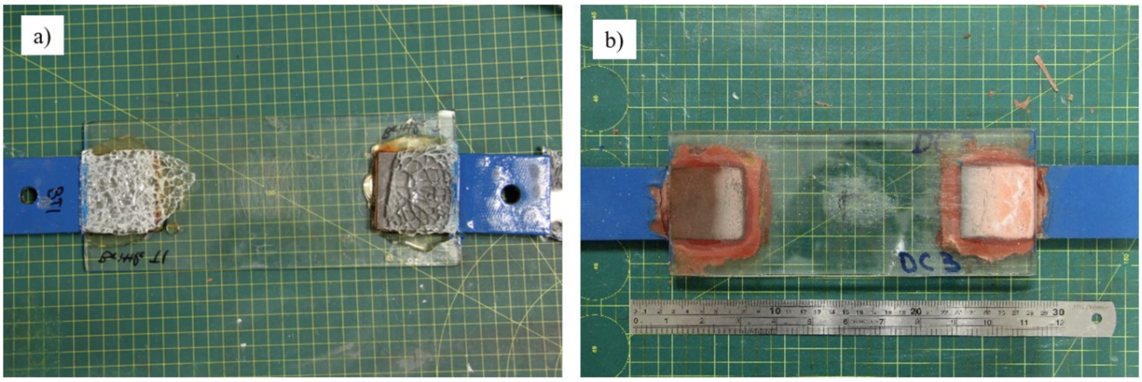

Figure 8.11: Typical glass/steel interfaces after failure for a) brittle and b) ductile joints under uniaxial loading. All bonded overlap regions are 50 mm x 50 mm.

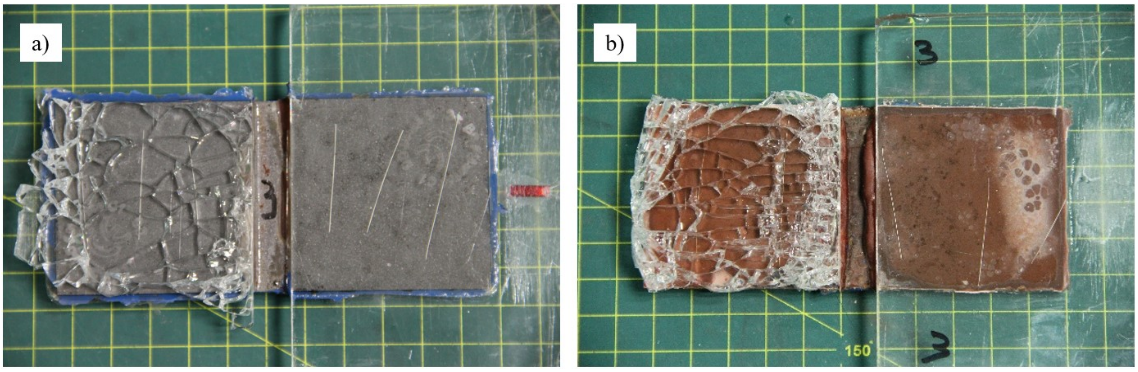

Figure 8.12: Typical glass/steel interfaces after failure for a) brittle and b) ductile joints under out-of-plane bending loading. All bonded overlap regions are 50 mm x 50 mm.

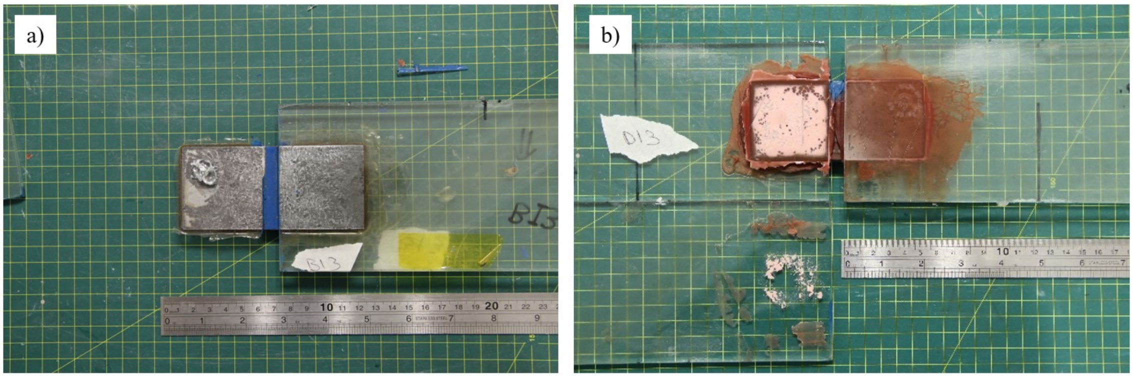

Figure 8.13: Typical glass/steel interfaces after failure for a) brittle and b) ductile joints under in-plane bending loading. All bonded overlap regions are 50 mm x 50 mm.

Numerically, both methodologies previously evaluated for the unaged joints were also used for the joints after exposure. In the continuum mechanics approach, the linear Drucker-Prager model was coupled with the ductile damage model. The bulk properties were taken from Table 8.1, while the hardening curve of the two adhesives was extracted from Figure 8.3. The pressure sensitivity factor and Poisson's ratio were assumed to be the same as for the unaged adhesives. For the CZM approach, the traction-separation laws established in Section 8.4 were used.

Both numerical methodologies were initially evaluated by comparing the numerical predictions to the experimental data in terms of failure loads. Table 8.10 summarises the numerical predictions for the failure loads of the two methods and compares them with the experimental data. This comparison served as an initial evaluation of the two methodologies in order to assess their respective ability to capture the joint degradation following environmental exposure. The highlighted cells indicate which method has a better agreement with the experimental data.

Table 8.10: Evaluation of the numerical predictions of the failure loads, using two different methodologies for brittle and ductile adhesive joints after exposure.

	Failure loads for the brittle adhesive			Failure loads for the ductile adhesive		
	Experimental (kN)	Continuum mechanics (kN)	CZM (kN)	Experimental (kN)	Continuum mechanics (kN)	CZM (kN)
Tension	21.4 ± 1.5	40.5	27.2	34.2 ± 5.7	29.5	29.9
Compression	29.7 ± 4	47.7	27.2	34.6 ± 5.5	29.6	29.9
Out-of-plane bending	0.42 ± 0.03	1.13	0.58	1.05 ± 0.16	1.34	1.33
In-plane bending	8.78 ± 1.41	15.9	10.4	13.83 ± 3.49	14.4	12.6

It can be seen that for the brittle adhesive the continuum mechanics methodology is unable to capture the degradation by simply reducing the bulk properties of the adhesive. It is obvious that the damage takes place mostly in the interface and thus cannot be captured with this approach. In comparison, the CZM approach also slightly overestimates the performance of the joints in all load cases, but the predictions are much closer to the experimental data.

For the case of the ductile adhesive, both methodologies produce similar results. This indicates that the degradation of the joints is mostly due to the degradation of the adhesive, but the interface is not as affected. Therefore, the damage is mostly cohesive and stress whitening is observed indicating that the adhesive yields and develops a plastic zone. As a result, in the case of the ductile adhesive joints both methodologies are able to capture the degradation. However, given that the CZM approach yielded consistent results for both adhesives, it will be used for the remainder of the numerical study.

Figure 8.14 shows the strain response in the midpoint of the joints for the tensile and compressive tests as measured experimentally and predicted numerically (using the CZM methodology). The evaluation of the strain response is based on the strain gauge measurements and the FE predictions at the midpoints of the joints.

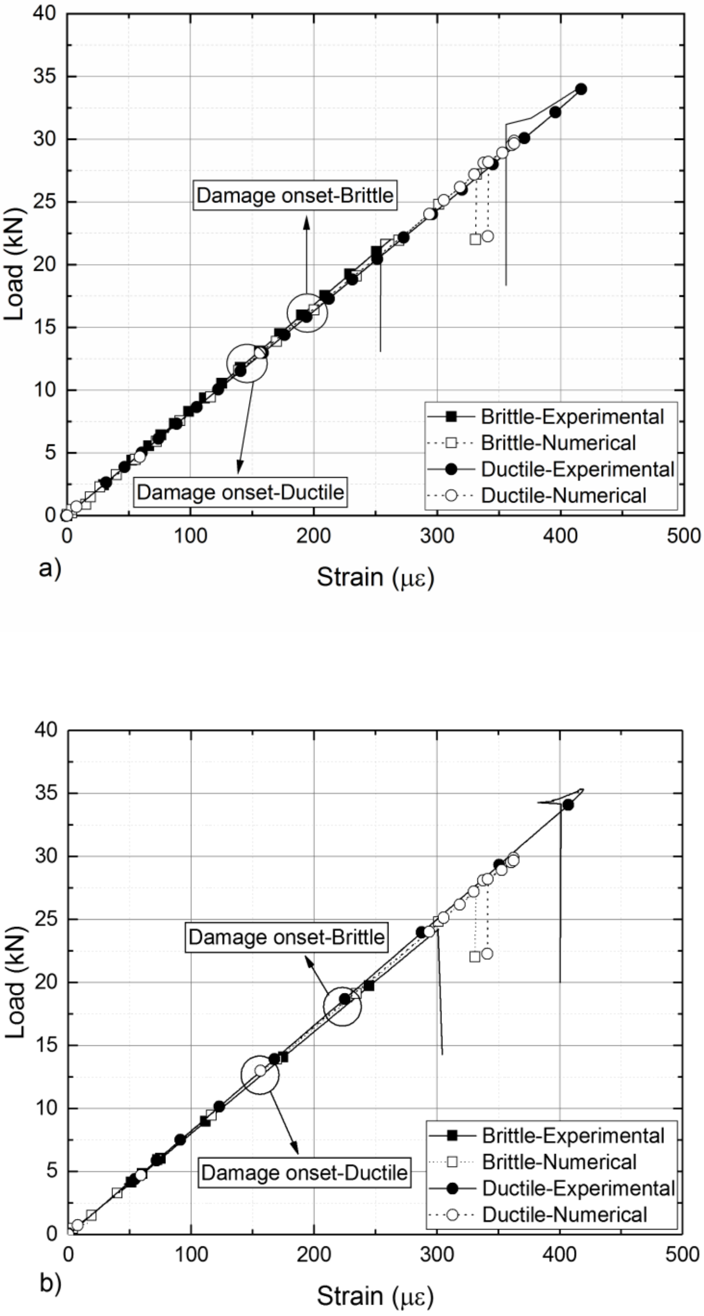

Figure 8.14: Strain response in the midpoints of the brittle and ductile adhesive joints under uniaxial a) tensile and b) compressive loading.

It can be seen that in terms of strain response the experimental and numerical methods have very good agreement. However, it is worth noting that for the brittle adhesive the numerical methods overestimate the failure load by 24% in tension and slightly underestimate in compression by 8%. On the other hand, for the ductile adhesive, the numerical methods underestimate the failure loads in both tension and compression by about 14%. Tables 8.11 and 8.12 show the predicted failure loads and mechanisms for the tensile and compressive tests and compares them with the experimental observations. In most cases the predictions of the cohesive laws were within the standard deviations of the experimental observations. Here, the standard deviations for the experimental testing were significantly larger compared to the unaged joints.

In terms of prediction accuracy, it is noted that the CZM model predicts the amount of interface degradation based on the DCB and SLB coupon geometries. The level of moisture ingress, however, is related to the exposed bonded area. It is therefore important to note that the surface areas for the moisture ingress are different when comparing the DCB/SLB specimens and the double lap shear joints. Additionally, excess adhesive material might more effectively seal surfaces, hence direct comparison is difficult. Nevertheless, clear similarities in terms of stress whitening and area reduction due to moisture ingress are found for the ductile adhesive and this explains the better agreement with the CZM approach as failure load reduction is controlled by interface moisture diffusion rather than bulk material degradation.

Table 8.11: Summary of the experimental and numerical predictions of the failure load/mechanism for brittle and ductile adhesive joints under tensile loading after exposure.

	Tension			
	Experimental		Numerical (CZM)	
Configuration	Failure load (kN)	Failure mechanism	Failure load (kN)	Failure mechanism
Brittle Adhesive (Araldite 2020)	21.4 ± 1.5	Significant damage in the adhesive layer/glass side interface leading to glass failure	27.2	Interface failure on glass side
Ductile Adhesive (Araldite 2047-1)	34.2 ± 5.7	Cohesive failure	29.9	

Table 8.12: Summary of the experimental and numerical predictions of the failure load/mechanism for brittle and ductile adhesive joints under compressive loading after exposure.

	Compression			
	Experimental		Numerical (CZM)	
Configuration	Failure load (kN)	Failure mechanism	Failure load (kN)	Failure mechanism
Brittle Adhesive (Araldite 2020)	29.7 ± 4	Significant damage in the adhesive layer/glass side interface leading to glass failure	27.2	Interface failure on glass side
Ductile Adhesive (Araldite 2047-1)	34.6 ± 5.5	Cohesive failure	29.9	

Figure 8.15 shows the strain response of the joints under out-of-plane and in-plane bending. The strains were evaluated in the areas of stress concentrations of the glass for both joint types (in a similar way as the measurements in Chapters 5-7).

Once again the experimental and numerical CZM methods have good agreement in terms of the stiffness response of the joints. Experimentally, for the in-plane bending loading, gradual damage development in the adhesive layers led to uneven loadings on the four glass substrates which explains the change of stiffness towards the end of the test. The FE model could not capture the uneven loading conditions.

In terms of failure load, the FE predictions overestimated the performance of the joints under out-of-plane loading, by 32% for the brittle adhesive and 23% for the ductile adhesive. For the in-plane bending loading condition, the FE predictions overestimated the performance of the brittle adhesive joints by 17% and underestimated the performance of the ductile adhesive joints by 9%. Tables 8.13 and 8.14 summarise the predicted failure loads and mechanisms under out-of-plane and in-plane bending and compare them to the experimental observations.

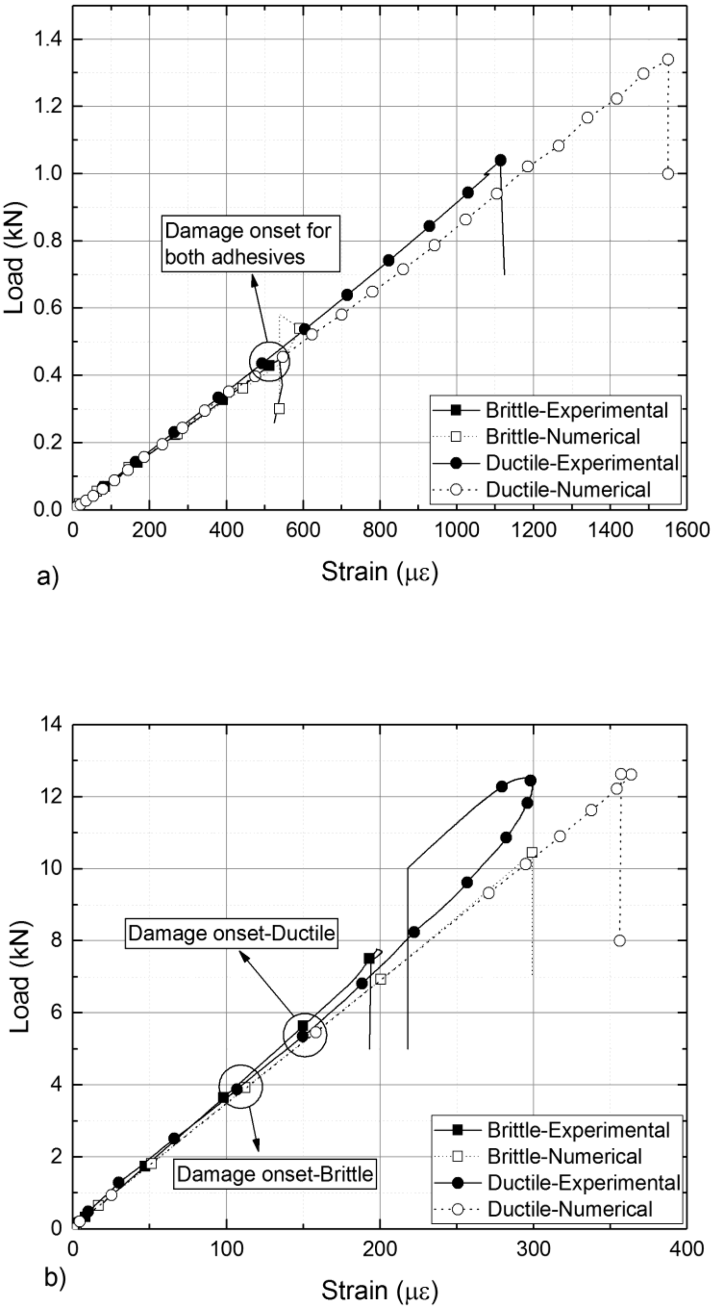

Figure 8.15: Strain response in the areas of stress concentrations of the brittle and ductile adhesive joints under a) out-of-plane and b) in-plane bending loading.

Table 8.13: Summary of the experimental and numerical predictions of the failure load/mechanism for brittle and ductile adhesive joints under out-of-plane loading after exposure.

	Out-of-plane bending			
	Experimental		Numerical (CZM)	
Configuration	Failure load (kN)	Failure mechanism	Failure load (kN)	Failure mechanism
Brittle Adhesive (Araldite 2020)	0.42 ± 0.03	Significant damage in the adhesive layer/glass side interface leading to glass failure	0.58	Interface failure on glass side
Ductile Adhesive (Araldite 2047-1)	1.05 ± 0.16		1.33	

Table 8.14: Summary of the experimental and numerical predictions of the failure load/mechanism for brittle and ductile adhesive joints under in-plane loading after exposure.

	In-plane bending			
	Experimental		Numerical (CZM)	
Configuration	Failure load (kN)	Failure mechanism	Failure load (kN)	Failure mechanism
Brittle Adhesive (Araldite 2020)	8.78 ± 1.41	Significant damage in the adhesive layer/glass side interface leading to glass failure	10.4	Interface failure on glass side
Ductile Adhesive (Araldite 2047-1)	13.83 ± 3.49	Adhesive/cohesive failure	12.6	

8.6 Summary

Chapter 8 described a study on the environmental exposure of glass/steel adhesive joints. The conditions of the exposure were based on a European guideline for sealants in buildings, and the degradation was reported for the bulk properties, the glass/steel interfaces and finally the glass/steel double lap shear joints. Experimentally, tensile tests were performed on the brittle and ductile adhesives for the extraction of the bulk properties, DCB and SLB tests were performed for both adhesives for the characterisation of the interfaces, and the double lap shear joints were tested in four load cases based on the designs described in previous chapters.

A significant drop was observed in the bulk properties of the two adhesives, with the elastic modulus and yield and failure stresses reducing significantly. In contrast, both adhesives increased their ductility. The maximum load recorded for the DCB tests gradually decreased as the exposure time increased, while a similar trend was also observed for the SLB samples. Similar strength drops (ranging from 27-49%) were recorded for the double lap shear joints under the four different load cases. Interestingly, even though the bulk properties of the ductile adhesive experienced a higher degradation (in terms of stiffness and strength), the reduction in the maximum loads for the DCB/SLB and the double lap shear joints are smaller compared to the brittle adhesive.

The experimental tests resulted in the extraction of cohesive laws for the interfaces after exposure. The cohesive laws were extracted considering the degradation on the DCB/SLB specimens and adopting an inverse method as the one described in Chapter 4. These cohesive laws were later used as numerical inputs for the double lap shear joints to compare the effects of interface degradation with the experimental observations.

The continuum mechanics methodology developed in Chapter 6 was also used and compared with both the experimental data and the CZM approach. It was observed that the continuum mechanics approach, based on a bulk property deterioration, could not capture the degradation of the brittle joints (when the damage was adhesive) predicting very high failure loads. When however, the damage of the joints was mostly cohesive (as for the ductile joints) the continuum mechanics approach resulted in good agreement with the experimental data. On the other hand, the CZM methodology was not affected by the mode of failure and produced consistent predictions for both adhesives. Based on these observations, the CZM methodology was considered more versatile for predicting the degradation in the adhesive joints.

It is worth noting however, that even with the CZM methodology the accuracy of the predictions is not as high as with the cohesive laws established for the unaged joints. For the brittle and ductile adhesive joints the FE predictions overestimated/underestimated the failure loads by a maximum of 32% and 23% respectively. However, it is worth noting, that the DCB/SLB tests had large standard deviations which made the calibration of the cohesive laws less accurate. Large standard deviations were also observed in the double lap shear joints.

Chapter 9 **Concluding remarks**

9.1 Introduction and structure

A wide range of issues relating to the experimental and numerical analysis of bolted and adhesive glass/steel joints was presented in this thesis. Benchmark designs in four different load cases were introduced and tested experimentally for bolted and brittle/ductile adhesive joints. Strain gauges and high-speed cameras were used for the monitoring of the joint performance and characteristics during testing. Continuum mechanics finite element models were developed taking into consideration the pressure-sensitive plasticity that polymers typically display. In addition, a cohesive zone modelling approach was also developed for the prediction of damage initiation and propagation in the adhesive layers. For both numerical approaches extensive experimental testing was required in order to establish the constitutive and failure models.

In addition, a numerical tool based on the continuum mechanics approach was developed for the optimal selection of adhesives, which identified optimum combinations of adhesive strength/ductility for the given adhesive joint design. The optimum selection was validated experimentally leading to a significant strength increase in every load case. Finally, the effect of high humidity/temperature on adhesive joints was assessed experimentally by evaluating the degradation on the bulk properties of the adhesives and the glass/steel interfaces. Both the continuum mechanics and CZM approaches were used to simulate the effect of elevated temperatures and humidity, but it was concluded that only the CZM approach was able to capture the strength reduction due to the combined degradation of the bulk properties of the adhesives and the interface bonding.

This chapter discusses the most important results, summarises the main findings of the thesis and finally highlights the limitations of the thesis and suggests areas of future research on the topic. Figure 9.1 provides a graphical abstract of the project highlighting the key activities undertaken.

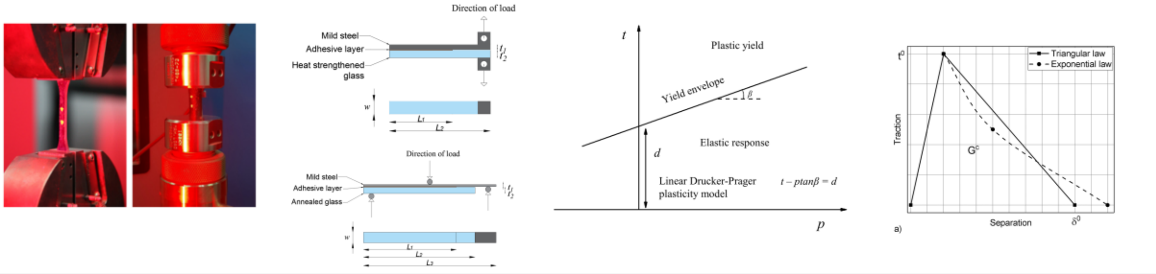

Adhesive and interface characterisation that led to the development of a) continuum mechanics modelling methodology by coupling Drucker-Prager yield model and Ductile damage failure model and b) a cohesive zone modelling approach

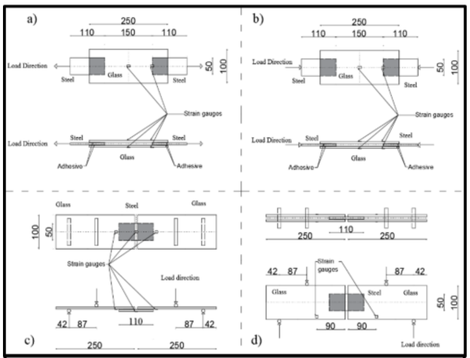

Benchmark designs

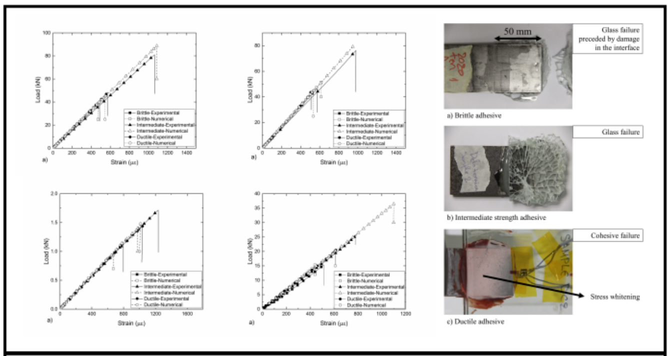

Response and failure of glass/steel adhesive joints

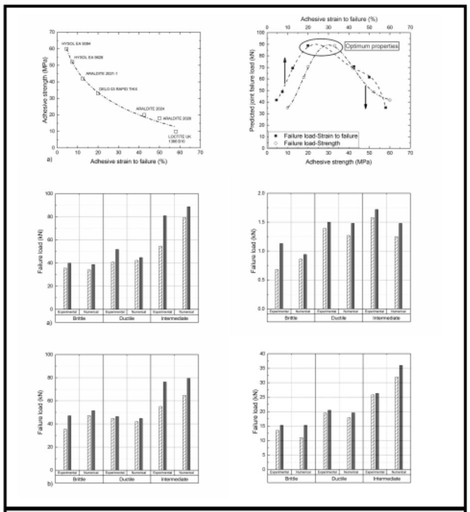

Development of numerical tool for the selection of optimum mechanical properties and experimental validation

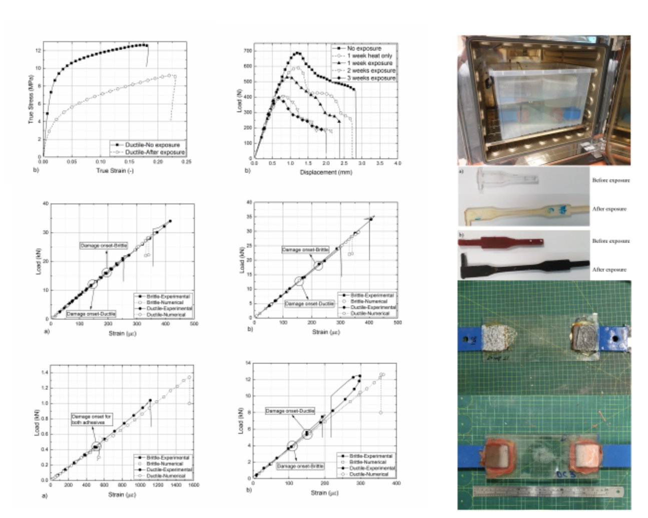

Response and failure of glass/steel adhesive joints after environmental exposure

Figure 9.1: Graphical abstract of the PhD project.

9.2 Discussion

9.2.1 Experimental/numerical analyses of bolted/adhesive joints

The experimental comparison of the benchmark designs of bolted and brittle/ductile adhesive joints revealed that adhesive joints were significantly stronger for quasi-static loading under ideal laboratory conditions. In addition, adhesive joints in most cases avoided catastrophic glass fracture and displayed adhesive/cohesive modes of failure. Especially the ductile adhesive ensured a gradual damage propagation with a large plastic zone developing that in most cases was extending across most of the adhesive layer. The presence of the plastic zone was visualised experimentally by the presence of significant stress whitening.

The strength increase achieved with adhesive joints under uniaxial loading compared to bolted joints was 337% and 370% for the brittle and ductile adhesives, respectively. For the case of out-of-plane bending, the strength increase is not as significant as the ductile adhesive joints are about 21% stronger compared to bolted joints but the brittle adhesive joints fail at slightly lower loads.

An interesting trend was observed when the brittle and ductile adhesive joints were compared. Even though the brittle adhesive has about 4 times higher strength (in terms of bulk properties), it led to weaker adhesive joints. More specifically, under uniaxial loading the ductile adhesive joints were 7-23% stronger, under out-of-plane loading 75% stronger and finally under in-plane loading 40% stronger. The failure mechanisms of the ductile adhesive joints were more favourable as mostly cohesive damage was observed, as opposed to a combination of adhesive and glass failure mostly witnessed for the brittle adhesive joints.

This trend can be explained by the development of a much larger plastic zone for the ductile adhesive within the adhesively bonded region. This led to a larger area resisting the loading, redistribution of the stress concentrations in the corners of the adhesive layers and as a result stronger joints. However, important questions remained regarding: 1) the effect of strength/ductility on the performance of the joint and 2) the sensitivity of these parameters considering the geometry of the joint. These questions were addressed via numerical modelling approaches.

Numerically, FE models were developed for simulating the response of glass adhesive joints utilising two different approaches. The first approach was based on continuum mechanics, considered the complex stress state of the adhesive layer and coupled a pressure sensitive yield criterion (Linear Drucker-Prager model) with a damage/failure model (ductile damage model). The second approach was based on cohesive zone modelling, by introducing a triangular traction-separation law. Both methods showed good agreement with the experimental data for room temperature testing and accurately predicted the failure loads and mechanisms observed.

For both methodologies, different characterisation tests were required. Before selecting a numerical methodology it is important to assess the ability to perform these characterisation tests. For the continuum mechanics approach, characterisation tests were conducted for the extraction of the bulk properties of the adhesives in two stress states (uniaxial tension and compression). These tests led to the calibration of the pressure sensitivity factor, the extraction of the adhesive hardening curve and the critical fracture strain. For the cohesive zone modelling approach, standardised methods for the extraction of the cohesive properties in modes I and II (DCB and SLB) were modified. An in-house thermal strengthening methodology had to be developed for small glass coupons in order to avoid premature glass failure during the interface characterisation testing. The in-house thermal strengthening methodology led to a 75% strength increase compared to typical annealed glass.

9.2.2 Development of a numerical tool for optimum adhesive selection

The experimental analysis of the glass adhesive joints revealed that the lower strength, but ductile adhesive (in terms of bulk properties) outperformed the stronger, stiffer but more brittle adhesive in every load case (in terms of joint strength). Numerical analysis of the adhesive layers during damage initiation and propagation revealed that the size of the plastic zone played a crucial role in the performance of the joint. This conclusion was investigated further by performing a broad screening of adhesives suitable for glass/steel adhesive connections based on their mechanical properties. The screening revealed that with increasing strength, the stiffness increases and the strain-to-failure and fracture toughness decrease.

Based on these observations, and assuming linear elastic-perfectly plastic responses, these adhesives were used to predict joint strength under tensile loading. The numerical analyses revealed that there is an optimum combination of adhesive properties for the given design geometry that is expected to lead to significant strength increases in every load case. Accordingly, the optimum selected adhesive was characterised and tested experimentally in similar joints.

Under tensile loading the strength increase recorded with the optimum adhesive was 86% and 51% compared to the brittle and ductile adhesives, respectively. Under compressive loading, buckling effects were observed and therefore the numerical analysis was also adjusted to consider buckling. An initial imperfection was added to the model, and this led to joint buckling in the numerical analysis and very good agreement was achieved between the experimental and numerical data. Even with buckling, however, the optimum adhesive led to a 54% and 43% strength increase, respectively, compared to the brittle and ductile adhesives.

Under out-of-plane bending loading, the strength increase compared to the brittle adhesive was 99%. The comparison with the ductile adhesive revealed a smaller strength increase (14%) but this was justified by the fact that for this load case the damage for these two types of joints was introduced in the glass substrates and not in the adhesive layers. Finally, under in-plane bending loading, the joints manufactured with the optimum adhesive failed prematurely in the glass substrate due to the stress concentrations in the load introduction points, which could not be captured numerically. Even with the premature failures however, the strength increase recorded was significant (81% and 30% compared to the brittle and ductile adhesive, respectively).

The conclusions were found to be dependent on the geometry tested. Bonded areas of different size were analysed numerically. It was shown that the size of the bonded area is strongly related to the effect of the strength or the ductility of the adhesive. For smaller bonded areas the strength of the adhesive is more important, given that there is not enough space for a large plastic zone development. As a result, for smaller bonded areas the failure load of the joints is mostly governed by the stress concentrations in the corners of the adhesive layer and therefore the strength of the adhesive is more crucial. However, as the size of the bonded area increases, the adhesive has a larger area to develop a plastic zone and therefore the effect of ductility starts to become more important.

It is important to highlight that the experimental test campaign conducted confirmed the parametric study and further validated the capability of the nonlinear FE analyses for joint design and optimisation. It should also be noted that a similar approach can be utilized as an initial screening test for any type of joint geometry and loading condition.

9.2.3 Environmental exposure

High temperature/humidity conditions were used for the exposure study. The effect of the environmental exposure focused on two different areas: 1) the degradation of the bulk properties of the brittle and the ductile adhesives was considered by repeating tests on tensile coupons and 2) the effect on the glass/steel interfaces was also studied by repeating the DCB/SLB tests after exposure. These input data were used to predict the degradation of the double lap shear joints for the four load cases that were described previously.

The tensile tests on the dogbone specimens revealed that the strength and stiffness of both adhesives dropped while the ductility increased. More specifically, the Young's modulus dropped 27% and 39%, while the strength dropped 8% and 30% for the brittle and ductile adhesives, respectively. In addition, the ductility of both adhesives increased by 41% and 46% respectively. A similar trend (strength reduction/increase in ductility) has been reported by other authors as well [82, 106, 148].

It can be seen that the exposure to high temperature/humidity affected the ductile adhesive more in terms of bulk properties. However, when considering the interface tests this trend was reversed with the brittle adhesive retaining 45% and 74% of its initial strength and the ductile adhesive retaining 61% and 85% of its initial strength for the DCB and SLB tests, respectively. This shows that the interface degradation is not necessarily related to the degradation of the mechanical properties of the adhesives.

Double lap shear joints were also exposed to the same conditions and tested under the four load cases described in the previous chapters. Significant load reductions were recorded for both adhesive joint types ranging from 29% to 48%. In terms of failure mechanisms, it is interesting to note that all the brittle adhesive joints failed in the glass substrate. This is related to the degradation of the adhesive layers however, since in Chapters 5-7 it was shown that the strength of glass is not reached at such relatively low loads. Damage initiation in the adhesive layer however, can lead to instant delamination, unbalance the joints and cause shock effects that lead to subsequent glass fracture.

It is worth noting that even after environmental exposure, adhesive joints failed at significantly higher loads under uniaxial loading compared to bolted joints. More specifically, the brittle and ductile adhesive failed at 200% and 250% higher loads compared to the reference unaged bolted joints. However, this trend changed under out-of-plane bending loading. There bolted joints outperformed (in terms of failure load) both types of adhesive joints. Especially brittle adhesive joints failed at about 3 times lower loads compared to bolted joints. It is worth noting, however, that this was the only load case in which bolted joints displayed a comparable performance with adhesive joints even before exposure.

In terms of numerical methodology, both the continuum mechanics and CZM approaches were implemented and evaluated based on their ability to capture the degradation of the adhesive joints. As discussed in the literature review both methodologies have been examined in the past. Continuum mechanics approaches have shown potential to capture the degradation when the damage is cohesive, while CZM was preferred when the damage was adhesive.

The continuum mechanics approach was established by considering the degradation of the bulk properties of the two adhesives and assuming the same values for pressure sensitivity as in the unaged adhesives. For the CZM approach the degraded traction-separation laws were extracted from the DCB/ENF tests.

It was shown that the CZM approach resulted in good agreement with the experimental data for both adhesives. However, larger standard deviations were observed for both the characterisation and the double lap joints tests and therefore the agreement was not as strong as for the case of the unaged joints.

Regarding the continuum mechanics approach, the results showed good agreement with the CZM and the experimental data for the ductile adhesive when the damage was mostly cohesive. However, this approach failed to capture the degradation of the brittle joints when the damage was mostly adhesive. It was therefore concluded that it is safer to utilise a CZM approach when the environmental degradation of adhesive joints is considered numerically since this approach can capture both the degradation of the bulk properties and the interfaces. A continuum mechanics approach fails to account for the interface damage and is therefore only accurate when the damage is cohesive.

9.3 Conclusions

The main aim of this research project was to understand the load response and failure behaviour of glass adhesive joints by analysing their performance under different loading conditions both experimentally and numerically. The objectives set in Chapter 1 were all addressed by building a coherent, interconnected narrative throughout this thesis. The main conclusions of the research are as follows:

- Adhesive joints outperform (in terms of failure loads) bolted joints under quasi-static loading in different load cases in ideal laboratory conditions. All three adhesive types tested were significantly stronger, especially under uniaxial loading.
- Lower strength ductile adhesives (in terms of bulk properties) outperform (in terms of joint failure loads) stronger and stiffer adhesives by developing large plastic zones that redistribute stresses in the areas of stress concentrations.
- For given designs, optimum combinations of strength/ductility can be identified and lead to significant joint strength improvements and optimisation. FE methodologies can be used for the parametric studies required to lead to these optimised mechanical properties.
- Under ideal laboratory conditions, both continuum mechanics and CZM methodologies can be used for the simulation of damage initiation and propagation. Each methodology has its merits, but it is important to make a selection based on the ability to perform the material/interface characterisation tests.
- Elevated temperatures and humidity have a degrading effect on both the bulk properties of the adhesives and the interfaces. However, different adhesives experience different types of degradation. For example, the brittle adhesive was damaged more at the interface and less in the bulk, while the opposite trend was observed for the ductile adhesive. Therefore, it is

important to perform both types of tests (bulk and interface) when environmental exposure is considered for adhesive joints.

- Numerically, the degradation was simulated with two ways. First, by considering the reduction of the bulk properties and second, by considering the degradation of the interface. It was shown that the CZM approach was able to capture the effect of the environmental exposure for both adhesives, regardless of the mode of failure. On the other hand, the continuum mechanics approach was only able to capture the damage for the ductile adhesive (where the damage was cohesive), but not the brittle one (where the damage was adhesive at the glass interface). This was explained by the fact that the brittle adhesive bonding degraded more at the interface. It can therefore be concluded that it is safer to model environmental exposure of adhesive joints with CZM approaches which can consider all modes of failure more accurately.

9.4 Future work

The research presented has led to an improved understanding of the response and failure behaviour of glass/steel adhesive connections. However, the study had certain limitations which could form the basis of an extended study on the use of glass adhesive joints:

- Examine the effects of different geometries and sizes of the hybrid joints. While a numerical parametric study was used to evaluate the effect of the bonded area, it would be useful to develop an experimental/numerical campaign that examines different geometries/sizes and fillet shapes. For instance, thinner/thicker glass substrates can be used to switch the failure more to the interfaces or to the glass substrates and study those in more detail.
- The adhesive thickness effect was not studied in this project. However, adhesive thickness plays a very important role in the performance of the joints. Thicker bondlines are more susceptible to internal flaws and voids [149]. At the same time, however, thicker bondlines might have the capacity to develop a larger plastic zone before damage and failure.
- Surface treatment plays an important role in the quality of the adhesion. This study did not consider different surface treatments for the substrates. In many instances, however, the failure initiated on the glass/adhesive interface indicating that a study on different surface treatments and/or the use of primers could improve the strength of the joints and change the failure mechanisms. The modified DCB/SLB tests can be utilised as a cost-effective solution to evaluate the effectiveness of the interface treatments.
- The study was limited to quasi-static loadings. However, higher strain rates should also be studied. Adhesives are known to be affected by viscoelasticity and therefore the strain rate will play an important role in the response of the joints. As a result, different models that also consider viscoelasticity would need to be developed and coupled with the ones

presented in this study. In addition, it would be interesting to see the effect of high strain rates on cohesive laws.

- Effects of thermal mismatch for hybrid joints were minimised in this study by selecting room temperature curing adhesive systems. Curing at elevated temperatures, however, could lead to residual stresses in both steel and glass substrates affecting the adhesive layer.
- The cohesive shapes of the traction-separation laws were assumed to be triangular. However, more precise measurements could be employed using the direct method.
- While the environmental exposure effect on the bulk adhesives, the hybrid interfaces and the joints was studied, there are still more parameters to be considered. Since glass substrates are used, UV radiation might play an important role and needs to be researched more thoroughly. In addition, higher and lower temperature effects along with longer exposure periods should be considered.

Appendix A

Analytical solutions for the stress distribution of single lap adhesive joints

A.1 Volksersen's analysis

The analytical solution of Volkersen for the determination of the shear stress in a single lap joint was provided in equation 2.2. The parameters used in equation 2.2 are related to the applied load P, the width of the joint b, the overlap length l, the relative position on the adhesive layer X and parameter w which is related to the thickness and the elastic and shear moduli of the substrates and the adhesive.

More specifically, w is related to parameter ψ which is the ratio of the thickness of the top to the bottom substrate and parameter φ which correlates the shear modulus G of the adhesive to the overlap length, the elastic modulus of the substrates E and the thickness of the substrates and the adhesive. The origin of the longitudinal coordinate x is the middle of the overlap and therefore X can only take values between -0.5 and 0.5. The aforementioned parameters are defined as

$$w^2 = (1+\psi)\varphi\,, \tag{A.1}$$

$$\psi = \frac{t_t}{t_b}, \tag{A.2}$$

$$\varphi = \frac{Gl^2}{Et_t t_a}, \tag{A.3}$$

$$X = \frac{x}{l}. \tag{A.4}$$

A.2 Goland and Reissner's analysis

Goland and Reissner provided analytical solutions for the distribution of shear (eq. 2.4) and peel stresses (eq. 2.5) along an adhesive layer in a single lap adhesive joint and correlated them to the bending moment factor k which can be calculated as shown in equation A.5. The bending factor depends on the initial geometry and characteristics (via parameters u_2 and c) of the adherends and the adhesive as follows

$$k = \frac{\cosh(u_2 c)}{\cosh(u_2 c) + 2\sqrt{2}\sinh(u_2 c)}. \tag{A.5}$$

The term u_2 (eq. A.6) can be calculated as

$$u_2 = \sqrt{\frac{3(1-v^2)}{2}}\frac{1}{t}\sqrt{\frac{\bar{P}}{tE}}, \tag{A.6}$$

where E is the Young's modulus, v is Poisson's ratio and t the thickness of the adherends while c is half of the overlap length and $\bar{P}$ the load per unit width.

The parameters $\beta, \lambda, \gamma, R_1, R_2, \Delta$ found in equations 2.4 and 2.5 are related to the stiffness, the thickness of the adherends and the adhesive and the geometry of the joint, E and t are the elastic modulus and thickness of the adherends, E_a, G_a and t_a are the elastic, shear modulus and thickness of the adhesive respectively, k' is the transverse force factor and is related to the loading conditions and the geometry, and finally x is the longitudinal coordinate and its origin is considered to be in the middle of the overlap. Equations A.8—A.14 define these parameters as

$$\beta = \sqrt{8\frac{G_a t}{E t_a}}, \tag{A.8}$$

$$\lambda = \gamma\frac{c}{t}, \tag{A.9}$$

$$\gamma^4 = 6\frac{E_a t}{E t_a}, \tag{A.10}$$

$$k' = \frac{kc}{t}\sqrt{3(1-v^2)\frac{\bar{P}}{tE}}, \tag{A.11}$$

$$R_1 = \sinh(\lambda)\cos(\lambda) + \cosh(\lambda)\sin(\lambda), \tag{A.12}$$

$$R_2 = \sinh(\lambda)\cos(\lambda) - \cosh(\lambda)\sin(\lambda), \tag{A.13}$$

$$\Delta = \frac{1}{2}(\sin(2\lambda) + \sinh(2\lambda)). \tag{A.14}$$

A.3 Hart-Smith's analysis

Hart-Smith provided analytical solutions for the distribution of shear (eq. 2.6) and peel stresses (eq. 2.7) along an adhesive layer in a single lap adhesive joint. The authors correlated the shear and peel stresses to the bending moment M of the adherend. The bending moment can be calculated in equation A.15 and depends on the loading conditions and geometry of the joint while the parameter ξ (eq. A.16) depends on the load per unit width and the bending stiffness (eq. A.17) of the adherends as follows

$$M = \bar{P}\left(\frac{t + t_a}{2}\right)\frac{1}{1 + \xi c + \left(\frac{\xi^2 c^2}{6}\right)}, \tag{A.15}$$

$$\xi^2 = \frac{\bar{P}}{K}, \tag{A.16}$$

$$K = \frac{Et^3}{12(1 - v^2)}. \tag{A.17}$$

Finally, the parameters $\lambda', A_2, C_2, \chi, A, B$ found in equations 2.6 and 2.7 are related to the loading conditions, the geometry and the mechanical characteristics of the adherends and adhesive and are defined in equations A.18-A.23 as

$$\lambda' = \sqrt{\left[\frac{1 + 3(1 - v^2)}{4}\right]\frac{2G_a}{t_a Et}}, \tag{A.18}$$

$$A_2 = \frac{G_a}{t_a Et}\left[\bar{P} + \frac{6(1 - v^2)M}{t}\right]\frac{1}{2\lambda' \sinh(2\lambda' c)}, \tag{A.19}$$

$$C_2 = \frac{1}{2c}\left[\bar{P} - 2\frac{A_2}{2\lambda'}\sinh(2\lambda' c)\right], \tag{A.20}$$

$$\chi^4 = \frac{E_\alpha}{2Kt_a}, \tag{A.21}$$

$$A = -\frac{E_a M[\sin(\chi c) - \cos(\chi c)]}{t_a D\chi^2 e^{(\chi c)}}, \tag{A.22}$$

$$B = \frac{E_a M[\sin(\chi c) + \cos(\chi c)]}{t_a D\chi^2 e^{(\chi c)}}. \tag{A.23}$$

In equations A.18−A.23 E, G, v, t are the elastic modulus, the shear modulus, Poisson's ratio and the thickness of the substrates while E_a, G_a and t_a are the elastic modulus, the shear modulus and the thickness of the adhesive. Finally, c is half of the overlap length and x is the origin of the longitudinal coordinate and is found in the midpoint of the adhesive overlap.

Bibliography

[1] Achintha M., 5 - Sustainability of glass in construction, in: Khatib J.M. (Ed.), Sustainability of Construction Materials (Second Edition), Woodhead Publishing, 2016, pp. 79-104.

[2] Chen C., Habert G., Bouzidi Y., Jullien A., Environmental impact of cement production: detail of the different processes and cement plant variability evaluation, Journal of Cleaner Production, 18 (2010) 478-85.

[3] Hammond G.P., Jones C.I., Embodied energy and carbon in construction materials, Proceedings of the Institution of Civil Engineers - Energy, 161 (2008) 87-98.

[4] Parker J., Engineering The Shard, London: tallest building in western Europe, Proceedings of the Institution of Civil Engineers - Civil Engineering, 166 (2013) 66-73.

[5] Snijder A.H., Nijsse R., Louter C., The glass truss bridge, Heron, 63 (2018).

[6] IStructE, Structural use of glass in buildings, Institution of Structural Engineers, SETO, London, 1999.

[7] Adams R.D., Comyn J., Wake W.C., Structural adhesive joints in engineering, 2nd ed., Chapman & Hall, London, 1997.

[8] Haldimann M., Luible A., Overend M., Structural use of glass, International Association for Bridge and Structural Engineering, Zürich, Switzerland, 2008.

[9] Schittich C., Staib G., Balkow D., Schuler M., W. S., Glass construction manual, 2nd rev. and expanded ed., Birkhäuser, Basel, 2007.

[10] Weller B., Härth K., Tasche S., Unnewehr S., Glass in Building-Principles, Applications, Examples, Birkhäuser, 2009.

[11] ISO, ISO 572-1:2012 Glass in building-Basic soda lime silicate glass products, Part 1: Definitions and general physical and mechanical properties, British Standards International, London, 2012.

[12] Button D., Pye B., Glass in building : a guide to modern architectural glass performance : Pilkington, Butterworth Architecture, Oxford, 1993.

[13] IStructE, Structural use of glass in buildings, Second edition. ed., Institution of Structural Engineers, SETO, London, 2014.

[14] Silvestru V.A., Englhardt O., Application study for hynrid adhesively bonded glass-steel facade elements, in: Louter C., Bos F., Belis J., Lebet J.P. (Eds.), Challenging Glass 4 & COST Action TU0905 Final Conference, CRC Press, Lausanne, 2014, pp. 277-84.

[15] Budynas R.G., Nisbett J.K., Shigley's mechanical engineering design, 9th ed. ed., McGraw-Hill Higher Education ; London : McGraw-Hill [distributor], New York, 2011.

[16] Kinloch A.J., Adhesion and adhesives : science and technology, Chapman and Hall, London, 1987.

[17] Dillard D.A., Pocius A.V., The mechanics of adhesion, Elsevier, Amsterdam ; London, 2002.

[18] da Silva L.F.M., Öschsner A., Adams R.D., Handbook of adhesion technology, 2nd ed., Springer, Berlin, 2011.

[19] Volkersen O., Die Nietkraftverteilung in zugbeanspruchten Nietverbindungen mit konstanten Laschenquerschnitten, Luftfahrtforschung, 15 (1938) 41.

[20] Goland M., Reissner E., The stress in cemented joints, Journal of Applied Mechanics, 66 (1944) A17.

[21] Hart-Smith L.J., Adhesive-bonded single lap joints, CR-112236, NASA NASA CR-112236, 1973.

[22] da Silva L.F.M., das Neves P.J.C., Adams R.D., Spelt J.K., Analytical models of adhesively bonded joints—Part I: Literature survey, Int J Adhes Adhes, 29 (2009) 319-30.

[23] Ojalvo I.U., Eidinoff H.L., Bond Thickness Effects upon Stresses in Single-Lap Adhesive Joints, AIAA Journal, 16 (1978) 204-11.

[24] Bigwood D.A., Crocombe A.D., Elastic analysis and engineering design formulas for bonded joints, Int J Adhes Adhes, 9 (1989) 229-42.

[25] Frostig Y., Thomsen O.T., Mortensen F., Analysis of Adhesive-Bonded Joints, Square-End, and Spew-Fillet—High-Order Theory Approach, Journal of Engineering Mechanics, 125 (1999) 1298-307.

[26] Mortensen F., Thomsen O.T., Analysis of adhesive bonded joints: a unified approach, Composites Science and Technology, 62 (2002) 1011-31.

[27] Adams R.D., Mallick V., A Method for the Stress Analysis of Lap Joints, The Journal of Adhesion, 38 (1992) 199-217.

[28] Tong L., Bond strength for adhesive-bonded single-lap joints, Acta Mechanica, 117 (1996) 101-13.

[29] Crocombe A.D., Bigwood D.A., Development of a full elasto-plastic adhesive joint design analysis, The Journal of Strain Analysis for Engineering Design, 27 (1992) 211-8.

[30] Wang R.X., Cui J., Sinclair A.N., Spelt J.K., Strength of adhesive joints with adherend yielding: I. Analytical model, The Journal of Adhesion, 79 (2003) 23-48.

[31] da Silva L.F.M., das Neves P.J.C., Adams R.D., Wang A., Spelt J.K., Analytical models of adhesively bonded joints—Part II: Comparative study, Int J Adhes Adhes, 29 (2009) 331-41.

[32] Quispe Rodríguez R., de Paiva W.P., Sollero P., Bertoni Rodrigues M.R., de Albuquerque É.L., Failure criteria for adhesively bonded joints, Int J Adhes Adhes, 37 (2012) 26-36.

[33] da Silva L.F.M., Campilho R.D.S.G., Advances in Numerical Modelling of Adhesive Joints, Springer-Verlag Berlin Heidelberg, Berlin, 2012.

[34] Lee S.J., Lee D.G., Development of a Failure Model for the Adhesively Bonded Tubular Single Lap Joint, The Journal of Adhesion, 40 (1992) 1-14.

[35] da Silva L.F.M., Carbas R.J.C., Critchlow G.W., Figueiredo M.A.V., Brown K., Effect of material, geometry, surface treatment and environment on the shear strength of single lap joints, Int J Adhes Adhes, 29 (2009) 621-32.

[36] Ikegami K., Takeshita T., Matsuo K., Sugibayashi T., Strength of adhesively bonded scarf joints between glass fibre-reinforced plastics and metals, Int J Adhes Adhes, 10 (1990) 199-206.

[37] Harris J.A., Adams R.A., Strength prediction of bonded single lap joints by non-linear finite element methods, Int J Adhes Adhes, 4 (1984) 65-78.

[38] Dean G., Crocker L., Read B., Wright L., Prediction of deformation and failure of rubber-toughened adhesive joints, Int J Adhes Adhes, 24 (2004) 295-306.

[39] Santarsiero M., Louter C., Nussbaumer A., A novel triaxial failure model for adhesive connections in structural glass applications, Engineering Structures, 166 (2018) 195-211.

[40] Dean G., Crocker L., Prediction of the Impact Performance of Plastics Using Finite Element Methods, National Physical Laboratory, Teddington, 2006.

[41] Ignjatovic M., Chalkley P., Wang C., The yield behaviour of a structural adhesive under complex loading, DSTO, Australia, Report DSTO-TR-0728, 1998.

[42] de Morais A.B., Pereira A.B., Teixeira J.P., Cavaleiro N.C., Strength of epoxy adhesive-bonded stainless-steel joints, Int J Adhes Adhes, 27 (2007) 679-86.

[43] Liljedahl C.D.M., Crocombe A.D., Wahab M.A., Ashcroft I.A., Damage modelling of adhesively bonded joints, International Journal of Fracture, 141 (2006) 147-61.

[44] Özer H., Öz Ö., The use of the exponential Drucker-Prager material model for defining the failure loads of the mono and bi-adhesive joints, Int J Adhes Adhes, 76 (2017) 17-29.

[45] Marques E.A.S., da Silva L.F.M., Joint Strength Optimization of Adhesively Bonded Patches, The Journal of Adhesion, 84 (2008) 915-34.

[46] Wang C.H., Chalkley P., Plastic yielding of a film adhesive under multiaxial stresses, Int J Adhes Adhes, 20 (2000) 155-64.

[47] Yu C.M., Huang Z.H., Burgess I.W., Plank R.J., Development and Validation of 3D Composite Structural Elements at Elevated Temperatures, Journal of Structural Engineering-Asce, 136 (2010) 275-84.

[48] Nguyen A.T.T., Pichitdej N., Brandt M., Feih S., Orifici A.C., Failure modelling and characterisation for pin-reinforced metal-composite joints, Compos. Struct., 188 (2018) 185-96.

[49] Sugiman S., Ahmad H., Comparison of cohesive zone and continuum damage approach in predicting the static failure of adhesively bonded single lap joints, Journal of Adhesion Science and Technology, 31 (2017) 552-70.

[50] Simulia D.S., ABAQUS 6.14, Providence, RI, USA., 2014.

[51] Zhao X., Adams R.D., da Silva L.F.M., Single Lap Joints with Rounded Adherend Corners: Stress and Strain Analysis, Journal of Adhesion Science and Technology, 25 (2011) 819-36.

[52] Zhao X., Adams R.D., da Silva L.F.M., Single Lap Joints with Rounded Adherend Corners: Experimental Results and Strength Prediction, Journal of Adhesion Science and Technology, 25 (2011) 837-56.

[53] Crocombe A.D., Global yielding as a failure criterion for bonded joints, Int J Adhes Adhes, 9 (1989) 145-53.

[54] Dragoni E., Mauri P., Intrinsic static strength of friction interfaces augmented with anaerobic adhesives, Int J Adhes Adhes, 20 (2000) 315-21.

[55] Feih S., Shercliff H.R., Adhesive and composite failure prediction of single-L joint structures under tensile loading, Int J Adhes Adhes, 25 (2005) 47-59.

[56] Campilho R.D.S.G., Banea M.D., Pinto A.M.G., da Silva L.F.M., de Jesus A.M.P., Strength prediction of single- and double-lap joints by standard and extended finite element modelling, Int J Adhes Adhes, 31 (2011) 363-72.

[57] Campilho R.D.S.G., Banea M.D., Neto J.A.B.P., da Silva L.F.M., Modelling adhesive joints with cohesive zone models: effect of the cohesive law shape of the adhesive layer, Int J Adhes Adhes, 44 (2013) 48-56.

[58] Sorensen B.F., Jacobsen T.K., Determination of cohesive laws by the J integral approach, Engineering Fracture Mechanics, 70 (2003) 1841-58.

[59] Sorensen B.F., Kirkegaard P., Determination of mixed mode cohesive laws, Engineering Fracture Mechanics, 73 (2006) 2642-61.

[60] Carlberger T., Stigh U., Influence of Layer Thickness on Cohesive Properties of an Epoxy-Based Adhesive—An Experimental Study, The Journal of Adhesion, 86 (2010) 816-35.

[61] Högberg J.L., Stigh U., Specimen proposals for mixed mode testing of adhesive layer, Engineering Fracture Mechanics, 73 (2006) 2541-56.

[62] De Moura M.F.S.F., Gonçalves J.P.M., Chousal J.A.G., Campilho R.D.S.G., Cohesive and continuum mixed-mode damage models applied to the simulation of the mechanical behaviour of bonded joints, Int J Adhes Adhes, 28 (2008) 419-26.

[63] Campilho R.D.S.G., Banea M.D., Neto J.A.B.P., da Silva L.F.M., Modelling of Single-Lap Joints Using Cohesive Zone Models: Effect of the Cohesive Parameters on the Output of the Simulations, The Journal of Adhesion, 88 (2012) 513-33.

[64] Jung Lee M., Min Cho T., Seock Kim W., Chai Lee B., Ju Lee J., Determination of cohesive parameters for a mixed-mode cohesive zone model, Int J Adhes Adhes, 30 (2010) 322-8.

[65] Domingues N.R.E., Campilho R.D.S.G., Carbas R.J.C., da Silva L.F.M., Experimental and numerical failure analysis of aluminium/composite single-L joints, Int J Adhes Adhes, 64 (2016) 86-96.

[66] Campilho R.D.S.G., de Moura M.F.S.F., Ramantani D.A., Morais J.J.L., Domingues J.J.M.S., Buckling Behaviour of Carbon–Epoxy Adhesively-Bonded Scarf Repairs, Journal of Adhesion Science and Technology, 23 (2009) 1493-513.

[67] Fernandes R.L., Campilho R.D.S.G., Testing different cohesive law shapes to predict damage growth in bonded joints loaded in pure tension, The Journal of Adhesion, 93 (2017) 57-76.

[68] de Moura M.F.S.F., Gonçalves J.P.M., Magalhães A.G., A straightforward method to obtain the cohesive laws of bonded joints under mode I loading, Int J Adhes Adhes, 39 (2012) 54-9.

[69] ASTM, ASTM D3433-99, Standard Test Method for Fracture Strength in Cleavage of Adhesives in Bonded Metal Joints, ASTM International, West Conshohocken, PA, 2012.

[70] de Moura M.F.S.F., Numerical simulation of the ENF test for the mode-II fracture characterization of bonded joints, Journal of Adhesion Science and Technology, 20 (2006) 37-52.

[71] Borg R., Nilsson L., Simonsson K., Simulating DCB, ENF and MMB experiments using shell elements and a cohesive zone model, Composites Science and Technology, 64 (2004) 269-78.

[72] Yoon S.H., Hong C.S., Modified end notched flexure specimen for mixed-mode interlaminar fracture in laminated composites, International Journal of Fracture, 43 (1990) R3-R9.

[73] Chaves F.J.P., da Silva L.F.M., de Moura M.F.S.F., Dillard D.A., Esteves V.H.C., Fracture Mechanics Tests in Adhesively Bonded Joints: A Literature Review, The Journal of Adhesion, 90 (2014) 955-92.

[74] IStructE, Guide to the structural use of adhesives, Institution of Structural Engineers, SETO, London, 1999.

[75] Clarke J.L., Structural design of polymer composites : EUROCOMP design code and handbook, E & FN Spon, London, 1996.

[76] European Organisation for Technical Approvals, ETAG 002 Guideline for European Technical Approval for Structural Sealant Glazing Kits (SSGK), European Organisation for Technical Approvals, Brussels, Belgium, 2012.

[77] Staudt Y., Odenbreit C., Schneider J., Investigation of Bonded Connections with Silicone under Shear Loading, Challenging Glass Conference Proceedings; Vol 5 (2016): Challenging Glass 5DO - 10.7480/cgc.5.2259, (2016).

[78] Watson J., Overend M., Jin Q., Lai W., Premature Failure in UV-Cured Adhesive Joints, ISAAG 2010 conference, Munich, Germany, 2010.

[79] Overend M., Jin Q., Watson J., The selection and performance of adhesives for a steel–glass connection, Int J Adhes Adhes, 31 (2011) 587-97.

[80] Nhamoinesu S., Overend M., The Mechanical Performance of Adhesives for a Steel-Glass Composite Facade System, Challenging Glass 3, 2012, pp. 293-306.

[81] Machalicka K., Horcickova I., Eliasova M., Sahmenko G., Shear Adhesive Connections for Glass Structures, in: Rucevskis S., Bajare D. (Eds.), 2nd International Conference on Innovative Materials, Structures and Technologies, 2015.

[82] Machalicka K., Eliasova M., Adhesive joints in glass structures: effects of various materials in the connection, thickness of the adhesive layer, and ageing, Int J Adhes Adhes, 72 (2017) 10-22.

[83] Dispersyn J., Hertelé S., Waele W.D., Belis J., Assessment of hyperelastic material models for the application of adhesive point-fixings between glass and metal, Int J Adhes Adhes, 77 (2017) 102-17.

[84] Dispersyn J., Belis J., Numerical research on stiff adhesive point-fixings between glass and metal under uniaxial load, Glass Structures & Engineering, (2016).

[85] Dispersyn J., Belis J., De Jaegher J., Influence of corner and edge distance of adhesive point-fixings for glass structures, Engineering Structures, 105 (2015) 174-85.

[86] Dispersyn J., Santarsiero M., Belis J., Louter C., A preliminary study of the nonlinearity of adhesive point-fixings in structural glass facades, Journal of Facade Design and Engineering, 2 (2014) 85-107.

[87] Van Lancker B., Dispersyn J., De Corte W., Belis J., Durability of adhesive glass-metal connections for structural applications, Engineering Structures, 126 (2016) 237-51.

[88] Santarsiero M., Louter C., Nussbaumer A., Laminated connections under tensile load at different temperatures and strain rates, Int J Adhes Adhes, 79 (2017) 23-49.

[89] Santarsiero M., Louter C., Nussbaumer A., Laminated connections for structural glass applications under shear loading at different temperatures and strain rates, Construction and Building Materials, 128 (2016) 214-37.

[90] Belis J., Van Hulle A., Callewaert D., Dispersyn J., Out B., Experimental Investigation of Unconventional Canopy Prototypes, Suspended by Adhesive Bonds, in: Bos F., Louter C., Nijsse R., Veer F. (Eds.), Challenging Glass 3, 2012, pp. 177-86.

[91] Silvestru V.A., Drass M., Englhardt O., Schneider J., Performance of a structural acrylic adhesive for linear glass-metal connections under shear and tensile loading, Int J Adhes Adhes, 85 (2018) 322-36.

[92] Silvestru V.A., Englhardt O., Schneider J., Linear adhesive connections at the edge of laminated glass panes: an experimental study under tensile, compressive and shear loading, Glass Structures & Engineering, (2018).

[93] Van Lancker B., De Corte W., Belis J., Mechanical properties of continuous adhesive glass-steel connections under monotonic and cyclic loading, Glass Structures & Engineering, 3 (2018) 197-211.

[94] Santarsiero M., Louter C., Nussbaumer A., Laminated connections for structural glass components: a full-scale experimental study, Glass Structures & Engineering, (2016) 1-23.

[95] Santarsiero M., Bedon C., Louter C., Experimental and numerical analysis of thick embedded laminated glass connections, Compos. Struct., 188 (2018) 242-56.

[96] Bedon C., Santarsiero M., Laminated glass beams with thick embedded connections – Numerical analysis of full-scale specimens during cracking regime, Compos. Struct., 195 (2018) 308-24.

[97] Nhamoinesu S., Overend M., Silvestru V.A., Englhardt O., The mechanical performance of adhesively bonded steel-glass composite panels: Medium-scale tests and numerical models, Challenging Glass 4 & COST Action TU0905 Final Conference, CRC Press, 2014, pp. 269-76.

[98] Pascual C., Nhamoinesu S., Overend M., The flexural response of large scale steel-framed composite glazing panels, Glass Structures & Engineering, 4 (2019) 199-207.

[99] Overend M., Nhamoinesu S., Watson J., Structural Performance of Bolted Connections and Adhesively Bonded Joints in Glass Structures, Journal of Structural Engineering, 139 (2013) 04013015.

[100] Bedon C., Machalická K., Eliášová M., Vokáč M., Numerical Modelling of Adhesive Connections Including Cohesive Damage, Challenging Glass Conference Proceedings, (2018) 309-20%V 6.

[101] Bedon C., Louter C., Structural glass beams with embedded GFRP, CFRP or steel reinforcement rods: Comparative experimental, analytical and numerical investigations, Journal of Building Engineering, 22 (2019) 227-41.

[102] Machalická K., Vokáč M., Eliášová M., Influence of artificial aging on structural adhesive connections for façade applications, Int J Adhes Adhes, 83 (2018) 168-77.

[103] Machalicka K., Vokac M., Kostelecka M., Eliasova M., Structural behavior of double-lap shear adhesive joints with metal substrates under humid conditions, International Journal of Mechanics and Materials in Design, 15 (2019) 61-76.

[104] Machalická K.V., Vokáč M., Kostelecká M., Eliášová M., Durability of structural adhesive joints for facade applications exposed to the extended cataplasm test, J. Adhes., 95 (2019) 632-52.

[105] ISO, ISO 9142:2003, Adhesives - Guide to the selection of standard laboratory ageing conditions for testing bonded joints, International Organization for Standarization, 2003.

[106] Sugiman S., Crocombe A.D., Aschroft I.A., Experimental and numerical investigation of the static response of environmentally aged adhesively bonded joints, Int J Adhes Adhes, 40 (2013) 224-37.

[107] Han X., Crocombe A.D., Anwar S.N.R., Hu P., The strength prediction of adhesive single lap joints exposed to long term loading in a hostile environment, Int J Adhes Adhes, 55 (2014) 1-11.

[108] Hua Y., Crocombe A.D., Wahab M.A., Ashcroft I.A., Continuum damage modelling of environmental degradation in joints bonded with EA9321 epoxy adhesive, Int J Adhes Adhes, 28 (2008) 302-13.

[109] Liljedahl C.D.M., Crocombe A.D., Wahab M.A., Ashcroft I.A., Modelling the Environmental Degradation of the Interface in Adhesively Bonded Joints using a Cohesive Zone Approach, The Journal of Adhesion, 82 (2006) 1061-89.

[110] Crocombe A.D., Hua Y.X., Loh W.K., Wahab M.A., Ashcroft I.A., Predicting the residual strength for environmentally degraded adhesive lap joints, Int J Adhes Adhes, 26 (2006) 325-36.

[111] Liljedahl C.D.M., Crocombe A.D., Wahab M.A., Ashcroft I.A., The effect of residual strains on the progressive damage modelling of environmentally degraded adhesive joints, Journal of Adhesion Science and Technology, 19 (2005) 525-47.

[112] Blandini L., The glass dome, Glass Processing Days 2005, 2005.

[113] Blandini L., Structural use of adhesives for the construction of frameless glass shells, Int J Adhes Adhes, 27 (2007) 499-504.

[114] Weller B., Nicklisch F., Prautzsch V., Vogt I., Outline of Testing and Evaluation Program Used in Selection of Adhesives for Transparent Adhesive Joints in All-Glass Load-Bearing Structures, Journal of ASTM International, 9 (2012) 1-17.

[115] Oikonomopoulou F., Bristogianni T., Veer F.A., Nijsee R., Challenges in the Construction of the Crystal Houses Facade, in: Belis J., Bos F., Louter C. (Eds.), Challenging Glass 5, Ghent University, 2016.

[116] Oikonomopoulou F., Veer F., Nijsee R., Baardolf K., A completely transparent, adhesively bonded soda-lime glass block masonry system, Journal of Facade Design and Engineering, 2 (2014) 201-21.

[117] Oikonomopoulou F., Bristogianni T., Veer F.A., Nijsse R., The construction of the Crystal Houses façade: challenges and innovations, Glass Structures & Engineering, 3 (2018) 87-108.

[118] Katsivalis I., Thomsen O.T., Feih S., Achintha M., Strength evaluation and failure prediction of bolted and adhesive glass/steel joints, Glass Structures & Engineering, 3 (2018) 183-96.

[119] Huntsman, Araldite 2020 (XW 396 / XW 397) - Technical Data Sheet, Basel, 2007.

[120] Delo Industrial Adhesives, Delo-Duopox 03 rapid thix - Technical Data Sheet, Delo Industrial Adhesives, Windach, 2018.

[121] Huntsman, Araldite 2047-1 -Technical Data Sheet, Basel, 2010.

[122] ISO, ISO 527-1:2012, Plastics – Determination of tensile properties, Part 1: General principles, International Organization for Standarization, 2012.

[123] ISO, ISO 527-2:2012, Plastics – Determination of tensile properties, Part 2: Test conditions for moulding and extrusion plastics, International Organization for Standarization, 2012.

[124] ASTM, ASTM D695-15, Standard Test Method for Compressive Properties of Rigid Plastics, ASTM International, West Conshohocken, PA, 2015.

[125] Aben H., Guillemet C., Photoelasticity of glass, Springer-Verlag, Berlin ; London, 1993.

[126] Aben H., Anton J., Errapart A., Modern photoelasticity for residual stress measurement in glass, Strain, 44 (2008) 40-8.

[127] Nielsen J.H., Olesen J.F., Stang H., Characterization of the residual stress state in commercially fully toughened glass, Journal of Materials in Civil Engineering, 22 (2010) 179-85.

[128] Zacaria M., Overend M., The mechanical performance of bi-treated glass, in: Louter C., Bos F., Belis J., Lebet J.P. (Eds.), Challenging Glass 4 & COST Action TU0905 Final Conference, CRC Press, Lausanne, 2014, pp. 747-53.

[129] Achintha M., Balan B.A., An experimentally validated contour method/eigenstrains hybrid model to incorporate residual stresses in glass structural designs, The Journal of Strain Analysis for Engineering Design, 50 (2015) 614-27.

[130] Balan B.A., Achintha M., Assessment of Stresses in Float and Tempered Glass Using Eigenstrains, Exp Mech, 55 (2015) 1301-15.

[131] Oberg E., McCauley C.J., Machinery's handbook : a reference book for the mechanical engineer, designer, manufacturing engineer, draftsman, toolmaker, and machinist, 29th ed. ed., Industrial Press, New York, 2012.

[132] Katsivalis I., Thomsen O.T., Feih S., Achintha M., Development of Cohesive Zone Models for the Prediction of Damage and Failure of Glass/Steel Adhesive Joints, Int J Adhes Adhes, (2019) 102479.

[133] Nguyen A.T.T., Brandt M., Orifici A.C., Feih S., Hierarchical surface features for improved bonding and fracture toughness of metal–metal and metal–composite bonded joints, Int J Adhes Adhes, 66 (2016) 81-92.

[134] Katsivalis I., Thomsen O.T., Feih S., Achintha M., Failure prediction and optimal selection of adhesives for glass/steel adhesive joints, Engineering Structures, 201 (2019) 109646.

[135] Wurm J., Glass structures : design and construction of self-supporting skins, Birkhäuser, Basel ; Boston, 2007.

[136] Blau P.J., Friction science and technology : from concepts to applications, 2nd ed. ed., CRC Press, Boca Raton, Fla. ; London, 2009.

[137] Maggi Y.I., Gonçalves R.M., Leon R.T., Ribeiro L.F.L., Parametric analysis of steel bolted end plate connections using finite element modeling, Journal of Constructional Steel Research, 61 (2005) 689-708.

[138] Loctite, LOCTITE EA 9394 AERO - Technical Data Sheet, 2013.

[139] Loctite, LOCTITE EA 9628 AERO - Technical Data Sheet, 2013.

[140] Loctite, LOCTITE UK 1366 B10 / LOCTITE UK 5452 - Technical Data Sheet, 2014.

[141] Huntsman, Araldite 2024 (XD 4666 A/B) - Technical Data Sheet, Duxform, Cambridge, 2004.

[142] Huntsman, Araldite 2026 - Technical Data Sheet, Basel, 2011.

[143] Huntsman, Araldite 2021-1 Technical Datasheet, Basel, 2016.

[144] Feih S., Kandare E., Lattimer B.Y., Mouritz A.P., Structural Analysis of Compression Deformation and Failure of Aluminum in Fire, Journal of Structural Engineering-Asce, 137 (2011) 728-38.

[145] Mubashar A., Ashcroft I.A., Critchlow G.W., Crocombe A.D., Moisture absorption–desorption effects in adhesive joints, Int J Adhes Adhes, 29 (2009) 751-60.

[146] Liljedahl C.D.M., Crocombe A.D., Gauntlett F.E., Rihawy M.S., Clough A.S., Characterising moisture ingress in adhesively bonded joints using nuclear reaction analysis, Int J Adhes Adhes, 29 (2009) 356-60.

[147] Bowditch M.R., The durability of adhesive joints in the presence of water, Int J Adhes Adhes, 16 (1996) 73-9.

[148] Machado J.J.M., Marques E.A.S., Barbosa A.Q., da Silva L.F.M., Effect of hygrothermal aging on the quasi-static behaviour of CFRP joints varying the overlap length, Compos. Struct., 214 (2019) 451-62.

[149] Duncan B., 14 - Developments in testing adhesive joints, in: Dillard D.A. (Ed.), Advances in Structural Adhesive Bonding, Woodhead Publishing, 2010, pp. 389-436.